Title
Synthesis of Doped Graphene Nanoribbons from Molecular and Polymeric Precursors

Author
Cloke, Ryan

Publication Date
2015

Peer reviewed|Thesis/dissertation

Synthesis of Doped Graphene Nanoribbons from Molecular and Polymeric Precursors

By

Ryan Randal Cloke

A dissertation submitted in partial satisfaction of the

requirements for the degree of

Doctor of Philosophy

in

Chemistry

in the

Graduate Division

of the

University of California, Berkeley

Committee in charge:

Professor Felix Fischer, Chair
Professor John Arnold
Professor Jeff Bokor

Fall 2015

Synthesis of Doped Graphene Nanoribbons from Molecular and Polymeric Precursors

by Ryan Randal Cloke

Abstract

Synthesis of Doped Graphene Nanoribbons from Molecular and Polymeric Precursors

by

Ryan Randal Cloke

Doctor of Philosophy in Chemistry

University of California, Berkeley

Professor Felix Fischer, Chair

As electronic devices continue to shrink and energy problems continue to grow, nanoscale materials are becoming increasingly important. Graphene is a material with exceptional promise to complement silicon in next-generation electronics because of its extraordinary charge carrier mobility, while also finding a role in cutting-edge energy solutions due to its high surface area and conductivity. Improving on this material even further by reducing the width of graphene to nanoscale dimensions with atomically-precise dopant patterns is the subject of this thesis. Nanometer-wide strips of graphene, known as graphene nanoribbons (GNRs), offer the advantages of semiconducting behavior, combined with more accessible surface area compared to bulk graphene (Chapter 1). Additionally, it is demonstrated that GNRs can be doped with atomic precision, allowing for intricate modulation of the electronic properties of this material, which was studied by STM, STS, and nc-AFM (Chapter 2). Controlled growth of GNRs on surfaces is still an outstanding challenge within the field, and to this end, a variety of porphyrin-GNR template materials were synthesized (Chapter 3). The GNRs obtained in this work were also synthesized in solution, and it was shown that these materials possess excellent properties for applications in hydrogen storage, carbon dioxide reduction, and Li-ion batteries (Chapter 4). A prerequisite for solution-synthesized GNRs, conjugated aromatic polymers are an important class of materials in their own right. Therefore, Ring-Opening Alkyne Metathesis Polymerization was developed using conjugated, strained diynes (Chapter 5). The resulting conjugated polymers were explored both for their own materials properties due to a remarkable self-assembly process that was discovered, and also used as precursors to GNRs (Chapter 6). This work advances the fundamental understanding of carbon-based nanostructures, as well as the large-scale production of GNRs for next-generation energy and electronics applications.

Contents

Chapter 1
Introduction

In the first chapter of this thesis, an overview of the discovery of graphene and motivation for graphene nanoribbons is provided. A summary of current methods to isolate graphene and synthesize graphene nanoribbons is presented. The electronic properties and many emerging applications of graphene are discussed, with special attention to the notion of utilizing graphene in next-generation electronic devices. Particular emphasis is placed on the distinction between top-down and bottom-up approaches to graphene nanoribbons. While various approaches to graphene nanoribbon synthesis are presented in detail, it is the highly promising bottom-up approach through chemical synthesis that will be the focus of this thesis.

1.1.1 Introduction

First isolated in pristine form in 2004, graphene is a material with tremendous scientific and technological interest.[1] Consisting of a single sheet of sp^2-hybridized carbon atoms arranged in a hexagonal lattice, the structure of graphene has been confirmed by transmission electron microscopy (TEM)[2] and scanning tunneling microscopy (STM)[3] (Figure 1.1.1).

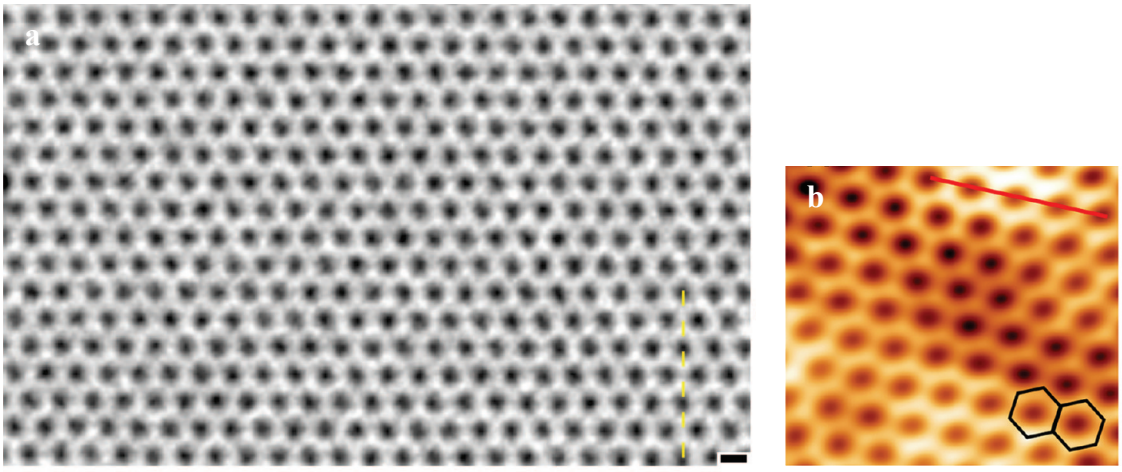

Figure 1.1.1 (a) TEM image (scale bar 0.2 nm) and (b) STM image of graphene [reproduced from refs. 2 and 3, respectively].

Although this seminal work, known colloquially as "the Scotch-tape method," has received over 25,000 citations and a Nobel Prize, the history and chemistry of graphene are, in reality, much more nuanced. As early as the 1840's, the German scientist Schafhaeutl described a procedure to obtain exfoliated graphite oxide by treating graphite with nitric and sulfuric acid.[4] This important discovery served as the basis of the report, over 100 years later, by Boehm *et al.* that exfoliated graphite oxide could be reduced with hydrazine to obtain carbon sheets with reduced oxygen content.[5] It is quite likely that Boehm and coworkers observed a single graphene sheet with this approach, but the lack of modern scanning probe and electron microscopy tools obscured the actual result. Theoretical interest in graphene also predated its isolation by almost 60 years. Predictions as early as 1946 claimed that graphene should have a conductivity 100 times greater within a sheet compared with between sheets.[6] As scientific interest in isolated carbon sheets intensified, Boehm realized that the nomenclature surrounding intercalated graphite compounds was misleading, and so he coined the term, "graphene," in 1986.[7] While it remains possible that Novoselov and Geim were not the first to observe graphene, their work simplified the ability of any group in the world to produce high-quality single-layer graphene and therefore opened the door to a generation of dedicated researchers in this area. Their discovery not only enabled the modern era of graphene research, but moreover, popularized the notion of graphene in the public imagination. Since 2004, the field has expanded rapidly, and it is worth considering the many other approaches to graphene synthesis developed besides micromechanical exfoliation.

1.1.2 Graphene Synthesis via Graphite Oxide

In 2014, the worldwide production of graphite was over 1,165,000 metric tons.[8] At the low price of $700 per metric ton of graphite, any synthesis of graphene beginning from this inexpensive feedstock is incredibly attractive from an economic point of view.[9] For this reason, combined with the more than 170 years of established graphite oxide chemistry, the synthesis of graphene by oxidation and reduction of graphite is a popular option.

The most common method for producing graphite oxide (GO) is known as Hummers' method, which produces 28% oxygen by mass,[10] with an uncontrollable mixture of mostly epoxide and hydroxyl groups in the center of the sheet, as well as carboxyl and carbonyl groups at the edges (Scheme 1.1.1).[11] The polar oxygen containing groups encourage the intercalation of water within the GO sheets, increasing dispersability at the cost of destroying conjugation.

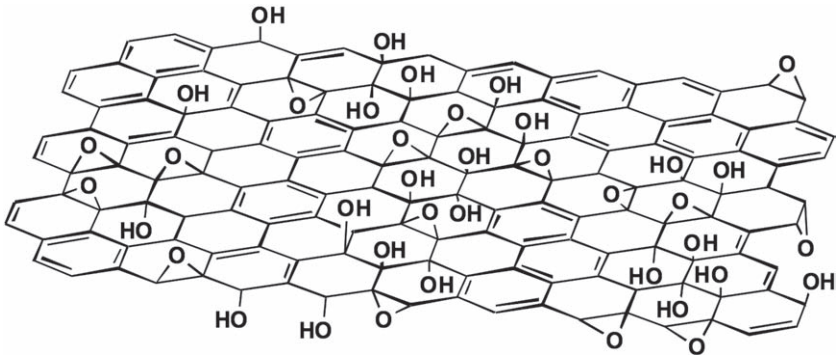

Scheme 1.1.1 Chemical representation of a portion of GO in the Lerf-Klinowski model [reproduced from ref. 11].

Once exfoliated and dispersed, the GO sheets can be reduced by hydrazine. The exact mechanism of reduction is unclear, but it is known through XPS that the overall oxygen content is decreased while the nitrogen content is only slightly increased (Figure 1.1.2b).[12] From this study, it is clear that drastic oxygen removal is effected by reduction with hydrazine. The C-O, C=O, and C(O)(O) peaks are almost completely removed according to XPS, while the C-C peak intensifies and sharpens after reduction. Solid-state ^{13}C NMR reveals that the hydroxyl and epoxide carbons near 50 ppm, along with carbonyl peaks near 200 ppm, are removed, while the aromatic peak near 120 ppm remains after reduction (Figure 1.1.2d). The conditions are too mild for Wolff-Kishner reduction to be operant, but the proposed mechanism of using hydrazine to remove epoxides is shown (Figure 1.1.2c). It seems likely that the nucleophilic hydrazine could ring-open an epoxide, which could form an aminoaziridine that is thermally eliminated to give a new double bond.

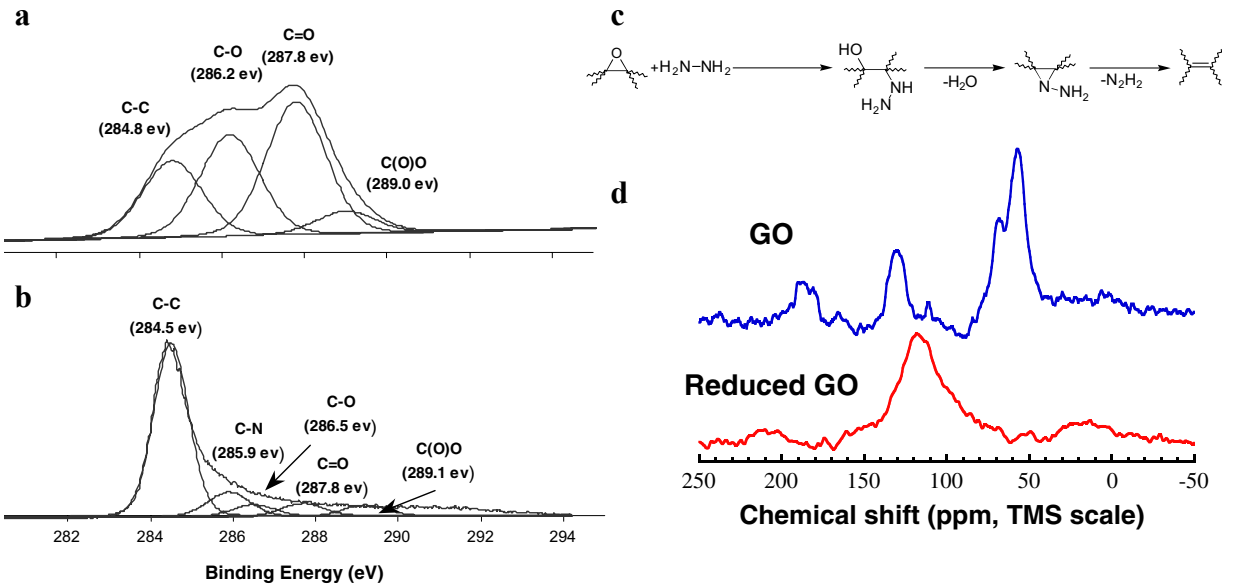

Figure 1.1.2 Chemical nature of GO and reduced GO. XPS analysis of C1s region of (a) GO and (b) reduced GO. (c) Proposed mechanism of epoxide removal. (d) Solid-state ^{13}C NMR of GO and reduced GO. [reproduced from ref. 12].

This same study also demonstrated the dispersability and conductivity loss of GO (Figure 1.1.3).

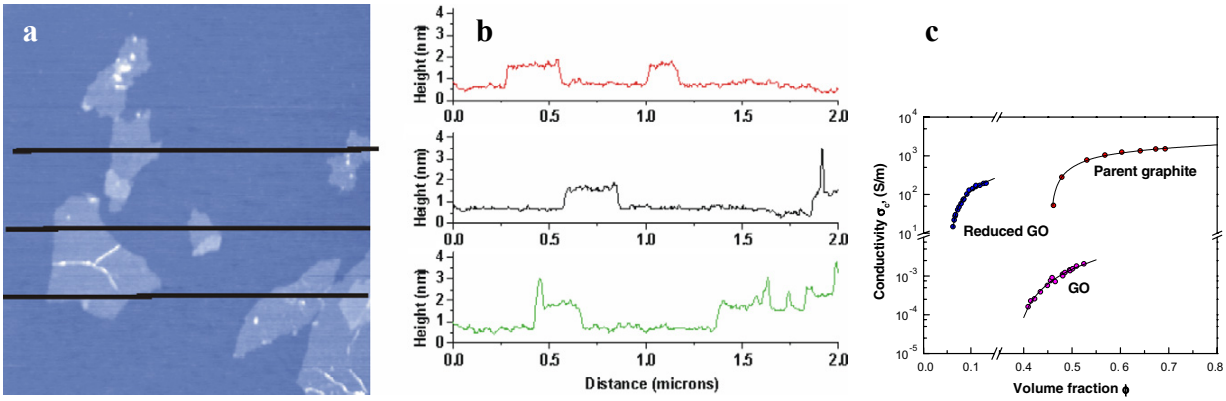

Figure 1.1.3 (a) AFM topography of GO on mica with (b) associated height profiles. (c) Conductivity measurements of graphite, GO, and reduced GO [reproduced from ref. 12].

AFM measurements show a consistent height of ~1 nm. This is much taller than the expected 0.34 nm of a single graphene sheet, but can be attributed to dangling epoxide and hydroxyl groups, as well as the association of water molecules to the sheet. As expected, the parent graphite has a high conductivity near 10^3 S/m. Upon oxidation, the measured conductivity of GO is lowered by six orders of magnitude. Then, as evidence of the success of reduction by hydrazine, conductivity is restored to quite nearly that of bulk graphite.

Recently, the group of Richard Kaner at UCLA has developed a scalable approach to producing single-layer graphene from commercially-available graphite oxide (Figure 1.1.4).[13] By stirring graphite oxide in neat hydrazine for one week, reduced GO sheets were easily dispersed and spin-coated onto silicon oxide. An annealing step removed hydrazine to obtain pure graphene (Figure 1.1.5).

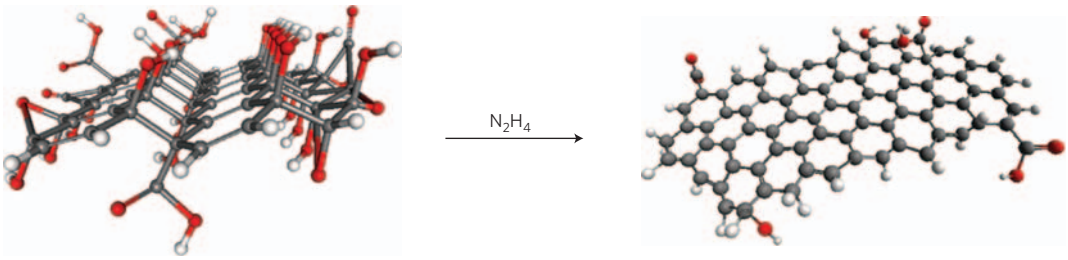

Figure 1.1.4 Chemical reduction of graphene oxide using hydrazine [reproduced from ref. 13].

Although the AFM height profile of 0.6 nm is closer to the expected 0.34 nm of pristine graphene, it suggests that some residual oxygen containing functional groups are still present.

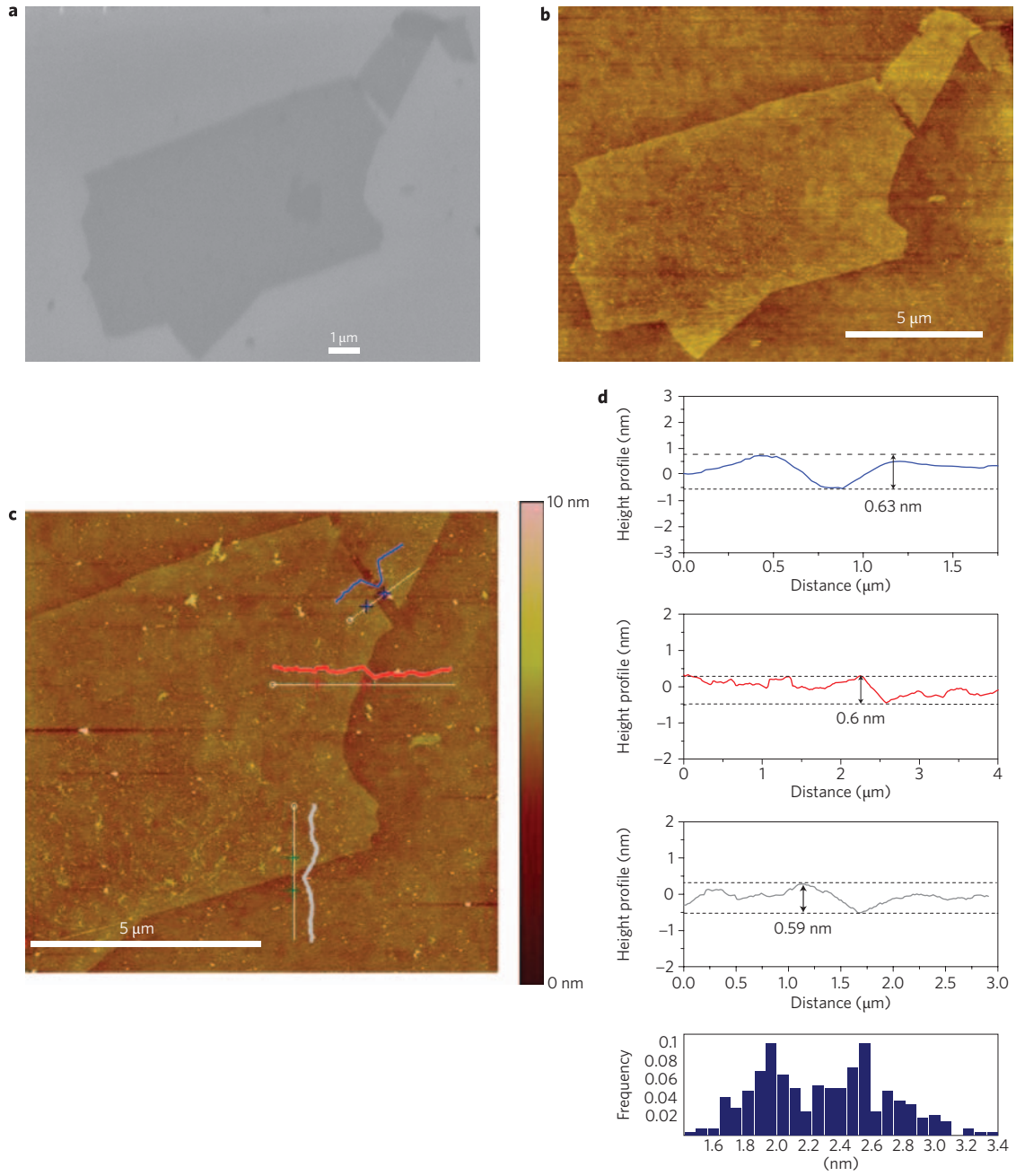

Figure 1.1.5 (a) SEM image and (b) AFM topography of the same single-layer of graphene. (c) Closer inspection by AFM and (d) subsequent height profile analysis proves the presence of a single sheet [reproduced from ref. 13].

Having developed a method to disperse and obtain single graphene sheets, the Kaner Group fabricated field-effect transistors (FETs) from solution-processed reduced graphene oxide (Figure 1.1.6).

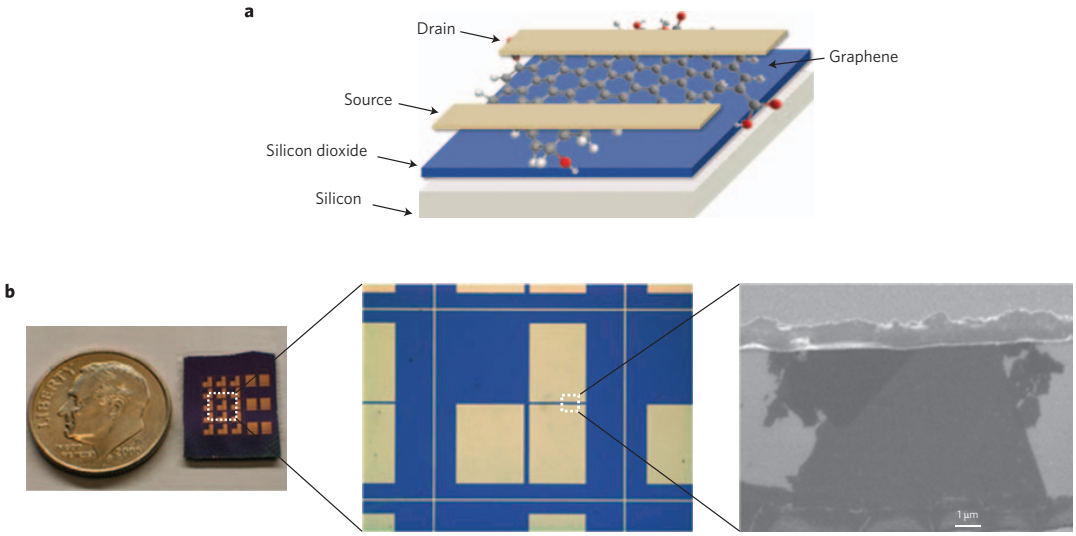

Figure 1.1.6 Fabrication of FETs from solution-processed reduced GO. (a) Representation of graphene field-effect transistor. (b) Photograph, optical image, and SEM image, respectively, of a working FET [reproduced from ref. 13].

Electrical measurements of these transistors show that the devices are metallic at all biases (Figure 1.1.7a). Remarkably, the current collected in the device is improved by eight orders of magnitude after reduction of graphene oxide with hydrazine (Figure 1.1.7b).

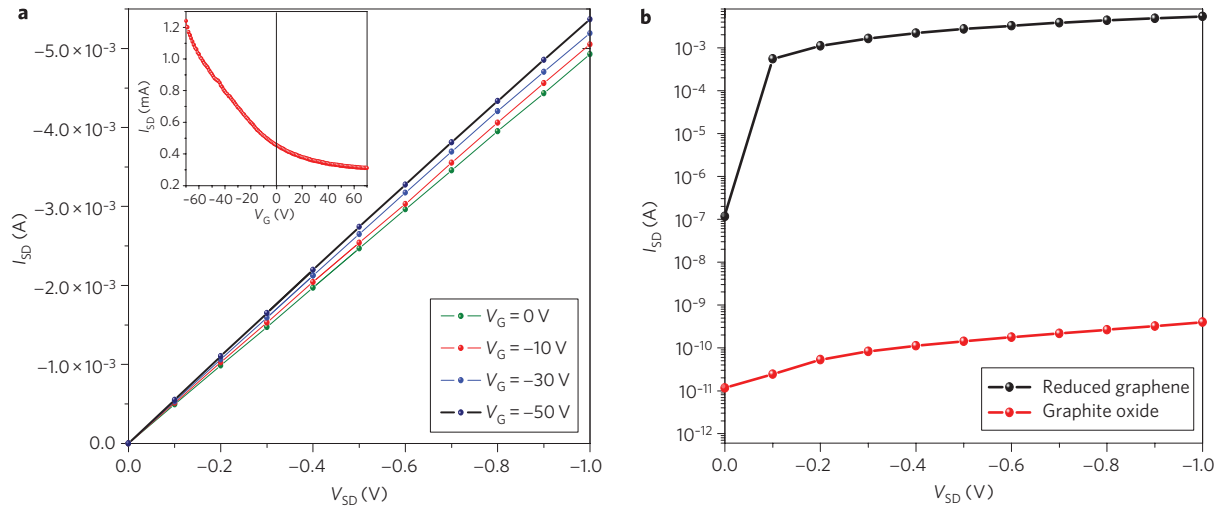

Figure 1.1.7 Electrical data for graphene transistors from solution-processed reduced GO. (a) I-V curves for graphene FETs at different gate biases and (b) I-V curves of reduced GO and GO [reproduced from ref. 13].

While the production of graphene from graphite oxide via oxidation and reduction provides a scalable route to single-layer graphene, it leaves an undesirable amount of unknown defects in

the residual graphene. As such, it remains useful for many applications as well as academic research.

1.1.3 Graphene Synthesis via Reduction of SiC

While the solution-based approaches (liquid-exfoliation and GO reduction) have clear advantages in terms of ease and scale in graphene production, the preparation of pristine graphene under UHV conditions on surfaces is unrivaled in terms of purity and lack of defects. Just two years after the announcement of graphene isolation by Novoselov and Geim, the group of De Heer at the Georgia Institute of Technology developed an epitaxial route to graphene islands in UHV by simply heating silicon carbide.[14] This process works by desorbing silicon atoms at 1000 °C, leaving behind patches of graphitized carbon.[15] Using this method, excellent images of graphene have been produced by STM (Figure 1.1.8).[16]

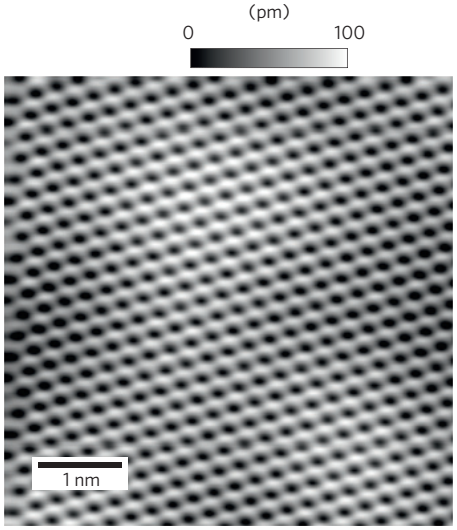

Figure 1.1.8 STM image of graphene produced from reduction of SiC [reproduced from ref. 16].

1.1.4 Graphene Synthesis via Chemical Vapor Deposition

Although the reduction of SiC to graphene is attractive in terms of its simplicity and quality, it is difficult to imagine wafer-scale production of graphene with this method. In contrast, chemical vapor deposition (CVD) of methane on various metal surfaces has demonstrated the ability to grow single-crystal domains of graphene over several milimeters.[17,18] The initial example of large-area CVD of high-quality graphene was reported in 2008 using methane as a carbon precursor on copper foil.[19] Since then, a number of reports have emerged and the CVD approach routinely produces electronics-grade graphene with charge carrier mobilities of 13,000 $cm^2\ V^{-1}\ S^{-1}$ under ambient conditions (Figure 1.1.9).[20] In this report, a single-crystal of graphene as large as 3 mm was achieved. This makes the CVD route of graphene production extremely attractive for next-generation electronics applications.

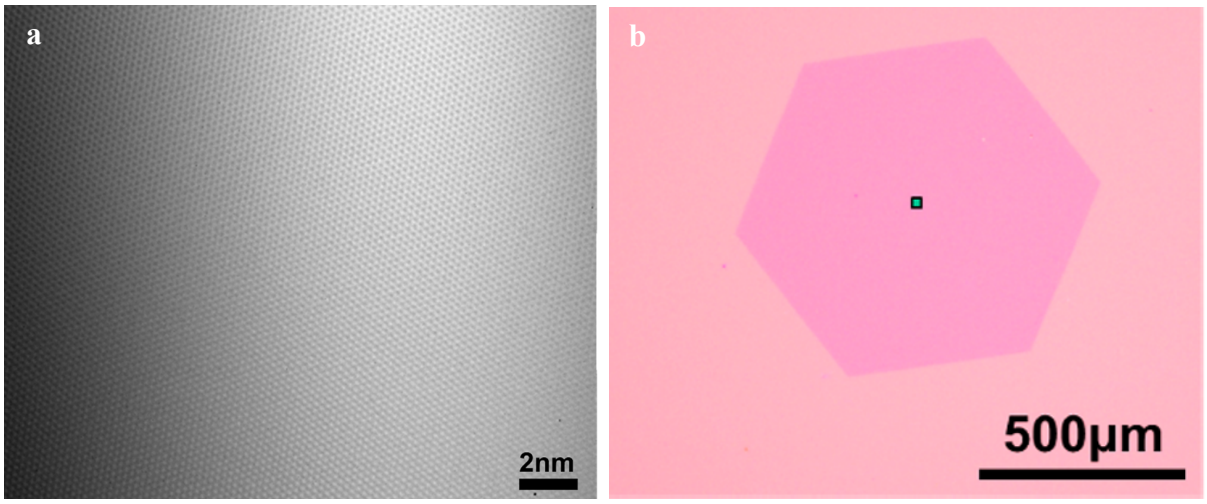

Figure 1.1.9 (a) Abberation-corrected, monochromated TEM image of CVD-grown single-crystal graphene with (b) optical image of the same sample [reproduced from ref. 20].

1.1.5 Applications of graphene

As the production of high-quality single-layer graphene becomes routine, its use in flexible display[21], conductive ink[22], energy[23,24], anti-corrosion[25], genomic sequencing[26], biomedical[27], spintronic[28], and even aeronautic[29] applications has rapidly expanded. Perhaps the most exotic property of graphene, however, is its ballistic electron transport, with charge carrier mobilities exceeding 10^5 cm^2 V^{-1} s^{-1}.[30-32] By comparison, polycrystalline silicon exhibits a mobility of 10^1 – 10^3 cm^2 V^{-1} s^{-1} for electrons, depending on dopant concentration.[33] For this reason, combined with its atomic-scale dimensions, graphene holds extraordinary promise for next-generation electronics.

Unfortunately, graphene is a zero band gap semimetal, which limits its utility in electronic applications requiring semiconductor logic.[34] This is because the conduction and valence bands meet at a single point, known as Dirac cones, in the Brillouin zone (Figure 1.1.10).[35,36]

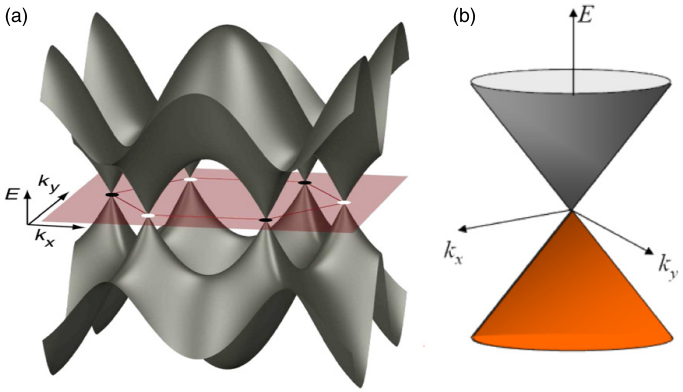

Figure 1.1.10 3D band structure of graphene [reproduced from ref. 35].

However, confinement of graphene to nanometer-wide stripes in one-dimension opens a significant band gap, which makes the synthesis of this material an exigent challenge.

1.2.1 Graphene Nanoribbons: Introduction

If a graphene sheet is cut in a straight line, it can be cut in many different ways. However, only two configurations have well-defined edges, and are described as armchair or zigzag GNRs (Figure 1.2.1a). The properties of zigzag and armchair GNRs differ markedly. The former are considered metallic, while the latter display an inverse dependence of band gap with width. This trend was described by the Louie Group in 2008 (Figure 1.2.1b).[37]

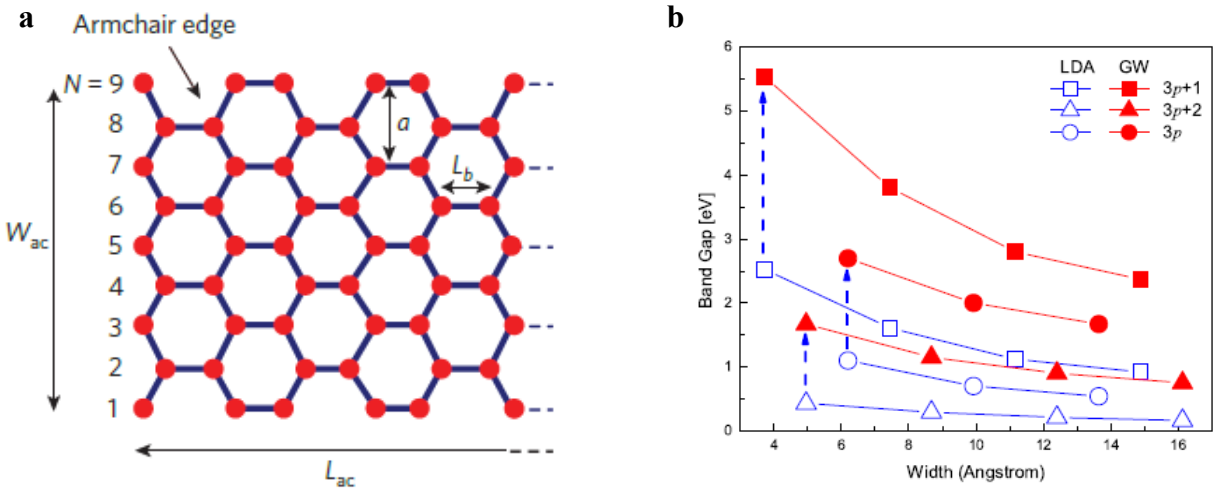

Figure 1.2.1 (a) Overview of armchair and zigzag edge nomenclature in GNRs. (b) Band gap dependence on the width of armchair GNRs calculated at the DFT-LDA and GW-corrected theory levels [reproduced from ref. 37].

Zigzag GNRs are particularly interesting because they are predicted to possess an antiferromagnetic ground state, leading to half-metallic states in electric fields that could potentially transport spin-polarized currents.[38,39] Unfortunately, the localization of spin-polarized electrons to the zigzag edges makes them especially reactive with singlet oxygen, and even small-molecule analogs react deleteriously under mild conditions (Figure 1.2.2).[40]

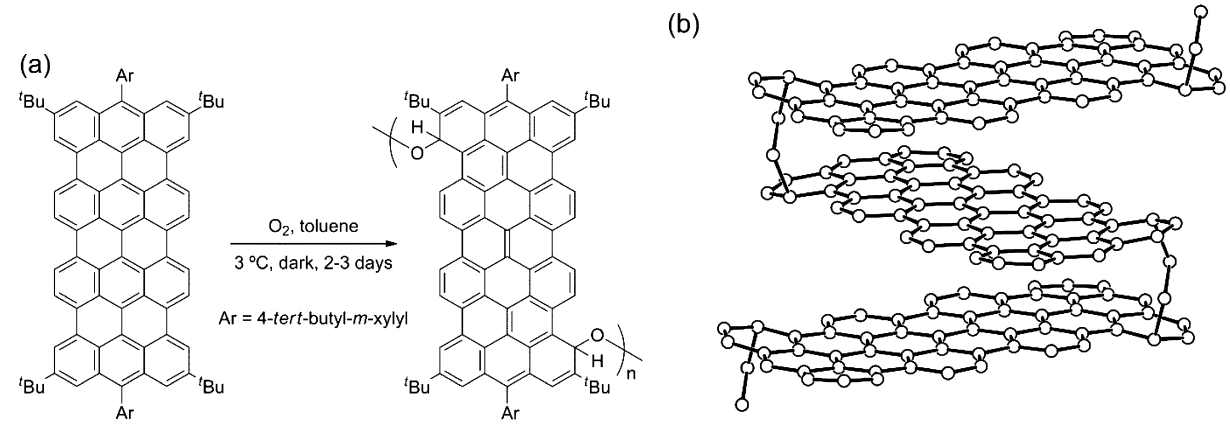

Figure 1.2.2 (a) Reactivity of a model zigzag compound with oxygen. X-ray crystal structure of oligomeric product (*tert*-butyl groups and hydrogens omitted for clarity) [reproduced from ref. 40].

Instead, armchair GNRs are quite stable, and given their semiconducting nature and tunable band gap, considered as highly attractive targets for energy and electronics applications.

1.2.2 Top-Down Approaches to GNRs: Lithography

The most straightforward, and chemically oblivious, approach to GNRs is to simply cut a sheet of graphene into very narrow strips. One such approach is the use of helium ion beam lithography inside of a helium ion microscope to cut and image a GNR device (Figure 1.2.3).[41]

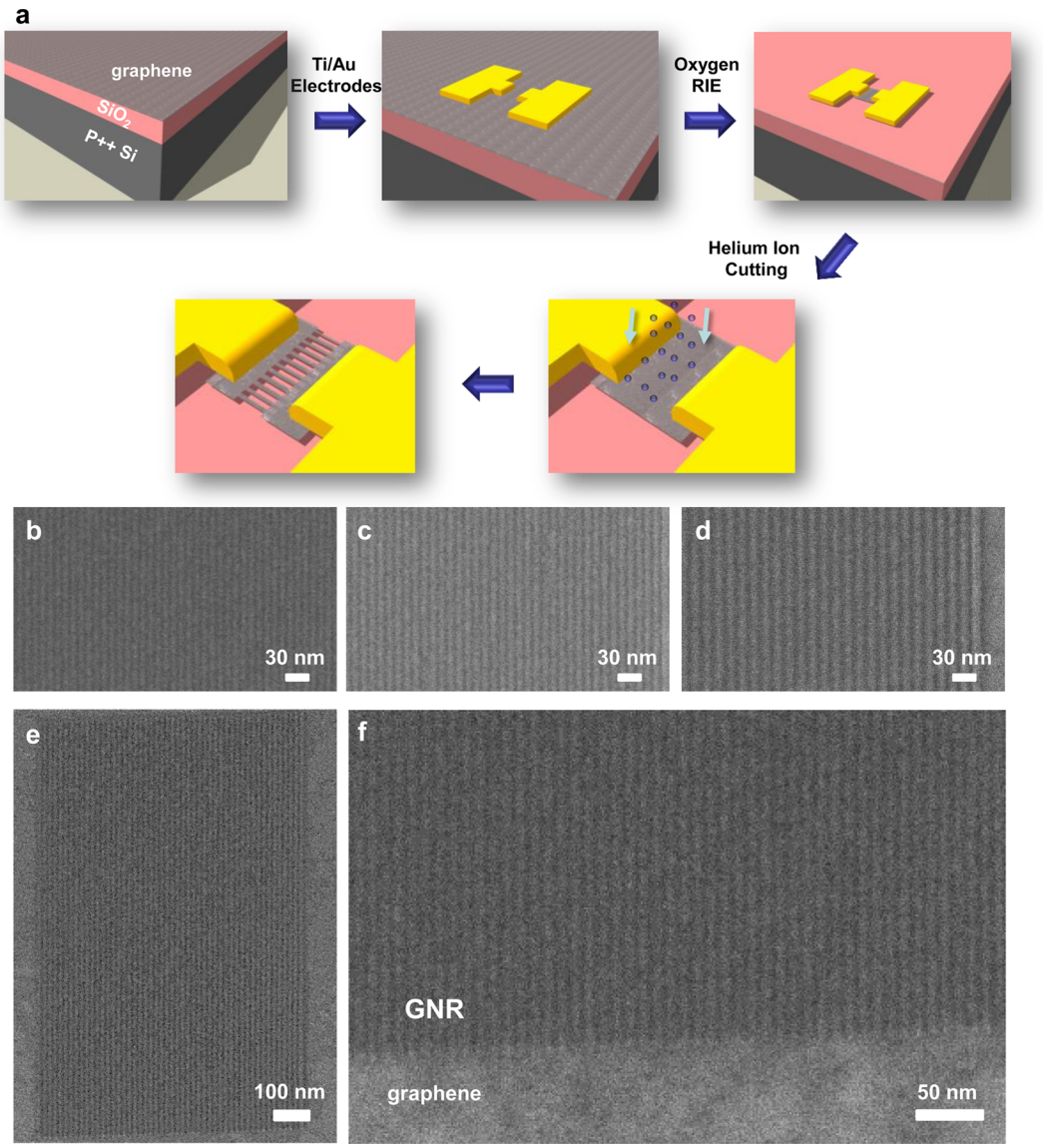

Figure 1.2.3 (a) Schematic of GNR transistor fabrication. Helium ion microscope image of (b) 5nm, (c) 6 nm, and (d) 7.5 nm half-pitch arrays. (e) Large area image of aligned GNRs (5 x 1200 nm long). (f) Helium ion microscope image of the graphene - GNR interface [reproduced from ref. 41].

Despite the ability to pattern GNRs on the 5-nm scale, the on / off ratio in FETs measured in this work had a maximum of 4.75 at low temperature (77 K). This is over five orders of magnitude lower than standard carbon nanotube FETs, and not useful for modern semiconductor applications.[42] The low performance of this device is likely due to the destructive nature of the helium ions on the sensitive edges of the GNR. Since it is unlikely that e-beam or extreme UV lithography can achieve significantly better resolution than 5 nm, or can be less damaging to the GNR edges, other approaches to GNR synthesis are being pursued as well.

1.2.3 Top-Down Approaches to GNRs: Unzipping of CNTs

Another approach to GNR synthesis involves unzipping carbon nanotubes using either chemical or plasma etching means. The concept of unzipping CNTs was reported concomitantly by the Tour Group and the Dai Group. Tour and coworkers used potassium permanganate to oxidize carbon-carbon double bonds within the CNT to make new ketones (Figure 1.2.4).[43] The release of strain at one point in the CNT weakens the adjacent bonds, which oxidize successively to unzip the nanotube.[44]

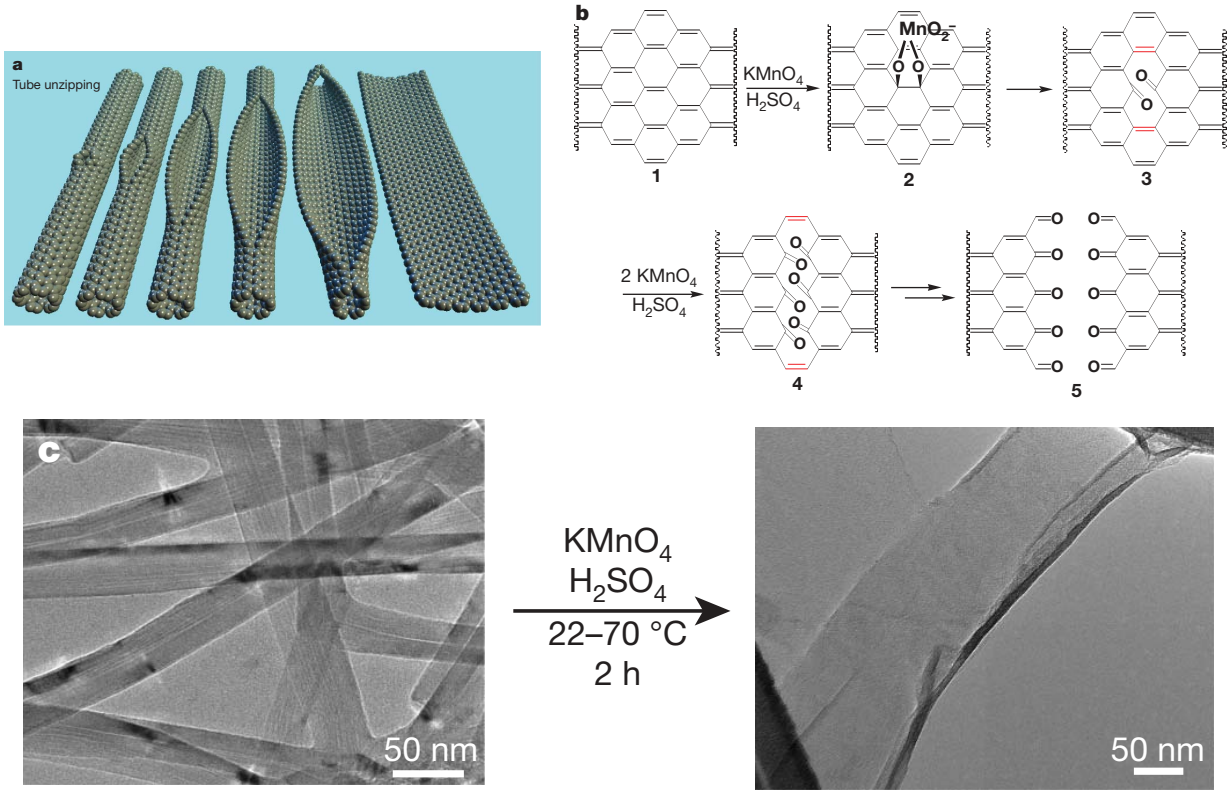

Figure 1.2.4 Unzipping of CNTs reported by the Tour Group using oxidative chemistry. (a) Schematic representation of unzipping. (b) Chemical representation of the oxidation process. (c) TEM images of MWCNTs being converted to GNRs [reproduced from ref. 43].

This report represented a creative new approach, but produced GNRs that were hundreds of nanometers wide and metallic in nature, which is hardly an improvement over graphene itself. Meanwhile, the Dai approach produced very narrow GNRs (Figure 1.2.5 and Figure 1.2.6).[45]

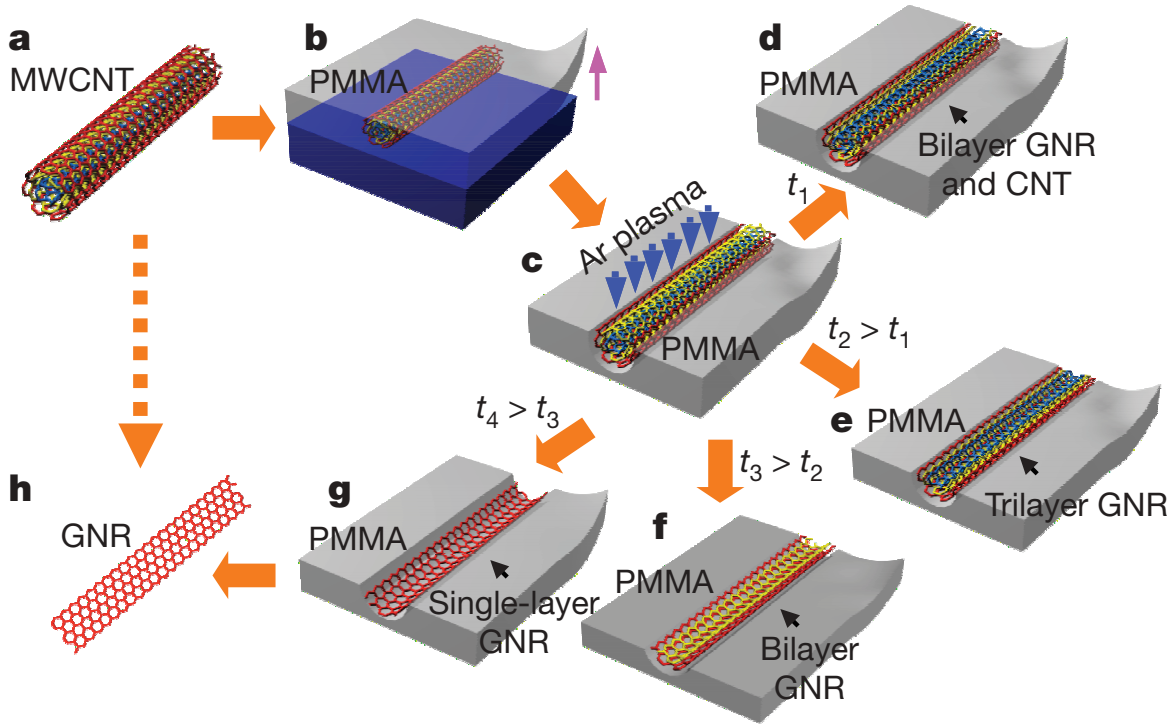

Figure 1.2.5 Schematic representation of GNR synthesis from (a) MWCNTs. (b) MWCNT was deposited on Si and coated with PMMA. (c) The film was peeled, flipped over, and exposed to Ar plasma. (d–g) Single to multi-layer GNRs were obtained depending on etching time. (h) PMMA was removed to obtain the GNR [reproduced from ref. 45].

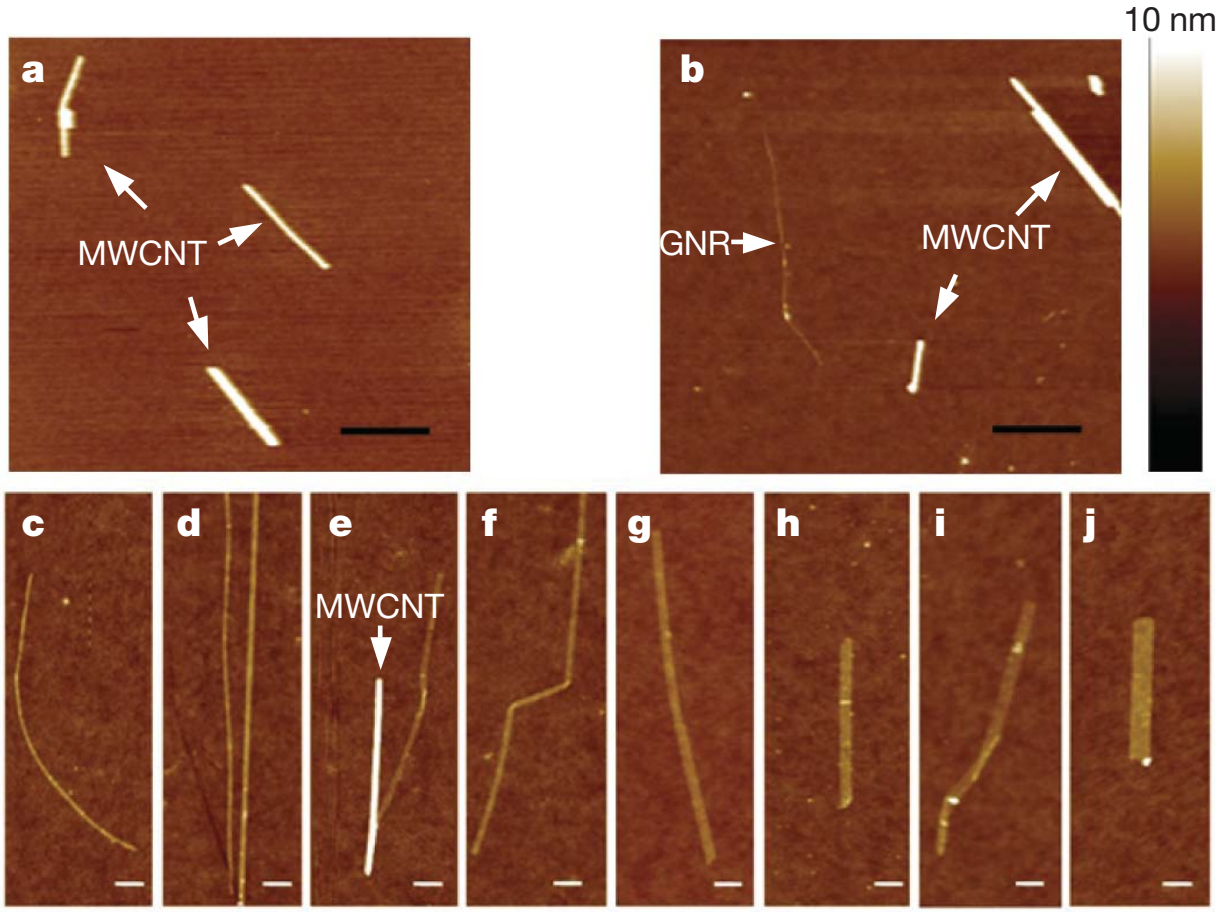

Figure 1.2.6 AFM images of GNRs derived from MWCNTs showing (a) MWCNTs, (b) coexistence of MWCNTs and GNRs after Ar plasma, and (c–j) single- or few-layer GNRs. Height scale for all images is 10 nm and scale bar is 100 nm [reproduced from ref. 45].

The Dai group used these GNRs on SiO_2 to fabricate FETs. The best device was derived from a GNR of approximately 6 nm in width and had an on / off ratio of over 100. This ratio is more than 20 times the value obtained by current lithographic techniques, even though the widths are equal (or at least within the experimental error of width estimation). This indicates that the electronic transport properties of GNRs are intimately related to the chemical structure and integrity of the GNR edges. While an improvement over lithography, the on / off ratio is still at least four orders of magnitude below the minimum in current electronic devices.

1.2.4 Top-Down Approaches to GNRs: Exfoliation of Graphite

After exfoliation of graphite at 1000 °C in forming gas, Dai and coworkers were able to produce narrow strips of graphene and visualize them with Atomic Force Microscopy (AFM) (Figure 1.2.7). [46]

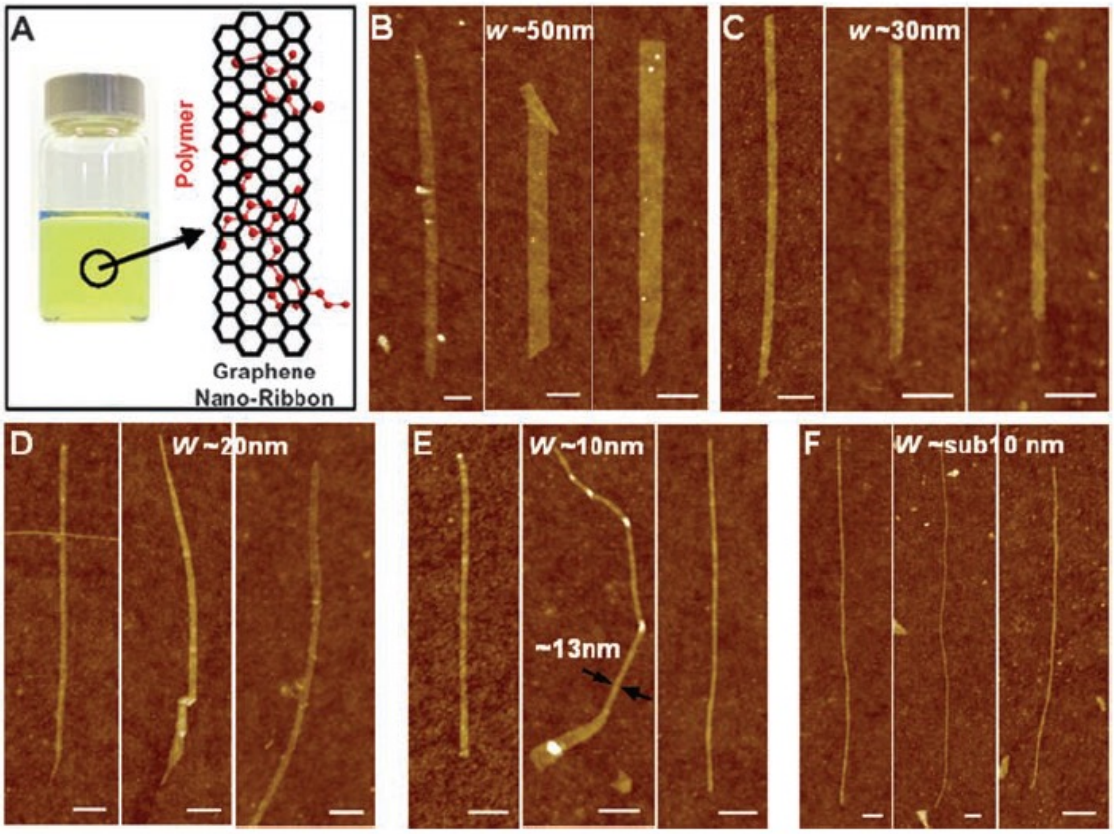

Figure 1.2.7 Graphene nanoribbons produced by exfoliation of graphite (A) and visualized by AFM (B–F). All scale bars indicate 100 nm [reproduced from ref. 46].

Using the GNRs derived from this method, the Dai group was able to demonstrate the dependence of GNR band gap on width (Figure 1.2.8). At 10 nm, the observed band gap is approximately 0.1 eV with a very low on / off current ratio. Below 10 nm, the on / off ratio and band gap increase exponentially. By constructing field-effect transistor (FET) devices from GNRs, the Dai group was able to obtain a maximum on / off ratio near 10^7. This value is at or near the value required for advanced displays and resistive memories,[47] as well as the value obtained by the best carbon nanotube (CNT) transistors.[48] While CNT-FETs are promising for next-generation electronics, they are invariably contaminated with a certain amount of metallic tubes, which is prohibitive for very large scale integration (VLSI).[49] Instead, it is hoped that graphene can overcome this problem through the development of a method to produce only semiconducting GNRs.

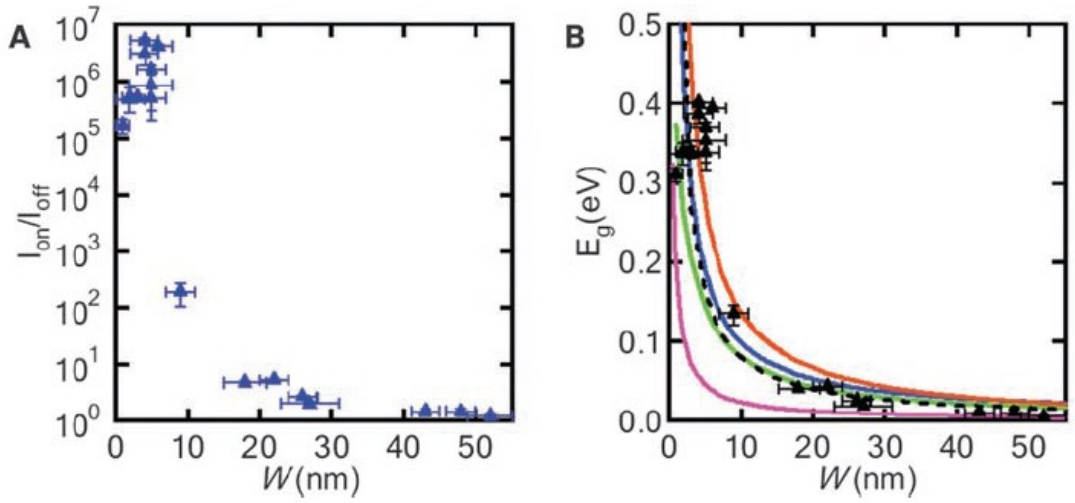

Figure 1.2.8 Dependence of GNR electrical properties on width of GNR. (A) On / off current ratio in GNR FETs with 0.5 eV bias and (B) band gap dependence on width of GNR as determined by AFM. Black dashed line is the experimental fit while colored lines indicate theoretical predictions [reproduced from ref. 46].

While this seminal work demonstrated the exceptional promise of GNRs, the mixture of widths obtained by this route meant that an inseparable batch of both semiconducting and metallic GNRs were produced, precluding their use in VLSI. In a separate study, the Dai group also found that the charge carrier mobility in GNRs depended inversely on the apparent width (Figure 1.2.9).[50] The transport properties of GNRs depend crucially on their edge structure. Increased scattering results from most lithographic methods, while quantum wire behavior results for near-perfect edges.[51]

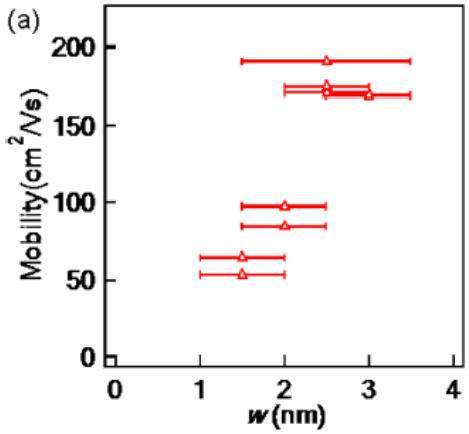

Figure 1.2.9 Inverse dependence of charge carrier mobility on the width of GNRs [reproduced from ref. 50].

Despite the many top-down routes available to produce GNRs, intractable mixtures of GNRs with different widths, and therefore band gaps, are always the result. This makes their incorporation into logic-based semiconductor applications impractical.[52]

1.3 Bottom-Up Approaches to GNRs: the Era of Chemical Synthesis

In 2009, a breakthrough in GNR synthesis occurred in the groups of Klaus Müllen and Roman Fasel. Utilizing a molecular precursor, 10,10'-dibromo-9,9'-bianthracene, the team demonstrated the first example of atomically precise GNRs, where the width of the nanoribbon was completely preordained by the width of the molecular precursor used (Figure 1.3.1).[53] By subliming the molecular precursor onto a Au(111) surface in ultra high vacuum (UHV) within a scanning tunneling microscope (STM), the molecule first polymerizes at 200 °C and subsequently undergoes cyclodehydrogenation at 400 °C to yield the target graphene nanoribbon (Figure 1.3.2).

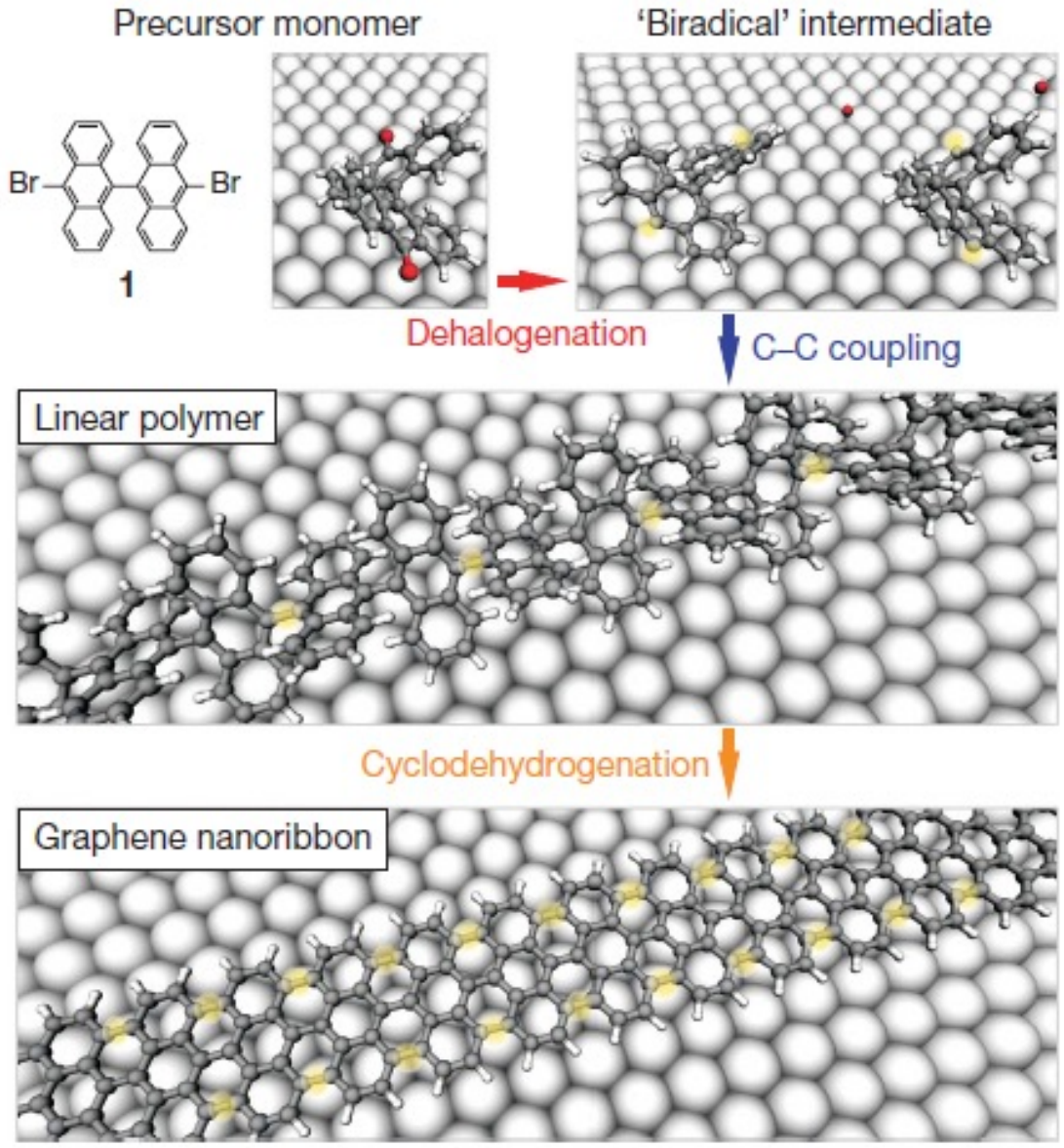

Figure 1.3.1 Overview of surface-assisted GNR synthesis showing the evolution from small-molecule to GNR [reproduced from ref. 53].

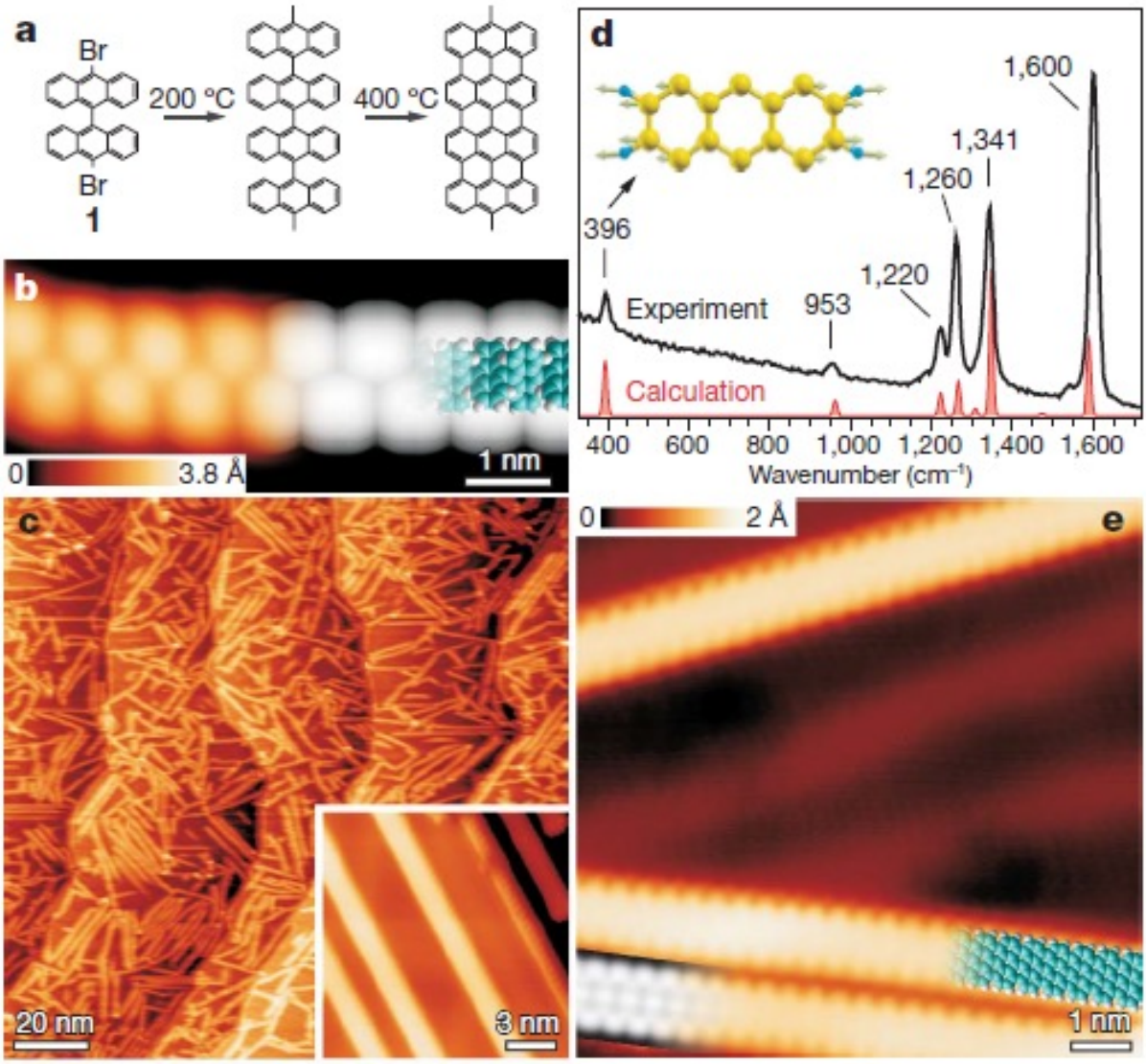

Figure 1.3.2 STM images of the first example of atomically precise GNRs. (a) Schematic overview, (b) STM image of the polymer stage, (c) large-area STM image of GNRs (d) Raman spectrum of n =7 AGNR along with predicted spectrum, and (e) high-resolution STM image are shown [reproduced from ref. 53].

This revolutionary methodology opens the door for the synthesis of GNRs with a single, deterministic width, allowing for unambiguous determination of their physical properties and incorporation into next-generation electronic devices. The discovery of the Au(111) catalyzed polymerization and cyclodehydrogenation heralded the start of a new phase in GNR research, one in which chemical synthesis will play a defining role. The GNRs that can be made by this approach, and consequently the exotic physics that can be studied, are only limited by the creativity and capacity of organic chemists to design and synthesize the right molecules.

Chapter 2
Site-Specific Substitutional Doping of Armchair Graphene Nanoribbons

A fundamental requirement for next-generation electronic devices based on graphene nanoribbon (GNR) technology is the ability to control the band structure and charge carrier concentration by substituting specific carbon atoms in the hexagonal graphene lattice with p- or n-type dopant heteroatoms. Here we report the atomically precise introduction of boron dopant atoms into bottom-up fabricated semiconducting armchair GNRs (AGNRs). Trigonal-planar B-atoms along the backbone of the GNR share an empty p-orbital with the extended π-band, which causes substantial changes in its electronic structure. Scanning tunneling microscopy (STM) topography reveals a characteristic modulation of the local density of states along the backbone of the GNR that is consistent with the expected position and concentration of dopant B-atoms. First-principles calculations support the experimental findings and provide additional insight into the electronic structure of B-doped 7-AGNRs. Non-Contact AFM supports that hypothesis that the boron atoms exhibit a complex interaction with the Au(111) substrate.

Parts of this chapter have been published in:
Cloke, R.R.; Marangoni, T.; Nguyen, G.; Joshi, T.; Rizzo, D.J.; Bronner, C.; Cao, T.; Louie, S.G.; Crommie, M.F.; Fischer, F.R. *J. Am. Chem. Soc.* **2015**, *137*, 8871–8875.

2.1 Introduction

Atomically defined graphene nanoribbons (GNRs), two-dimensional configurations of single-layer graphene featuring high aspect ratios, have attracted increased interest for their exotic electronic and magnetic properties emerging from quantum interference effects at the nanometer scale.[53-58] Atomically precise control over the boundary conditions imposed by the width, the crystallographic symmetry, and the edge structure of GNRs is paramount for the rational design of device-critical parameters such as the band gap, the Fermi level, and the position and concentration of dopant atoms.[59-66] Recent advances in the bottom-up fabrication of atomically precise GNRs from molecular precursors have demonstrated the rational modulation of the width, the symmetry, the edge structure (armchair, chevron, cove) and the incorporation of nitrogen atom dopants in the form of pyridine and pyrimidine rings into the edges of chevron-GNRs.[45-49] Since the lone-pair of the N-heteroatom in these structures is not in conjugation with the extended π-system of the GNR, edge doping only shifts the position of both the conductance and valence band edges of the ribbon without introducing dopant states into the gap.[62] Controlled n-/p-doping, i.e. the controlled introduction of filled/empty donor or acceptor states into the gap of atomically defined GNRs, instead requires the incorporation of dopant heteroatoms at precise positions along the backbone of the ribbon where the filled/empty p-orbitals are in conjugation with the extended π-system.

Here we report the bottom-up synthesis and characterization of atomically-defined hydrogen terminated n = 7 armchair GNRs featuring a regioregular pattern of B-atoms along the central backbone of the ribbon.

We performed the thermally-induced radical step-growth polymerization/cyclization of the molecular precursor, 5,10-bis(10-bromoanthracene-9-yl)-5,10-dihydroboranthrene, on Au(111) in ultra high vacuum (UHV). Low-temperature scanning tunneling microscopy (STM) imaging of fully cyclized B-doped 7-AGNRs (B-7AGNRs) reveals a unique, characteristic stripe pattern along the length of the ribbon with a period corresponding to the distance between the expected position of dopant atoms in the molecular repeat unit. This is consistent with the empty p-orbitals of boron conjugating to the extended π-system of the 7-AGNR and acting as substitutional dopants. Density functional theory (DFT) calculations reveal that B-7AGNRs have a deep acceptor band at energies within the gap of undoped 7-AGNRs, which is localized along the backbone of a B-7AGNR and verified experimentally through dI/dV imaging. Dr. Tomas Marangoni of the Fischer Group grew X-ray quality crystals and assisted with the scale-up of **1**. Giang Nguyen, Daniel Rizzo, Trinity Joshi, and Chris Bronner of the Crommie Group performed STM, STS, and nc-AFM of B-7AGNRs. Ting Cao of the Louie Group provided first-principle DFT calculations.

2.2 Synthesis of Boron-Doped GNR Monomers

Strategically, we envisioned a new paradigm of doping for graphene nanoribbons by placing the dopants in the interior of the GNR (Figure 2.1). This serves the dual purpose of placing the dopant atoms in full conjugation with the GNR as well as sterically shielding the more reactive dopant atoms from the harsh conditions of polymerization and cyclodehydrogenation. This necessitates the redesign of the bisanthracene building block to a trisanthracene type structure.

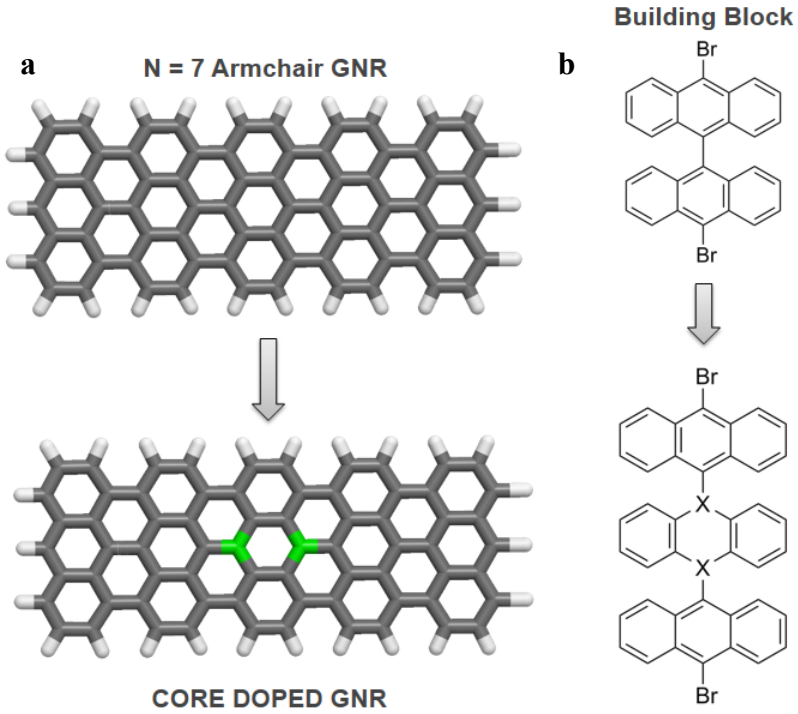

Figure 2.1 (a) Concept of core-doping in graphene nanoribbons and (b) extension of bisanthracene type monomers to core-doped GNR monomers.

The requisite monomer **1** was synthesized in three steps from *o*-dichlorobenzene (Scheme 2.1). First, Mg-halogen exchange and quenching with TMSCl afforded bis-silane **3**. Subsequent insertion of BBr_3 into the C-Si bonds and cyclization yielded the extremely air sensitive boranthracene **4**.

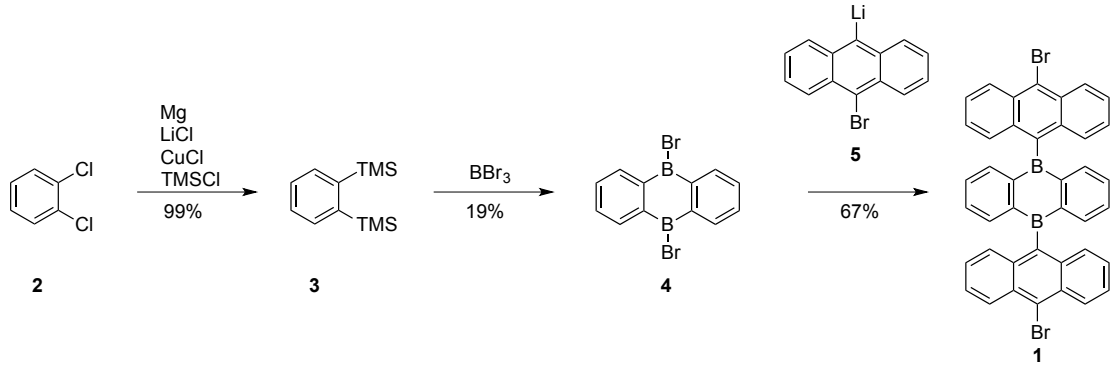

Scheme 2.1 Synthesis of boron-doped monomer **1**.

The boron-doped 7-AGNR precursor **1** was obtained through selective mono-lithiation of dibromoanthracene to obtain **5**, followed by borylation with 5,10-dibromo-5,10-dihydroboranthrene **4** in 67% yield. The structure of **1** was unambiguously confirmed by X-ray diffraction (Figure 2.2). Orange crystals suitable for X-ray diffraction were obtained by slow evaporation of a $C_2H_2Cl_4$ solution. **1** adopts a C_i symmetry in the crystal lattice. The geometry

around the boron atom is trigonal-planar with bond angles and bond distances ranging between 119.7–120.9° and 1.56–1.78 Å, respectively. While the two 9-bromoanthracene units are coplanar, the central boranthrene is twisted out of planarity (dihedral angle C(2)-C(1)-B(1)-C(15) = 97.6°). This non-planar conformation is crucial as it sterically shields the Lewis acidic B-atoms from nucleophilic attack and imparts a favorable non-planar geometry to the molecule, a prerequisite for an efficient radical step-growth polymerization on the Au(111) substrate.[75-78]

Despite the reported instability of this class of substituted boranthrenes, crystals of **1** are stable in air at 24 °C, showing no signs of degradation over several months, as indicated by ^{1}H NMR spectroscopy (Figure 2.3a).[73,74,79] DSC and TGA analysis revealed a melting point above 350 °C and a gradual mass loss associated with partial dehalogenation above this temperature (Figure 2.3b), indicating that this molecule was thermally stable enough to be sublimed in ultra-high vacuum (UHV) without degradation.

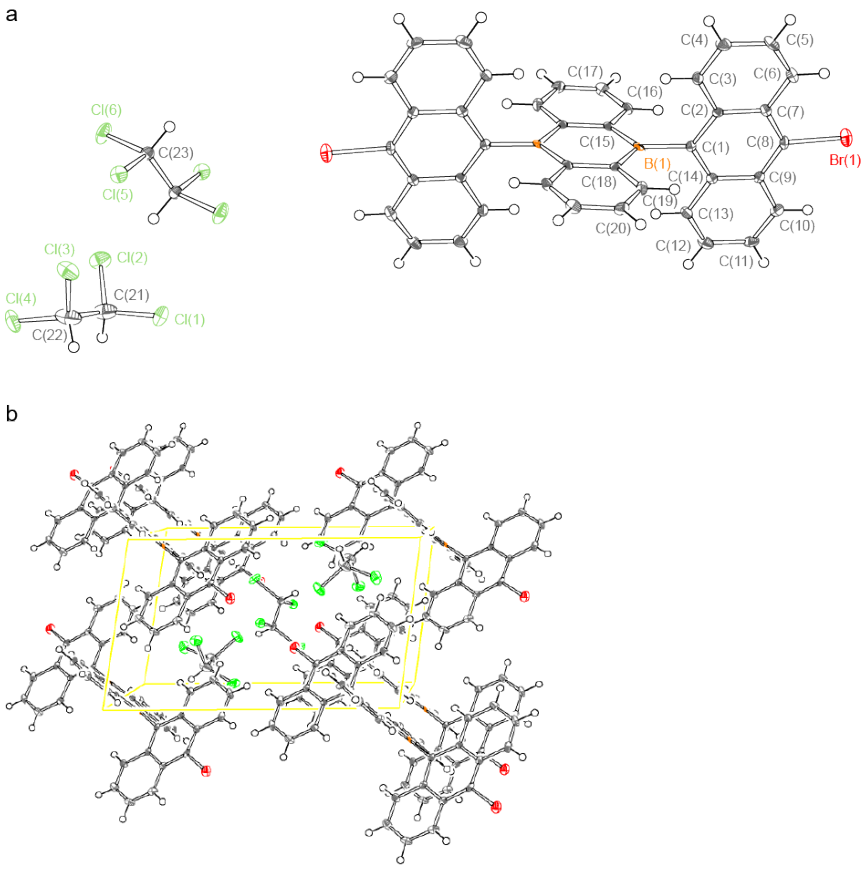

Figure 2.2 ORTEP representation of the (a) X-ray crystal structure and (b) unit-cell packing of **1**. Thermal ellipsoids are drawn at the 50% probability level. Color coding: C (gray), Br (red), B (orange). Relevant structural parameters: C(1)-B(1), 1.578(5) Å; C(15)-B(1), 1.561(5) Å; C(18)-B(1), 1.562(5) Å; C(2)-C(1)-B(1)-C(15), 97.6°; $C_{46}H_{30}B_2Br_2Cl_{12}$; 1189.54 g mol^{-1}; triclinic; P-1; orange; a = 8.6046(3) Å; b = 9.8632(4) Å; c = 14.5013(6) Å; α = 82.148(2)°, β = 82.067(2)°; γ = 74.011(2)°; 100 (2) K; Z = 1; R1 = 0.0387; GOF on F^2 = 1.036.

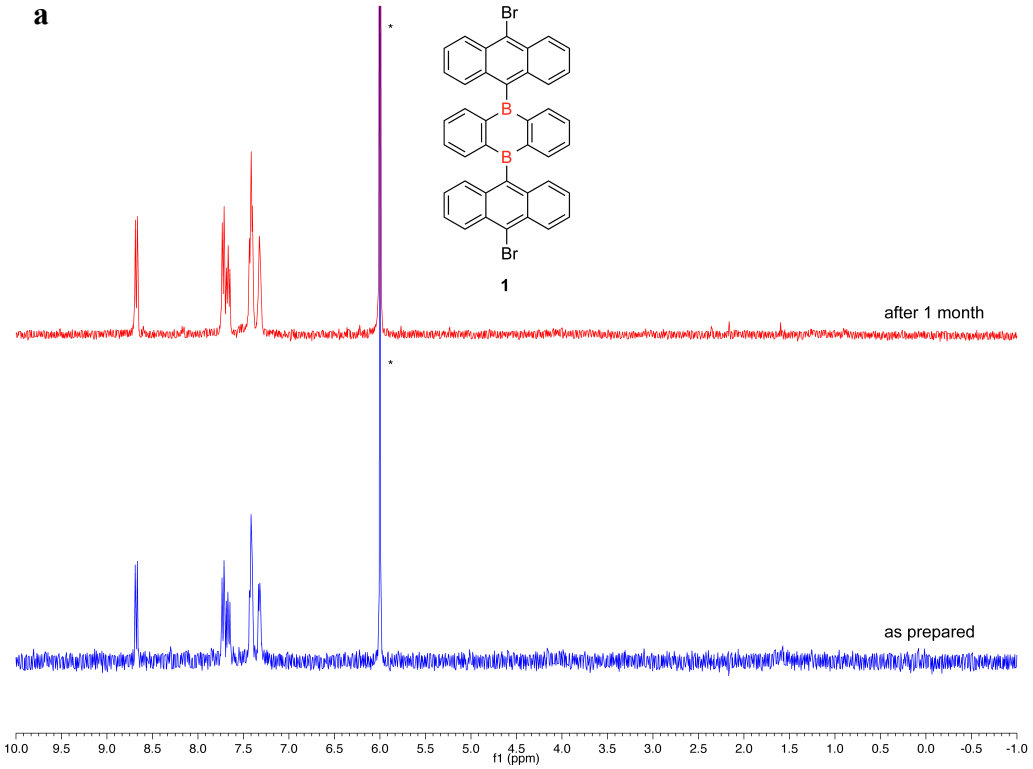

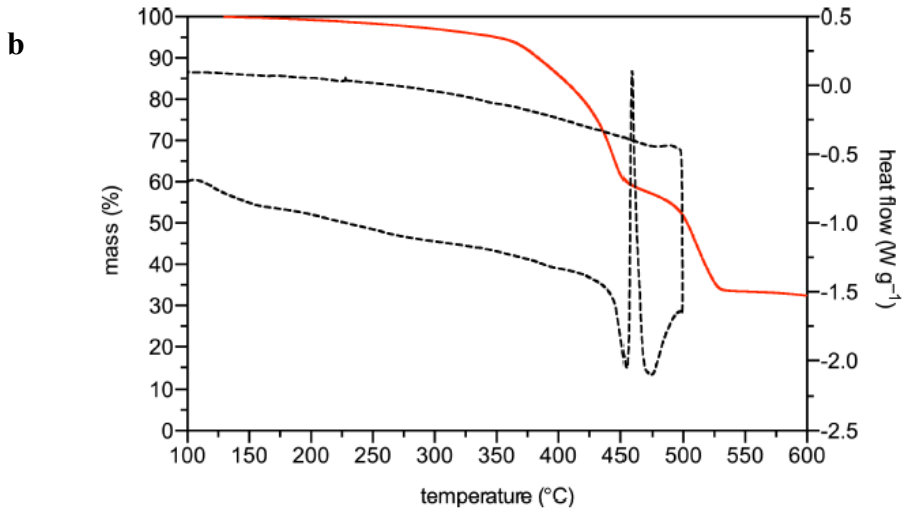

Figure 2.3 Stability of boron-doped monomer **1** as demonstrated by (a) ^{1}H NMR after one month of air exposure in the solid state and (b) Thermogravimetric (TGA) analysis (red line) under Ar and differential scanning calorimetry (DSC) (black dashed line) under N_2.

2.3 Synthesis and Characterization of Boron-Doped GNRs

Fully cyclized B-doped 7-AGNRs were fabricated by sublimation of molecular building block **1** at 250–270 °C in UHV onto pristine Au(111) held at 24 °C (Figure 2.4). STM imaging at 13 K prior to polymerization revealed that the molecules assemble into irregular islands with an apparent height of 0.4 nm (Figure 2.4b), clustered around the Au(111) herringbone reconstruction. Gradual annealing of sub-monolayer samples of **1** on Au(111) to 220 °C (20 min) induces homolytic cleavage of the labile C-Br bond, followed by step-growth polymerization of the carbon-centered diradical intermediates to form *poly*-**1** (Figure 2.4c).

STM images (T = 13 K) of polymer chains display a characteristic pattern of alternating protrusions (average distance between white marker 0.85 ± 0.04 nm, Figure 2.4c) along the polymer backbone. The repulsive interaction between *peri*-hydrogen atoms in adjacent anthracene units prevents a coplanar arrangement of monomer units in the polymer backbone (this observation is consistent with images of *poly*-anthracene, the precursor to undoped 7-AGNRs).[53]

Unique to the B-doped GNR precursors is a distinctive secondary structure along the polymer that correlates with the length of a monomer unit in *poly*-**1** (average distance between black marker 1.40 ± 0.04 nm, Figure 2.4c). While the anthracene fragments appear as brighter spots in topographic STM images, the more electron deficient boranthrenes correlate with a weaker signal that alternates along the edges of the ribbon. The observation of this characteristic secondary pattern in images of *poly*-**1** indicates that the exocyclic B-C bonds are stable under the polymerization conditions and no undesired fragmentation of monomer building blocks is observed during the step-growth process.

Further annealing of the Au(111) substrate at 300 °C (20 min) induces a thermal cyclization/dehydrogenation sequence that converts *poly*-**1** into fully conjugated B-doped 7-AGNRs (Figure 2.4d). The apparent width and average height of the resulting GNRs are 1.6 nm and 0.16 ± 0.04 nm, respectively. STM images at negative bias reveal a characteristic stripe pattern corresponding to a height modulation (0.14 ± 0.02 Å) along the length of the B-doped 7-AGNRs (Figure 2.4e). The periodicity of this topographic feature, 1.30 ± 0.05 nm, correlates well with the expected spacing between B-atoms along the backbone of a 7-AGNR (Figure 2.4a).

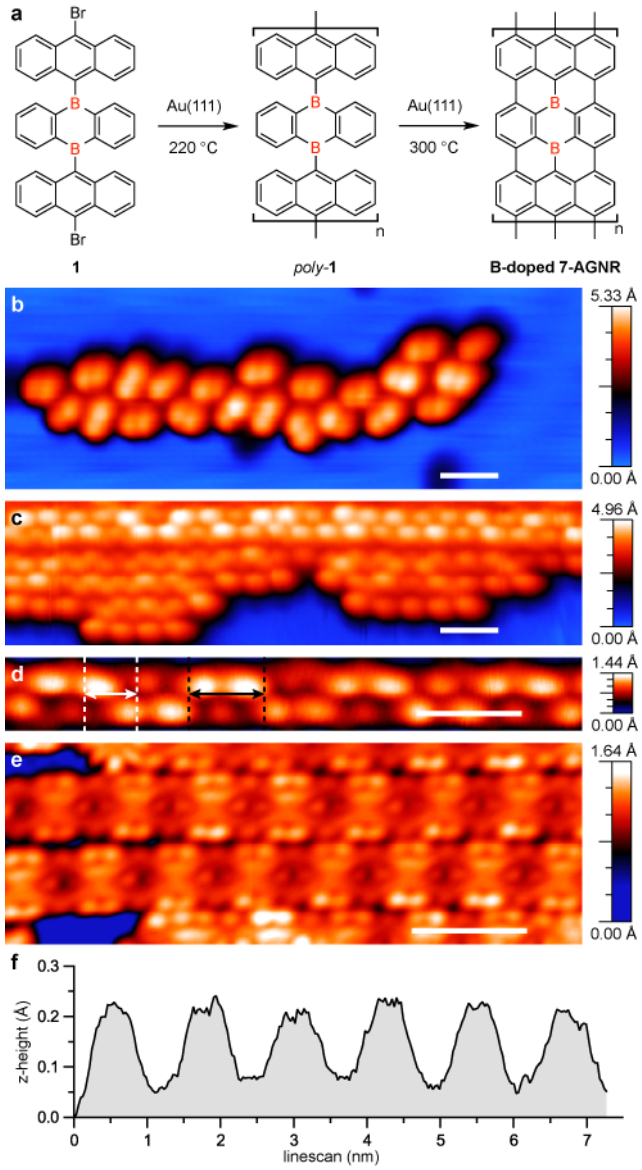

Figure 2.4 (a) Schematic representation of the bottom-up synthesis of B-doped 7-AGNRs. (b) STM topographic image of molecular building block **1** as deposited onto a pristine Au(111) surface held at 24 °C (sample voltage V_s = 1.5 V, tunneling current I_t = 40 pA, imaging temperature T = 13 K). Subsequent annealing steps induce the homolytic cleavage of the labile C-Br bonds, followed by radical step-growth polymerization (220 °C) and thermal cyclization/dehydrogenation (300 °C) to yield B-doped 7-AGNRs. (c, d) STM topographic image of *poly*-**1** (V_s = 1.0 V, I_t = 20 pA, T = 13 K) and (e) fully cyclized B-doped 7-AGNRs (V_s = −0.3 V, I_t = 30 pA, T = 13 K). (f) Representative z-axis profile showing the characteristic height modulation along the long axis of a B-doped 7-AGNR.

At relatively low cyclization temperatures (~300 °C), partially cyclized GNRs were observed (Figure 2.5). This observation supports the suggested mechanism of cooperativity in GNR synthesis.[80] That is, cyclization is not observed in patches or isolated regions in the GNR. Rather, cyclization starts at one point of the GNR and proceeds by "zipping-up" to the end of the GNR. At longer reaction times at 300 °C, fully cyclized structures were exclusively observed (Figure 2.4e). This is apparent from the height of all structures being less than 2 angstroms.

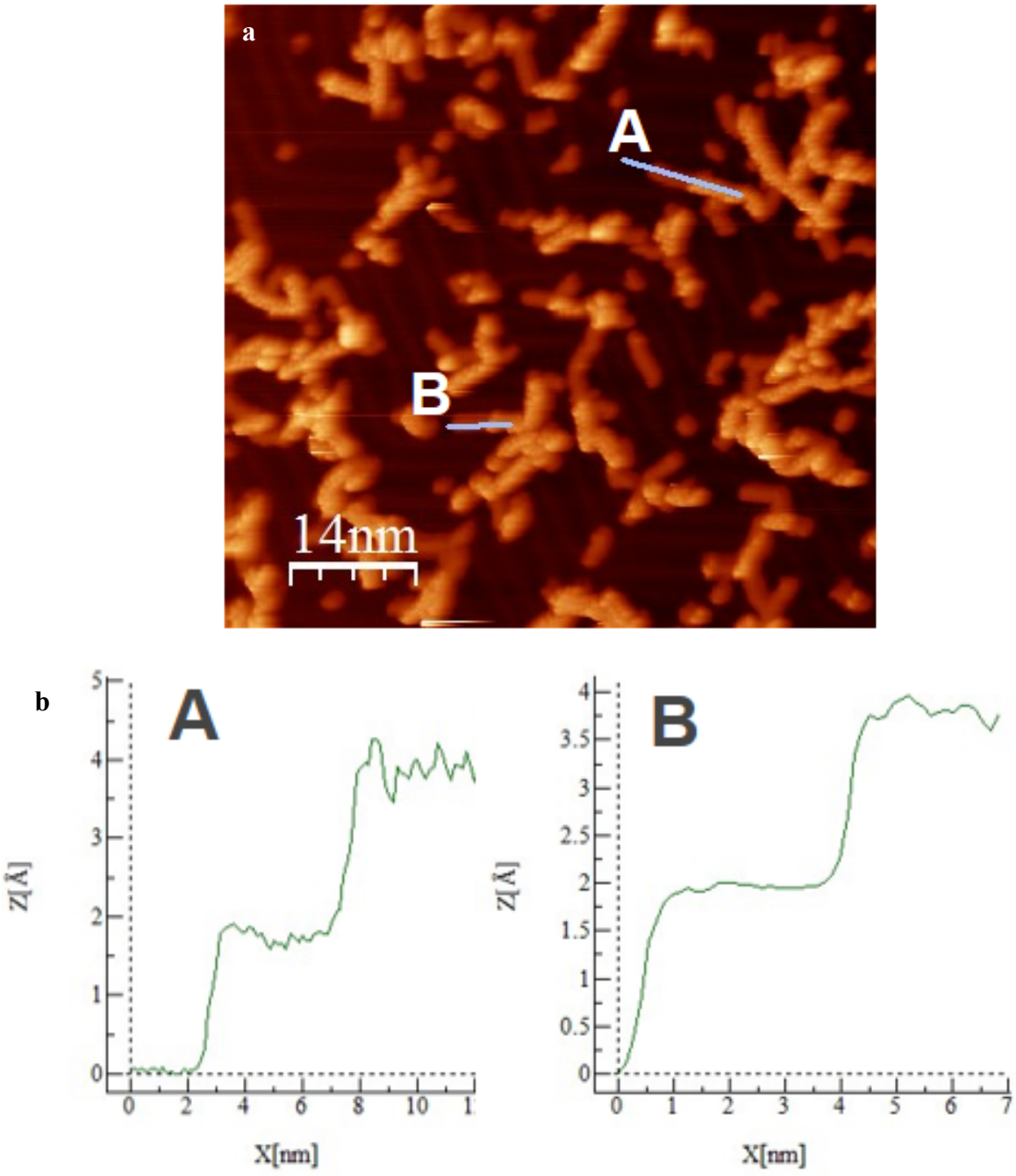

Figure 2.5 (a) STM images of partially cyclized B-7AGNRs and (b) topographic analysis of height profiles showing polymer (0.4 nm) and GNR (0.2 nm) coexistence.

The length and quality of the GNRs obtained by this method depended strongly on obtaining an optimized surface coverage of monomeric precursors. Under ideal conditions, atomically-precise GNRs with lengths exceeding 18 nm could be produced (Figure 2.6). A statistical analysis of a large number of GNR samples revealed that most of the GNRs lengths fall into the sub-10 nm category, making them an attractive candidate for next-generation FETs.

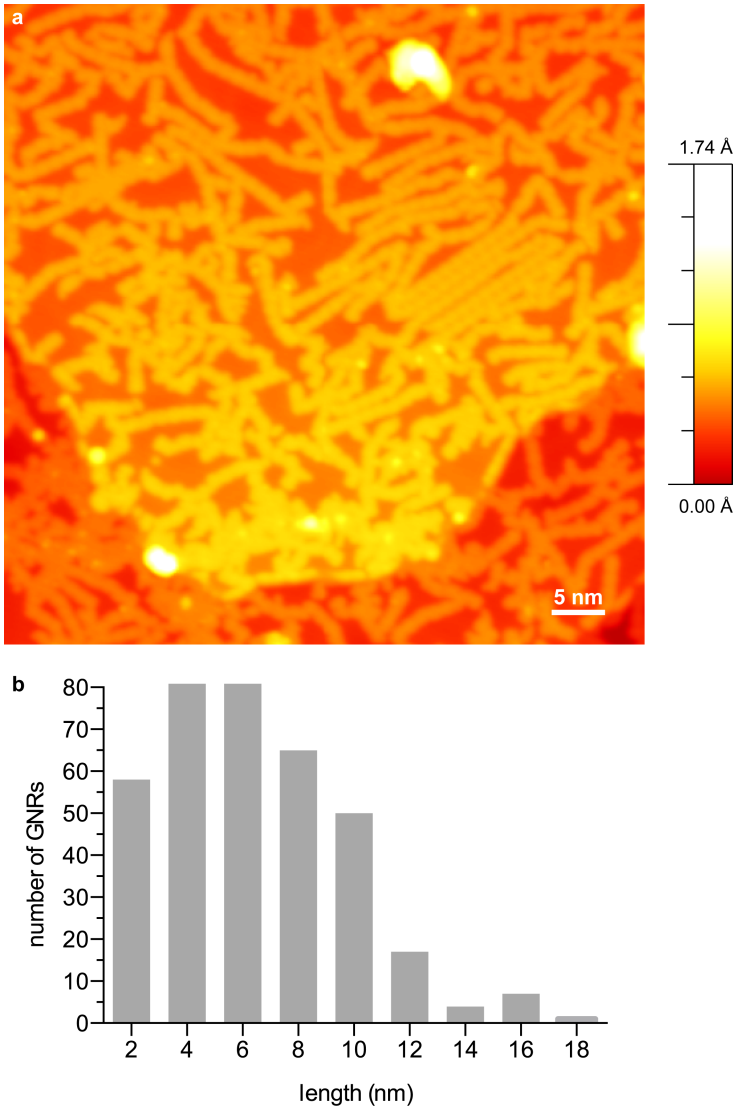

Figure 2.6 a) Large area STM image of B-7AGNR on a Au(111) surface (sample voltage V_s = 1.5 V, tunneling current I_t = 5 pA, imaging temperature T = 4 K). b) Statistical analysis of the length distribution of B-7AGNRs on Au(111) from many experiments.

2.4 DFT Calculations of Boron-Doped GNRs

In order to better understand the electronic effects of substitutive B-doping in B-7AGNRs, we performed first-principles calculations based on the GW approximation and included the screening effects from the underlying Au(111) substrate. The total density of states (DOS) at the GW level for a B-7AGNR is depicted in Figure 2.7a. The DOS of both the valence (VB) and the conduction (CB) bands show significant contributions (~10%) from B atoms. Comparing to the electronic structure of a pristine 7-AGNR (Figure 2.7a), substitutive B-doping along the backbone of a 7-AGNR introduces a deep acceptor band (CB) 0.8 eV above the VB maximum. The theoretically predicted quasiparticle band gap of B-7AGNRs, 0.8 eV (Figure 2.7b), is significantly smaller than that of the undoped 7-AGNRs (~2.1 eV) calculated with the same method (the undoped 7-AGNR DOS is shown in Figure 2.7a).

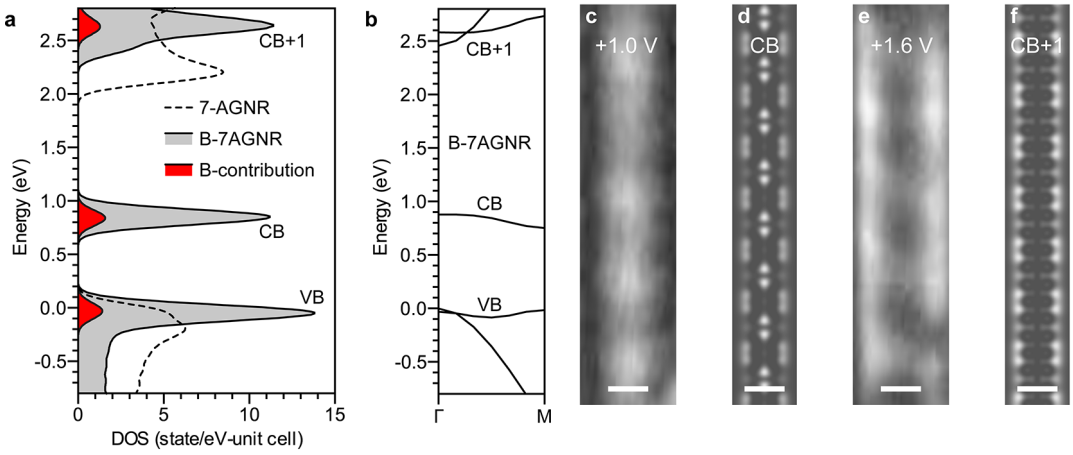

Figure 2.7 (a) Calculated total DOS for B-7AGNRs (gray) and contribution from B atoms to the DOS (red) using the GW approximation and including screening effects from Au(111) substrate. The total DOS for undoped 7-AGNRs is plotted as a dotted line. A Gaussian broadening of 0.1 eV is applied. The valence band maximum is set to 0 eV. (b) Caluculated quasiparticle band structure of B-7AGNRs (using GW approximation). (c) dI/dV spatial map of B-7AGNR recorded at 1.0 V (I_t = 30 pA, modulation voltage V_{rms} = 15 mV, modulation frequency 634 Hz, T = 13 K). (d) Calculated LDOS map of states at the conduction bandedge (CB) at a height of 4 Å above a B-7AGNR plane. (e) dI/dV spatial map of same B-7AGNR as in (c) recorded at 1.6 V (I_t = 30 pA, modulation voltage V_{rms} = 15 mV, modulation frequency 634 Hz, T = 13 K). (f) Calculated LDOS maps of CB+1 bandedge states at a height of 4 Å above a B-7AGNR plane. Calculated images average states over an energy range of 0.1 eV, scale bar 1nm.

The spatial distribution of the states associated with both the conductance band (CB) and the CB+1 band was investigated by dI/dV mapping. Figure 2.7c shows a B-7AGNR dI/dV map at V_S = 1.0 V, corresponding to states in the CB. The dI/dV map shows a predominance of local density of states (LDOS) along the backbone of the ribbon. This can be compared to the CB LDOS map calculated for a given energy range at a distance of 4 Å above a B-7AGNR plane (Figure 2.7d). In strong contrast to undoped 7-AGNRs, both the experimental and theoretical

LDOS maps at this energy show significant higher state density along the backbone of the B-7AGNR. Atomic scale features are not well-resolved experimentally, likely due to tip-induced broadening and substrate interactions that are not accounted for in the calculation. The dI/dV map recorded at a higher bias of V_S = 1.6 V (corresponding to an energy closer to CB+1) shows strong localization of the LDOS along the edges of the B-7AGNR (Figure 2.7e). This agrees with the calculated LDOS map of B-7AGNR CB+1 states (Figure 2.7f) and is reminiscent of bandedge LDOS observed in undoped 7-AGNRs. These spectroscopic maps provide additional evidence that the substitution of C atoms with trigonal planar B atoms in GNRs induces a change in their electronic structure.

The electronic structure was investigated by probing the GNR with STM at different potentials (Figure 2.8).

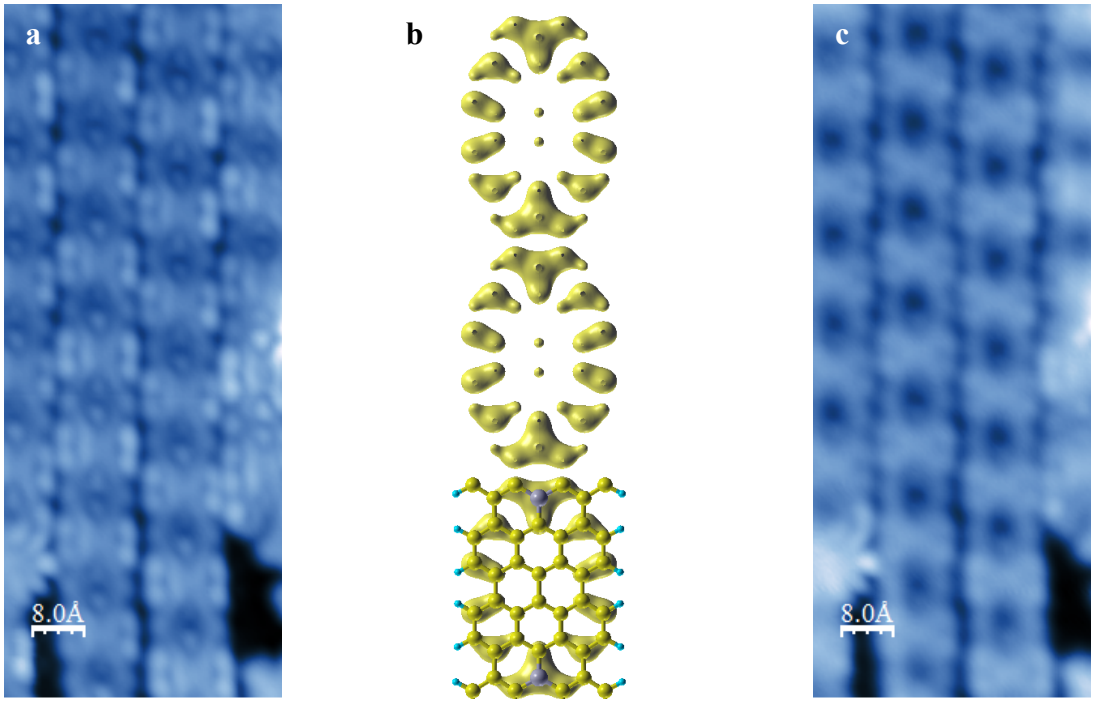

Figure 2.8 STM investigation of B-7AGNRs at (a) V_s = −0.1 V and (c) V_s = 0.4 V. (b) DFT charge density simulation of the valence band.

At negative potential, the STM images matched the valence band simulation quite well, which implies the electron density is localized on the boron atoms, while the small "dots" of electron density correspond to the 9, 10-positions in bisanthracene. At positive bias, the GNR was completely devoid of electron density in-between the regions of concentrated charge density. While the origin of these differences is electronic in nature, the absolute determination of the positions of the boron atoms could not be unambiguously determined by STM. For this reason, non-contact AFM was employed to further study this interesting GNR.

2.5 Non-Contact Atomic Force Microscopy of Boron-Doped GNRs

Although Scanning Tunneling Microscopy is a value technique for visualizing the electronics of molecules with atomic resolution, it is difficult to discern topographic information about the target molecule. This distinction becomes of paramount importance in studying boron-doped graphene nanoribbons. Specifically, from the STM images of B-7AGNR, it is difficult to discern if the periodic protrusions are due to a feature that is actually higher than other features, or if this difference is due purely to electronic differences within different segments of the graphene nanoribbons.

For this reason, non-contact Atomic Force Microscopy (nc-AFM) was employed to unambiguously assign the protrusions visualized in STM to particular regions of the graphene nanoribbon.

nc-AFM revealed that the B-7AGNR exhibited "holes" within the middle of the nanoribbon (Figure 2.9). A plausible explanation for this observation is that the Au(111) surface strongly binds the boron atoms in the center of the nanoribbon, creating an apparent absence of topographic features.

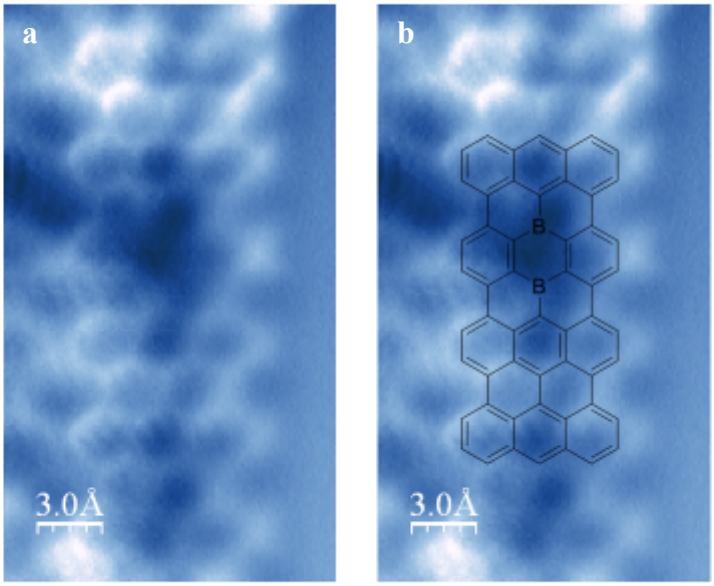

Figure 2.9 (a) nc-AFM image of B-7AGNRs and (b) possible correlation with chemical structure.

The comparison between nc-AFM and STM of the same B-7AGNR (Figure 2.10) is especially striking. The STM image appears highly periodic with some segments that appear as higher protrusions. In contrast, nc-AFM reveals the highly strained and complex structure resulting from boron atoms bonding to the gold surface.

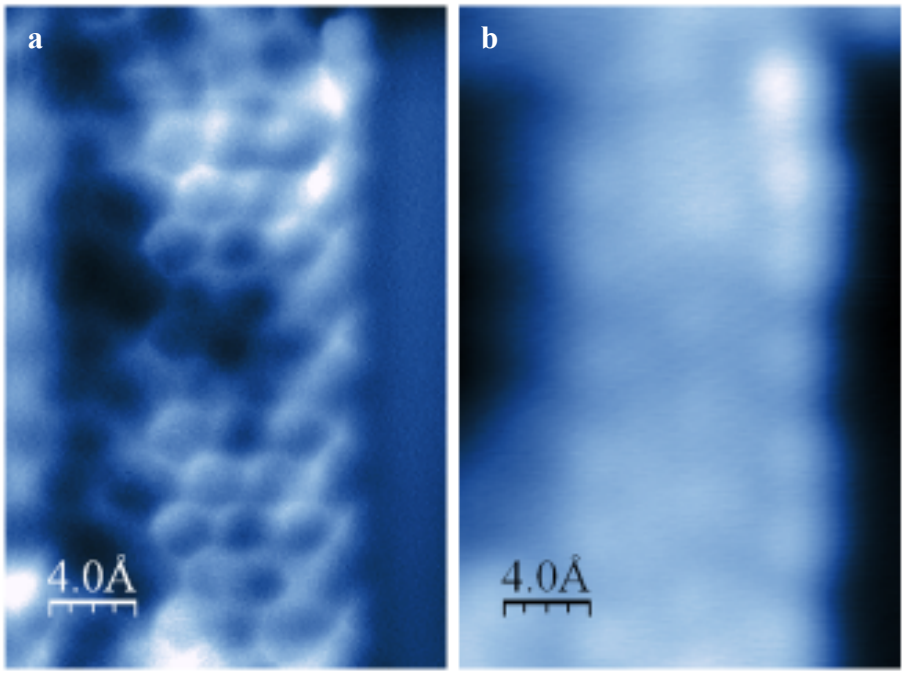

Figure 2.10 Comparison of (a) nc-AFM and (b) STM images of a single B-7AGNR.

The "holes" within the center of the nanoribbon were evident even over many periodic units, indicating the correlation between chemical structure and topography (Figure 2.11). Interestingly, the "holes" do not appear to be identical in every periodic unit. This could imply that the strain accumulated within the graphene nanoribbon bound to the gold surface is cumulative, forcing the structure to adopt kinks that can complicate the very sensitive nc-AFM measurement.

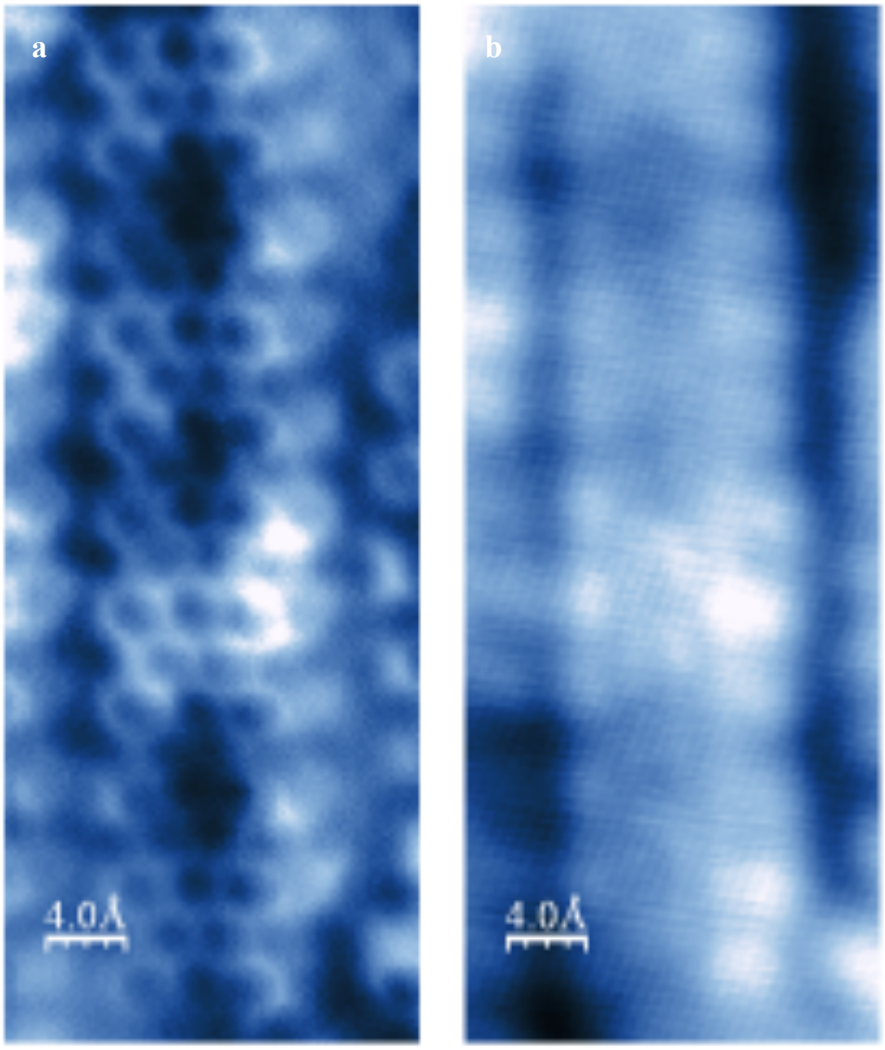

Figure 2.11 Comparison of (a) nc-AFM and (b) STM images of a single B-7AGNR over multiple periodic units.

2.6 Scanning Tunneling Spectroscopy and Future Directions

Because of the importance in achieving a technologically relevant band gap near 1 eV in graphene nanoribbons, experimental verification of this property is critical. While theoretical predictions provide useful insight into the initial investigation of the structures of interest, the actual band gap determination can be complicated and obscured by factors such as the interaction between GNRs and the metal surface inside of the STM. Preliminary scanning tunneling spectroscopy (STS) investigations of B-7AGNRs on Au(111) have proven ambiguous. This is not surprising when considering the hypothesis that the boron atoms are bonded to the underlying gold substrate as determined by nc-AFM. Therefore the strong coupling between the GNR and gold substrate obscures the determination of the valence and conduction bands by STS. A representative experiment is shown in Figure 2.12.

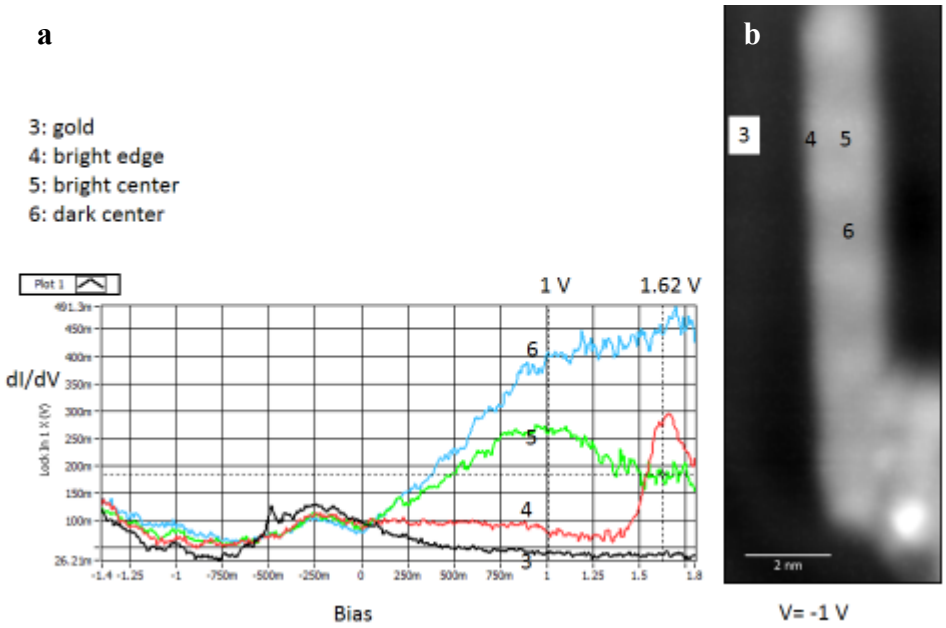

Figure 2.12 (a) Representative STS data for (b) B-7AGNR at particular locations.

The gold background exhibits the typical spectrum of a single peak at −250 mV. As expected given the heterogeneity in this structure, the d*I*/d*V* signal is strongly dependent on the measured location within the GNR. On a "bright" spot within a GNR, the edge displays a peak at +1.62 V but very little signal at +1 V. Within this same "bright spot" but closer to the center of the GNR, the situation is reversed and an extremely broad peak is observed at +1 V bias. When examining the "dark spot" within the GNR attributed to boron-gold binding, a gradual increase in the d*I*/d*V* signal is seen for all positive biases. This observation is difficult to explain, but it can be considered strong evidence for the presence of atoms other than gold within the "dark spots" observed in STM and NC-AFM, since it is likely that any true holes within the GNR would display a spectrum similar to that of gold. The unambiguous assignment of the band gap and electronic structure of this boron-doped graphene nanoribbon will take time to be completed and is the topic of a forthcoming paper.

In the meantime, ongoing synthetic efforts aim to further the concept of core-doped graphene nanoribbons by incorporating other dopant atoms. First-principle LDA-DFT calculations of a nitrogen core-doped GNR (N7AGNR) postulate the existence of a mid-gap dopant state (as in the case of the boron-doped GNR) having a band gap of 0.55 eV (Figure 2.13). The main difference between N7AGNR and B-7AGNR is a shifting of valence and conduction bands to higher energies. Specifically, the Fermi level changes from −4.00 eV to −2.96 eV in the case of boron and nitrogen-doping, respectively. The overall electronic structure of these two GNRs is quite similar, but the N7AGNR, having the extra electrons from the nitrogen lone pairs, has the "midgap" state occupied, effectively shifting the VB and CB to higher energy.

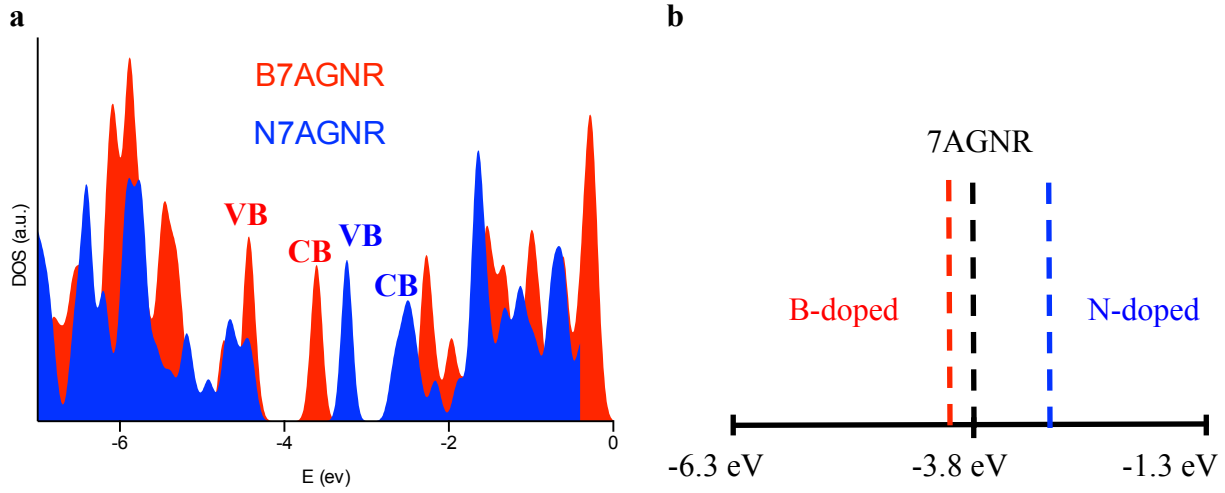

Figure 2.13 (a) Comparison of the density of states (DOS) for B-7AGNR and N7AGNR and (b) analysis of Fermi level shifting in core doped GNRs with respect to vacuum.

This level of control in GNR doping should allow for the selection of the carrier type for either electrons or holes. Relative to the undoped 7AGNR, nitrogen doping is predicted to have a much larger impact on the energy levels of the GNR compared with B-7AGNR (Figure 2.13b).

The synthesis of the requisite nitrogen core-doped monomer is shown in Scheme 2.2. While the boron-doped monomer presented extreme synthetic challenges in the form of atmospheric stability and isolation, the nitrogen-doped monomer is formally anti-aromatic, making its synthesis and purification especially challenging. Additionally, the geometry around the nitrogens within the central six-membered rings could be deleterious for the on-surface synthesis of GNRs, which is presumed to require planar, cruciform shaped molecules.

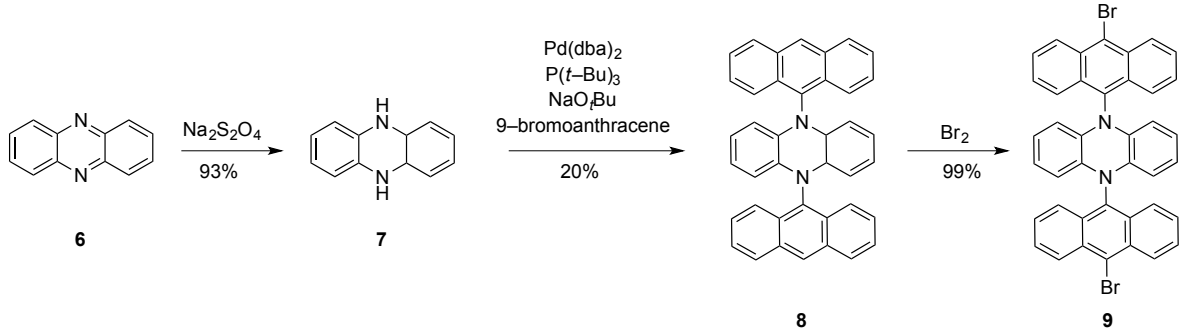

Scheme 2.2 Synthesis of nitrogen-core doped GNR precursor.

Starting from commercially available phenazine **6**, reduction with sodium dithionite under rigorously airfree conditions in the dark yields dihydrophenazine **7**. Subsequent Buchwald-Hartwig amination produces the desired heterocycle **8** along with a large amount of homocoupled bisanthracene. Subsequent bromination under electrophilic conditions furnished the expected product **9** due to the directing nature of the amino substituents (Figure 2.14).

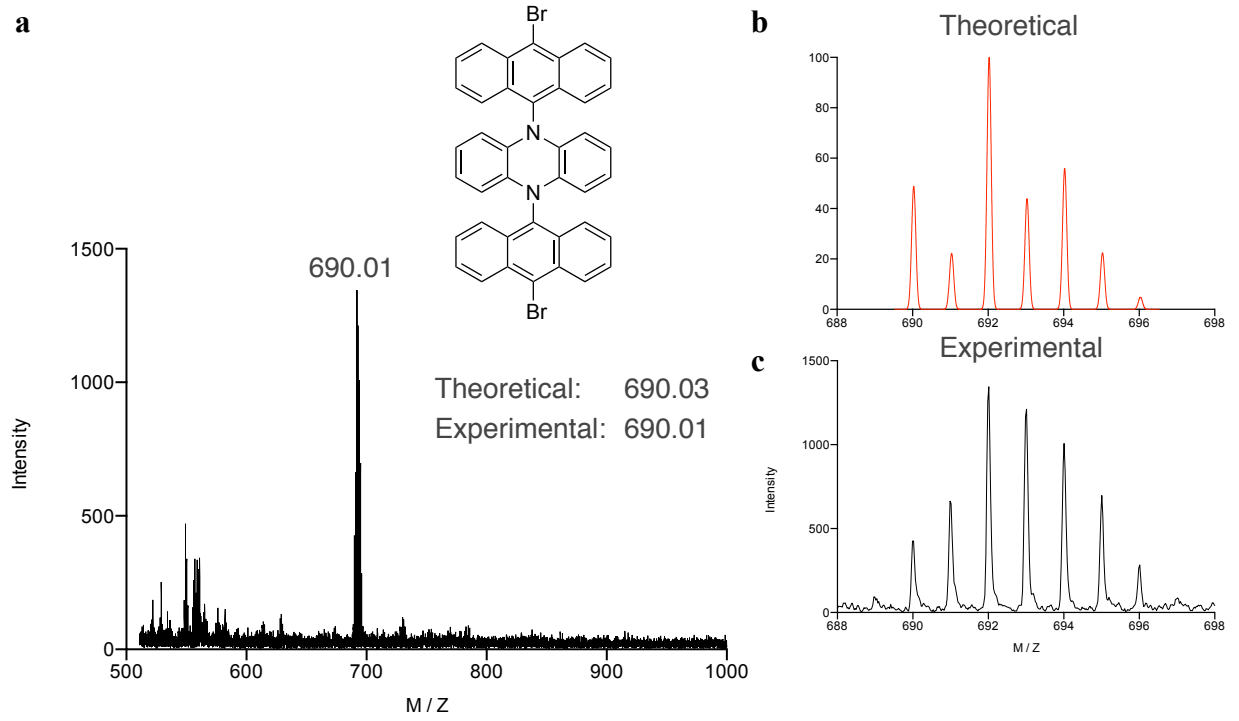

Figure 2.14 (a) MALDI-HRMS of nitrogen core-doped GNR precursor with (b) theoretical and (c) experimental isotope patterns.

In conclusion, we demonstrate the first atomically precise bottom-up synthesis of 7-AGNRs with dopant atoms inserted directly into the GNR backbone. The trigonal planar B-atoms incorporated at defined positions along the GNR thus share an empty p-orbital with the extended π-system, potentially providing electron-hole dopant concentrations in excess of 10^{14} cm^{-2} . The highly regular placement of p-dopants along the 7-AGNR is reflected in a characteristic modulation of the local density of states along the backbone of the ribbon visualized by high-resolution STM topographic imaging. The observation of partially cyclized GNRs upon gradual annealing of the Au(111) substrates supports the proposed mechanism for GNR formation on metal substrates that involves a cooperative cyclization/dehydrogenation cascade along the polymer. STS and nc-AFM studies provided valuable insight into the interaction between boron atoms and the underlying gold substrate. Further investigations of this topic, as well as the use of a nitrogen-doped GNR precursor, are ongoing. In summary, site-specific substitutional doping of GNRs will help pave the way toward the development of advanced functional device architectures based on GNR semiconductor technology.

Chapter 3
Hybrid Porphyrin-Graphene Nanoribbons

In this chapter, the notion of graphene nanoribbon junction formation is introduced. In addition to atomically-precise synthesis, a stringent requirement for advanced logic devices is the meticulous arrangement of GNRs into ordered arrays. Toward this end, the synthesis of a highly symmetric porphyrin containing four anthracene motifs, which will be used as a template for the on-surface synthesis of GNRs, is described. STM images prove that this porphyrin can be sublimed in UHV onto Au(111) surfaces, despite its high molecular weight. Therefore it is anticipated that this porphyrin will template GNRs into highly ordered junctions during the on-surface synthesis process. Additionally, the synthesis of a model porphyrin-anthracene dimer is reported. UHV-STM of this model compound shows that it readily undergoes surface-assisted cyclodehydrogenation. This model compound will be studied by non-contact atomic force microscopy in order to prove the complementarity of porphyrins and anthracenes for hybrid graphene nanoribbon systems.

3.1 Introduction

As a class of materials with interesting and tunable coordination and optoelectronic properties, porphyrins are ubiquitous both in the laboratory and in nature. The most prolific examples of porphyrinic materials are found in chloroplasts used in photosynthesis,[81] Heme proteins used to bind oxygen in red blood cells,[82] and cyanocobalamin (Vitamin B_{12}) for essential metabolic functions.[83] Increasingly, this important group of molecules is finding a role in nanostructured materials[84-86] and metal-organic frameworks,[87-90] due to their high degree of symmetry and rigidity.

The groups of Grill and Hecht produced a 2D network of porphyrins based on aryl halide coupling on metal surfaces in STM.[91] This groundbreaking work laid the foundation in many ways for bottom-up graphene nanoribbon methodology, but additionally, demonstrated the ability to incorporate porphyrins into highly ordered networks (Figure 3.1).

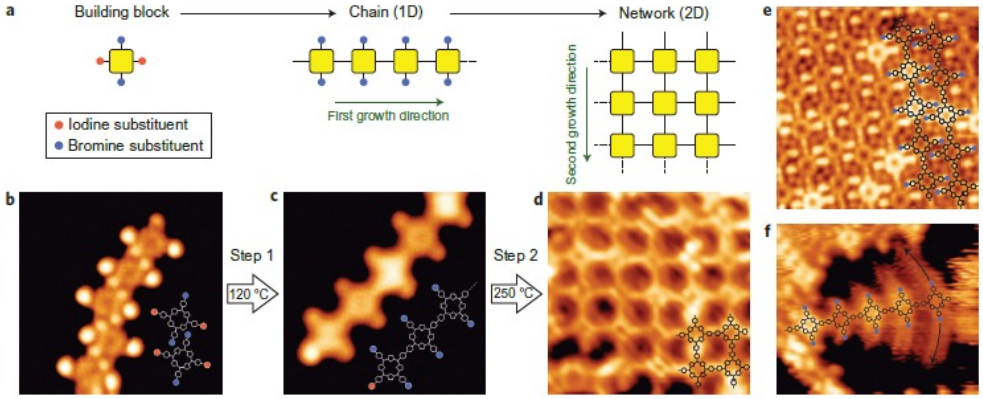

Figure 3.1 Porphyrin coupling on metal surfaces in STM. (a) Schematic representation of on-surface porphyrin coupling and (b–e) STM images of 2D networks [reproduced from ref. 91].

In recent years, on-surface porphyrinic architectures have become increasingly sophisticated. The Anderson Group synthesized a 12-porphyrin nano-ring using a hexapyridyl template by Glaser coupling tetramers of zinc porphyrin.[92] Interestingly, this 12-porphyrin nano-ring could be sublimed in UHV-STM and visualized despite its considerable size (Figure 3.2).

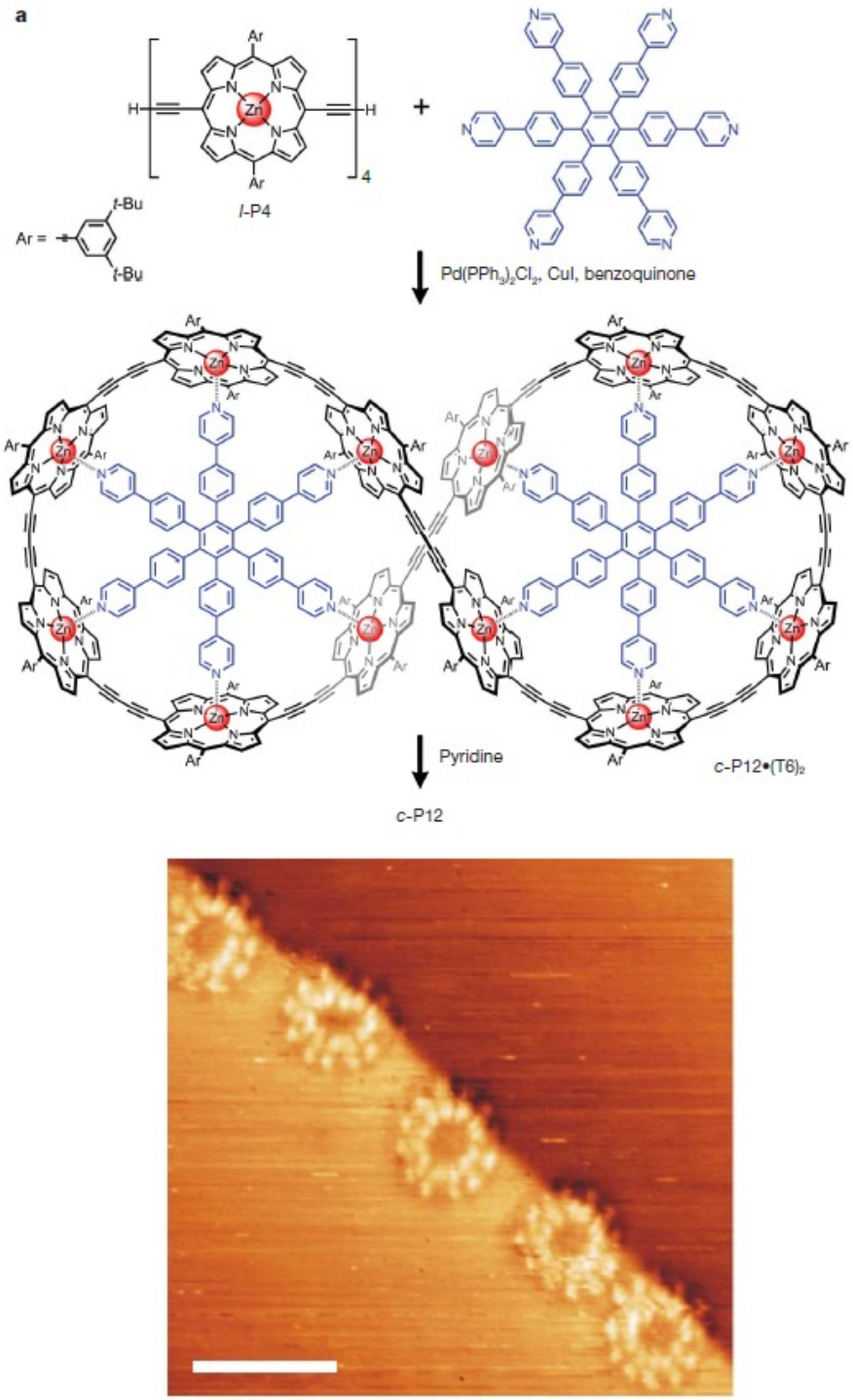

Figure 3.2 Synthesis (top) and STM images (below) of 12-porphyrin nano-ring [reproduced from ref. 92].

Recent synthetic advances in porphyrin chemistry have provided the foundation for hybrid porphyrin-GNR systems to be synthesized. In 2010, the group of Mathias Senge reported Suzuki conditions for extremely sterically congested porphyrins, even coupling two porphyrins onto a single anthracene.[93] The same year, the first fully fused porphyrin-anthracene compound was made in solution by the Anderson Group at Oxford (Figure 3.3).[94]

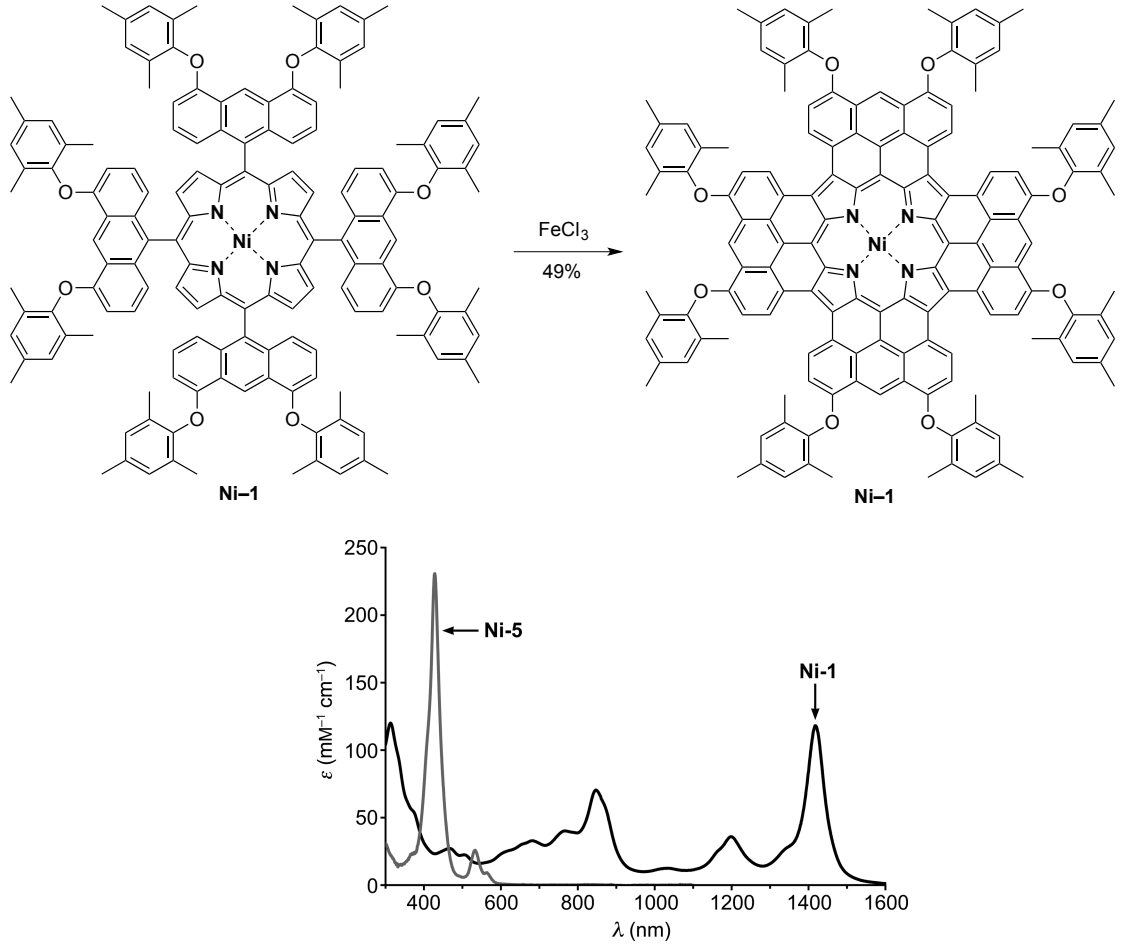

Figure 3.3 Synthesis and UV/vis absorption of the first example of a fused anthracene-porphyrin compound [reproduced and modified from ref. 94].

Cyclized **Ni-1** could only be obtained by using the directing oxy-groups on the anthracene rings *para* to the new bond formation sites. Once fully cyclized, the absorbance maximum was red-shifted by 1000 nm, indicating that these molecules could be useful for near-IR applications. However, this type of cyclization has only been shown in solution, and the synthesis of fused porphyrin-anthracene molecules by surface catalysis has yet to be demonstrated.

As electronic devices continue to decrease in size, the synthesis of ordered, quasi one-dimensional materials has become increasingly urgent.[95] Capitalizing on experience in porphyrin chemistry as well as expertise in graphene nanoribbon synthesis, a hybrid porphyrin-GNR material was envisioned (Figure 3.4). There are both electronic and geometric advantages to this

approach. By inserting a porphyrin into a graphene nanoribbon, the electronic structure of the GNR can be modified. Additionally, porphyrins can accommodate many transition metals into their central cavity, opening the possibility for metal-doped graphene nanoribbons with applications in magnetics, spintronics, and memory. The geometry of the porphyrin system is perfectly complementary to anthracene, allowing for controlled templating of GNRs reminiscent of logic-based junctions (Scheme 3.1).

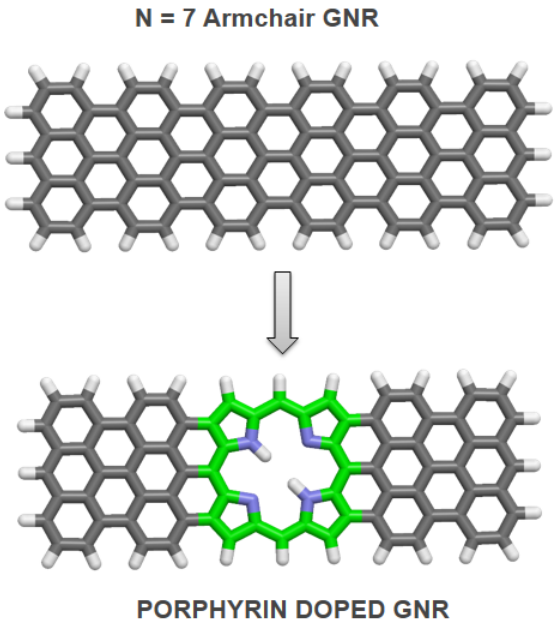

Figure 3.4 Hybrid GNR-porphyrin design.

A4-porphyrin **10** could be sublimed on Au(111) in UHV-STM with excess DBBA **11** to achieve submonolayer coverage (Scheme 3.1). By heating the surface first to the polymerization temperature (~200 °C) and then subsequently to the cyclodehydrogenation temperature (~400 °C), GNR-porphyrin junctions such as **12** will be studied by STM and STS.

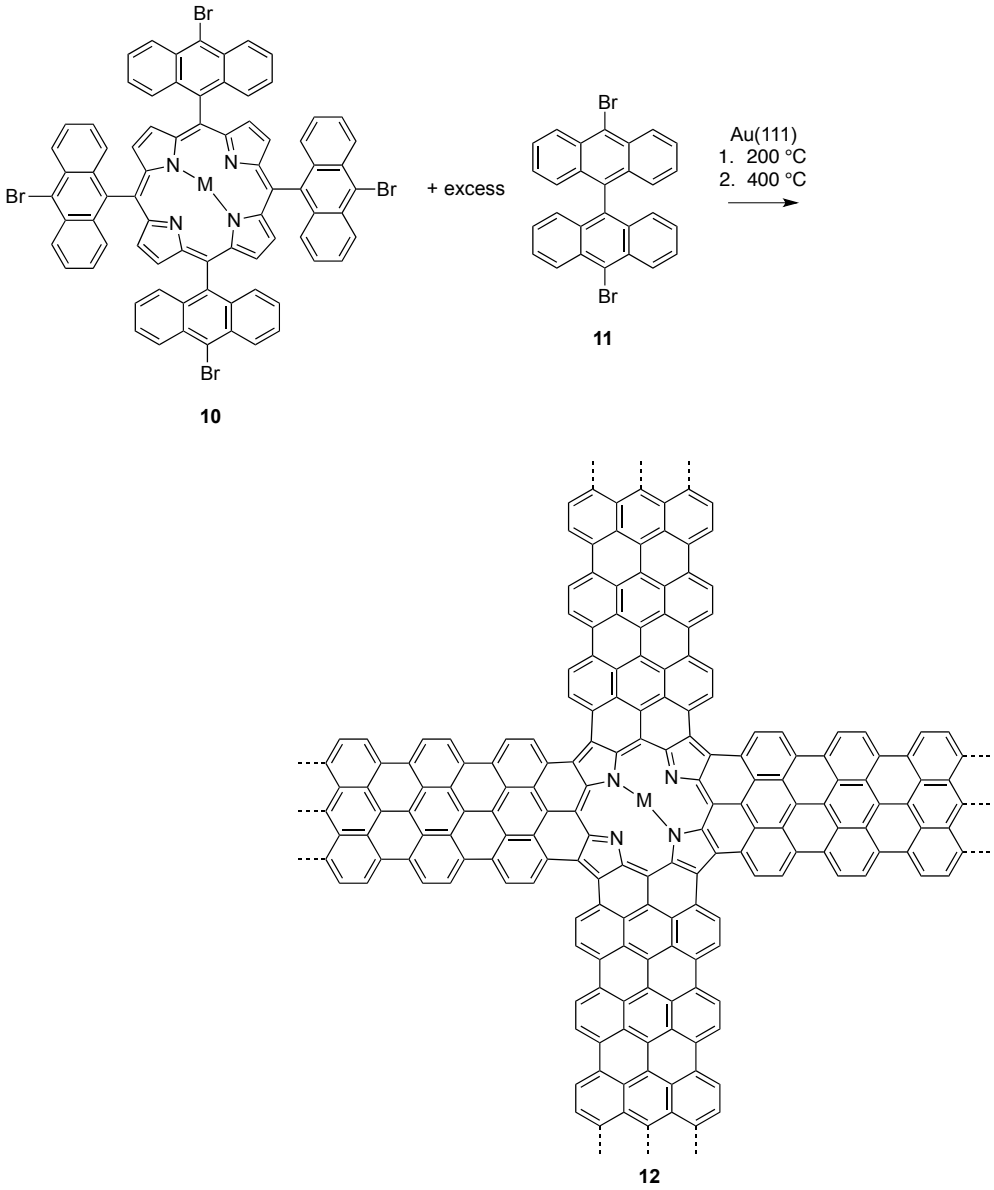

Scheme 3.1 Evolution of on-surface synthesized GNRs to templated GNR junctions. M = Zn, Cu, Ni, Co, Fe, Mn, Al.

The work reported in this chapter was conducted in collaboration with Dr. Tomas Marangoni and Dr. Danny Haberer of the Fischer Group, and Giang Nguyen, Daniel Rizzo, and Chris Bronner of the Crommie Group.

3.2 Synthesis of A4-Porphyrins for GNR Junctions

A4-porphyrin **16** was synthesized in a one-pot approach using 9,10-dibromoanthracene **13** and 2-formylpyrrole **14** (Scheme 3.2). After lithiation of 9,10-dibromoanthracene **13**, the electrophile **14** was added to form a bright-yellow intermediate lithium alkoxide **15**. Attempts to isolate this species after protonation with ice water or isopropanol proved unsuccessful. Instead, this intermediate was dropped cautiously into boiling propionic acid and refluxed in air. After purification, A4-porphyrin **16** was isolated in 3% yield (Figure 3.5).

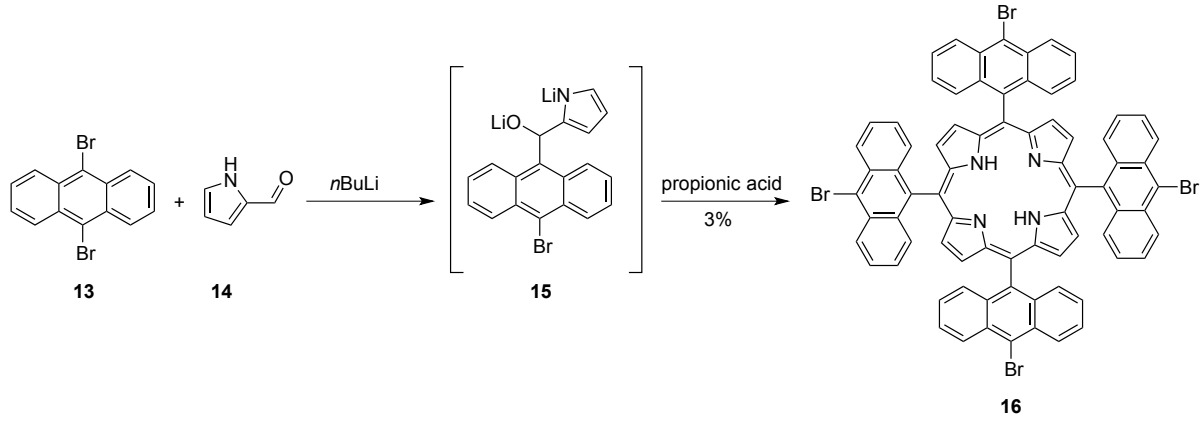

Scheme 3.2 Synthesis of A4-porphyrin **16**.

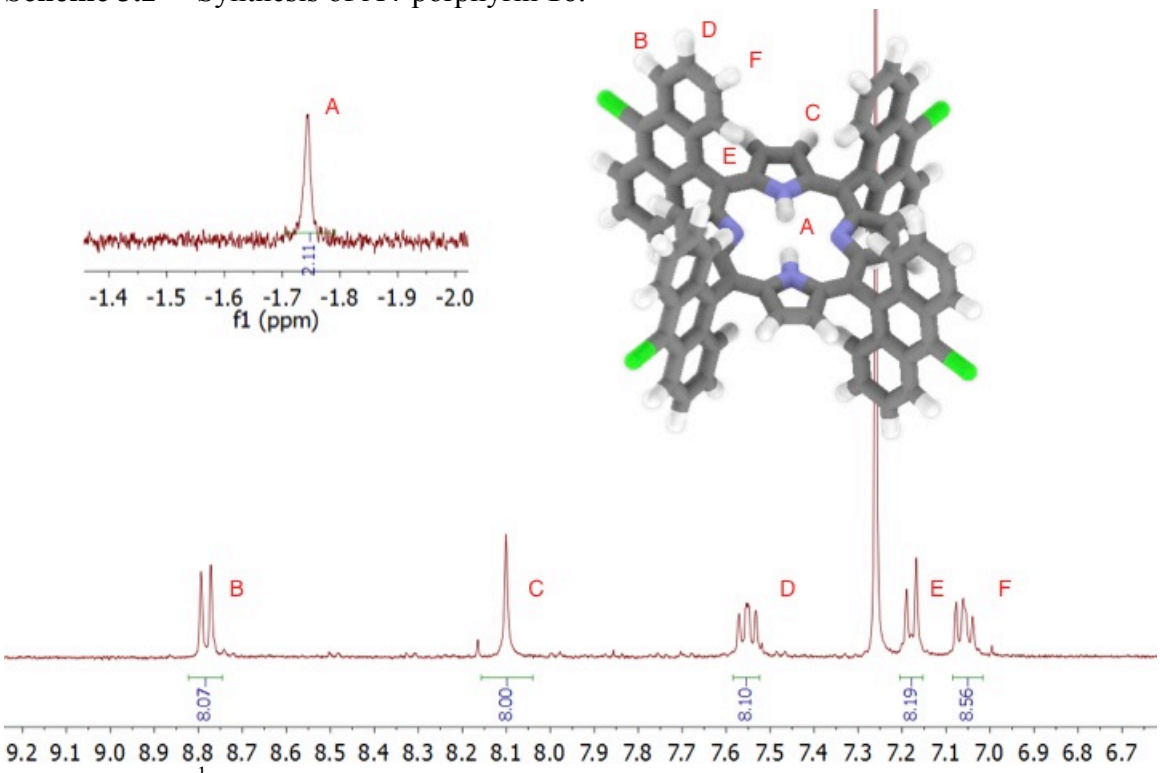

Figure 3.5 ^{1}H NMR of A4-porphyrin **16.**

The target porphyrin displayed a high-degree of symmetry in ^{1}H NMR, as expected for the intended structure. The characteristic protons for pyrrole were observed as singlets at −1.75 and 8.1 ppm due to the ring current throughout the porphyrin macrocycle.

The structure of A4-porphyrin **16** was further confirmed by MALDI-HR-MS (Figure 3.6a). Importantly, debromination, which would severely inhibit the on-surface junction formation, was not observed. Additionally, the highly complex isotopic pattern of four bromines (Figure 3.6c) agreed well with the simulated pattern (Figure 3.6b).

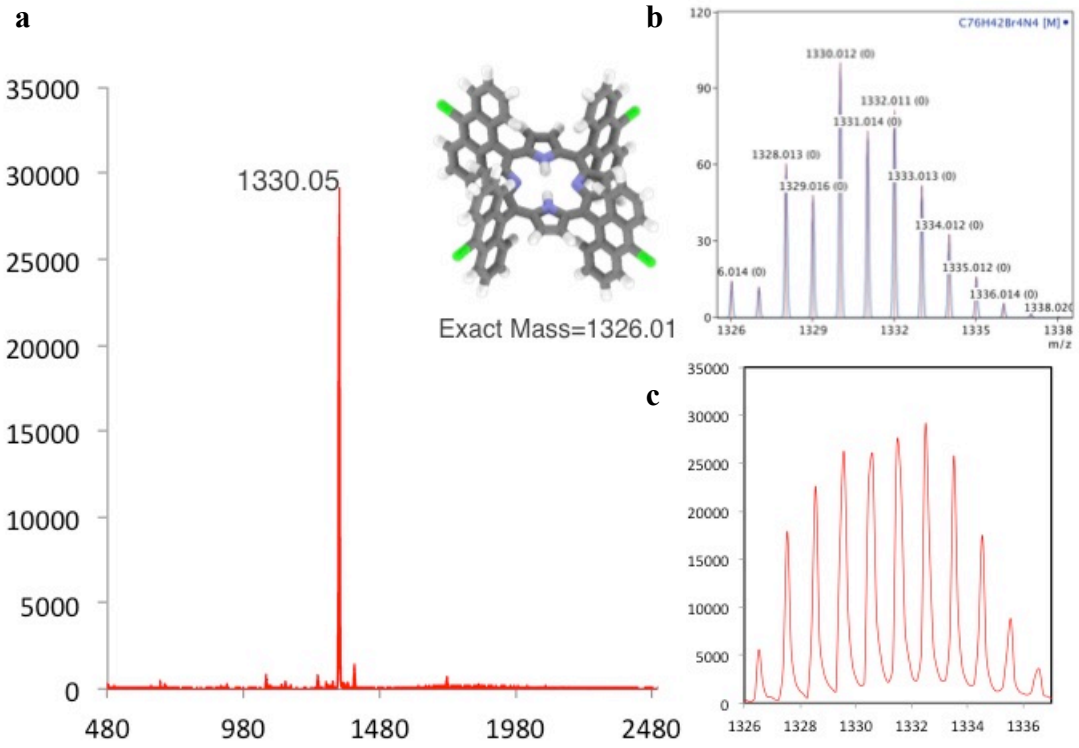

Figure 3.6 (a) MALDI-HR-MS of A4-porphyrin **16** with (b) theoretical and (c) experimental isotope patterns**.**

The UV/vis absorption of A4-porphyrin **16** was recorded at room temperature (Figure 3.7). The spectrum displayed the four peaks of the Q-band (661, 600, 557, 525 nm) and Soret peak (434 nm) expected for metal-free porphyrins as well as an additional absorption maxima corresponding to the bromoanthracene moieties (253 nm).

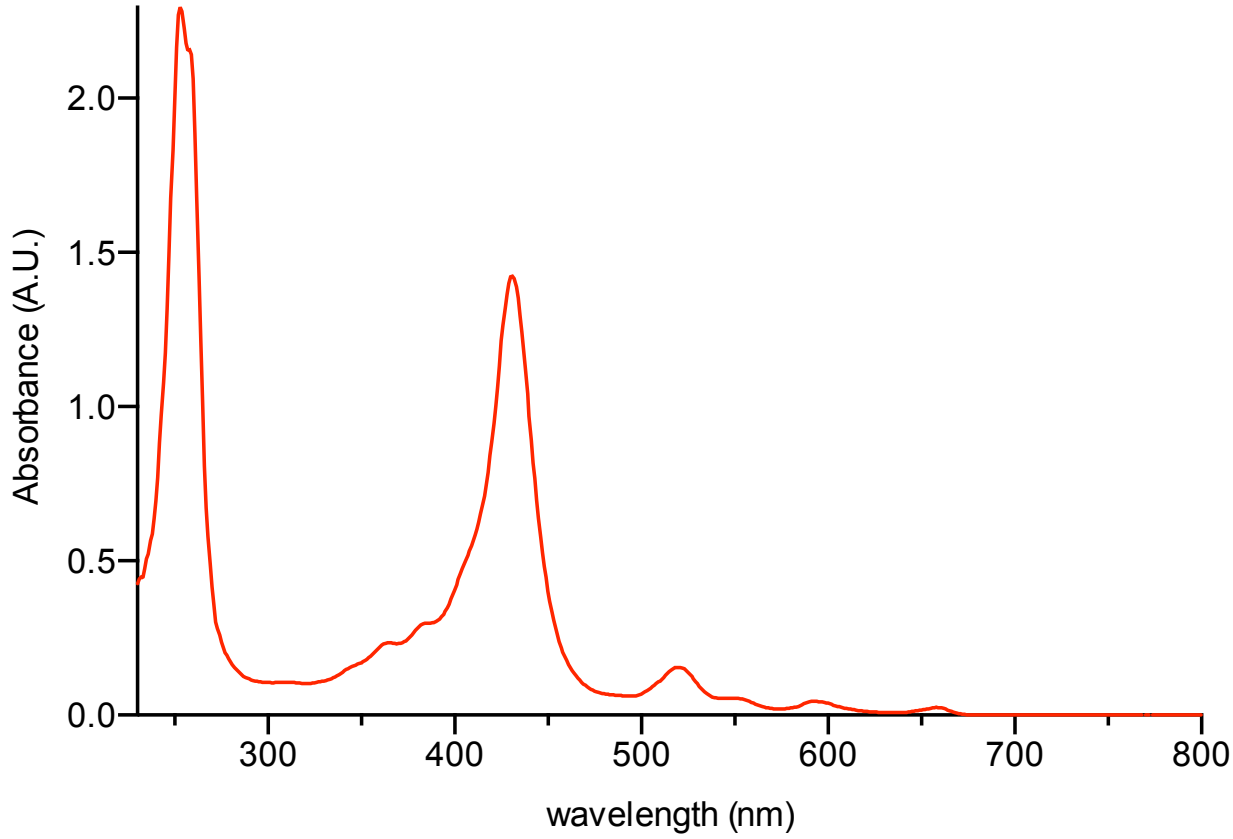

Figure 3.7 UV/vis of A4-porphyrin **16**.

3.3 STM imaging of A4-Porphyrins on Au(111) and Cu(110)

Before attempting the on-surface formation of porphyrin-GNR junctions, A4-porphyrin **16** was metallated with zinc and imaged on Au(111) and Cu(110) (Figure 3.8 and Figure 3.9, respectively). In both cases the surface was annealed to 200 °C before imaging at 13 K.

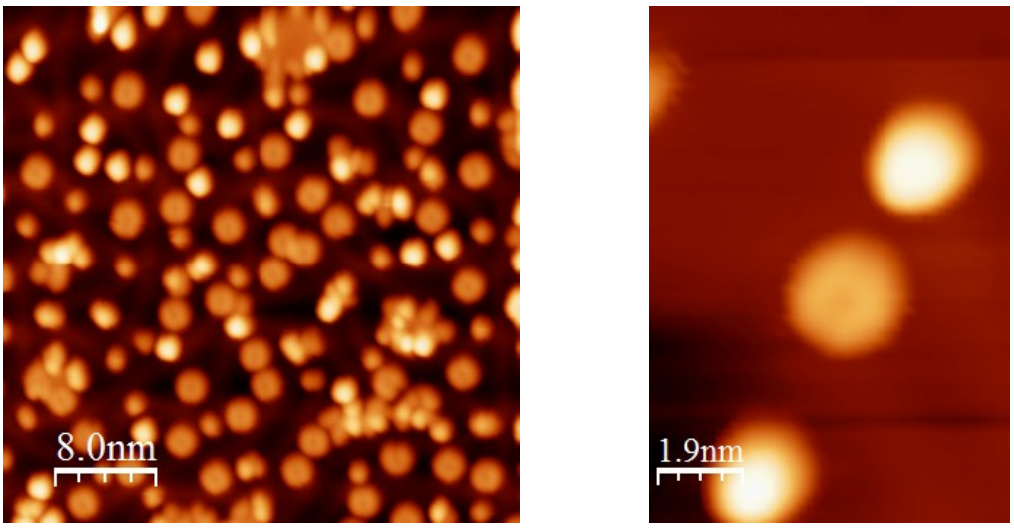

Figure 3.8 STM images of A4-porphyrin **Zn-16** on Au(111) at 13 K.

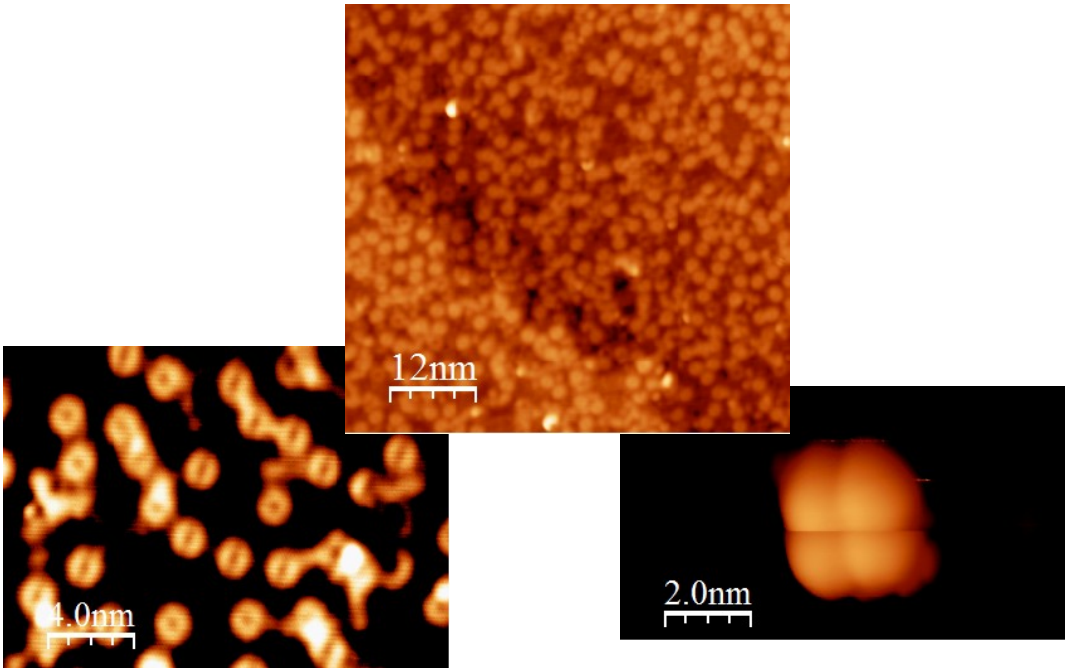

Figure 3.9 STM images of A4-porphyrin **Zn-16** on Cu(110) at 13 K.

On Au(111), a mixture of cyclized and uncyclized porphyrins was observed, while on Cu(110), only flat, cyclized molecules were seen. Very few cases of homocoupled porphyrins were detected, indicating that the porphyrins have a lower on-surface mobility than their DBBA counterparts. This is a promising result for on-surface porphyrin-GNR junctions, since porphyrin-porphyrin coupling would lead to undesired defects in the junction formation. Current experimental efforts include lowering the surface coverage of A4-porphyrin **Zn-16** on Au(111) in order to obtain the requisite excess of DBBA on the surface. Once the coverage conditions have been optimized, the highly ordered porphyrin-GNR junctions will facilitate the study of the rich physics underlying these interesting structures.

3.4 Synthesis of a Model Porphyrin-Anthracene Dimer

Because of the complexities associated with forming ordered graphene nanoribbon junctions from an A4-porphyrin template, a model system was also synthesized (Scheme 3.3). Since the propensity of the on-surface cyclodehydrogenation between porphyrins and anthracene has not yet been demonstrated, this approach represents a cogent strategy to ensure the electronic and geometric complementarity of these two motifs.

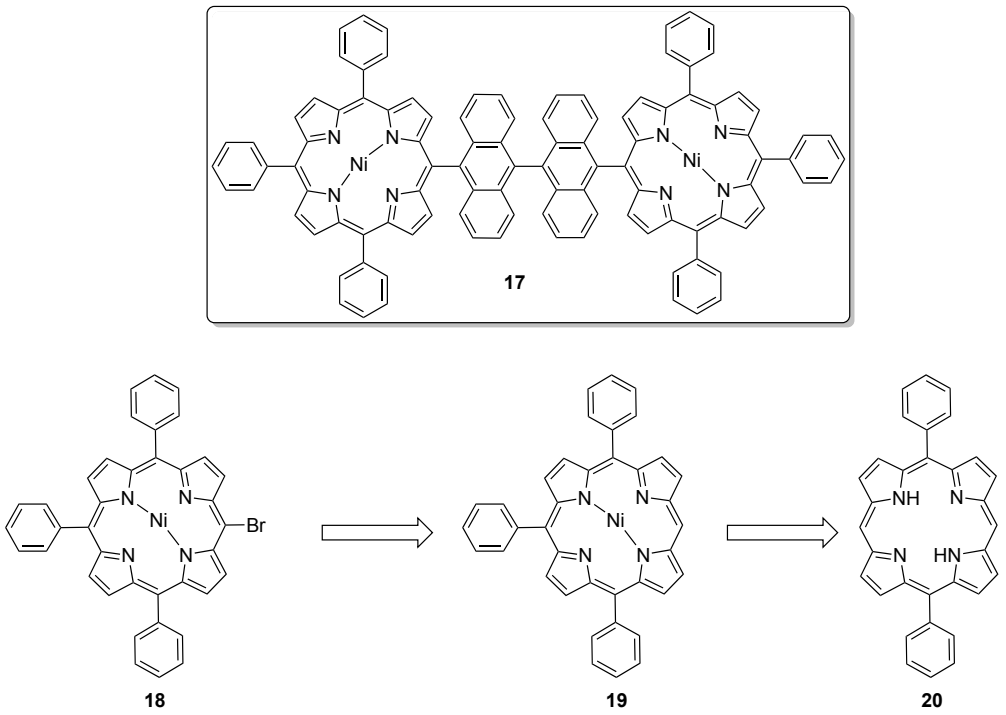

Scheme 3.3 Structure and retrosynthetic analysis of the target model compound **17**.

The synthetic strategy chosen permitted the disconnection around the bisanthracene unit. This required the synthesis of A3 porphyrin **18** (Scheme 3.4). First, A2 porphyrin **23** was synthesized by Macdonald-type condensation between benzaldehyde **21** and dipyrromethane **22**. This approach could be scaled to yield 0.5 g of pure A2 porphyrin **23**. Subsequent S_NAr2 reaction using phenyl lithium produced an anionic intermediate which, upon quenching with water and oxidation with DDQ, furnished A3 porphyrin **25**.

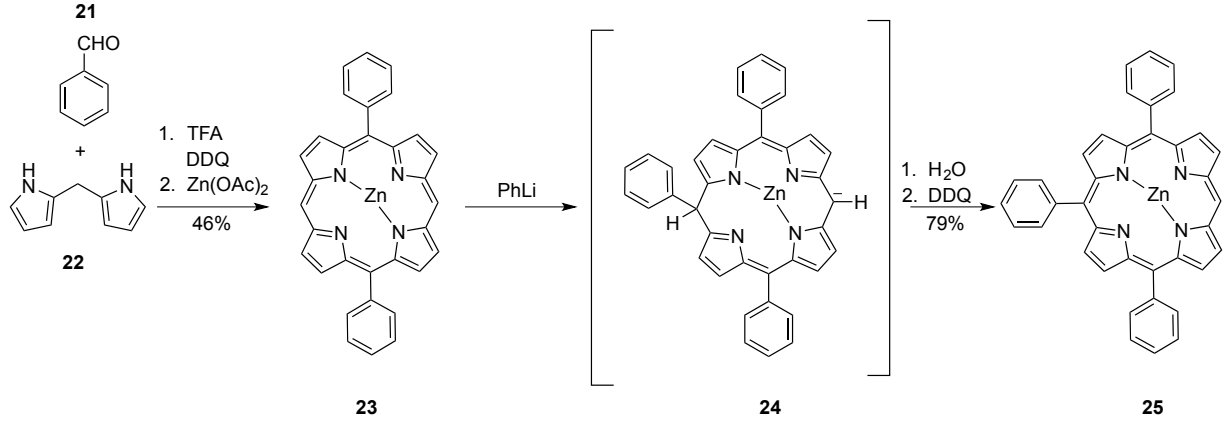

Scheme 3.4 Synthesis of A3 porphyrin **25**.

Removal of zinc by treatment with TFA yielded A3 porphyrin **26** and remetallation with nickel furnished A3 porphyrin **19** (Scheme 3.5). Bromination of **19** with NBS and pyridine in the

absence of oxygen and water provided A3 porphyrin **18** in 15 min. This asymmetric porphyrin was coupled with boronic ester **27** (Scheme 3.6). The use of triphenyl arsine was required to effect this sterically congested cross-coupling. After chromatography and recrystallization, model system **17** was isolated in pure form (Figure 3.10).

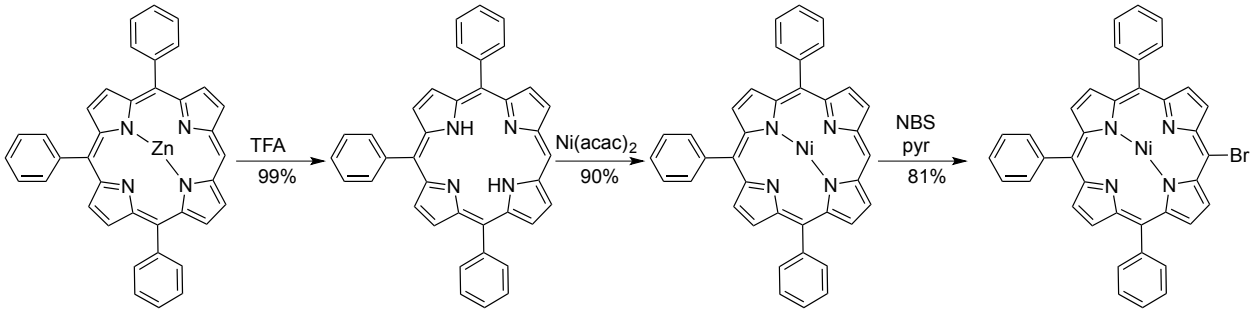

Scheme 3.5 Synthesis of A3 porphyrin **18**.

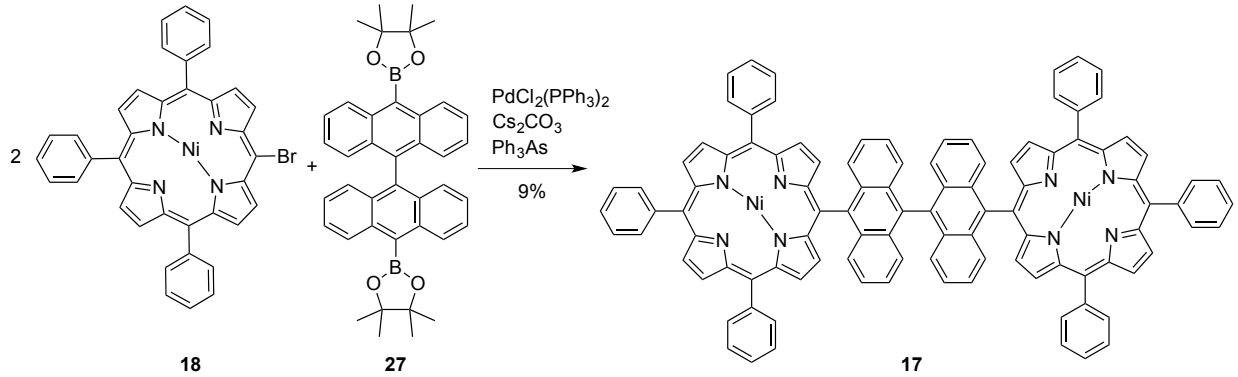

Scheme 3.6 Synthesis of model DBBA-porphyrin **17.**

The absence of a signal near −1.7 ppm in this ^{1}H NMR spectrum indicated the retention of the metal centers. Also, the structure was confirmed by MALDI-HR-MS (Figure 3.11a) with a complex isotope pattern (Figure 3.11c) that agreed well with theory (Figure 3.11b).

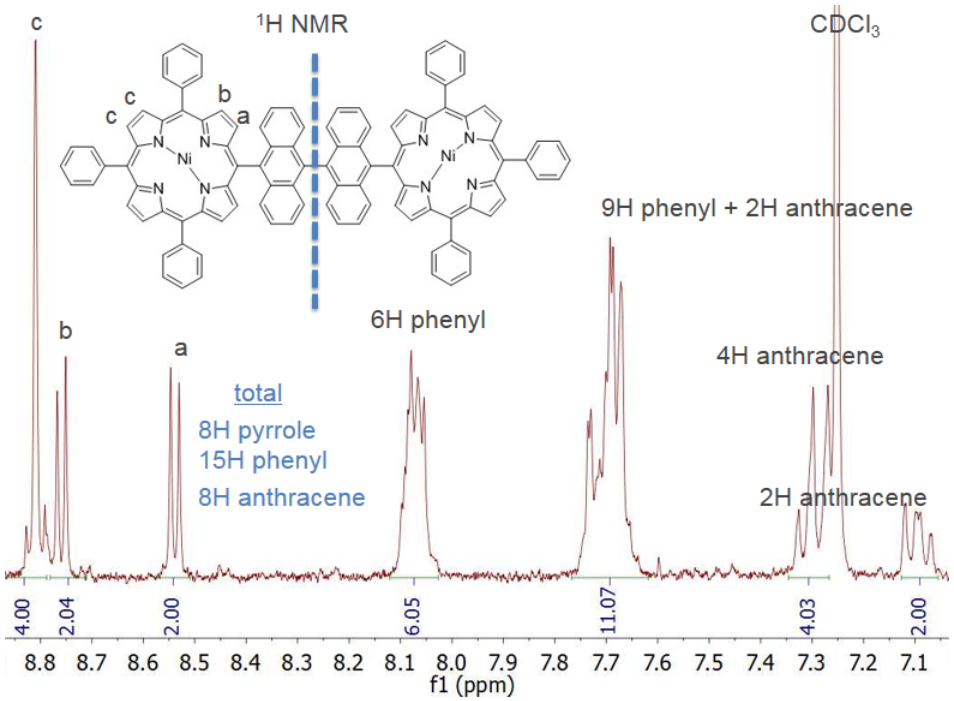

Figure 3.10 [1]H NMR of model compound **17.**

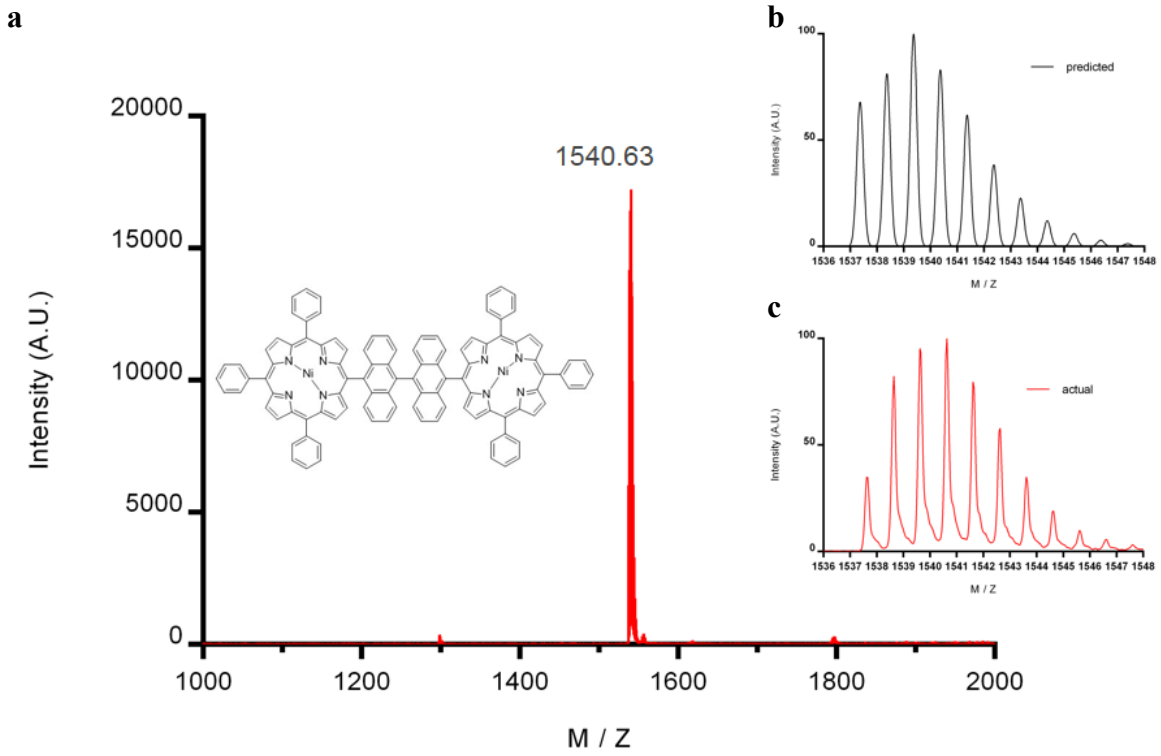

Figure 3.11 (a) MALDI-HR-MS of model compound **17** with (b) theoretical and (c) experimental isotope patterns**.**

3.5 STM Imaging of Porphyrin-Anthracene Dimer on Au(111)

In order to determine the ability of porphyrin-anthracene compounds to undergo surface-assisted cyclodehydrogenation, model system **17** was deposited on Au(111) and studied by STM (Figure 3.12 and Figure 3.13). Even without annealing, **17** appears to undergo complete cyclodehydrogenation. The height profiles both across (Figure 3.12b) and along (Figure 3.12d) the model system show that the compound is less than 2 angstroms tall. This is consistent with the observations made previously for completely cyclized graphene nanoribbons.[53] Therefore it is the first report of surface-assisted cyclodehydrogenation for hybrid porphyrin-GNR systems.

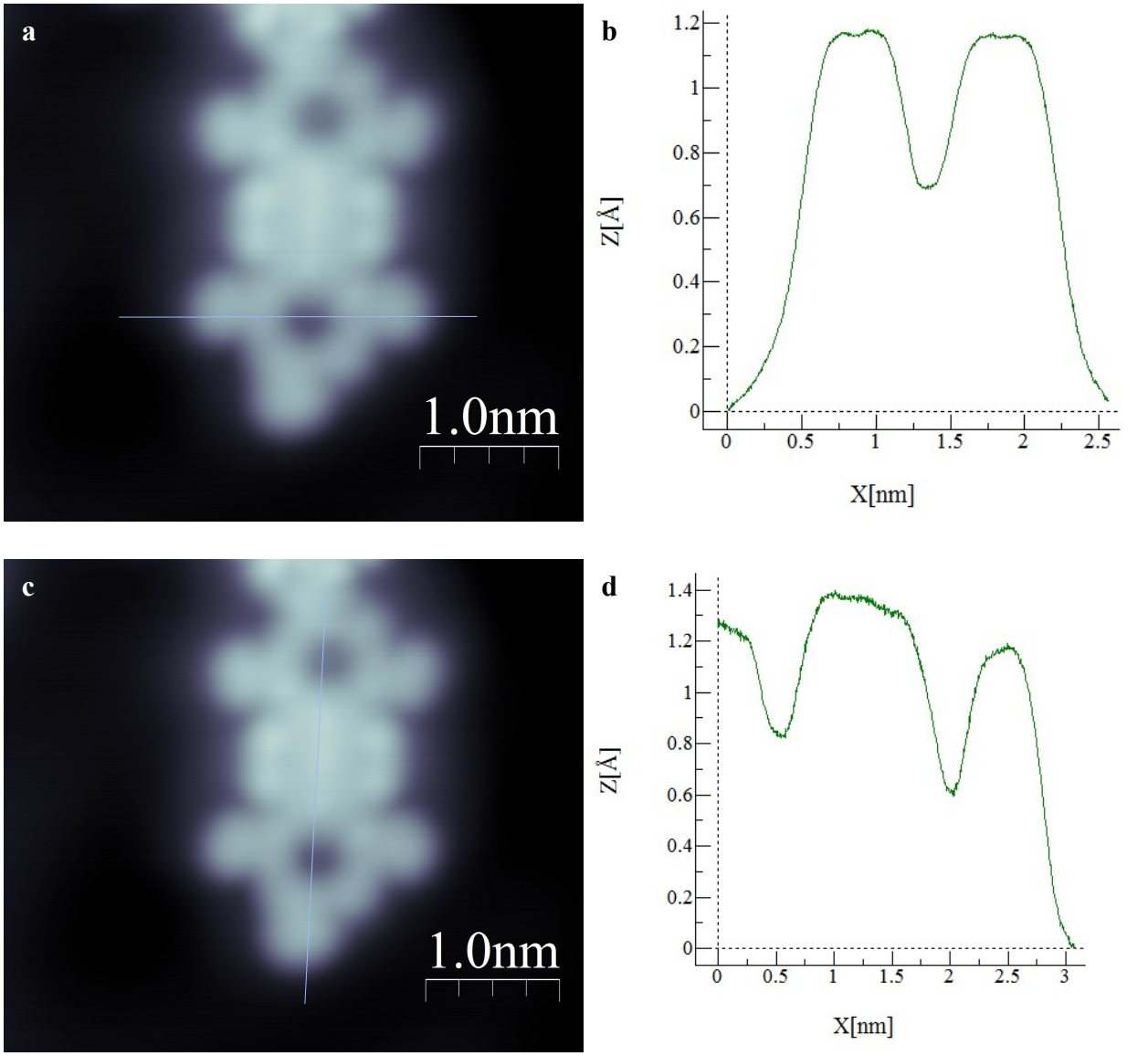

Figure 3.12 (a,c) STM images and (b,d) associated height profiles of model system **17** on Au(111) at 4 K.

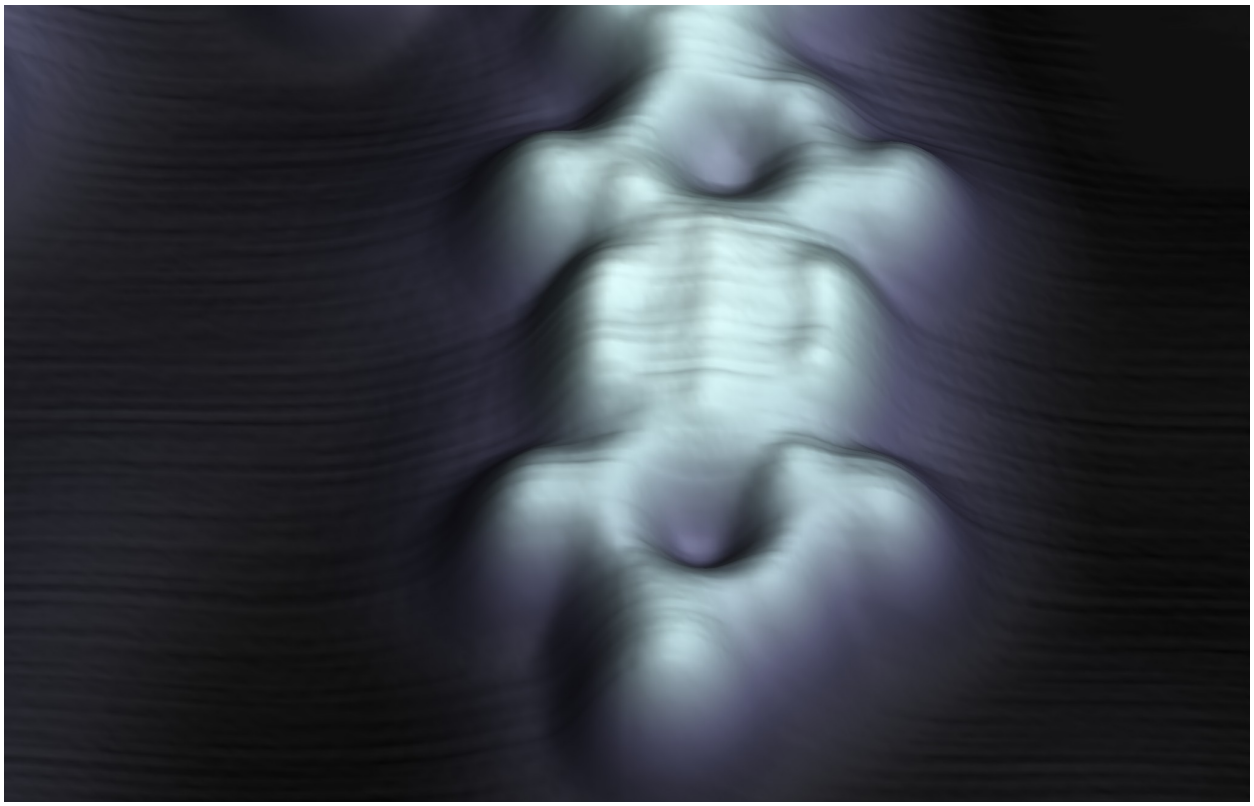

Figure 3.13 3D-representation of STM image of model system **17** on Au(111) at 4 K.

In conclusion, two new types of anthracene-based porphyrins were synthesized. In the first case, a tetrameric porphyrin containing bromoanthracene was studied in UHV-STM on Au(111) and Cu(110). A low-temperature cyclodehydrogenation was observed on both surfaces, indicating that additional optimization of reaction conditions and surface choice are required before attempting to form porphyrin-templated GNR junctions. In the second case, a large model system containing bis-anthracene between two A3 porphyrins was synthesized and fully characterized. UHV-STM of this model compound showed that it readily undergoes surface-assisted cyclodehydrogenation. The determination of the structure of this cyclized product with atomic resolution by non-contact AFM is currently the topic of intense investigation.

Chapter 4
Applications of Graphene Nanoribbons for Energy and Electronics

In this chapter, the concept of solution-based synthesis of graphene nanoribbons is discussed. Through the versatility of organic synthesis, a library of doped Chevron-type graphene nanoribbons was created. These differently functionalized GNRs were used to stabilize magnesium, gold, and tin oxide nanoparticles in applications of hydrogen storage, carbon dioxide reduction, and lithium-ion batteries, respectively. Using this strategy, structure-function relationships were derived that could be related back to the extent of doping in the nanoribbons. The results presented in this chapter are highly encouraging for renewable energy applications.

4.1 Introduction

In principle, GNR synthesis can take place on metal surfaces, entirely in solution, or as a combination of both approaches (Figure 4.1). Because of the limitations in scale of the surface-mediated approach to GNR synthesis, there is an urgent need for solution-based routes to GNRs. However, for application purposes, these different synthetic methods should be considered complementary rather than competitive. The solution-based route is especially attractive for energy applications given its scalability and the low cost of ferric chloride used in the cyclodehydrogenation reaction.

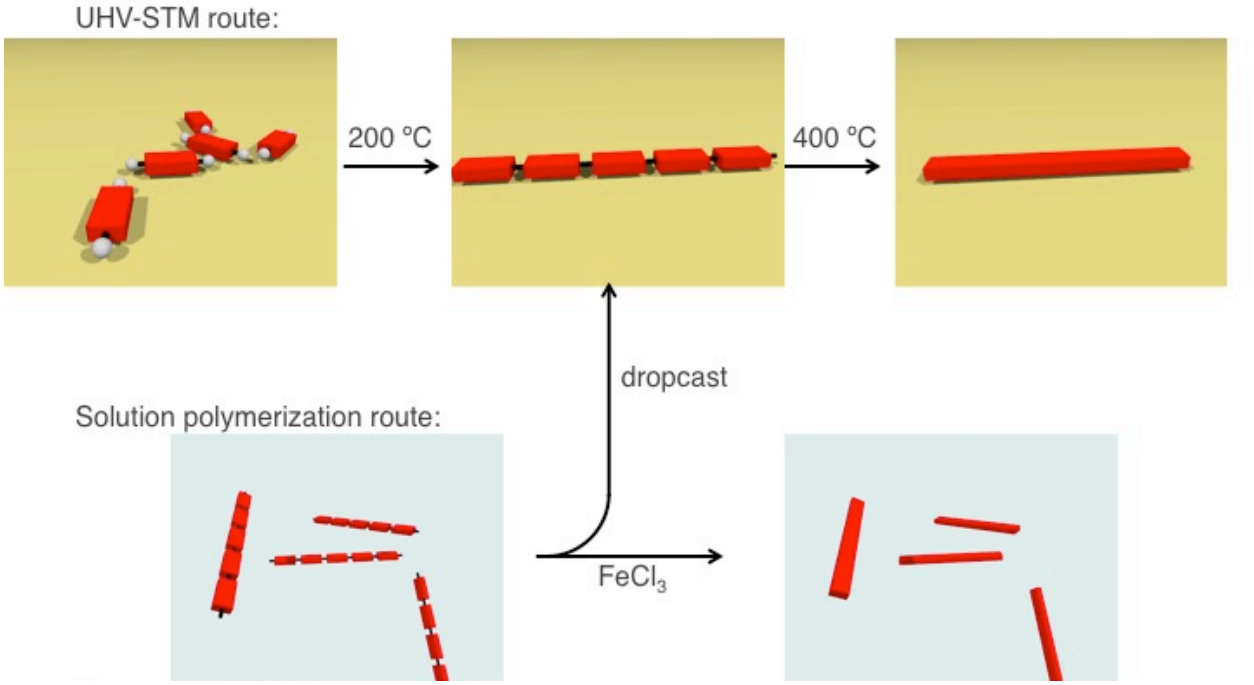

Figure 4.1 Overview of bottom-up routes to graphene nanoribbons.

Most prominently in the field of solution-based GNR synthesis, the Sinitskii Group pioneered the synthesis of chevron GNRs,[72] based on established chemistry from the Müllen Group.[96] In this approach, a hexabenzocoronene (HBC) type monomer was synthesized and subjected to Yamamoto polymerization and cyclodehydrogenation with ferric chloride (Figure 4.2). This family of GNRs was predicted to have a band gap of 1.57 eV based on DFT-LDA calculations. Therefore it is highly similar in terms of semiconducting behavior to the n = 7 armchair GNRs discussed previously, but has the advantages of facile doping through chemical synthesis in tandem with gram-scale synthesis in solution.

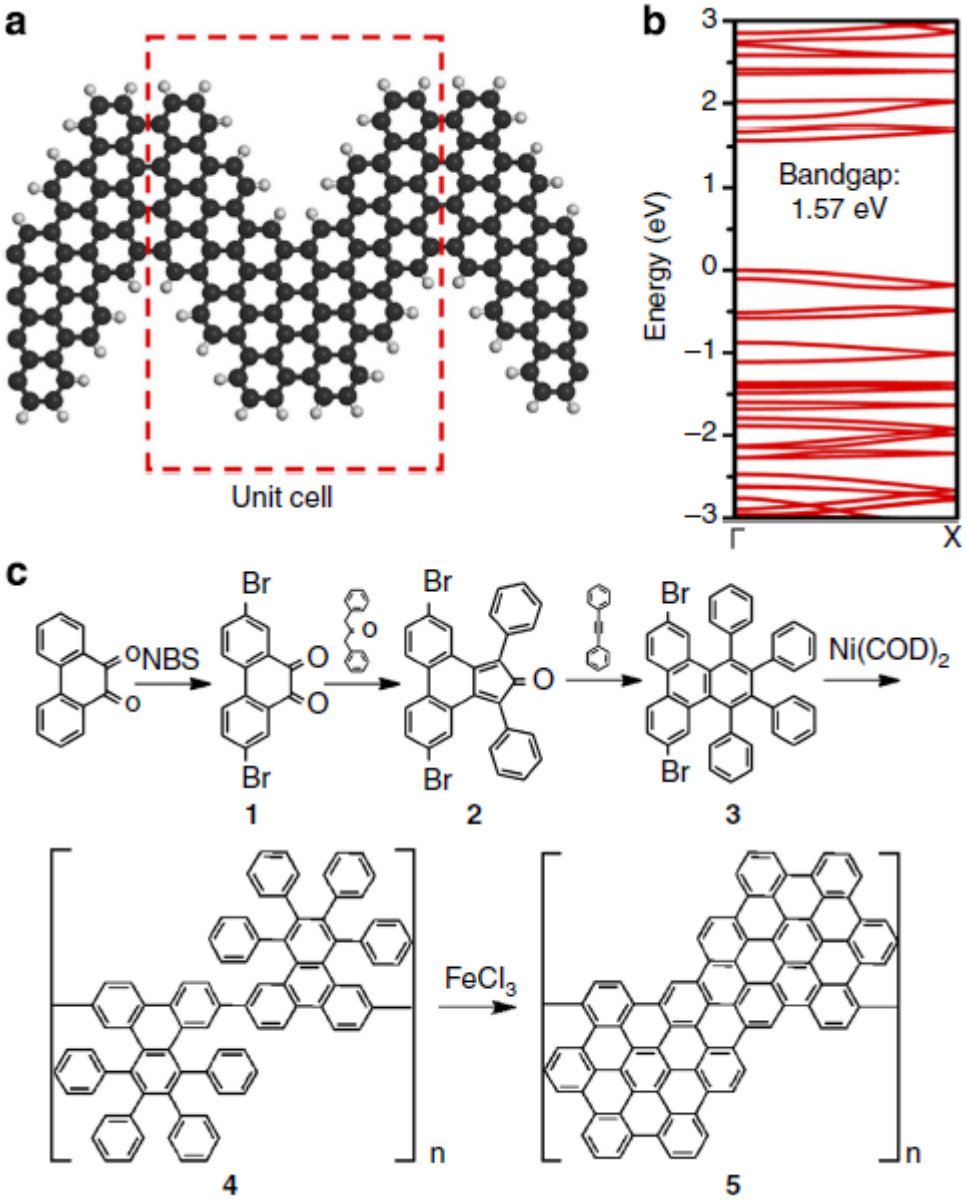

Figure 4.2 (a) Unit cell used to calculate the (b) band structure of this Chevron GNR. (c) Synthesis of Chevron GNRs [reproduced from ref. 72].

This established a new chemical methodology of GNR synthesis in solution, but still leaves much to be desired in terms of doping and solution processability. Additionally, these materials have not been utilized in any application that demonstrates their utility and justifies their synthesis. To this end, a library of Chevron GNRs was synthesized and utilized in transistor, Li-ion battery, hydrogen storage, and carbon dioxide reduction applications. The work reported in this chapter was conducted in collaboration with Dr. Tomas Marangoni and Cameron Rogers of the Fischer Group, Dr. Eun-Seon Cho of the Urban Group, Juan Pablo Llinás of the Bokor Group, Dr. Zhi Cao of the Chang Group, and Dr. Abhinav Gaikwad of the Arias Group.

4.2 Synthesis and Characterization of Doped Chevron GNRs

Following the general synthetic scheme outlined below (Scheme 4.1 and Scheme 4.2), three different Chevron GNRs were synthesized with varying amounts of nitrogen dopants.

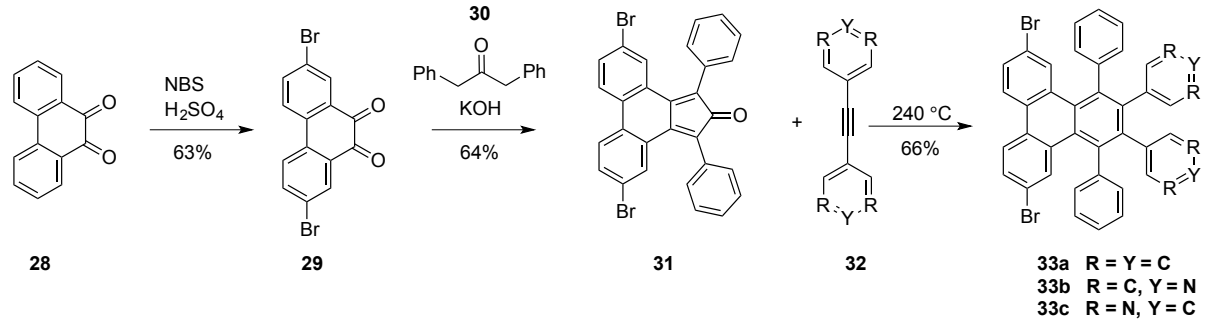

Scheme 4.1 Synthesis of nitrogen-doped Chevron GNR monomers.

Commercially available phenanthrenequinone **28** was subjected to electrophilic bromination with NBS in sulfuric acid. Importantly, **29** can be recrystallized from DMSO eliminating traces of the monobromo side product which would limit molecular weights of the desired polymer. Double Knoevenagel condensation of **31** with diphenyl acetone **30** yielded **31**, which can be reacted with symmetrical tolanes **32a–c** to give monomers **33a–c**. The structures of monomers **33a** and **33b** were proven unambiguously by X-ray diffraction of single crystals (Figure 4.3).

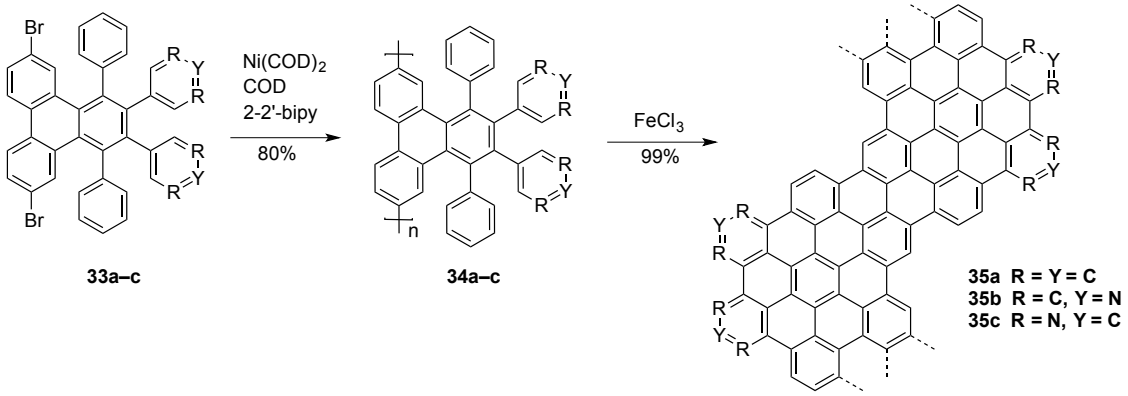

Scheme 4.2 Synthesis of nitrogen-doped Chevron GNRs.

Monomers **33a–c** were subjected to Yamamoto polymerization using Ni catalysis to yield polymers **34a–c**, which were isolated by precipitation and filtration. Scholl oxidation with ferric chloride yielded GNRs **35a–c**.

To complete the library of materials (Scheme 4.4) for applications in transistors, Li-ion batteries, hydrogen storage, and carbon dioxide reduction, ketone-doped GNR **44** was also synthesized (Scheme 4.3). Cyclization of commercially available diphenic acid **36** gave fluorenone **37** with the appropriate substitution pattern. Conversion into ester **38** and subsequent reduction with RED-Al yielded benzyl alcohol **39** without concomitant reduction of the ketone. Oxidation with PCC produced aldehyde **40** and Seyferth-Gilbert homologation furnished target alkyne **41** in excellent yield. Cycloaddition with cyclopentadieneone **31** and fluorenone **41** yielded monomer

42. Ni-mediated polymerization of **42** produced polymer **43**, which could be cyclized with ferric chloride to provide CO-GNR **44**.

a

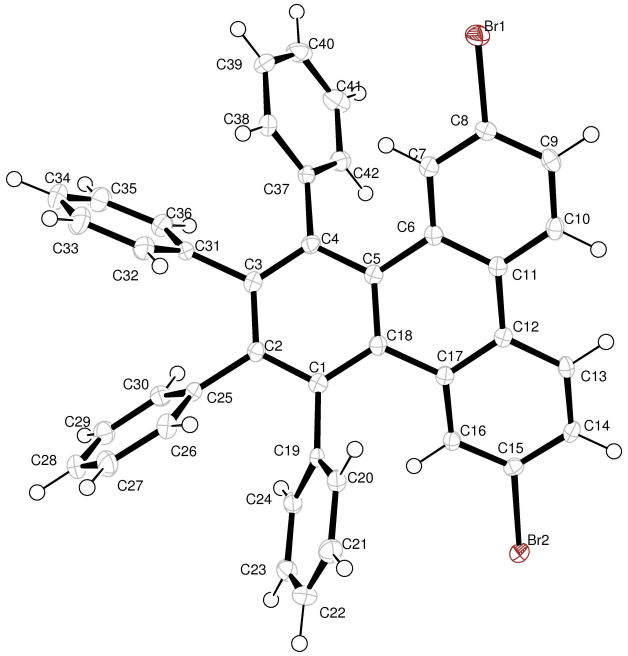

b

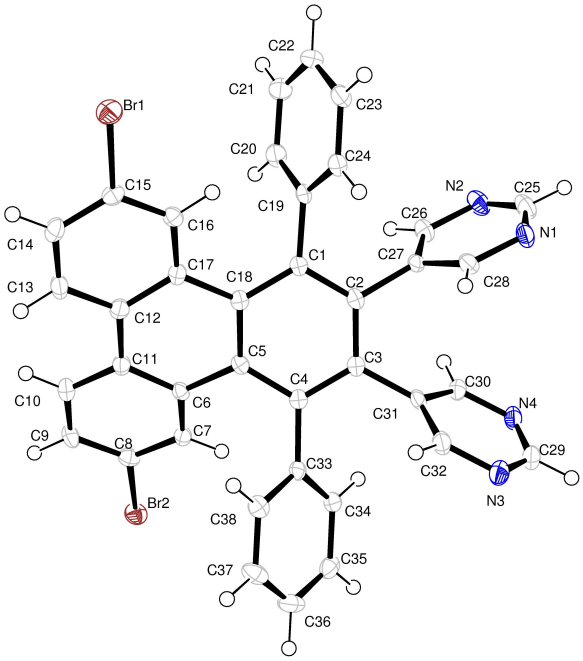

Figure 4.3 X-ray crystal structures of monomers (a) **33a** and (b) **33c**.

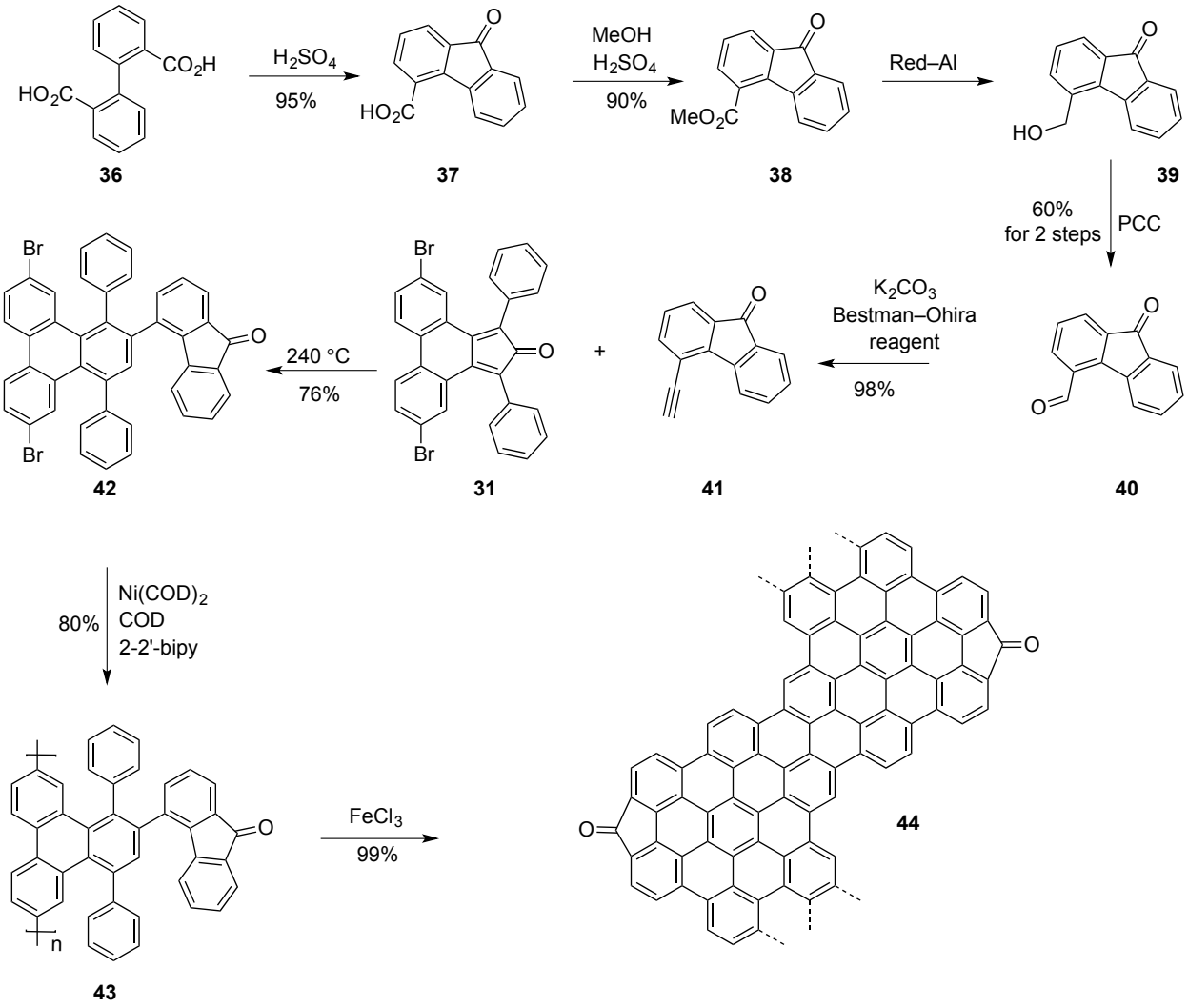

36 **37** **38** **39** **40** **41** **42** **31** **43** **44**

Scheme 4.3. Synthesis of ketone-doped Chevron GNR.

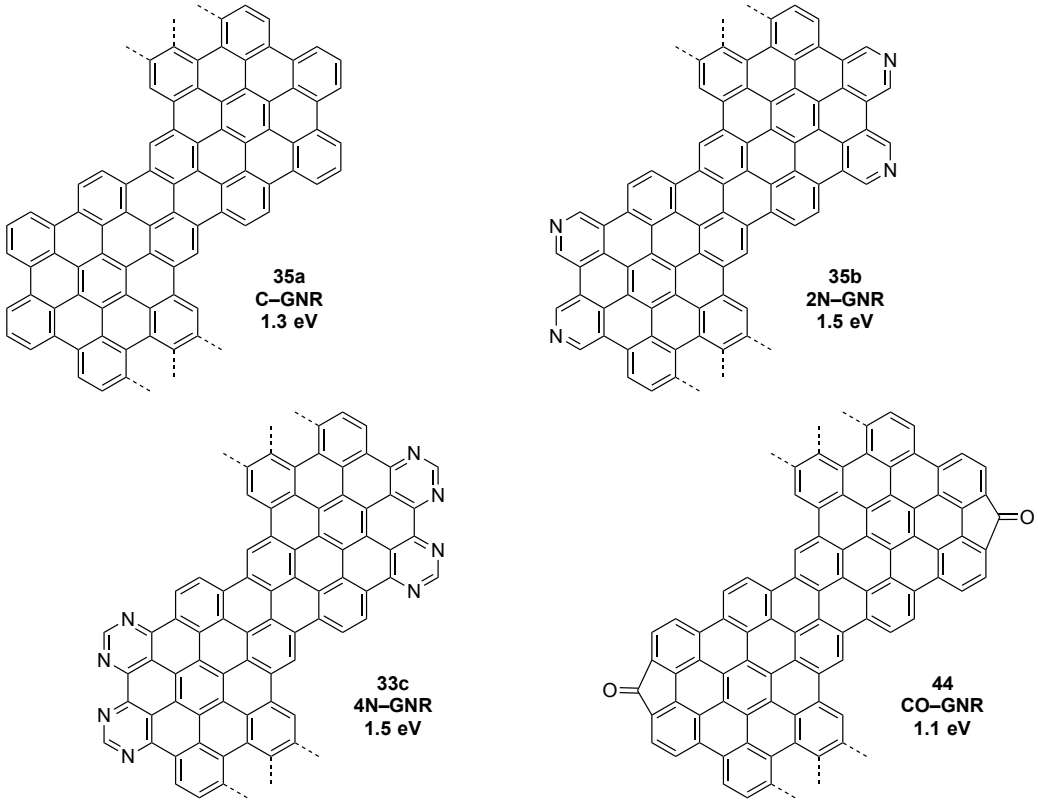

Scheme 4.4 Library of Chevron GNRs synthesized with band gaps calculated using the Quantum Espresso software package at the DFT-LDA level.

This library of GNRs was characterized by Raman spectroscopy, solid-state ^{13}C NMR, TGA, ICP, XPS, and AFM. Characterization of representative GNR samples is provided to demonstrate the effectiveness of this bottom-up synthetic approach (Figures 4.4–4.8).

The high quality Raman spectrum typical of these GNRs (Figure 4.3) is indicative of the structural integrity of graphene nanoribbons after Scholl oxidation.[72] This spectrum exhibits the characteristic D and G-peaks associated with GNRs. The D, or "defect" peak near 1300 cm^{-1}, which is not present in single layer graphene, is attributed to the edge C-H vibrations of the GNRs. The G, or "graphene" peak near 1600 cm^{-1}, is characterized by the sharpness of the peak as well as the ratio of D to G peaks. Additionally, the presence of 2D, D + G, and 2G overtones from ~2700 – 3200 cm^{-1} is a good indication of the sample quality. The presence of a radial breathing-like mode at 250 cm^{-1} suggests that, similar to carbon nanotubes, bottom-up GNRs are long enough to display longitudinal breathing along the ribbon axis.

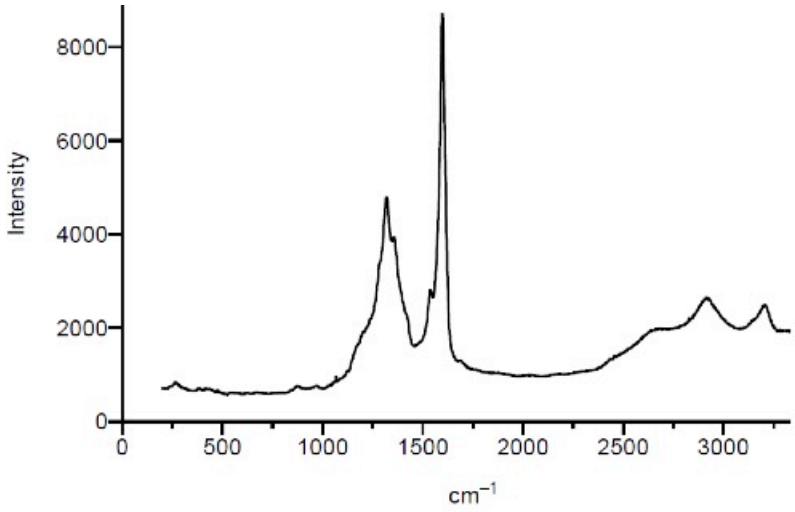

Figure 4.4 Raman spectrum of 4N-GNR **35c**

While the all-carbon and nitrogen containing GNRs exhibited essentially identical Raman spectra, CO-GNR **44** presented a much greater D / G peak ratio (Figure 4.5). Since the D-peak is associated with the edge structure, this could be explained by the presence of the ketone functional group along the edge of the graphene nanoribbon.

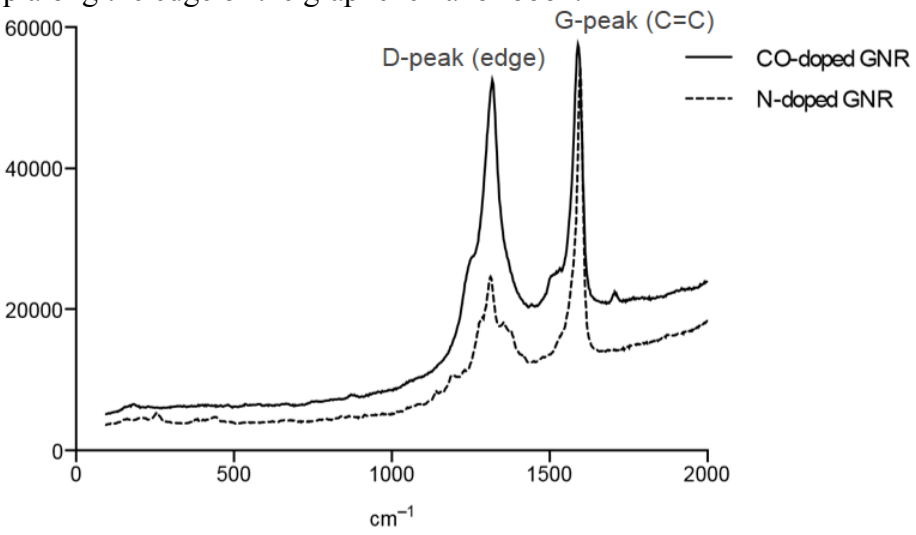

Figure 4.5 Comparison of Raman spectra for nitrogen-doped and ketone-doped GNRs.

GNRs are insoluble in all organic solvents, so 4N-GNR **35c** was studied by ^{13}C solid-state NMR (Figure 4.6). Consistent with the proposed structure of 4N-GNR **35c**, only one carbon peak was observed. This broad peak at 130 ppm suggests the presence of aromatic carbon, proving that all of the carbons in the material are sp^2 hybridized. The peaks observed at 210 and 30 ppm are equidistant from the broad aromatic signal, and are assigned as side spinning bands commonly detected in solid-state NMR.

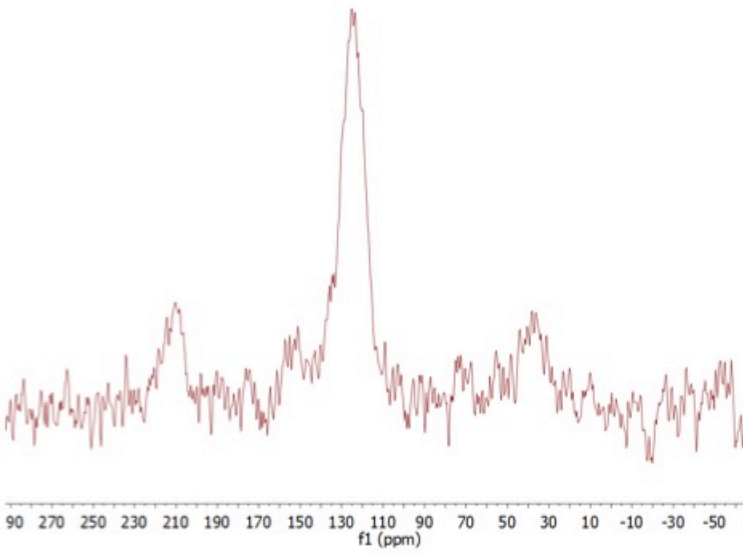

Figure 4.6 Solid-State ^{13}C NMR of 4N-GNR **35c**.

In order to quantify trace amounts of iron and nickel remaining in the GNR after Scholl oxidation and Yamamoto polymerization, 4N-GNR **35c** was subjected to Thermogravimetric Analysis (Figure 4.7). This GNR was stable up to 475 °C in air and rapidly decomposes after this temperature. The residual mass of 2.07% was assigned to trace metals trapped within GNR aggregates that could not be removed by repeated cycles of sonication and filtration in 1M HCl (aq.), water, THF, and acetone. This value agreed well with Inductively Coupled Plasma Optical Emission Spectrometry (ICP-OES), which provided 2.21% $\pm$ 0.04% (g/g) Fe and 0.17% $\pm$ 0.01% (g/g) Ni content, for an overall GNR purity of 97.6% (g/g).

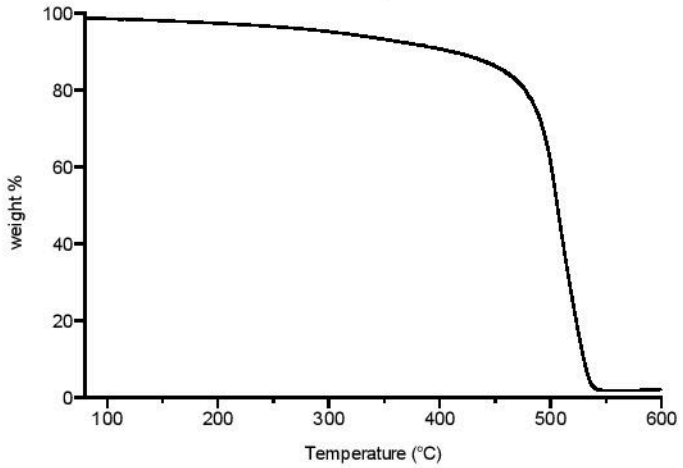

Figure 4.7 TGA in air of 4N-GNR **35c**.

X-ray Photoelectron Spectroscopy (XPS) on SiO_2 was used to quantify the overall nitrogen content within the GNR (Figure 4.8). As expected, C 1s, C 2p, N 1s, and N 2p electrons were

detected by this method. Additionally, a small amount of Cl 2p was observed, indicating that undesired chlorination of the GNR occurred during the reaction with ferric chloride. By integrating the carbon and nitrogen 1s peaks, a C:N ratio of 89.7 : 9.7 was obtained. This value was in excellent agreement with the expected C:N ratio of 90.48 : 9.52 based on the monomer structure. The iron content detected by this technique relative to carbon was 6 ppm. This demonstrated that the design of the molecular precursor can indeed determine the final GNR structure, and that this GNR can be obtained in high purity.

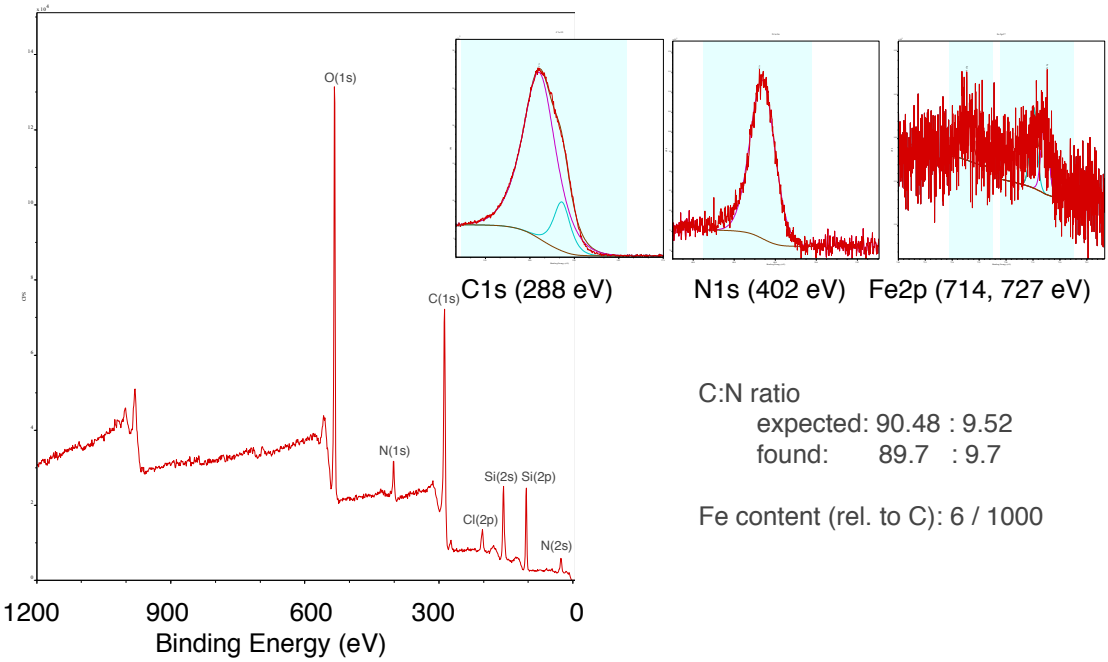

Figure 4.8 XPS survey of 4N-GNR **35c**. Inset shows detailed analyses of C, N, and Fe.

4.3. Scanning Probe Microscopy Investigation of Solution-Processed GNRs

Having verified the high degree of structural integrity and purity, Atomic Force Microscopy was employed to visualize the length distribution and morphology of bottom-up GNRs (Figure 4.9 – 4.11). After sonication of a 15µg per mL solution of GNRs in THF, the samples were dropcast on freshly cleaved mica and visualized by AFM. At the 5 micron scale, very large aggregates of GNRs were seen in both topography and amplitude (Figure 4.9a–c). Much smaller bundles were observed in the amplitude image at this length scale. Upon closer inspection, this bundle, which has a height of 3 nm and length of ~500 nm, consists of several GNRs. Higher resolution of this bundle reveals a single GNR extending from the end of the bundle (Figure 4.9g). The height of this GNR is 3.4 angstroms, which is consistent with the Van der Waals diameter of a single carbon atom. In an attempt to remove aggregates of GNRs, the dispersion was centrifuged prior to dropcasting and subsequently studied by AFM (Figure 4.10). This approach removed GNR bundles and single GNRs were easily visualized.

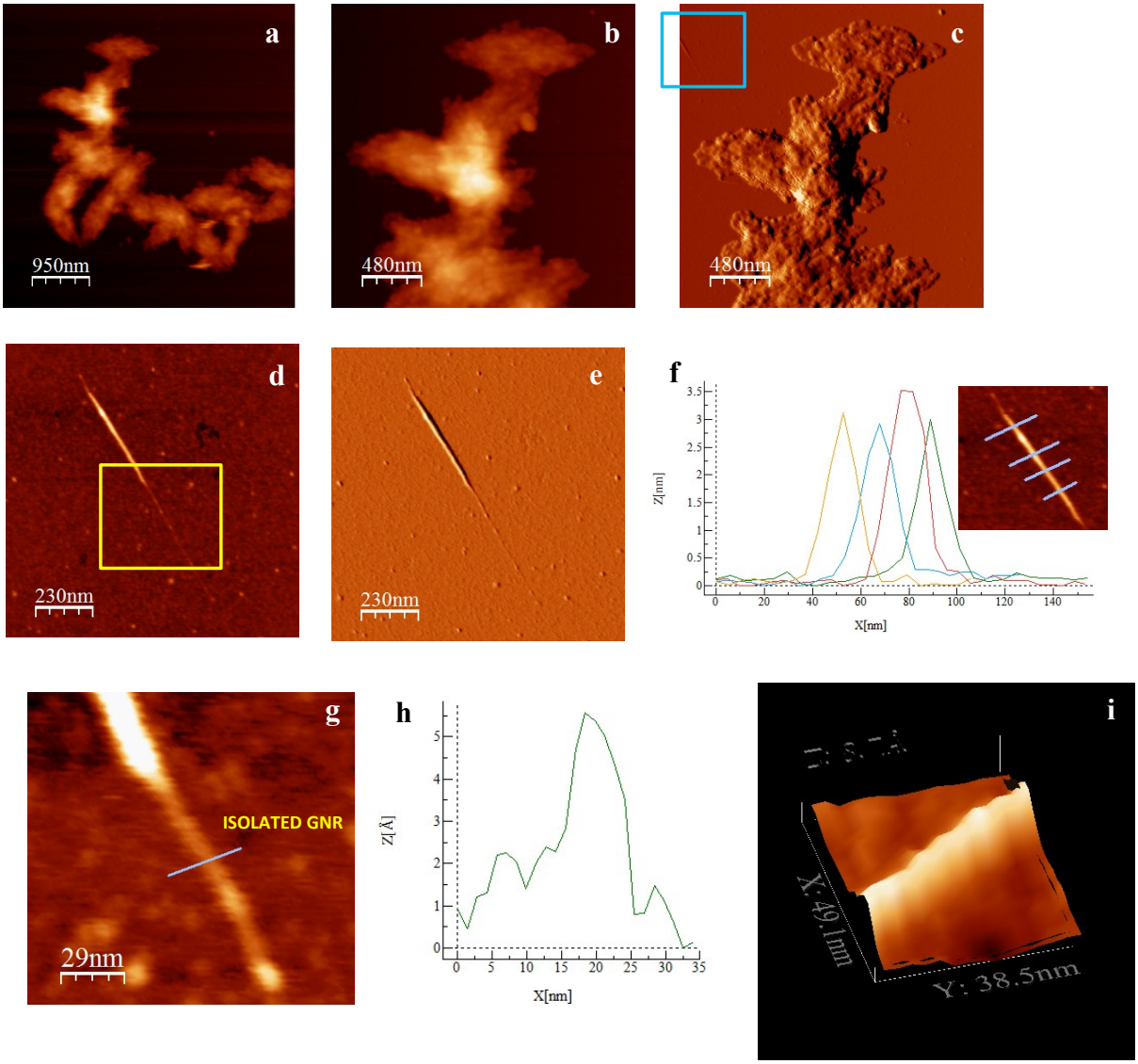

Figure 4.9 AFM of 4N-GNR **35c**. Topography images reveal micron-sized aggregates of GNRs (a,b). Very small bundles of several GNRs are visible in the amplitude of the same image (c). Rescanning the region shown with a blue box in (c) provides a clear view of the GNR bundles both in topography (d) and amplitude (e). Height profiles (f) measured along a GNR bundle in (d) demonstrates the majority of the structure is 3.5 nm tall. Rescanning the area indicated by the yellow box in (d) shows the topography of an isolated GNR (g) extending from the end of the bundle. 3D-representation (h) and a height profile measurement (i) across this structure in (g) prove that the height is consistent with a single, isolated GNR.

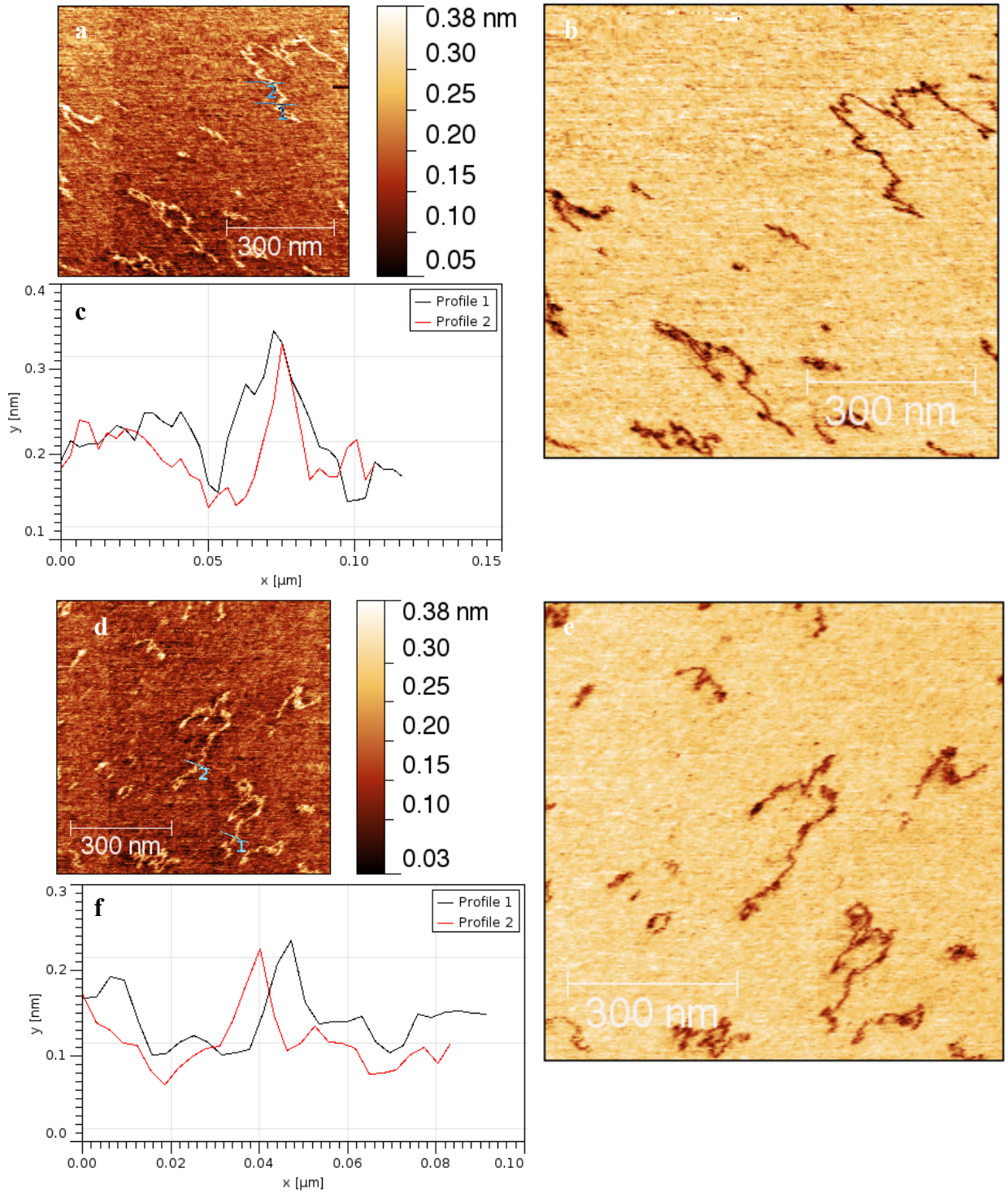

Figure 4.10 AFM at two different locations (a–c, d–f) of 4N-GNR **35c** after centrifugation and dropcasting on mica. Topography (a, d) and corresponding height profiles (c, f), along with phase (b, e) images, confirm the presence of single, isolated GNRs.

Because of the high degree of hydrophobicity and flexibility of graphene nanoribbons, they tend to interact more strongly with each other, rather than with polar surfaces. For this reason, GNRs on exfoliated boron nitride on silicon were studied by AFM (Figure 4.11). On BN, the GNRs form highly interconnected networks with bundles containing 1 – 10 nanoribbons. This demonstrates the importance of developing appropriate processing conditions in view of the goal to use GNRs for energy and electronics applications.

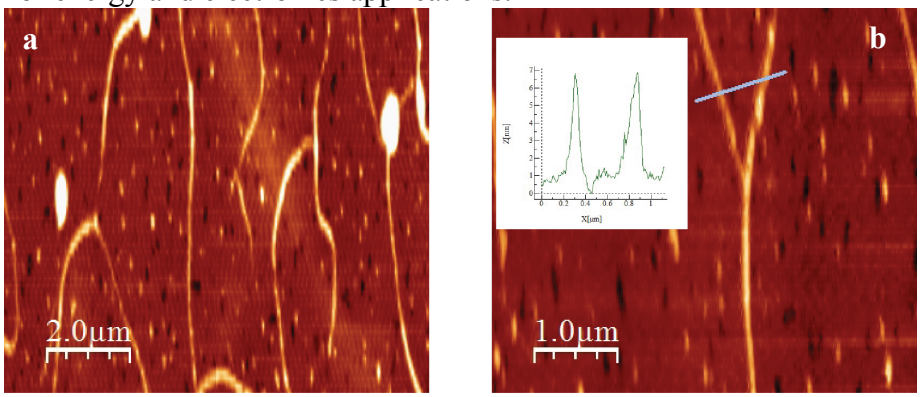

Figure 4.11 AFM topography images (a, b) of C-GNR **35a** on boron-nitride. The inset in (b) contains the height profile showing that the GNR bundles are 7 nm tall.

GNRs were also visualized by SEM on SiO_2 with pre-patterned contact pads (Figure 4.12).

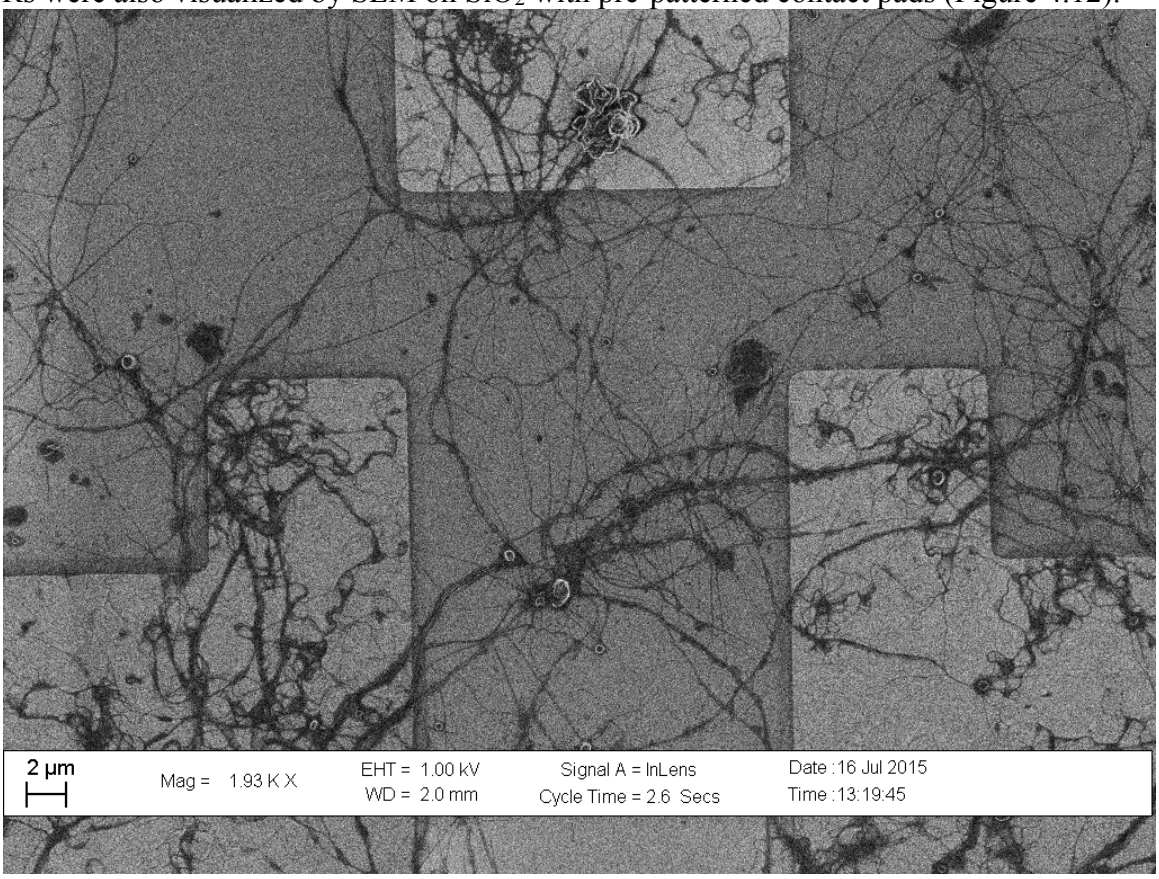

Figure 4.12 Scanning Electron Microscope (SEM) image of C-GNR **35a** with contact pads.

At this length scale, nanoscale bundles of C-GNR **35a** self-assemble to form "wires" of nanoribbons that can be visualized by SEM. The "wires" of graphene nanoribbons are in the range of 200 nm wide by 30 microns long. Since an individual GNR is expected to have dimensions of 1 nm by 200 nm, this means that several hundred nanoribbons assemble together to form wires.

With the goal of measuring the electrical behavior of single GNR wires, FETs devices were created from this sample (Figure 4.13). Transistors with a 2-micron pitch were fabricated by e-beam lithography and SEM clearly showed GNR wires spanning the source-drain gap. Unfortunately, no devices to date have demonstrated a measureable turn-on current. One hypothesis for this observation is that the work function of Pt (5.64 eV) is not well aligned to the valence or conduction band of C-GNR **35a**.[97]

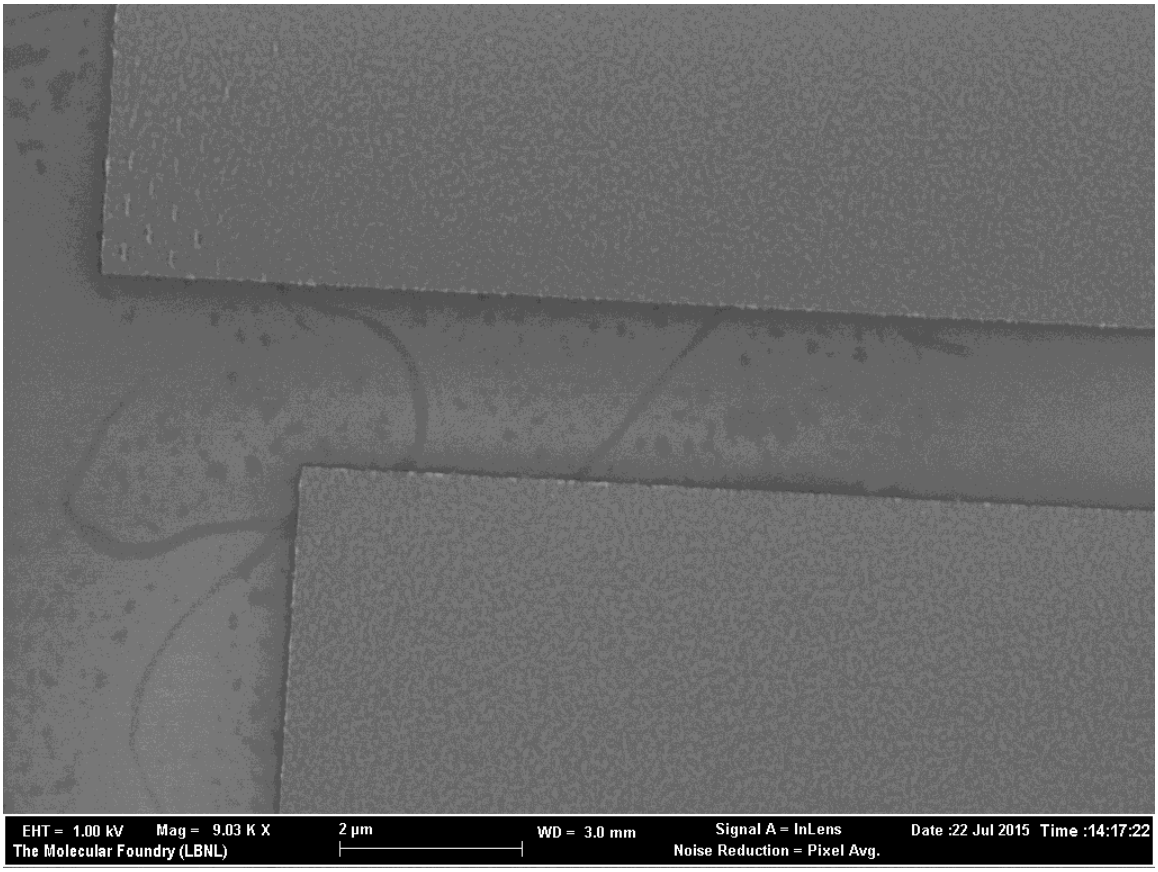

Figure 4.13 Attempted FET device fabrication of C-GNR **35a**.

4.4 Hydrogen Storage Using GNR-Mg^0 Nanoparticle Hybrid Materials

The use of hydrogen as a fuel has tremendous potential in a clean energy future. However, the inability to store this high energy fuel (142 MJ kg^{-1}) using mild temperatures and pressures has so far limited its utility in energy applications.[98] Nanostructured magnesium hydride is one of the most promising candidates for reversible H_2 storage (7.6 % H_2 by mass), but Mg^0 tends to immediately oxidize in air.[99] In order to overcome this problem, in a collaborative effort with the group of Dr. Jeff Urban at Lawrence Berkeley National Laboratory (LBNL), a novel class of

Mg^0 nanoparticle / GNR hybrid materials was synthesized. Stabilization of Mg^0 nanoparticles with GNRs was achieved and this material showed a remarkably high tolerance to atmospheric oxygen and an improved H_2 capacity (up to 7.2 % H_2 by mass) compared to isolated Mg^0 nanoparticles. This result is very near the DOE ultimate goal for H_2 storage and consequently warrants further investigation (Figure 4.14).[100]

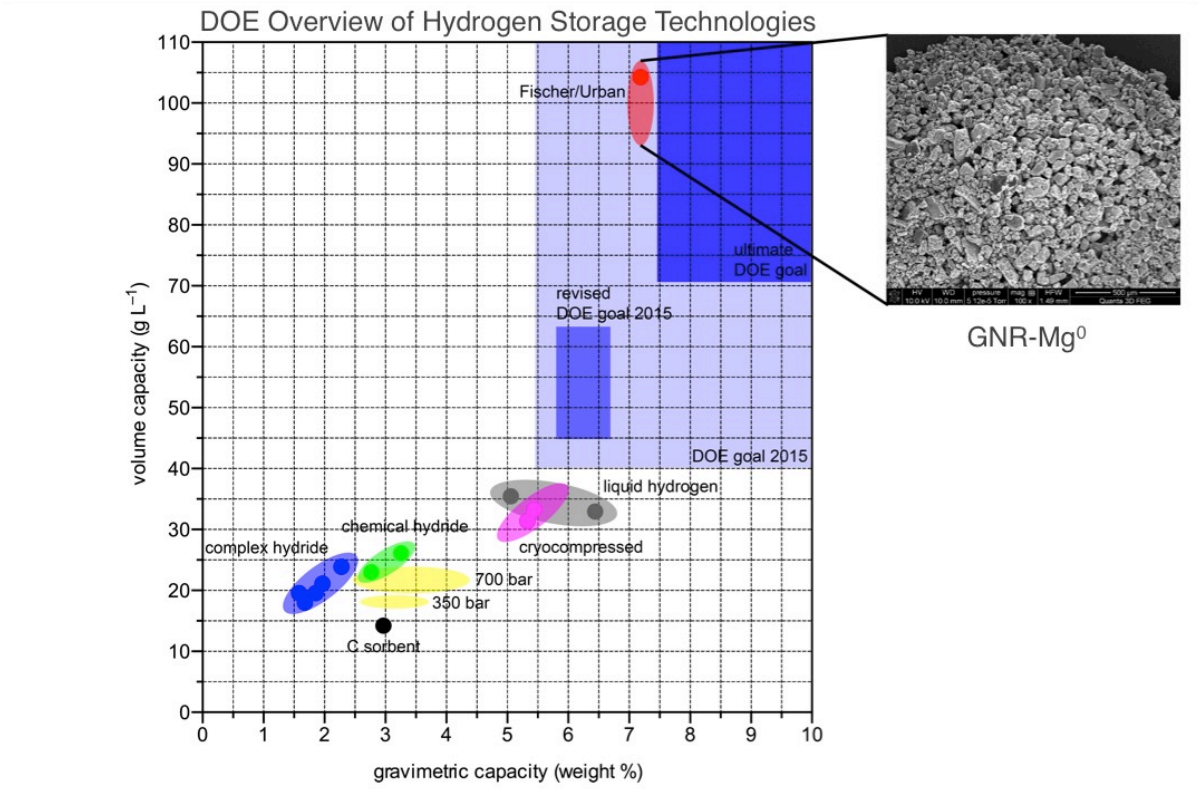

Figure 4.14 Summary of hydrogen storage technologies [modified from ref. 100]. The oval marked, "Fischer / Urban", gives the range of the hybrid materials synthesized in this collaboration and described in this chapter.

The composite material was synthesized *in situ* by reduction of $Mg(cp)_2$ with Li naphthalenide in the presence of GNRs **35a–c** and **44** (Scheme 4.5). After isolation by centrifugation, the air-stable composite materials were subjected to characterization by XPS (Figures 4.15 and 4.16), TEM (Figure 4.17), XRD (Figure 4.18), Raman spectroscopy (Figure 4.19), SEM (Figures 4.20), and hydrogen absorption / desorption cycling (Figures 4.21 – 4.25).

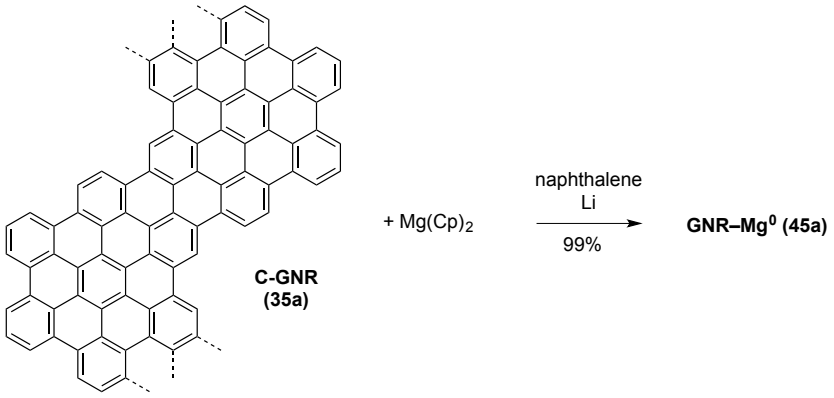

Scheme 4.5 Synthesis of hybrid GNR-Mg^0 materials.

The XPS survey shows the presence of Mg 1s, 2s, and 2p electrons in the material after synthesis (Figure 4.15). Closer inspection of the carbon edge of 4N-GNR **35c** before synthesis of the hybrid material reveals the presence of C-C, C-N, and a small amount of C-O bonds (Figure 4.16). After hybrid material synthesis, a new π-π* bond is observed. It is hypothesized that this new interaction between 4N-GNR **35c** and Mg^0 nanoparticles is responsible for the oxygen stability imparted to these hybrid materials.

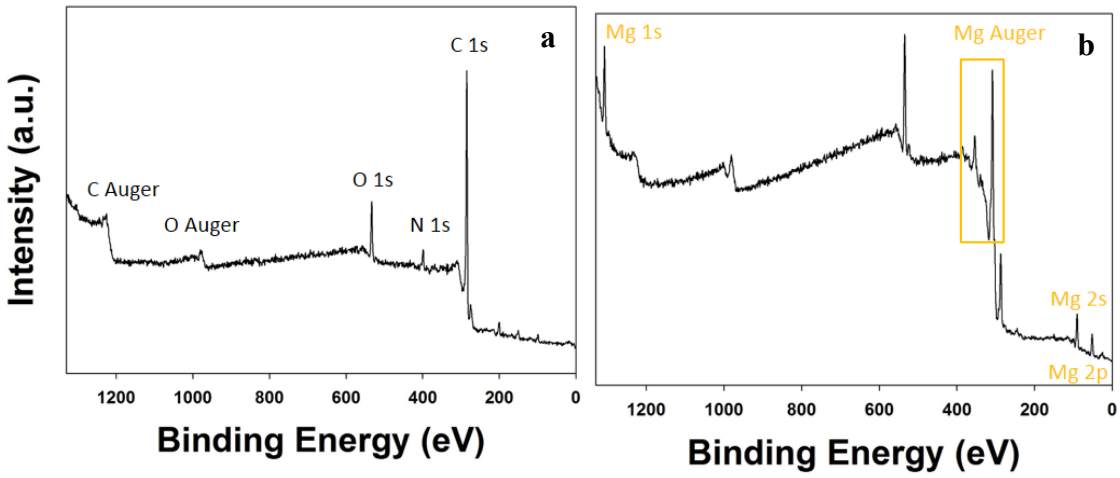

Figure 4.15 XPS survey of (a) 4N-GNR **35c** and (b) 4N-GNR / Mg^0 **45c**.

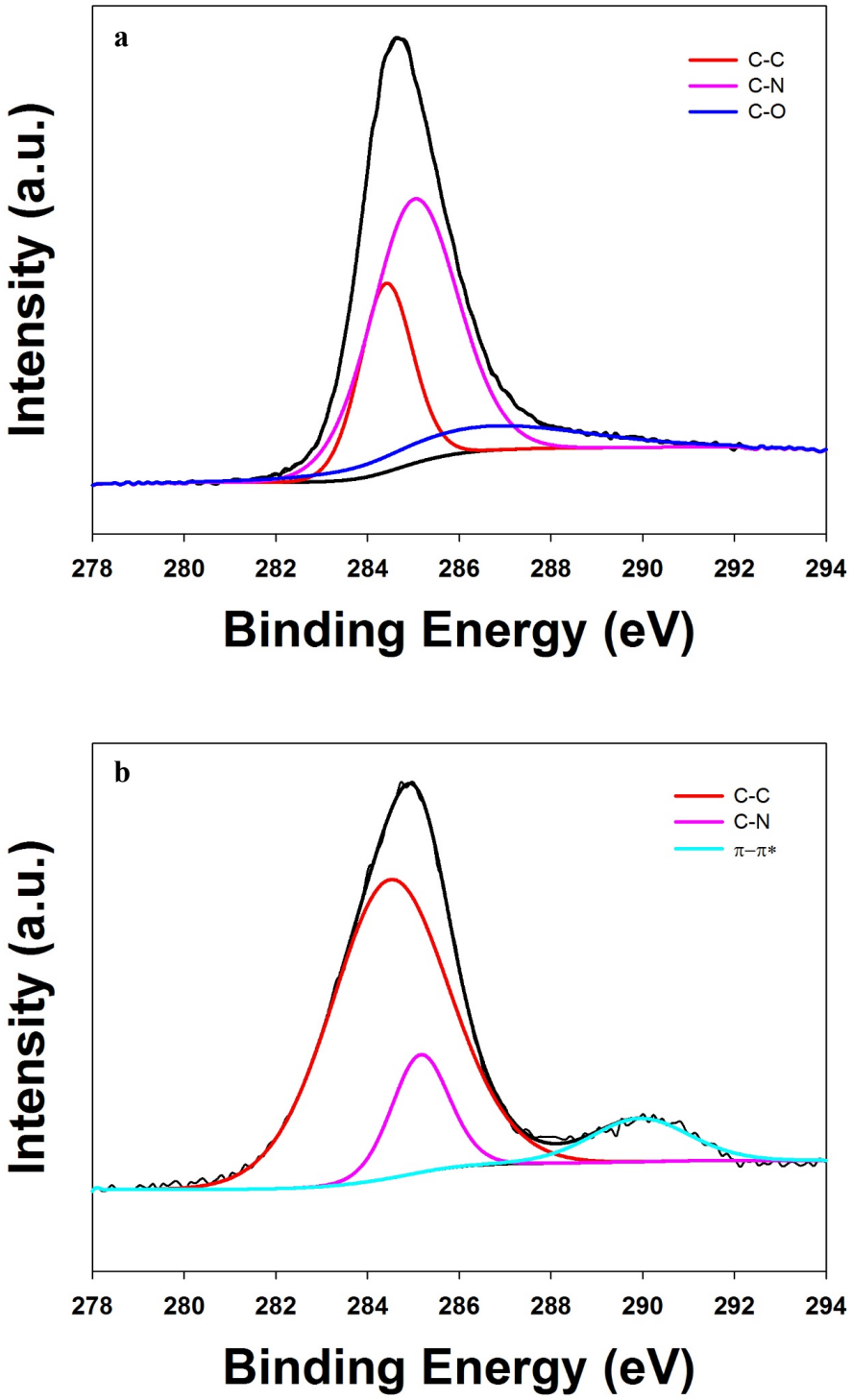

Figure 4.16 XPS analysis of C 1s region (a) before and (b) after hybrid material synthesis.

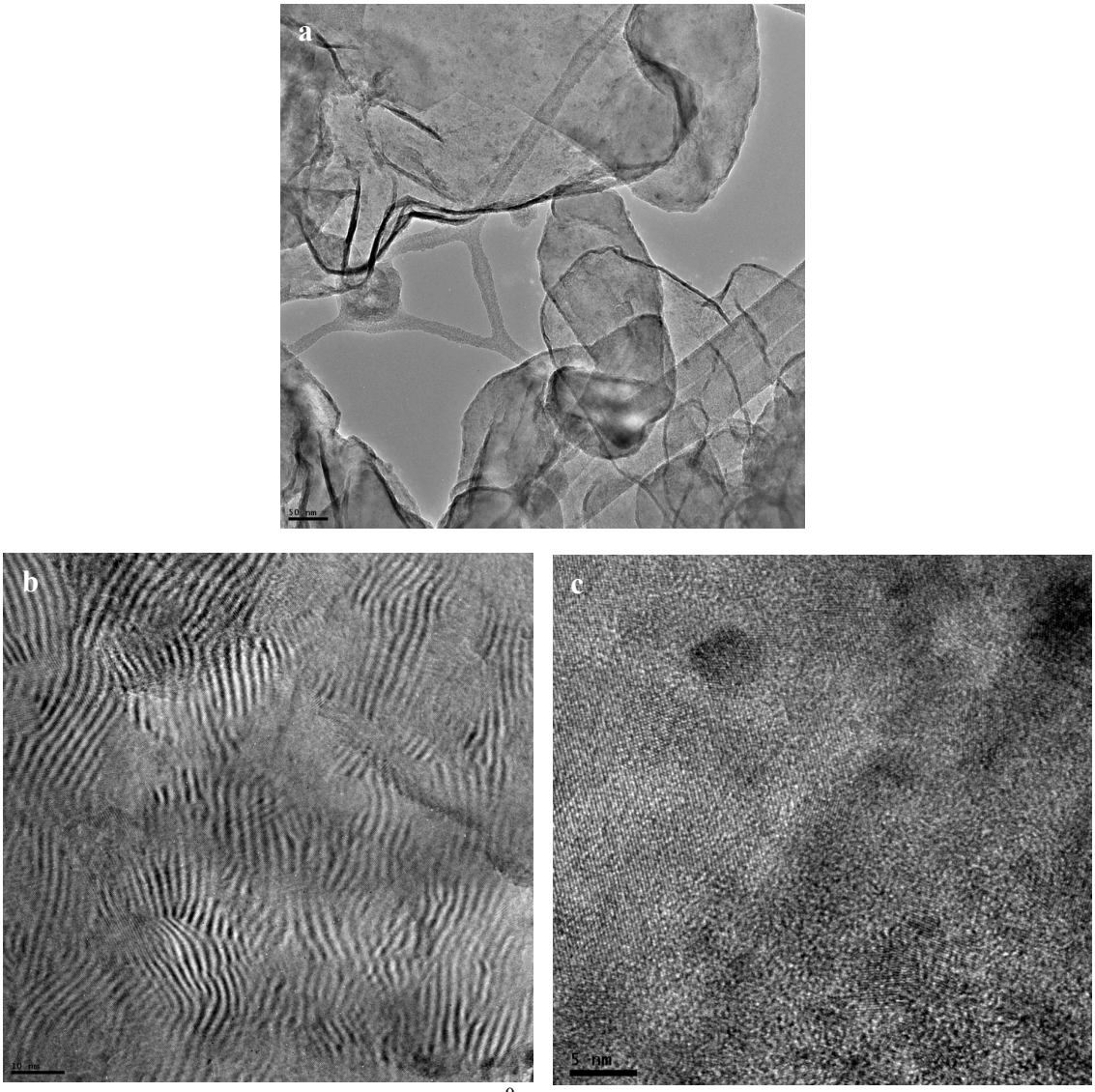

Figure 4.17 TEM of CO-GNR **44** / Mg^0 hybrid. The magnification is increased from (a) to (b) to (c). Scale bars are 30, 10, and 5 nm, respectively.

TEM analysis of CO-GNR **44** / Mg^0 hybrid material showed nanostructuration over multiple length scales (Figure 4.17). Over hundreds of nanometers, the material appeared as a sheet containing dark spots that were attributed to magnesium nanoparticles (Figure 4.17a). Upon closer inspection, the sheets contained arrays of oriented stripes, which were thought to consist of oriented GNRs (Figure 4.17b). At high magnification, dark spots attributed to Mg^0 nanoparticles are observed that can be as small as 4 nm (Figure 4.17c). The hierarchical structure of this hybrid material over multiple lengths scales is considered a great advantage in terms of stability and surface area enhancements and is a contributing factor to the success of this material in reversible hydrogen storage.

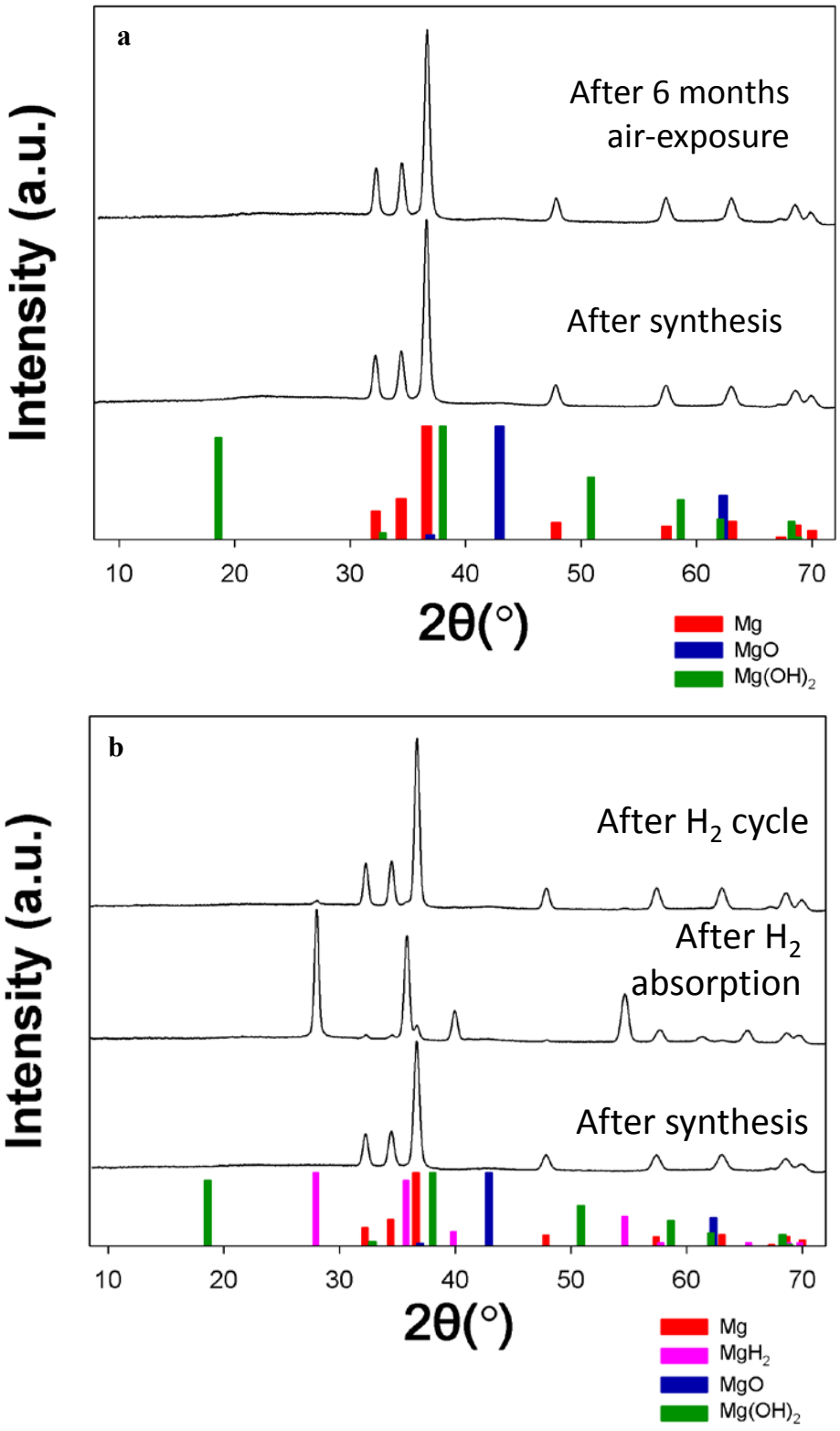

Figure 4.18 Powder XRD of 4N-GNR **35c** / Mg^0 hybrid material showing the (a) long-term air stability and (b) reversibility of hydrogen absorption and desorption for this material.

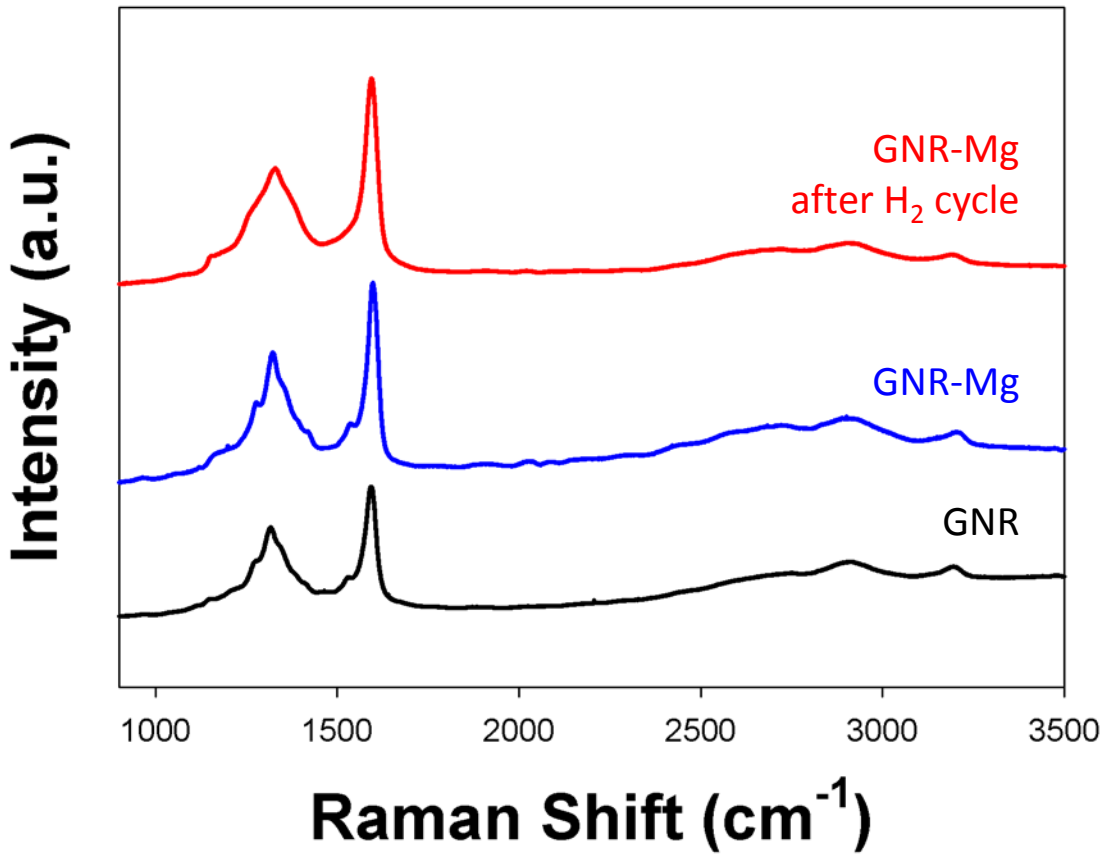

Figure 4.19 Raman spectroscopy of 4N-GNR **35c** and 4N-GNR **35c** / Mg^0 hybrid material.

Because of the intended application of hydrogen storage in fuel-cell vehicles, reversibility of absorption / desorption cycles in tandem with extreme air stability are paramount requirements for any useful technology in this field. Therefore, a series of XRD experiments was performed on hybrid GNR-Mg NPs. After synthesis of composite material 4N-GNR **35c** / Mg^0, there are no traces of MgO or $Mg(OH)_2$ species. Even after 6 months of exposure to ambient conditions, there are no traces of magnesium oxides (Figure 4.18a). After exposure to hydrogen at 15 bar and 250 °C for 3 hours, Mg^0 peaks had nearly vanished and been replaced by peaks matching the simulated pattern of MgH_2. After heating this material at 300 °C for 3 hours without an overpressure of hydrogen, the XRD patterns shows the nearly quantitative return to Mg^0 species (Figure 4.18b). Likewise, Raman spectroscopy shows that the GNRs remain undamaged throughout this process (Figure 4.19). This is a strong indication that hybrid GNR- Mg^0 NPs can be considered a promising platform for reversible hydrogen storage.

SEM images of hybrid GNR-Mg^0 NPs show a highly porous, somewhat amorphous structure (Figure 4.20). 2N-GNR **35b** / Mg^0 is the most amorphous and least porous of the series, which could explain its lower performance.

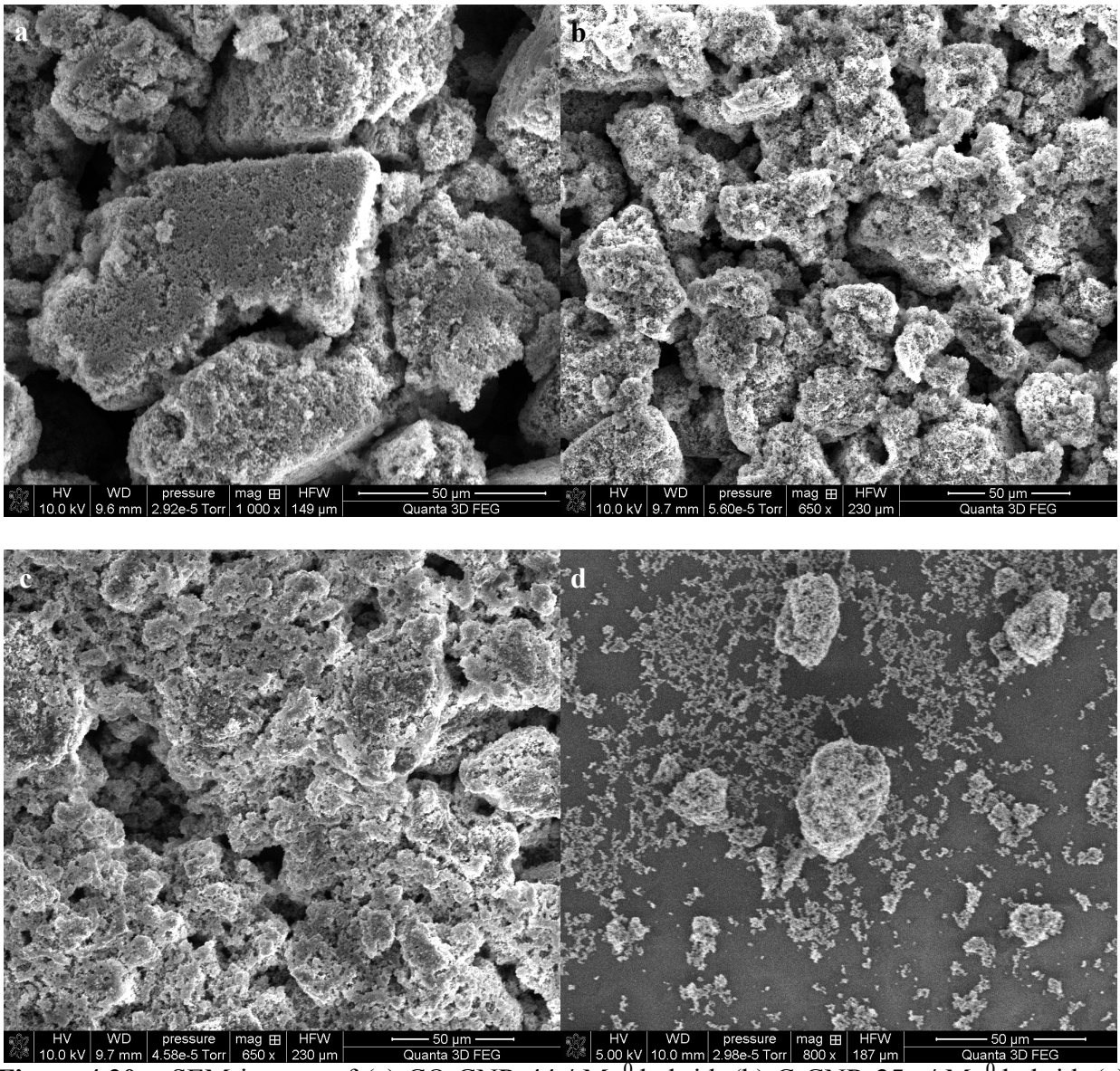

Figure 4.20 SEM images of (a) CO-GNR **44** / Mg^0 hybrid, (b) C-GNR **35a** / Mg^0 hybrid, (c) 2N-GNR **35b** / Mg^0 hybrid, and (d) 4N-GNR **35c** / Mg^0 hybrid materials.

Hydrogen absorption experiments with hybrid materials at 15 bar H_2 and various temperatures over 3 hours demonstrate a remarkable propensity for hydrogen uptake, exceeding 7 wt % in many cases (Figure 4.21). At 200 °C (Figure 4.21a), there is a very clear difference in the kinetics of hydrogen absorption for differently functionalized hybrid materials. Hybrid materials containing 4N-GNR **35c** or CO-GNR **44** absorb hydrogen faster than their C-GNR **35a** or 2N-GNR **35b** counterparts. There is also a difference in the magnitude of hydrogen absorption between the hybrid materials at this temperature. At 225 °C (Figure 4.21b), hybrid material containing C-GNR **35a** has the slowest absorption kinetics, while the other three hybrid materials perform similarly in terms of kinetics and absorption magnitude. At 250 °C (Figure 4.21c), all

hybrid materials display nearly identical kinetics and capacity, with the materials almost fully loaded within 30 minutes.

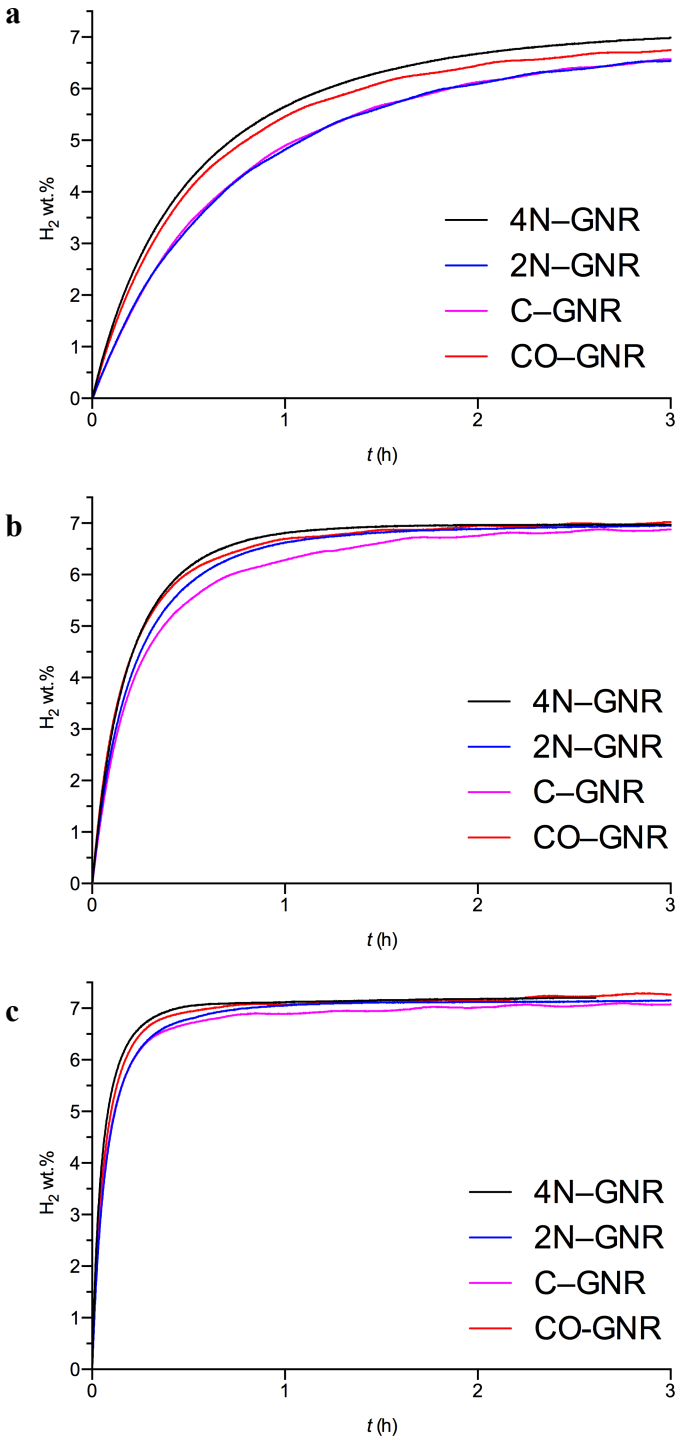

Figure 4.21 Hydrogen absorption experiments of GNR / Mg^0 hybrid materials at 15 bar H_2 and 200 °C (a), 225 °C (b), and 250 °C (c).

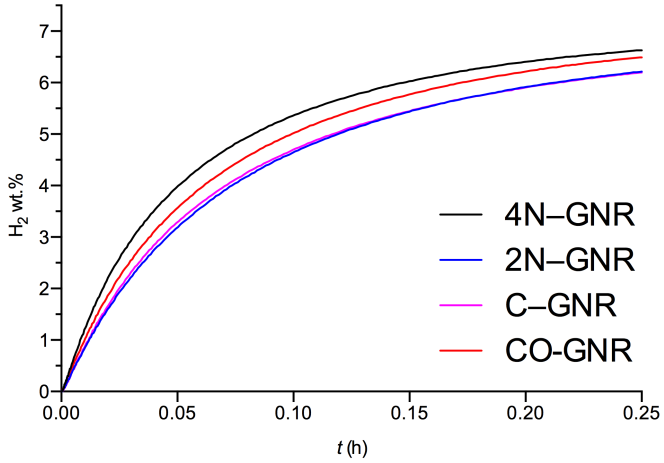

Figure 4.22 Hydrogen absorption experiments of GNR / Mg^0 hybrid materials at 15 bar H_2 and 250 °C over 15 minutes.

To examine the differences between these hybrid materials, hydrogen absorption was measured at 15 bar H_2 and 250 °C over just 15 minutes (Figure 4.22). Within this short period of time, hybrid material composed of 4N-GNR **35c** demonstrated the best kinetics and a capacity of over 6.5 wt% H_2. This makes it a potential candidate for commercial applications in hydrogen fuel cell vehicles. CO-GNR **44** hybrid material displayed the second best kinetics and capacity, while C-GNR **35a** and 2N-GNR **35b** hybrid materials were practically identical under these conditions.

The trends for hydrogen desorption are shown in Figure 4.23. As before, CO-GNR **44** and 4N-GNR **35c** hybrid materials possess the fastest kinetics for hydrogen release. However, C-GNR **35a** unloads hydrogen faster than 2N-GNR **35b**. At high temperatures (350 °C), all hybrid materials are essentially identical and completely unloaded in 15 minutes.

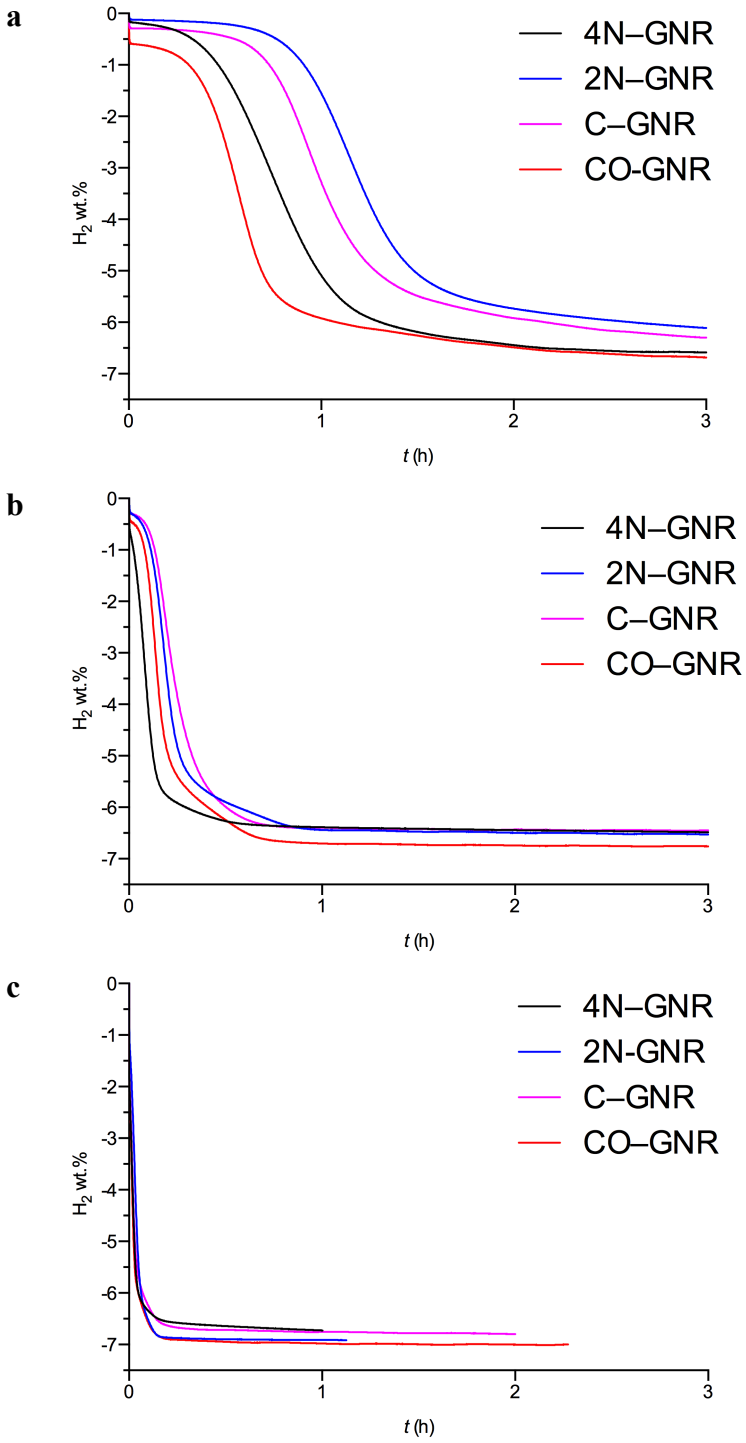

Figure 4.23 Hydrogen desorption experiments of GNR / Mg^0 hybrid materials at 0 bar H_2 and 300 °C (a), 325 °C (b), and 350 °C (c).

The performance of each GNR-Mg hybrid material is summarized in Table 4.1. CO-GNR **44** / Mg^0, which absorbs the most hydrogen on a weight basis, has the lowest absorption activation energy. In terms of lowering the activation energy required to desorb hydrogen, 4N-GNR **35c** / Mg^0 and 2N-GNR **35b** / Mg^0 have the lowest activation energies, respectively. At almost 40 kJ / mol lower in energy than their non-doped counterparts, it would seem that doping with nitrogen substantially lowers the activation barrier to hydrogen release, while ketone doping lowers the activation barrier to hydrogen uptake. These kinds of structure-function relationships will help drive the rational design of novel hybrid organic-inorganic future systems for hydrogen storage.

Hybrid material	H_2 Absorption (wt.%)	H_2 Desorption (wt.%)	Absorption Activation Energy (kJ/mol)	Desorption Activation Energy (kJ/mol)
CO-GNR **44** / Mg^0	7.2894	−7.0084	85.3	197.5
4N-GNR **35c** / Mg^0	7.2777	−6.7985	90.4	181.4
2N-GNR **35b** / Mg^0	7.1546	−6.9135	91.5	186.8
C-GNR **35a** / Mg^0	7.1022	−6.7252	91.8	220.2

Table 4.1 Summary of hydrogen storage results in hybrid GNR-Mg^0 materials.

An important consideration in these experiments is whether or not the GNRs themselves can store and release appreciable quantities of hydrogen. Given the high surface area of these materials, it is not unreasonable to assume hydrogen store in the GNR itself to take place through a physical adsorption mechanism. However, under identical conditions to the previous experiments (15 bar H_2, 200 °C), the GNRs adsorb less than 0.1 wt.% H_2 (Figure 4.24).

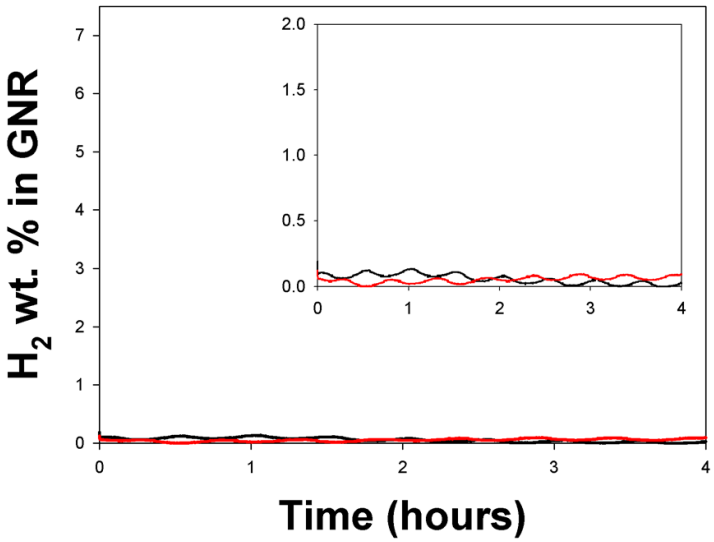

Figure 4.24 Hydrogen absorption (red) and desorption (black) for 4N-GNR **35c**.

Another important control experiment consists of comparing bottom-up GNRs with other forms of graphene (Figure 4.25). Under identical conditions, bottom-up GNRs outperform reduced graphene oxide-Mg^0 hybrid materials in terms of capacity and reversibility. Reduced graphene oxide does have an advantage in terms of increased kinetics for both absorption and desorption. This is presumably due to the fact that reduced graphene oxide contains considerably more defects through which hydrogen can easily escape compared with atomically-precise GNRs.

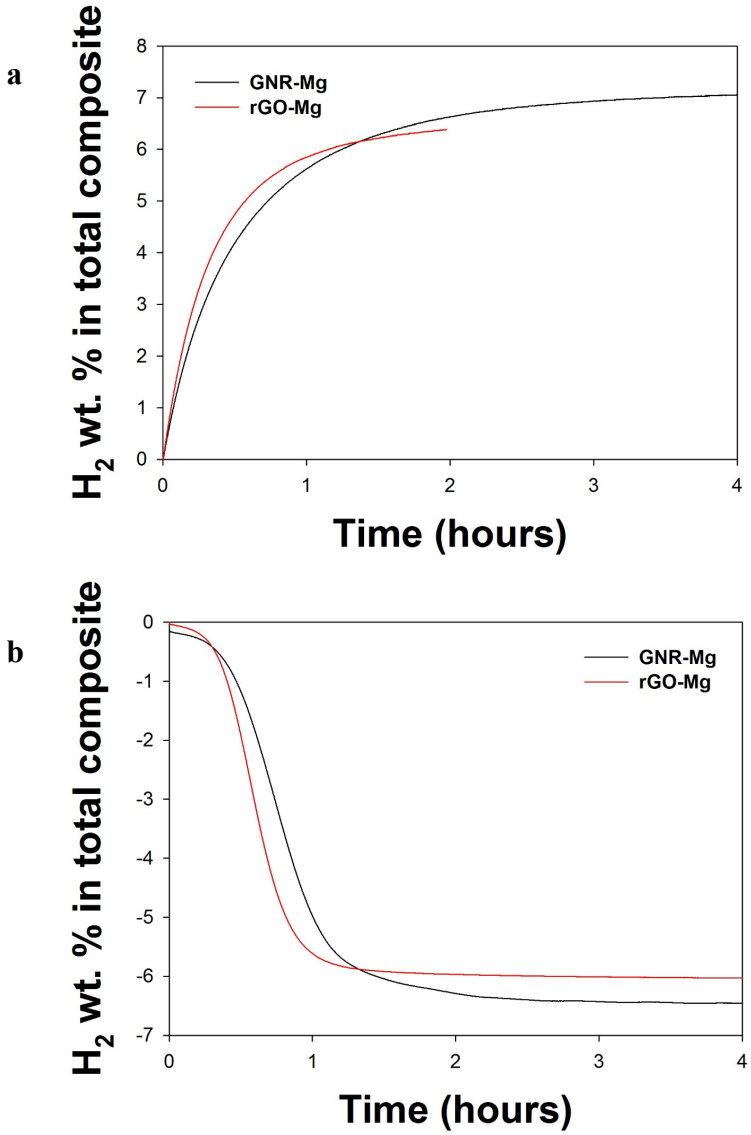

Figure 4.25 Comparison of hybrid 4N-GNR **35c** / Mg^0 to hybrid reduced graphene oxide / Mg^0 absorption (a) at 15 bar H_2 and 200 °C and desorption (b) at 0 bar H_2 and 300 °C.

4.5 CO_2 Reduction Using GNR-Au(111) Nanoparticle Hybrid Materials

The rapid increase in atmospheric greenhouse gases, in particular carbon dioxide, over the last century represents one of the most existential threats to society. As such, there is substantial scientific interest in reducing carbon dioxide into useful chemical intermediates that can be used either as feedstock chemicals or as fuel. The reduction of carbon dioxide requires either an excessive energy input (which likely negates the benefits of CO_2 reduction) or an exceptional catalyst.[101] Homogeneous catalysts for CO_2 reduction based on iridium[102,103] and manganese[104] have gained increased attention in recent years, but these systems suffer from relatively high overpotentials. Nanostructured catalysts, on the other hand, tend to lower overpotentials but suffer from low stability and lack of selectivity for CO_2 reduction over water splitting. Recent reports of nanostructured Au,[105-110] Cu,[111-113] Sn,[114] Bi,[115] and Pd[89] herald very encouraging progress in this area. Since graphene nanoribbons have an exceptionally high surface area and exhibit excellent charge carrier mobility, hybrid systems based on GNR-Au nanoparticles were synthesized.

TEM images of Au nanoparticles (Figure 4.26) and hybrid GNR-Au NP materials (Figure 4.27) show a high degree of monodispersity. The outline of a GNR in the hybrid material appears to show the nanoparticles being enveloped in a kind of protective shell.

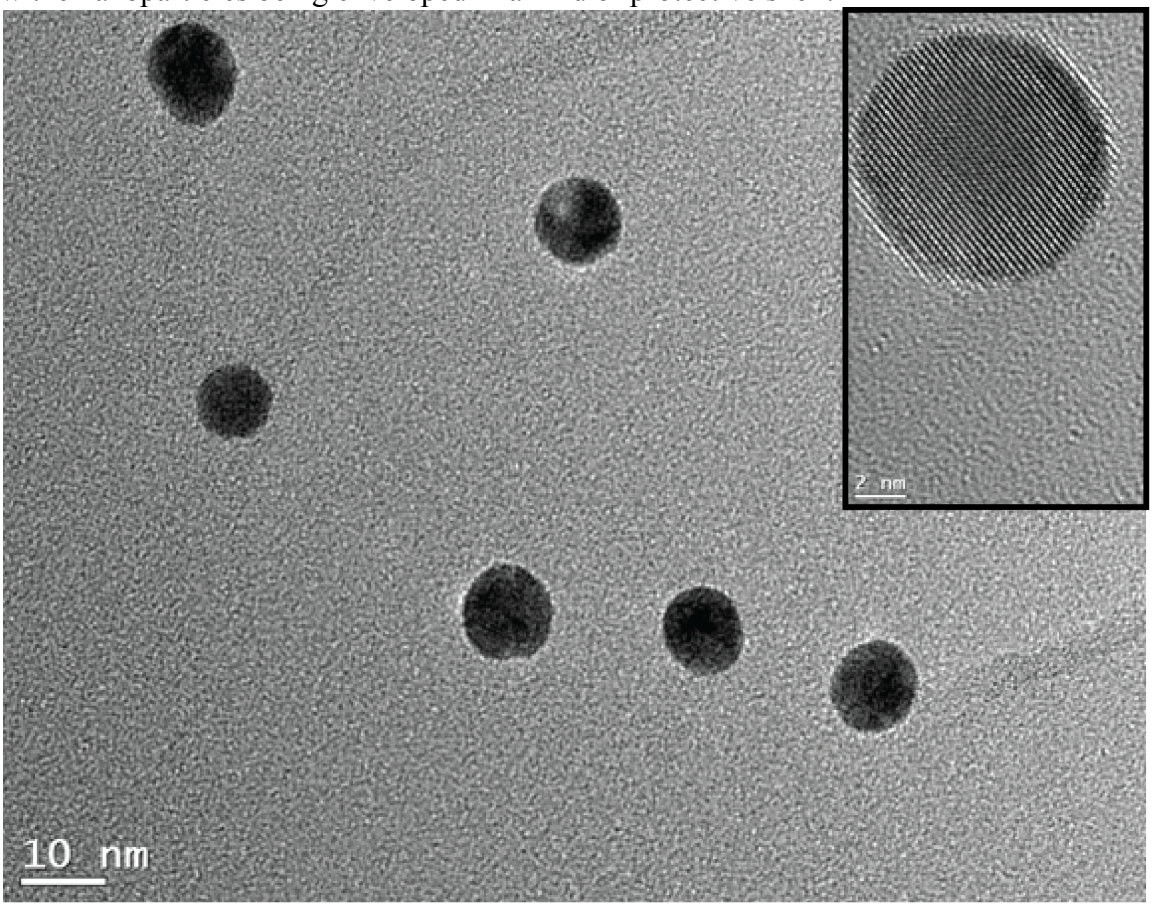

Figure 4.26 Transmission Electron Micrograph of Au nanoparticles used in this study.

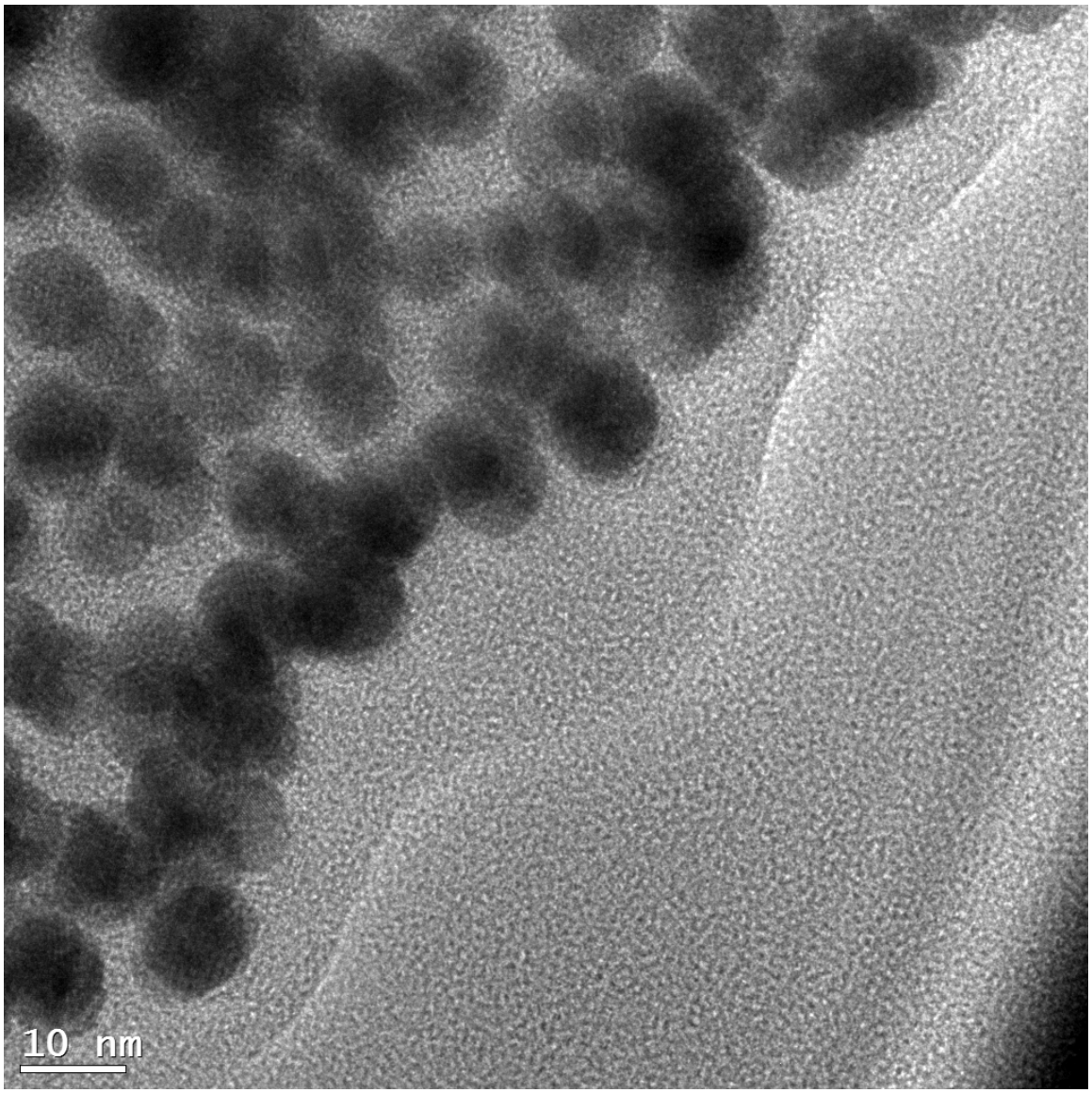

Figure 4.27 Transmission Electron Micrograph of 2N-GNR **35b** / Au nanoparticles**.**

By stripping away the ligand sphere of gold nanoparticles through an annealing process in air, and replacing them with GNRs, a new type of hybrid material was created. The hybrid material was dropcast onto conductive carbon paper and used as an electrode for the electrochemical reduction of CO_2. In addition to added stability, this has the dual advantage of increasing the catalytic surface area of the gold nanoparticles while simultaneously delivering more current via the conductive GNR matrix. While many combinations of doped GNR-Au nanoparticles were tested, most had either a low current output or a significant amount of undesired water splitting behavior. The most promising material tested consists of the 2N-GNR **35b** / Au nanoparticle hybrid. The Faraday efficiency and current output of this material in the electrochemical reduction of carbon dioxide to carbon monoxide, compared with a carbon black / Au NP hybrid control electrode are shown (Figure 4.28). The GNR hybrid material (Au-2NGNR) had double

the Faraday efficiency compared with the carbon black control (Au-C). At low overpotentials (−0.35 V), the current output is approximately the same for both materials. However, at modest overpotentials (−0.7 V), the bottom-up GNR hybrid material exhibits roughly three times the current output of the carbon black hybrid control electrode.

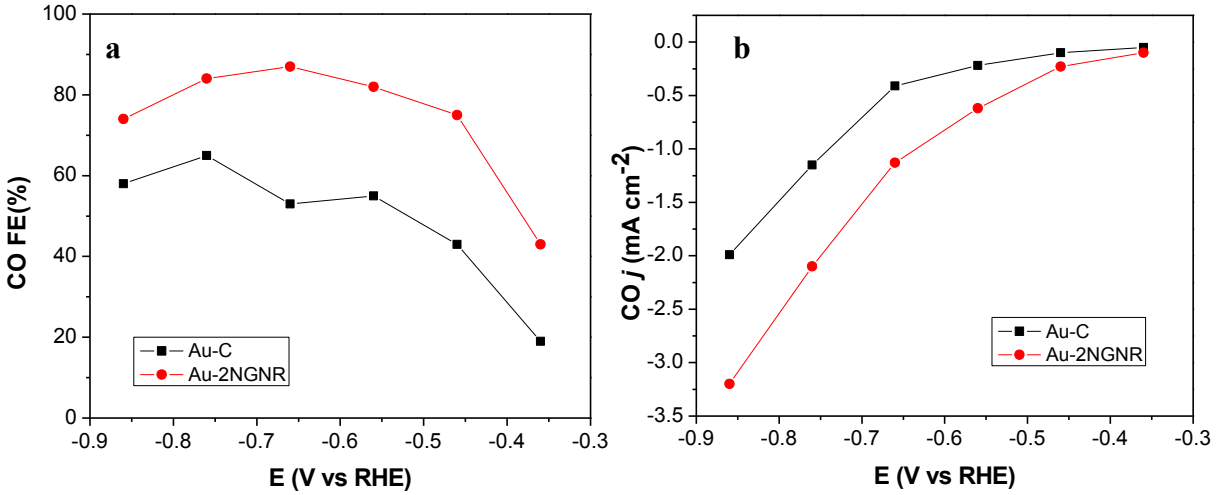

Figure 4.28 Electrochemical reduction of carbon dioxide using 2N-GNR **35b** / Au nanoparticle (Au-2NGNR) and a carbon black / Au nanoparticle (Au-C) control. Both Faraday efficiency with respect to CO production (a) and current (b) favor the GNR hybrid material.

This is a highly promising result that warrants further investigation, given the importance of carbon dioxide reduction in the coming decades.

4.6 Li-Ion Batteries Using GNR-SnO_2 Nanoparticle Hybrid Materials

Along with the rise of many new clean energy technologies comes an increasing dependence on storing that energy in the form of batteries. Li-ion batteries have emerged as the dominant type of commercial battery, but the most common anode material, graphite, has a theoretical specific capacity of only 372 mAh / g.[116] While silicon anodes have the highest known theoretical specific capacity of 4,200 mAh / g, serious problems remain in terms of reversible battery operation and scalable materials synthesis.[117] Therefore there is an intensive search for high capacity, low-cost anode materials for Li-ion batteries, with much room for improvement. Metal oxide nanoparticles, such as tin, manganese and iron, have high theoretical specific capacities, but the large volume expansion these particles experience upon lithium intercalation results in degradation of the nanoparticles and subsequently poor reversibility of battery operation.[118] In recent years, great progress has been made using top-down approaches to graphene nanoribbon synthesis in order to stabilize metal oxide nanoparticles.[119-121] However, because of the nascent arrival of solution-based graphene nanoribbon synthesis, there are currently no examples of bottom-up GNRs stabilizing metal oxide nanoparticles for Li-ion batteries. Because the surface area of bottom-up GNRs is much more accessible than bulk graphene, by virtue of their 1–2 nm width, it was theorized that these GNRs could impart even greater stability to metal oxide nanoparticles while increasing Li-ion diffusion to the anode. To test this hypothesis, hybrid materials based on C-GNR **35a** / SnO_2 nanoparticles were synthesized (Scheme 4.6) and

subjected to characterization by Raman (Figure 4.29), XRD (Figure 4.30), and cyclic voltammetry (Figure 4.31).

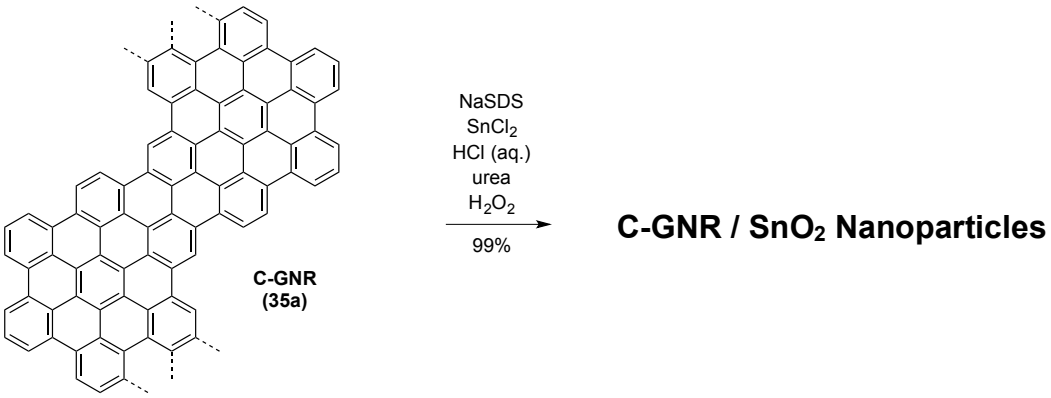

Scheme 4.6 Synthesis of hybrid C-GNR **35a** / SnO_2 nanoparticles.

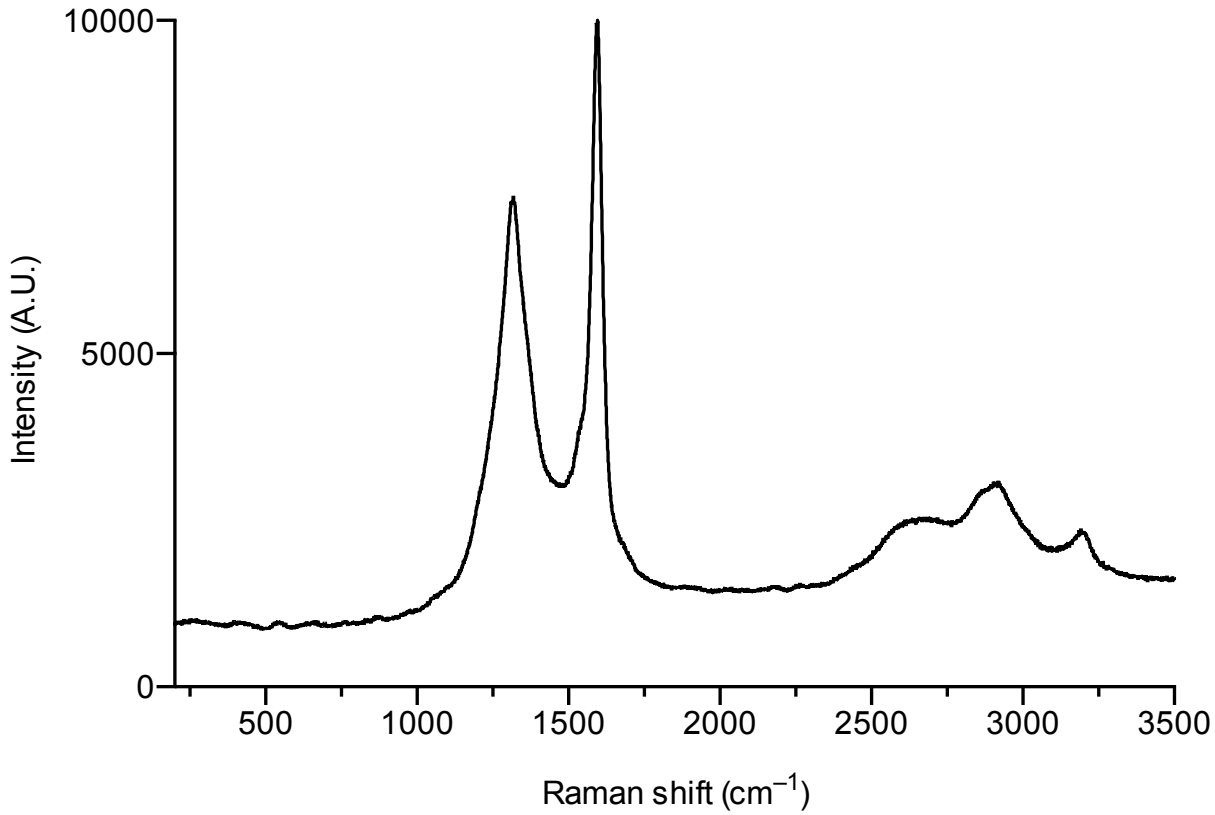

Figure 4.29 Raman spectrum of hybrid C-GNR **35a** / SnO_2 nanoparticles after annealing in air at 350 °C.

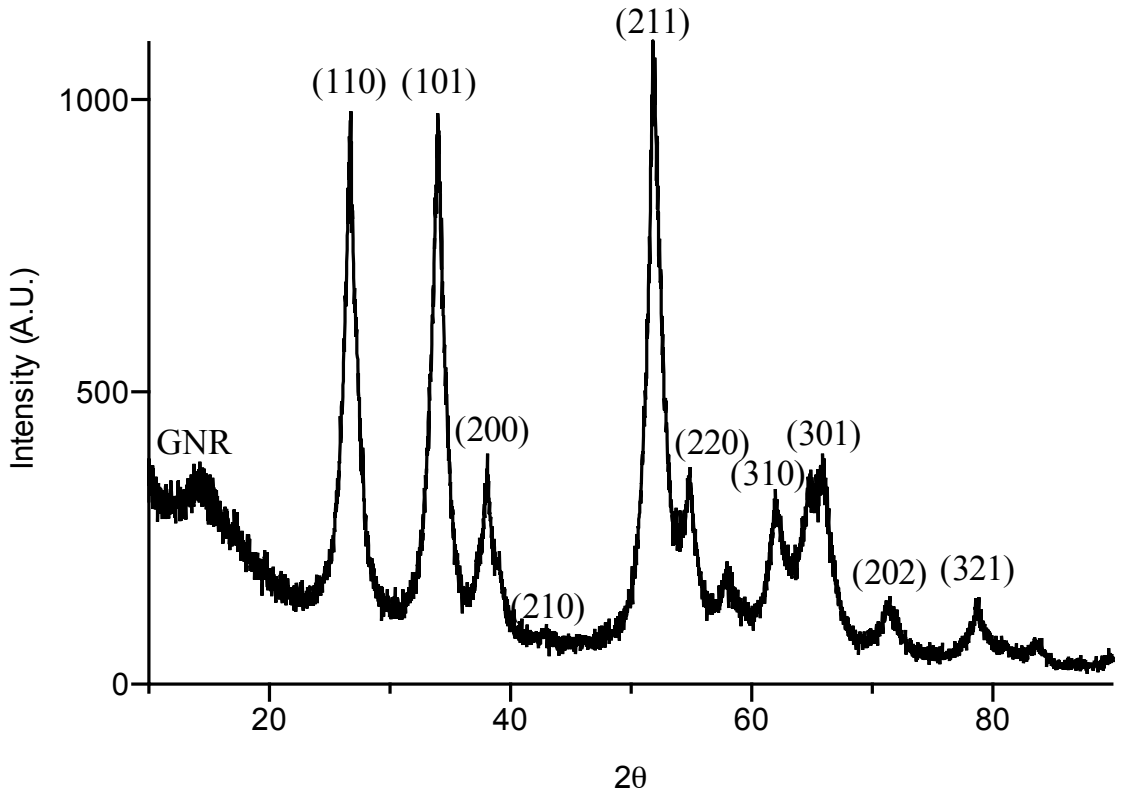

Figure 4.30 Powder XRD of hybrid C-GNR **35a** / SnO_2 nanoparticles after annealing in air at 350 °C.

After being synthesized and isolated by centrifugation, hybrid C-GNR **35a** / SnO_2 nanoparticles were annealed in air at 350 °C for 2 h. After annealing, Raman spectroscopy proved that the resulting GNR was still high quality and defect free. Powder XRD showed that the SnO_2 nanoparticles adopted a body-centered tetragonal unit cell. Using the Scherrer equation, the average particle sizes were estimated to be 7 nm. A small-angle peak that was not predicted for SnO_2 was attributed to short-range order due to π- π stacking in GNRs.

In order to better understand the electrochemistry of this hybrid material, cyclic voltammetry experiments were conducted using electrodes created on copper foil (Figure 4.31). The first peak of the first scan (0.7 V) is attributed to the formation of the solid electrolyte interphase. In subsequent scans, this peak is shifted to 0.9 V and represents the decomposition from SnO_2 to Sn.[122] The next peak at 0.1 V corresponds to the alloying process of metallic Sn to create various $SnLi_x$ species.[123] This peak decreases markedly in subsequent scans, indicating the lack of reversibility in this device due to the large volume change associated with the alloying process. During the reverse anodic sweep, the dealloying reaction increases in subsequent cycles. The last peak at 1.3 V corresponds to the reformation of SnO_2.

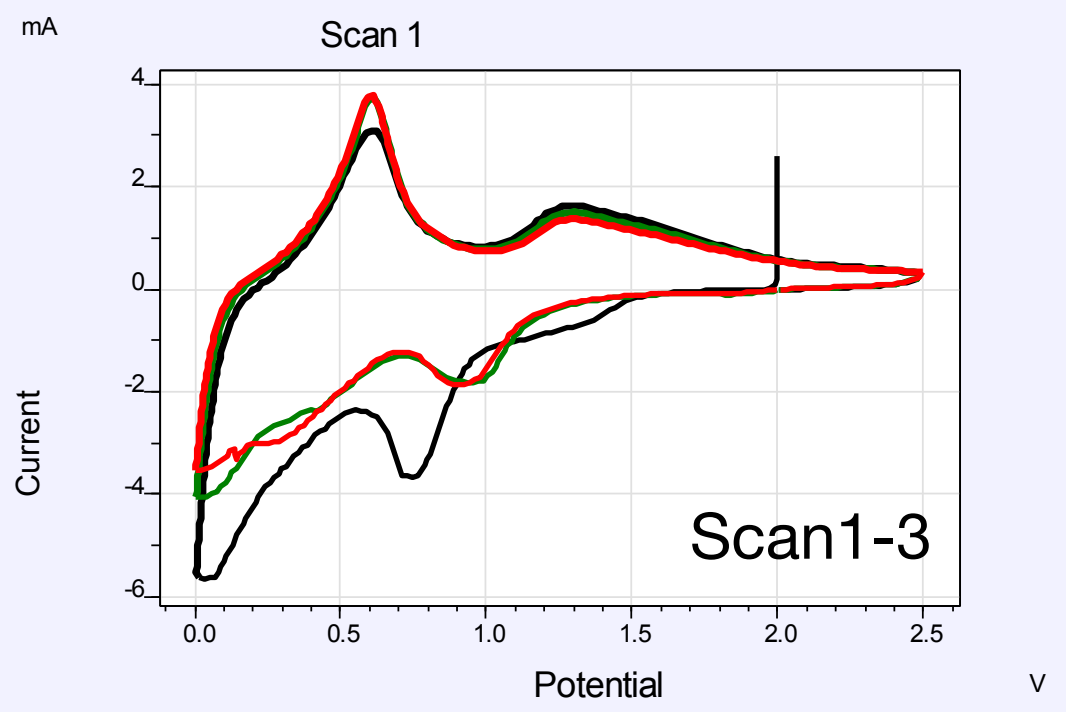

Figure 4.31 Cyclic voltammetry of hybrid C-GNR **35a** / SnO_2 nanoparticles anode in $LiPF_6$ (1M in 1:1:1 ethylene carbonate: dimethyl carbonate: diethyl carbonate) showing scans 1 (black), 2 (green), and 3 (red) at 0.2 mV / sec.

The batteries were sealed in flexible pouch-type cells and tested using galvanostatic cycling (Figure 4.32). Below 1.9 V, the cells are highly reversible. Beyond this voltage, there are detrimental side reactions that decrease the reversibility in subsequent cycles. Although optimization of this architecture is ongoing, the demonstrated capacity of 740 mAh / g (Figure 4.32) is a significant improvement over commercial Li-ion batteries.

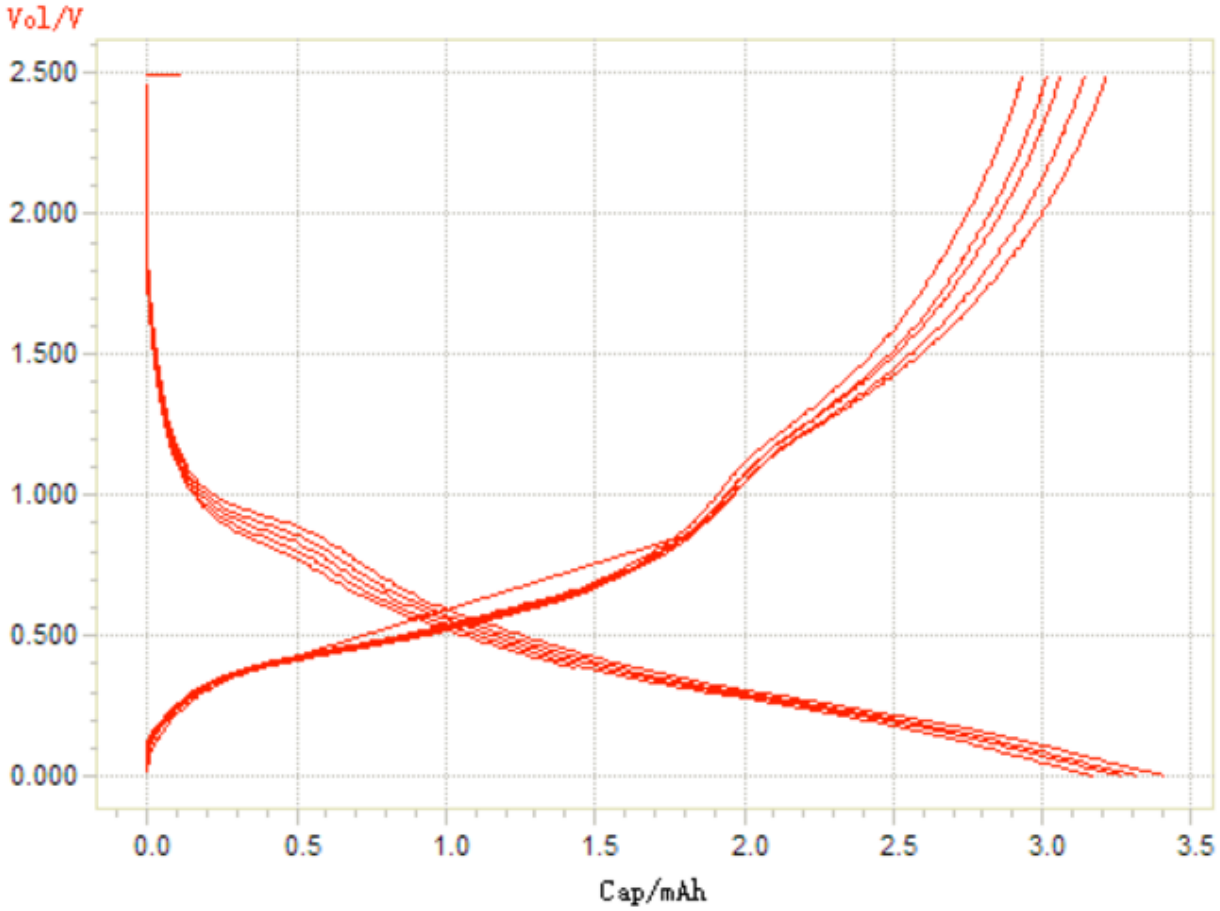

Figure 4.32 Galvanostatic cycling of C-GNR **35a** / SnO_2 nanoparticles battery in $LiPF_6$ (1M in 1:1:1 ethylene carbonate: dimethyl carbonate: diethyl carbonate).

In conclusion, the powerful methodology developed in this chapter for synthesizing doped graphene nanoribbons with precisely controlled dopant concentrations and locations enabled the production of grams of GNRs from solution-based synthesis. These GNRs were used to stabilize Mg, Au, and SnO_2 nanoparticles for hydrogen storage, carbon dioxide reduction, and Li-ion battery applications, respectively. The highly promising results from this section for renewable energy applications can be attributed to the excellent conductivity in GNRs, as well as the highly accessible surface area of ~1 nm strips of graphene. Further investigation of these hybrid systems is warranted in order to maximize the potential of GNRs for energy applications.

Chapter 5
GNR Polymer Precursors from Ring-Opening Alkyne Metathesis Polymerization

Conjugated polymers are an increasingly important class of materials, both for organic electronics applications, but also as precursors for GNRs. In this chapter, the controlled polymerization of strained diynes is reported using homogeneous molybdenum catalysts. The resulting conjugated polymers were isolated in either cyclic or linear form with complete selectivity depending on the catalyst employed. Carbon-13 labeling of diyne monomers enabled the observation of a rare metallocyclobutadiene intermediate and provided mechanistic insight into the polymerization process. This new strategy provides a controlled route to promising new materials for applications in light-emitting diodes, photovoltaics, field-effect transistors, and as precursors to graphene nanoribbons.

5.1 Introduction

The controlled synthesis of conjugated polymers has attracted significant scientific interest because of their applications in flexible electronic devices such as organic photovoltaics (OPVs),[124-125] organic light-emitting diodes (OLEDs),[126-127] and field-effect transistors (FETs).[128-130] Among this class of materials, poly(phenylene ethynylene) has achieved exceptional success in organic electronics applications (Scheme 5.1).[131-133]

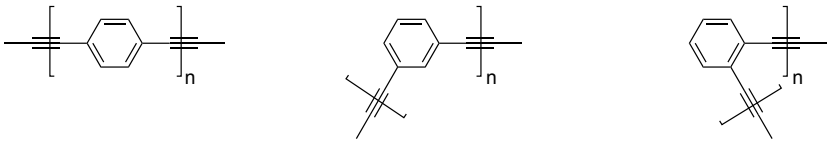

poly(*p*-phenylene ethynylene) poly(*m*-phenylene ethynylene) poly(*o*-phenylene ethynylene)

Scheme 5.1 Overview of the three possible substitutions in poly(phenylene ethynylene).

Poly(*o*-phenylene ethynylene) has been synthesized by alkyne cross-metathesis[134] and Sonogashira cross-coupling.[135] Alkyne cross-metathesis is based on a step-growth polymerization mechanism that relies on random cross-metathesis events. This results in polymers with a large polydispersity in molecular weight. Sonogashira cross-coupling polymerizations are inevitably contaminated with Glaser-coupling side products. Furthermore, oxidative addition of Pd^0 species into ortho-substituted aryl bromides is not efficient due to steric crowding, which limits the molecular weights achievable by this method.[136] The lack of robust synthetic methods for poly(*o*-phenylene ethynylene), despite its many interesting properties, implies that there is a pressing need for a better synthesis of this polymer.[137-141]

An improved synthesis of poly(*o*-phenylene ethynylene) would also facilitate its use as a precursor to graphene nanoribbons. Retrosynthetic analysis of this proposal is provided in Scheme 5.2. The cyclodehydrogenation of poly(*o*-phenylene naphthalene) can be effected either by Scholl oxidation in solution or by on-surface catalysis. Poly(*o*-phenylene naphthalene) can not be synthesized directly, so the polymer was obtained by benzannulation of the alkynes in the precursor poly(*o*-phenylene ethynylene).

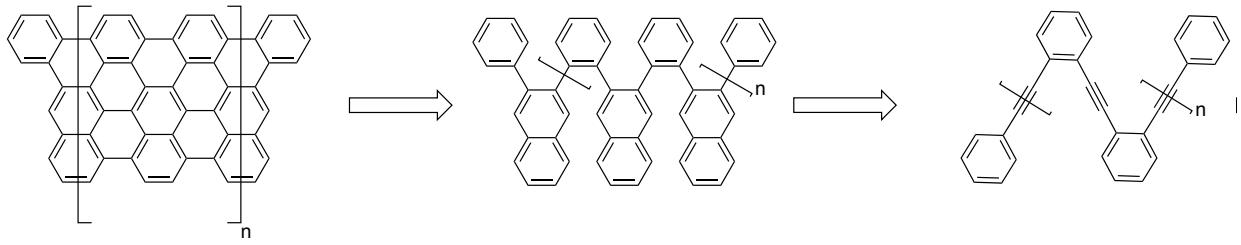

n = 8 armchair GNR poly(*o*-phenylene naphthalene) poly(*o*-phenylene ethynylene)

Scheme 5.2 Retrosynthetic analysis of n=8 armchair GNRs from poly(*o*-phenylene ethynylene).

In recent years, Ring-Opening Alkyne Metathesis Polymerization (ROAMP) has emerged as a promising methodology to create alkyne containing polymers (Scheme 5.3).[142,143] This polymerization is advantageous because the catalyst remains bound to the end of the growing polymer chain, allowing for low polydispersity in molecular weight and synthesis of block copolymers.[144] To date, only non-conjugated polymers have been prepared by ROAMP. Fully-conjugated diynes such as **51** would result in poly(*o*-phenylene ethynylene) after ROAMP.

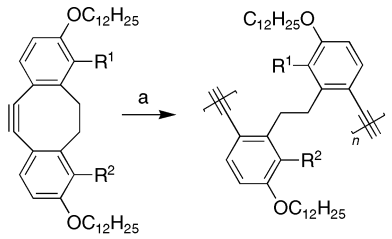

Scheme 5.3 Seminal example of ROAMP using non-conjugated strained alkynes. Reaction conditions: a) [(*t*BuO)$_3$WC*t*Bu], toluene, 24 °C, or [(N(*t*Bu)Ar)$_3$MoCCH$_2$CH$_3$] (Ar = 3,5-dimethylbenzene), alcohol/phenol, toluene, 24 °C [reproduced from ref. 142].

Therefore ROAMP using conjugated monomers was developed as a route to precisely controlled polymer architectures that could serve as precursors to GNRs. The work reported in this chapter was conducted in collaboration with Donatela Bellone and Stephen von Kugelgen of the Fischer Group.

5.2. Synthesis of Strained Alkyne Monomers

Following the general strategy outlined by the Otera Group, a library of strained alkyne monomers was synthesized.[145] Wittig-Horner dimerization of **48** initially formed a mixture of alkenes **49-E** and **49-Z** (Scheme 5.4).

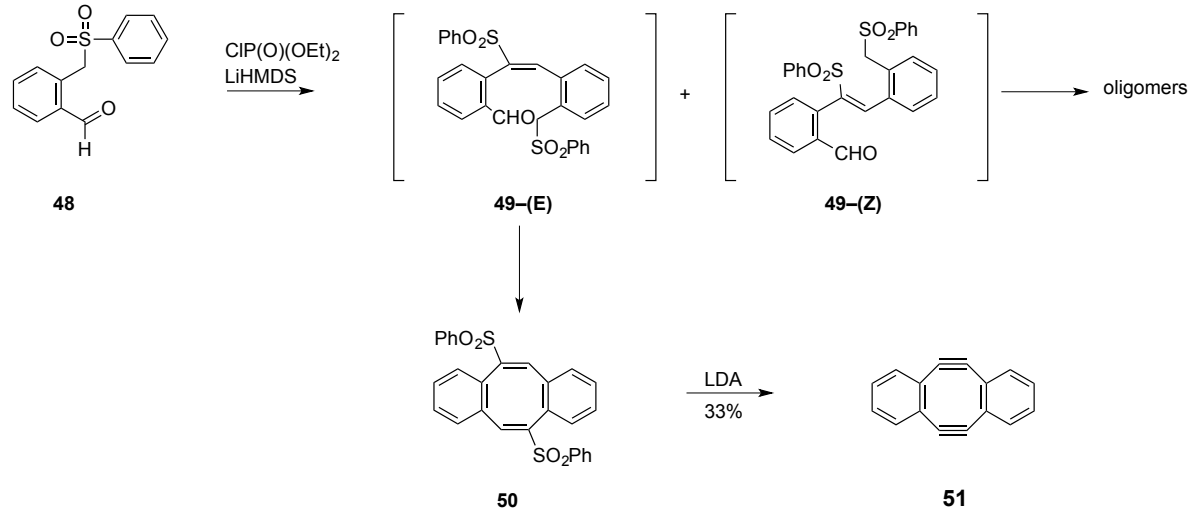

Scheme 5.4 Synthesis of strained diyne monomer **51.**

The (*Z*)-isomers formed oligomers while the (*E*)-isomer formed the desired diene **50**. The sulfone groups of **50** were doubly eliminated with LDA to give **51**.

In order to adjust the monomer electronics and increase the solubility of the resulting polymers from ROAMP, strained diynes **60a** and **60b** were synthesized (Scheme 5.5). Catechol **52** was alkylated with 1-bromooctane and 2-ethylhexyl bromide to give **53a** and **53b**, respectively. Bromination of **53** with NBS afforded **54**. Benzylic bromination of **54** using NBS and AIBN yielded **55a** and **55b**, which were used directly in a substitution reaction with benzenesulfinic acid to provide sulfones **56a** and **56b**. Conversion of **56a** and **56b** to nitriles **57a** and **57b** was achieved using copper cyanide at 200 °C. Reduction of **57a** and **57b** using DIBAL gave aldehydes **58a** and **58b**. Dienes **59a** and **59b** were synthesized by a Wittig-Horner dimerization. Double elimination of the sulfone leaving groups yielded diynes **60a** and **60b**. The branched alkyl chain provided much greater solubility than its linear counterpart to both the monomer and the resulting polymer. Both **60a** and **60b** rapidly decomposed under ambient conditions. Even storage overnight under vacuum at 24 °C resulted in decomposition. Therefore **60a** and **60b** were stored in an argon glovebox in the dark at −30 °C after purification.

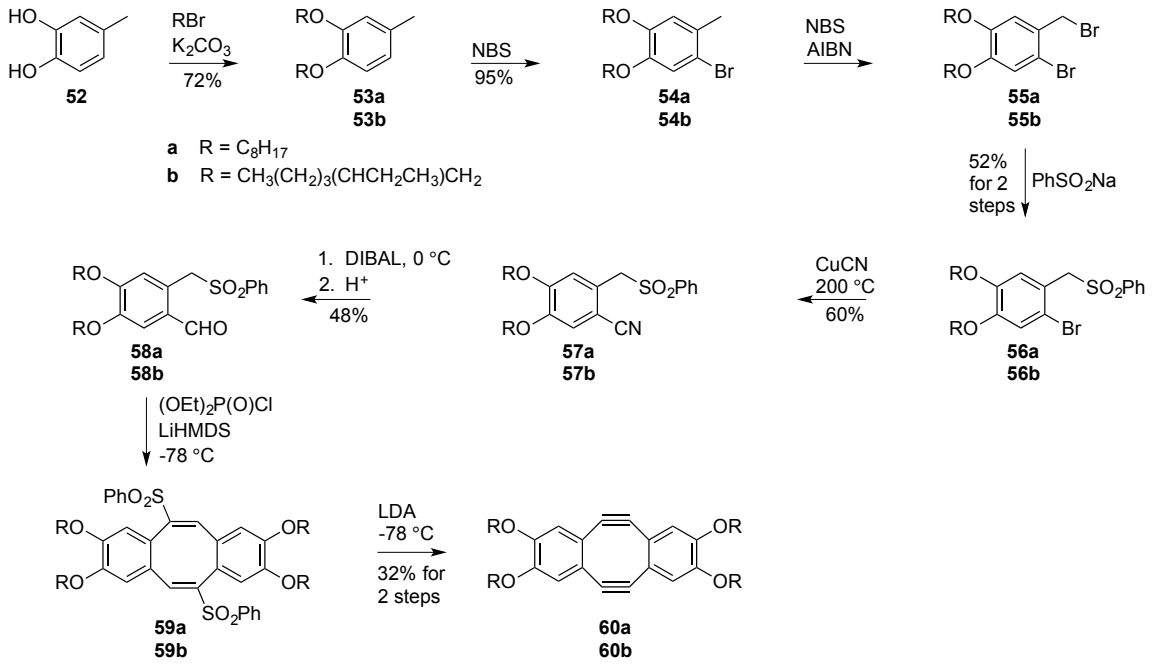

Scheme 5.5 Synthesis of electron-rich monomers for ROAMP.

The identity of strained monomer **60b** was verified by ^{1}H (Figure 5.1a) and $^{13}C\{^{1}H\}$ NMR (Figure 5.1b). Consistent with the assignment of this compound, only one aromatic resonance, a singlet at 6.2 ppm, is observed in the ^{1}H NMR spectrum of **60b**.

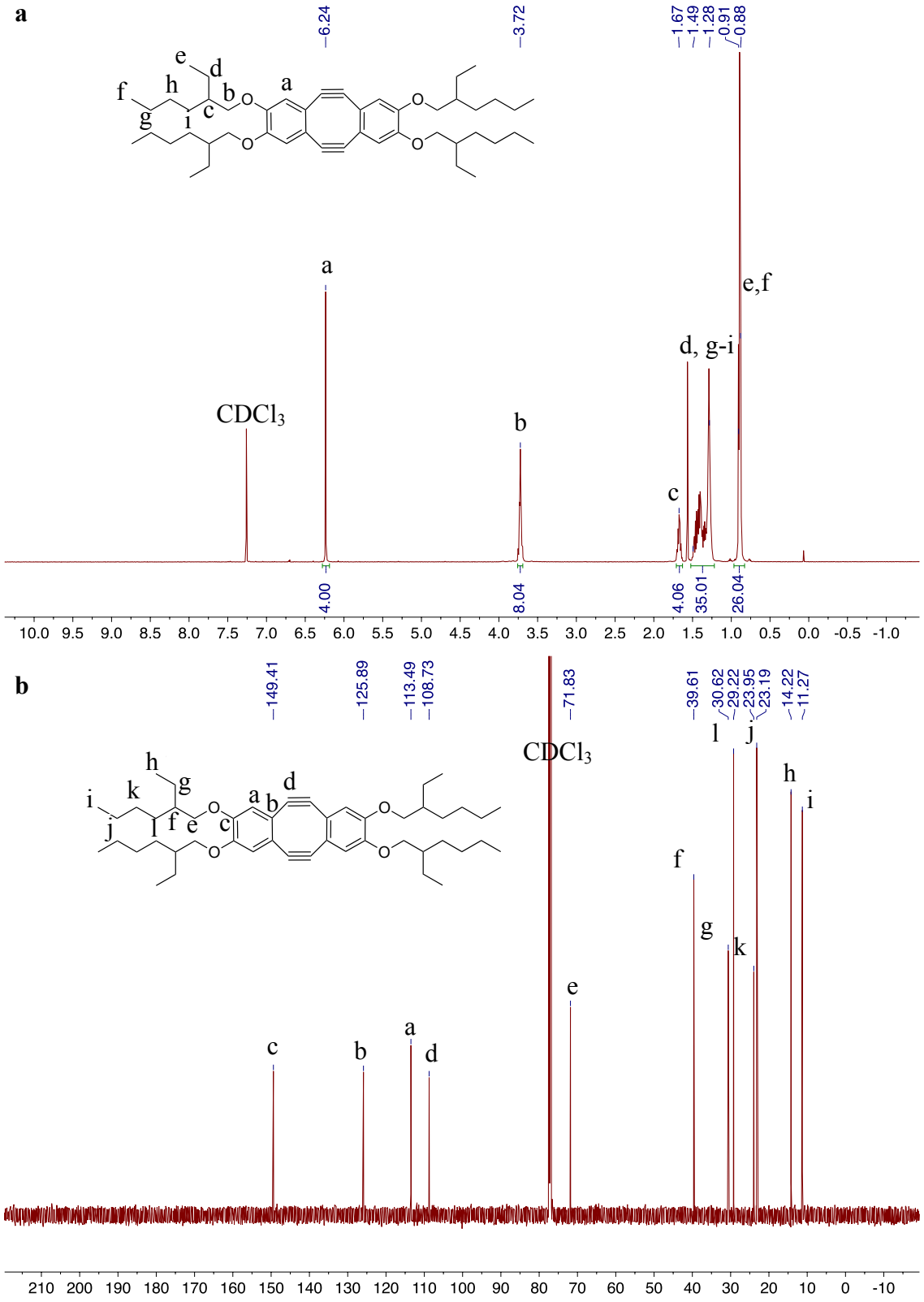

Figure 5.1 (a) ^{1}H NMR and (b) $^{13}C\{^{1}H\}$ NMR spectra for strained alkyne **60b**.

The alkyne resonance for **60b** is deshielded, due to the strain of the alkyne bonds incorporated within the 8-membered ring, and is observed at 109 ppm.

In the interest of expanding the scope and utility of ROAMP, the synthesis of larger annulene frameworks was explored. [12]annulene **66** was synthesized according to the route published by the Swager Group (Scheme 5.6).[146]

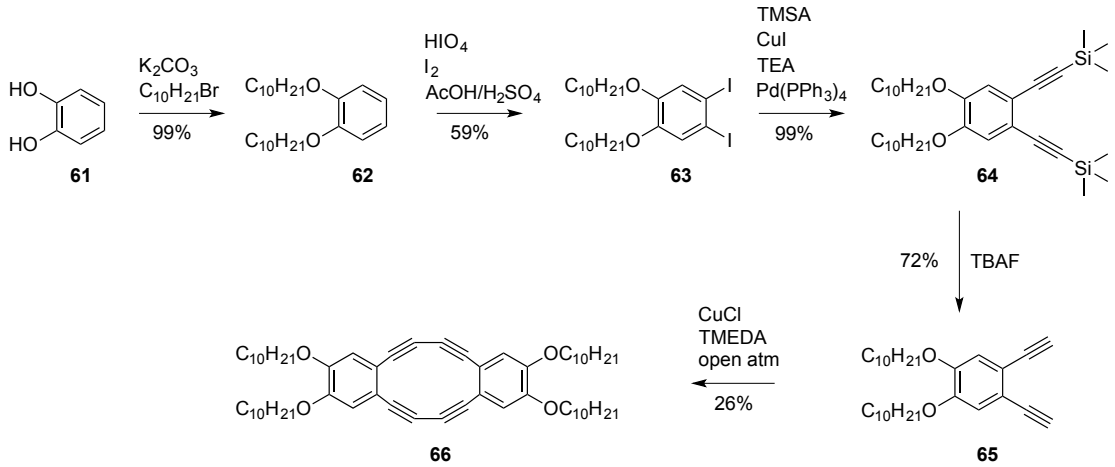

Scheme 5.6 Synthesis of dehydro[12]annulene **66** for ROAMP.

Alkylation of catechol **61** with 1-bromodecane yielded **62**, and iodination gave **63**. Sonogashira cross-coupling with TMS-acetylene provided diethynyl derivative **64**. Deprotection with tetrabutylammonium fluoride furnished **65**. Glaser-Hay homocoupling using CuCl under basic conditions afforded [12]annulene **66**.

Regardless of the catalyst employed, tetrayne **66** did not undergo Ring-Opening Alkyne Metathesis (ROAMP) polymerization. The butadiynes present in **66** differ in terms of electronics and strain from the alkynes in diyne **51** and cannot be directly compared.[147] The inability of larger annulenes to undergo ROAMP illustrates the importance of 8-membered alkyne-containing rings such as **51** for this polymerization.

5.3 Selective Synthesis of Linear or Cyclic Polymers from ROAMP

In order to synthesize conjugated polymers using ROAMP, diyne **51** and catalysts **67a** and **67b** were stirred in a toluene solution at 24 °C in a N_2-filled glovebox (Scheme 5.7). An immediate color change was observed upon adding the catalyst solution, and brown polymers precipitated from the reaction mixture in toluene after 1 h. The polymerization was terminated by the addition of MeOH, and the polymers were isolated by filtration.

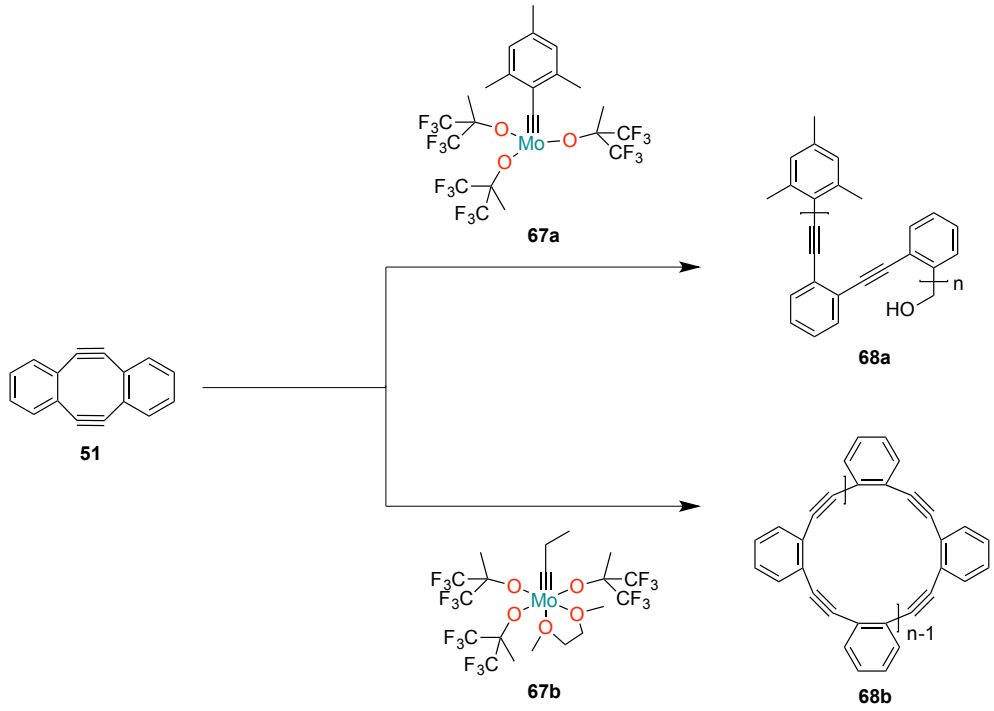

Scheme 5.7 Synthesis of linear or cyclic poly(*o*-phenylene ethynylene)s from ROAMP.

Polymer **68a**, obtained by the polymerization of **51** with catalyst **67b**, was characterized by NMR (Figure 5.2) and MALDI-MS (Figure 5.3). The two unique aromatic protons in ^{1}H NMR in Figure 5.2A confirmed the structure of polymer **68a**. The aromatic proton resonances are shifted from 6.7 and 6.9 ppm in monomer **51** to 7.5 and 7.1 ppm in polymer **68a**. This large downfield shift indicates the release of ring-strain. Likewise, ^{13}C{^{1}H} NMR of polymer **68a** in Figure 5.2b shows an upfield shift of the alkyne carbon from 110 ppm in monomer **51** to 90 ppm in polymer **68a**. The proton and carbon NMR signals were consistent with a previously reported polymerization of strained mono-alkynes.[142]

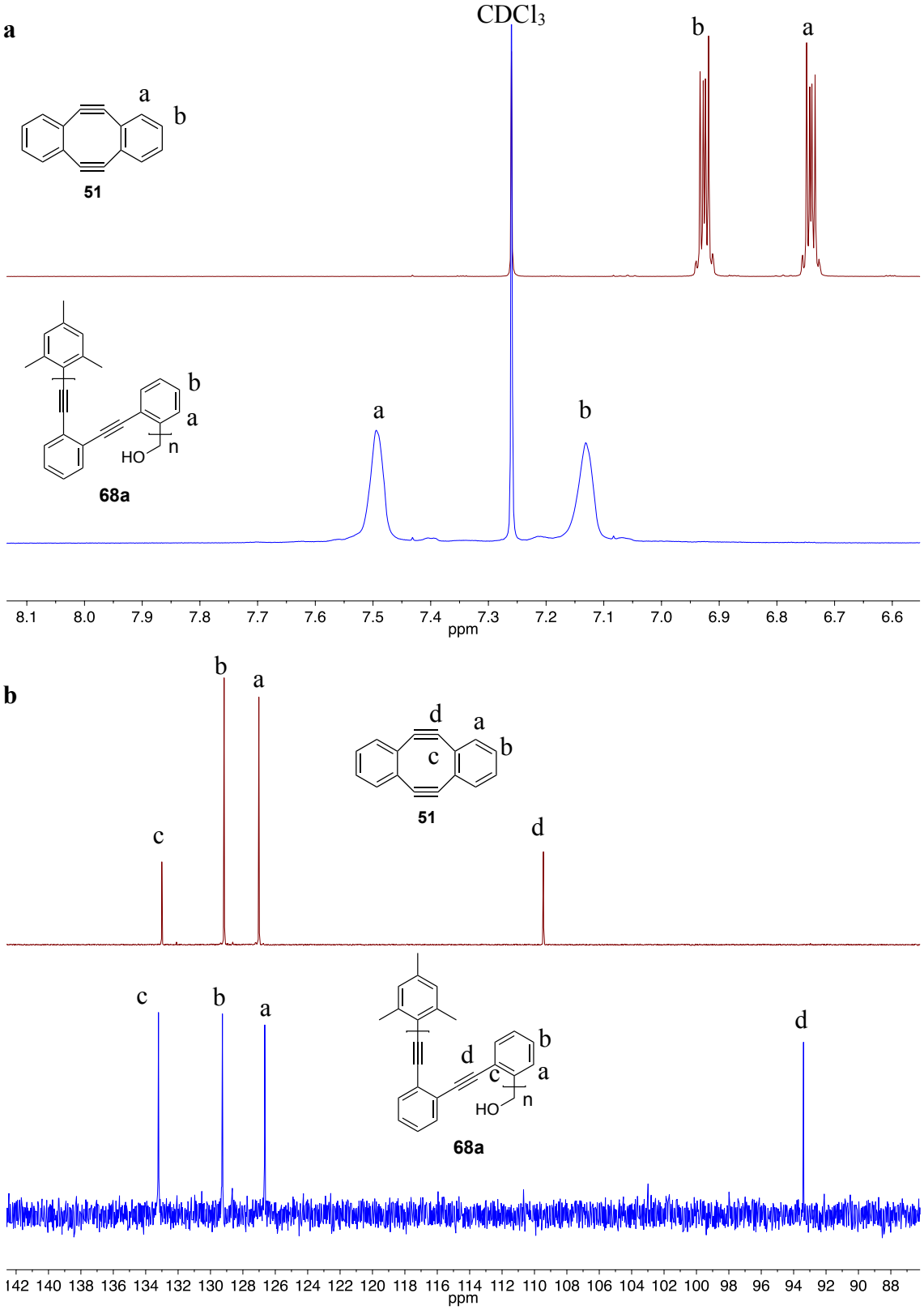

Figure 5.2 (a) ^{1}H NMR and (b) $^{13}C\{^{1}H\}$ NMR of monomer **51** (red) and polymer **68a** (blue).

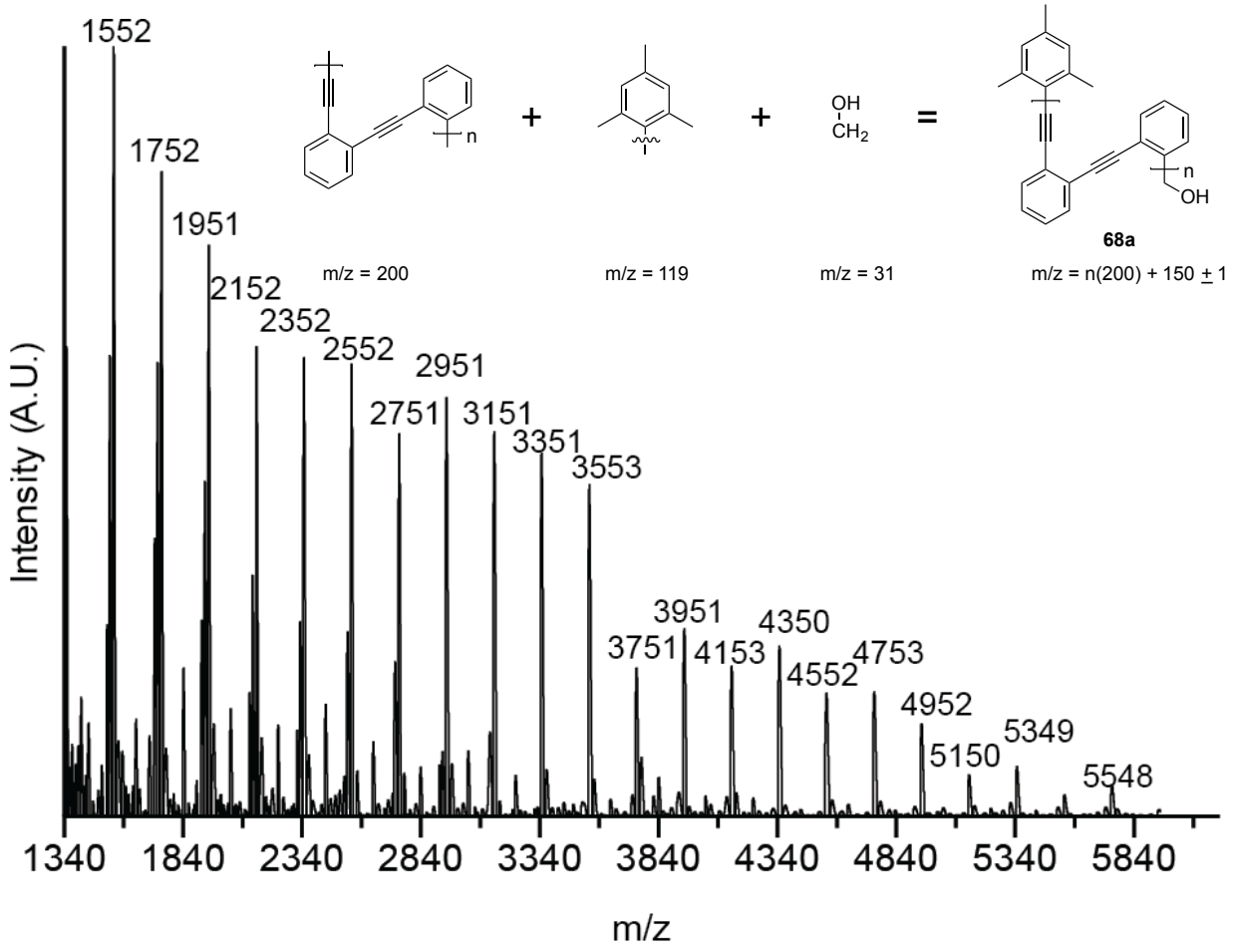

Figure 5.3 MALDI-MS of linear polymer **68a**.

The expected polymer structure of **68a** was also confirmed by MALDI-MS (Figure 5.3). Because catalyst **67a** was used, one endgroup was mesitylene. The other endgroup was determined to be CH_2OH, which results from deliberate termination of the polymerization with MeOH on workup. The repeating mass unit of polymer **68a** is 200 amu, while mesitylene and CH_2OH are 119 and 31 amu, respectively. The observed spectrum in Figure 5.3 matched the predicted pattern for this polymer.

When ROAMP was conducted with catalyst **67b**, a mixture of cyclic polymer **68b** and linear polymer **68a** was obtained as determined by ^{1}H NMR (Figure 5.4a). The broad peaks in the aromatic region were attributed to linear polymer **68a** while the pair of complex multiplets in this range was assigned to cyclic polymer **68b**. The mixture was purified by Soxlet extraction with hexanes. After extraction, ^{1}H NMR spectrum of cyclic polymer **68b** displayed only two complex multiplets in the aromatic region and no methylene resonances were detected (Figure 5.4b). Size-exclusion chromatography (SEC) was also used to monitor the purification process (Figure 5.5).

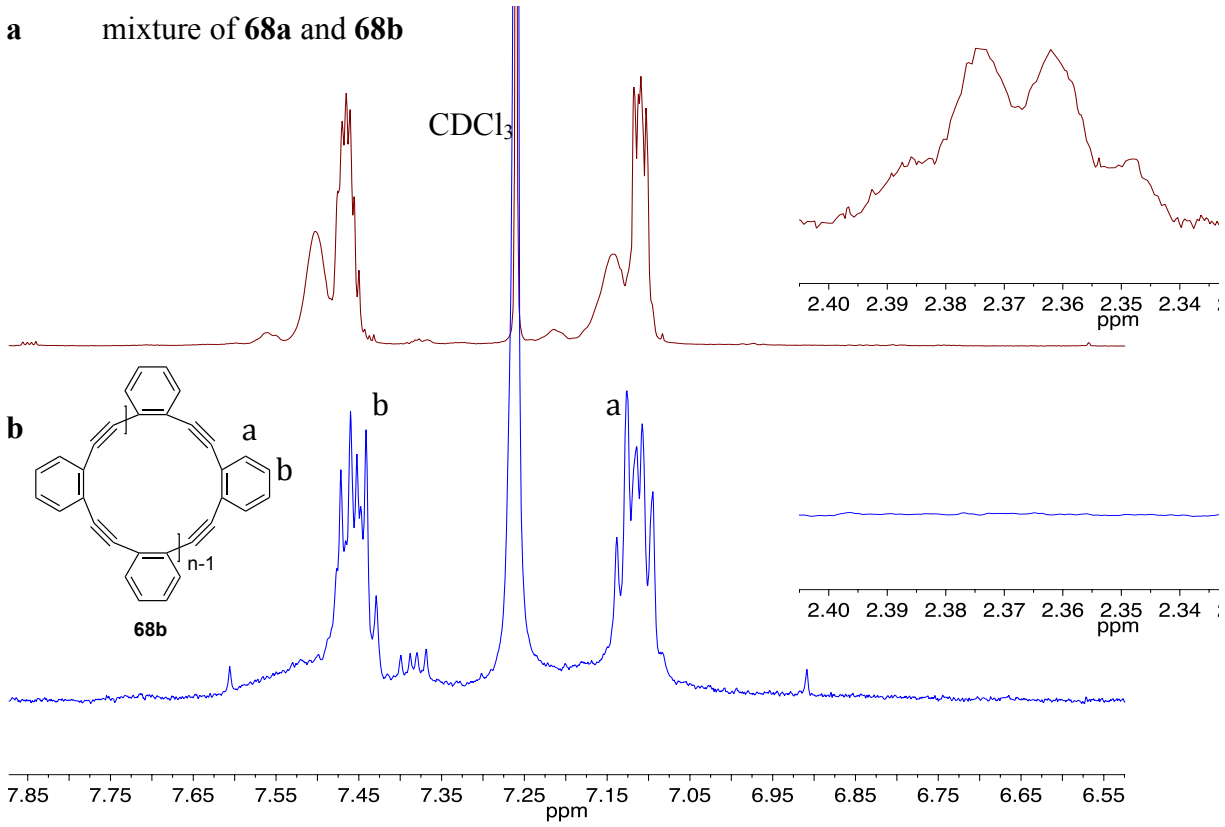

Figure 5.4 ^{1}H NMR of cyclic polymer mixture from catalyst **67b** (a) before and (b) after soxlet extraction. Inset depicts the methylene region of the ethyl endgroup in linear polymers.

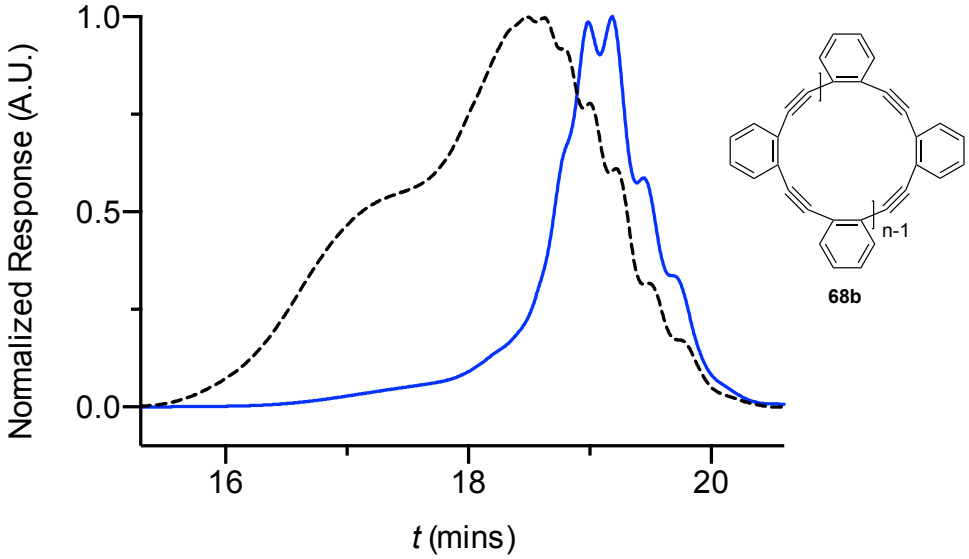

Figure 5.5 Normalized SEC of (dashed, black line) cyclic and linear polymer mixture resulting from catalyst **67b** and (solid, blue line) cyclic polymers **68b** after Soxlet extraction.

Prior to Soxlet extraction, the mixture consisted of cyclic and linear polymers in a 60:40 ratio. After extraction, the broad peaks in Figure 5.5 corresponding to larger hydrodynamic radii (linear structures) were not observed in SEC while the discrete peaks corresponding to smaller hydrodynamic radii remained (cyclic structures).

MALDI-MS unambiguously proved that polymer **68b** is cyclic (Figure 5.6). The observed peaks in Figure 5.6 were exact multiples of the monomer mass (200 amu). Peaks separated by 100 amu were not detected (e.g. 1500, 1600, 1700). This observation was critical, since it confirmed that random backbiting of the catalyst into the polymer chain was not observed.

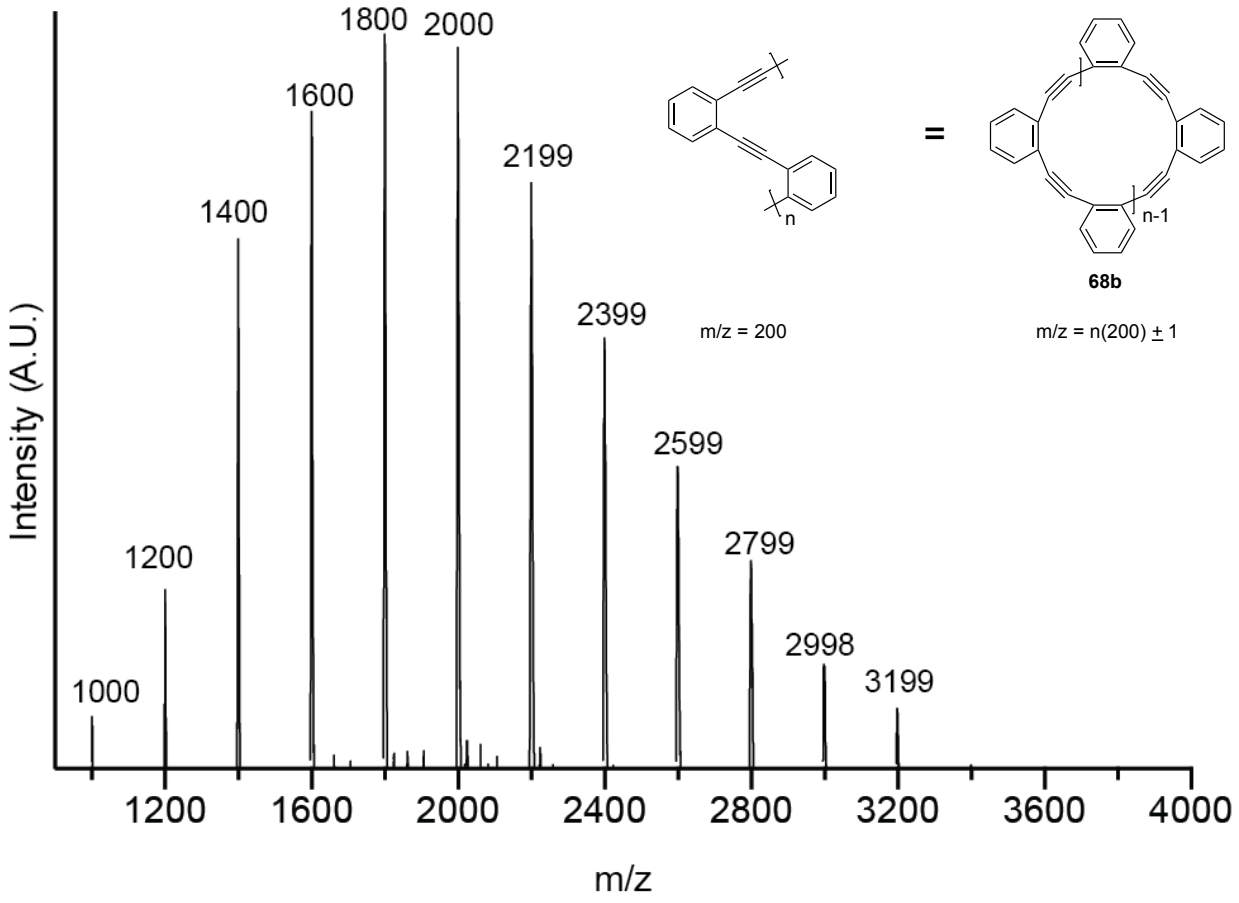

Figure 5.6 MALDI-MS of cyclic polymer **68b**.

Size-exclusion chromatography (SEC) of linear polymer **68a** and purified cyclic polymer **68b** demonstrated a large difference in retention times. This is because linear polymer **68a** has a much larger hydrodynamic radius than its cyclic counterpart **68b**. This means that the linear polymer **68a** interacted less with the porous column during chromatography, leading to faster elution and shorter retention times. Cyclic polymer **68b**, however, had a much smaller hydrodynamic radius, leading to greater interaction with the column, slower elution, and longer retention times. Although this effect makes it difficult to ascertain the exact molecular weights for **68b** by SEC, it does demonstrate the difference in topology of these two polymer species.

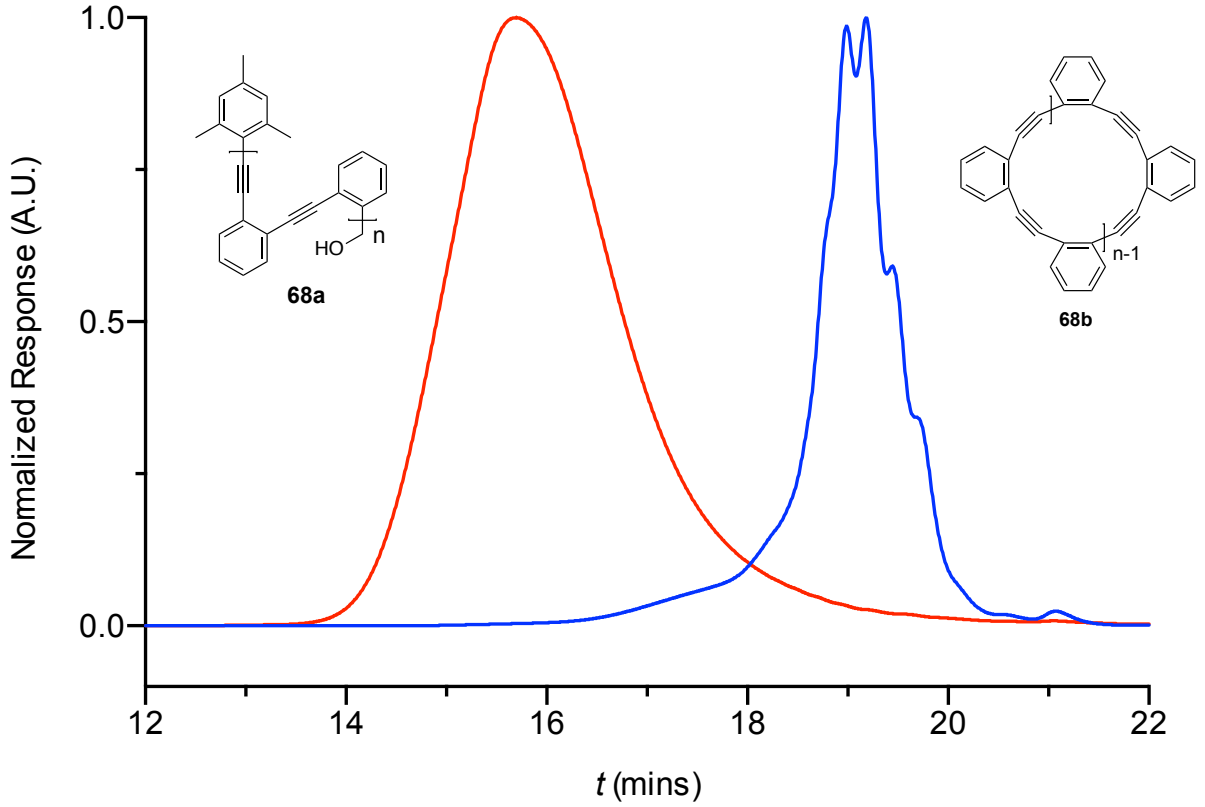

Figure 5.7 Size-Exclusion Chromatography of linear polymer **68a** (red) and purified cyclic polymer **68b** (blue).

In an attempt to understand the origin of the selectivity for cyclic or linear polymers in ROAMP, *in situ* NMR polymerization experiments were conducted with catalysts **67a** and **67b** (Figures 5.8, 5.10). The most significant distinction between these two catalysts is that **67a** contained a sterically bulky carbyne, while **67b** displayed a flexible propylidyne. The proposed catalytic cycle for ring-opening alkyne metathesis polymerization with catalyst **67a**, which produced linear polymers, is shown in Figure 5.8.

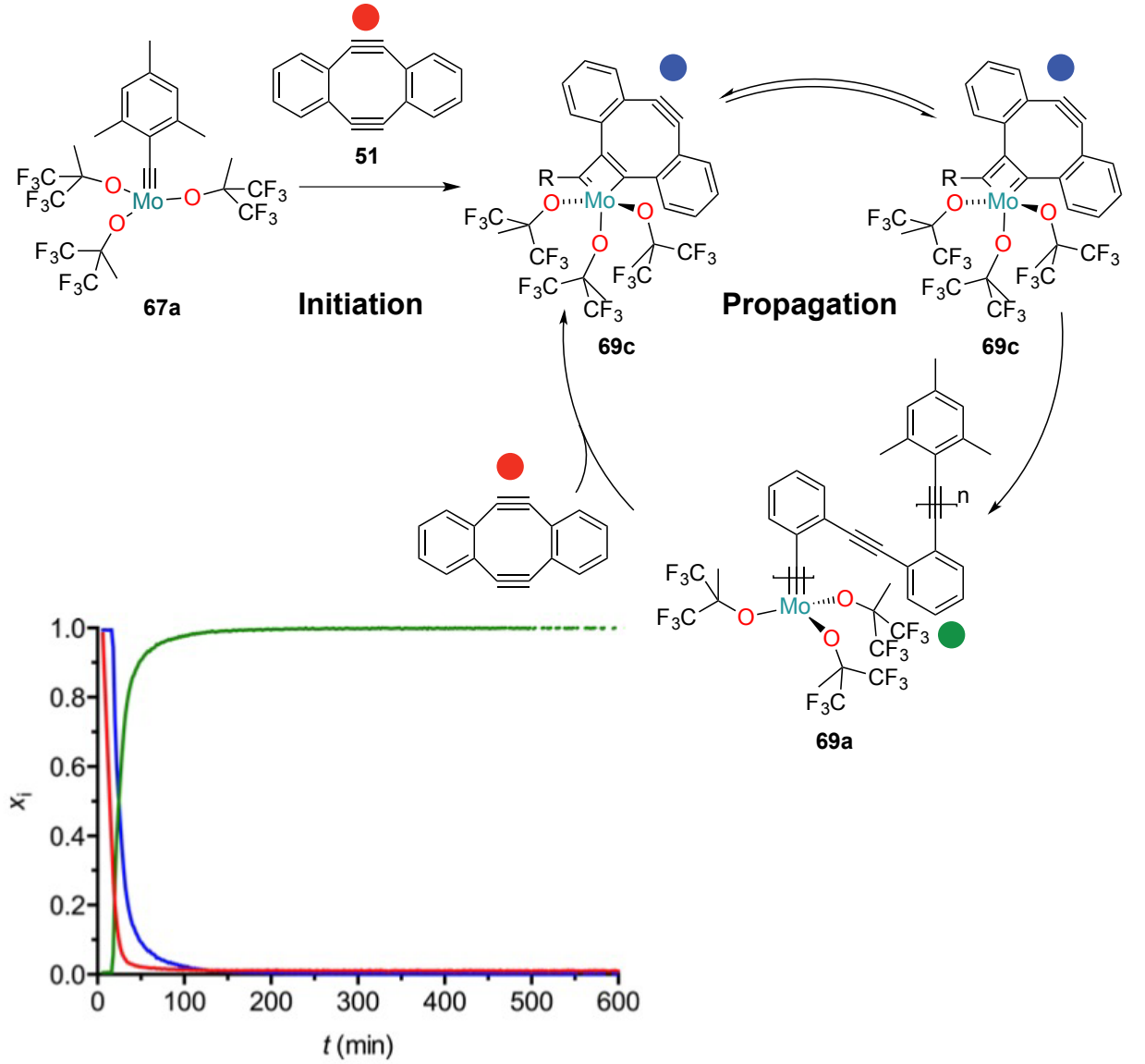

Figure 5.8 Proposed catalytic cycle for ROAMP of **51** with catalyst **67a**. Inset shows the relative mole fractions of diyne **51** (red curve), metallocyclobutadiene **69c** (blue curve), and active catalyst species **69a** (green curve) based on *in situ* ^{1}H NMR monitoring. R represents the endgroup or the growing polymer chain.

In the case of catalyst **67a** (Figure 5.8), cycloaddition with strained monomer **51** initiates the polymerization. During this step, the strained alkyne in **51** and the molybdenum carbyne in **67a** react to form metallocyclobutadiene **69c**. This structure can tautomerize and undergo ring-opening to give the active catalyst species **69a**. This cycle continues as long as monomer **51** is present, thereby propagating the polymerization indefinitely. The carbyne substituent on the molybdenum catalyst is important because it determines the endgroup of the polymer. In the case of catalyst **67a**, the endgroup of the growing polymer chain is mesitylene.

The inset of Figure 5.8 shows the progress of the *in situ* polymerization over time. While strained monomer **51** (red curve) is being consumed, both metallocyclobutadiene **69c** (blue curve) and active catalyst **69a** (green curve) are present. As the concentration of monomer **51** (red curve) decreases, the concentration of metallocyclobutadiene **69c** (blue curve) also decreases, but the concentration of **69a** (green curve) increases. As soon as monomer **51** is consumed (red curve), metallocyclobutadiene **69c** (blue curve) is no longer observed.

To confirm the presence of metallocyclobutadiene **69c** during ROAMP, carbon-13 labeled diyne monomer ***51** was synthesized (Scheme 5.8) and used in *in situ* $^{13}C\{^1H\}$ NMR polymerization experiments (Figure 5.10). Sulfone **70** was treated with ^{13}C enriched copper(I) cyanide at 210 °C to give labeled nitrile **71**. Reduction furnished labeled aldehyde **72** while Wittig-Horner dimerization afforded labeled diyne ***51**. The successful enrichment of carbon-13 in the alkyne carbons of monomer ***51** can be seen from the $^{13}C\{^1H\}$ NMR, in which the alkyne resonance intensity at 109 ppm is greatly increased (Figure 5.9).

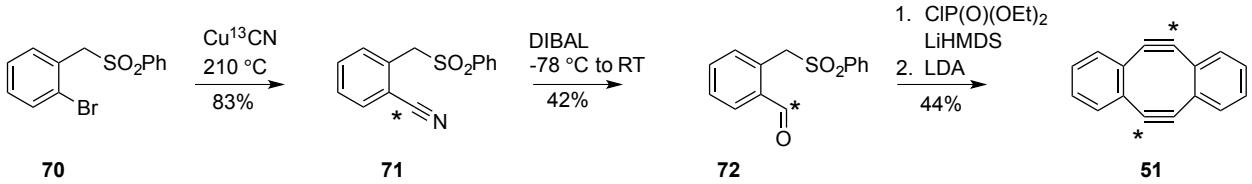

Scheme 5.8 Synthesis of carbon-13 labeled diyne monomer ***51**.

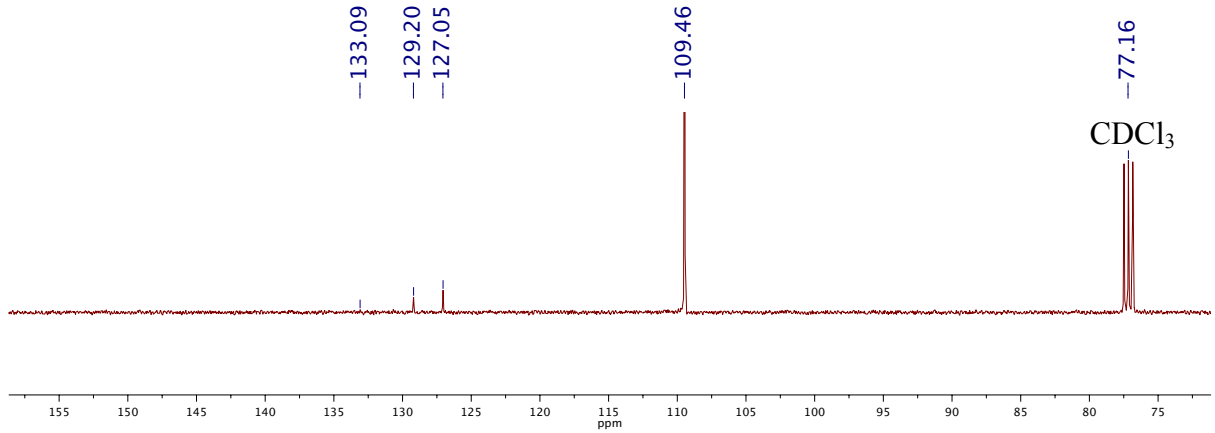

Figure 5.9 $^{13}C\{^1H\}$ NMR of carbon-13 enriched monomer ***51**.

By monitoring the polymerization of ***51** with catalyst **67a** by $^{13}C\{^1H\}$ NMR, the appearance of resonances associated with the expected metallocyclobutadiene **69c** was observed. Four min after mixing the catalyst with ^{13}C labeled monomer ***51**, four new groups of resonances appear at 104, 134, 175, and 190 ppm in the $^{13}C\{^1H\}$ NMR (Figure 5.10a). The carbons located alpha to molybdenum are assigned to the two most downfield groups of peaks at 190 and 175 ppm. The carbon situated beta to molybdenum is assigned to the resonances at 135 ppm. The most upfield

of the family of signals is attributed to the labeled alkyne in **69c** that is not involved in the metallocyclobutadiene formation. It is likely that the signals within each family of peaks are numerous because of the different possible substituents labeled as R (e.g. mesitylene, oligomer, polymer).

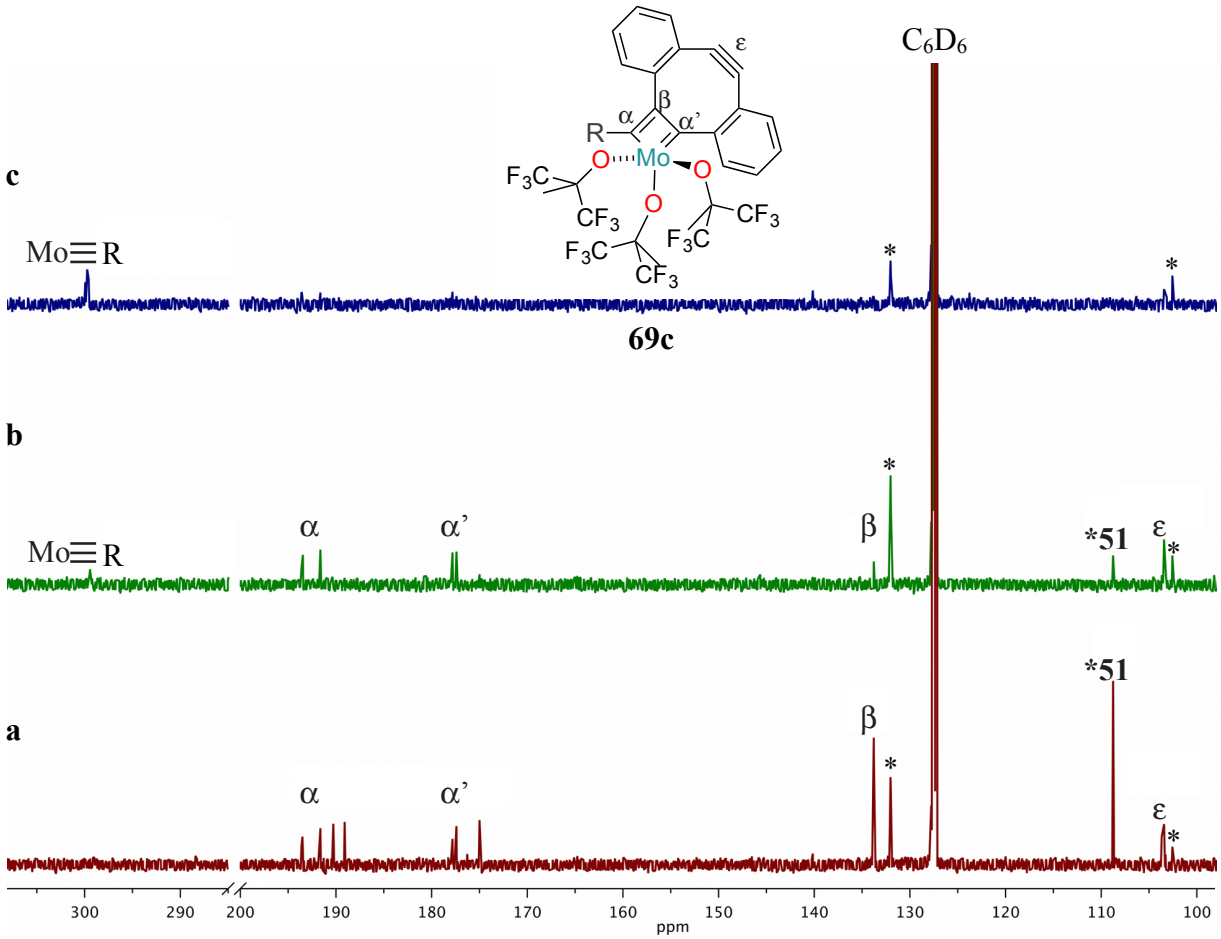

Figure 5.10 $^{13}C\{^{1}H\}$ NMR of labeled monomer ***51** during polymerization with catalyst **67a** in C_6D_6. (a) 4 min, (b) 19 min, and (c) 94 min after the initiation of polymerization. The peak marked with ***51** refers to the alkyne resonances in labeled monomer ***51**. The asterisks symbol is used to signify unknown carbon-13 labeled products.

After 19 min (Figure 5.10b), the resonances of the four labeled carbons attributed to metallocyclobutadiene **69c** are decreased. After 94 min (Figure 5.10c), these signals are not observed. The disappearance of these four resonances occurs concomitantly with the consumption of monomer ***51** and an increase in the Mo≡R signal. This finding supports the hypothesis that ROAMP proceeds through metallocyclobutadiene **69c**.

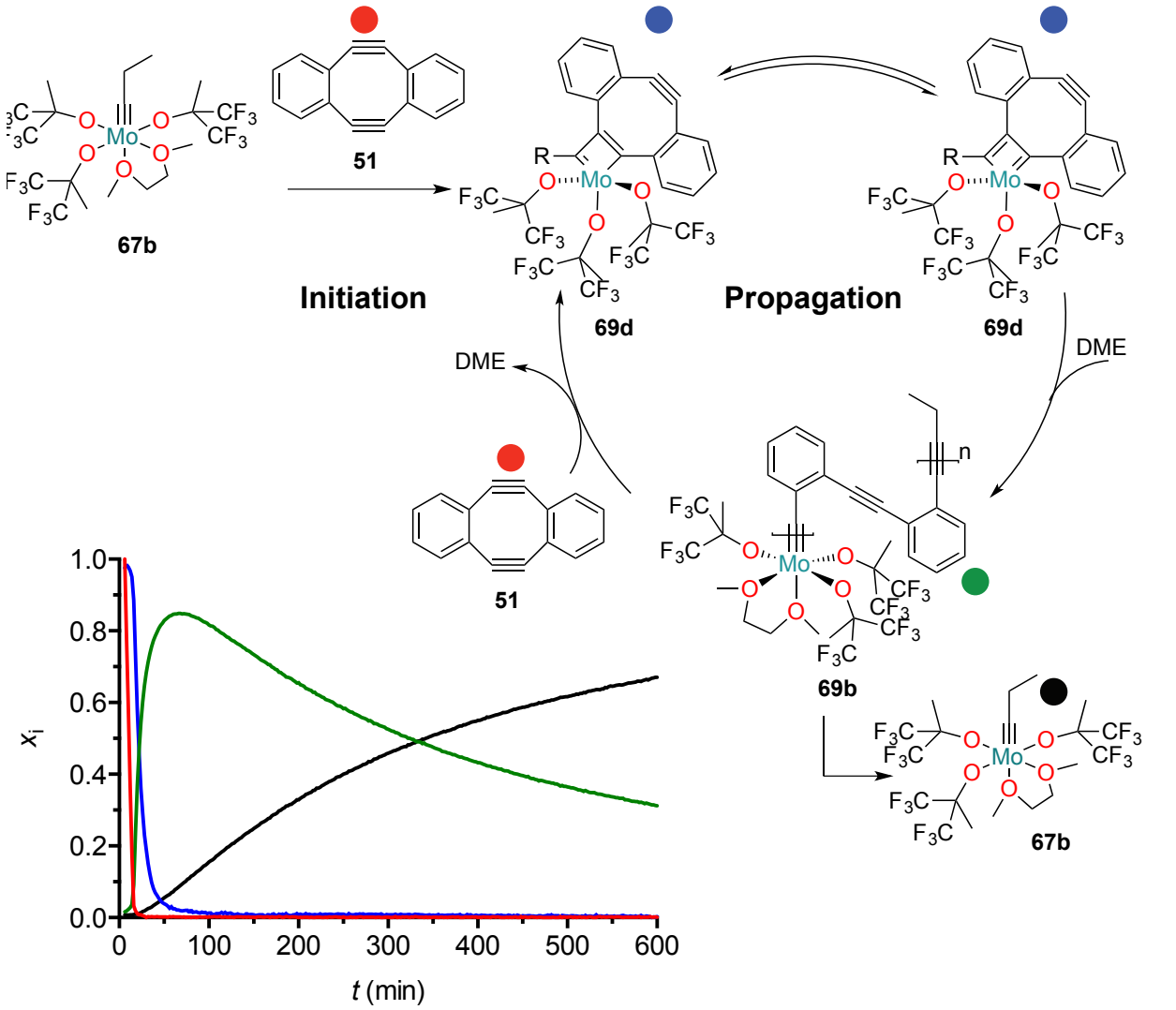

Figure 5.11 Proposed catalytic cycle for ROAMP of **51** with catalyst **67b**. Inset shows the relative mole fractions of diyne **51** (red curve), metallocyclobutadiene **69d** (blue curve), and active catalyst species **69b** (green curve), and regeneration of catalyst **67b** (black curve) based on *in situ* ^{1}H NMR monitoring. R represents the growing polymer chain.

In the case of catalyst **67b** (Figure 5.11), cycloaddition with strained monomer **51** initiates the polymerization. During this step, the strained alkyne in **51** and the molybdenum carbyne in **67b** react to form metallocyclobutadiene **69d**. This structure can tautomerize and undergo ring-opening to give the active catalyst species **69b**. This catalytic cycle is very similar to the one proposed in Figure 5.8, with the essential difference being that the endgroup of the growing polymer chain is ethyl rather than a sterically-bulky mesitylene. Therefore the active catalyst **69b** can do cross-metathesis on its endgroup, regenerating the initial catalyst **67b** and creating cyclic polymers in the process.

The inset of Figure 5.11 shows the progress of the *in-situ* polymerization over time. While strained monomer **51** (red curve) is being consumed, both metallocyclobutadiene **69d** (blue curve) and active catalyst **69b** (green curve) are present. As the concentration of monomer **51** (red curve) decreases, the concentration of metallocyclobutadiene **69d** (blue curve) also decreases, but the concentration of active catalyst species **69b** (green curve) increases. After the depletion of strained monomer **51**, the active catalyst **69b** performs cross-metathesis on its endgoup (ethyl), which simultaneously produces cyclic polymers and regenerates the initial catalyst **67b** (black curve).

Catalyst **67b** preferentially performs cross-metathesis on the ethyl endgroup, and not randomly throughout the polymer chain. This is supported by MALDI-MS that shows differences of 200 amu between the observed masses (Figure 5.6).

The propensity for backbiting of the catalyst into the polymer chain was related to the reaction temperature (Figure 5.12). By monitoring the polymerization at various temperatures by ^{1}H NMR, the emergence of cyclic and linear polymers, as well as other complex species, was evident after 5 minutes at 25 °C (Figure 5.12a). After 4 h at 25 °C (Figure 5.12b), the mixture was predominantly cyclic polymer **68b** and linear polymer **68a**. Even at 50 °C for 1 h (Figure 5.12c), the preference for backbiting into the endgroup rather than the polymer chain was maintained. Upon increasing the temperature to 80 °C (Figure 5.12d), the polymer aromatic signals were replaced by two doublets of doublets at 6.7 and 7.2 ppm. After 40 h at this temperature (Figure 5.12e), the remaining product was identified by NMR and mass spectrometry as trimer **68f**. This metathesis product can be considered the thermodynamic sink for ROAMP of **51**.

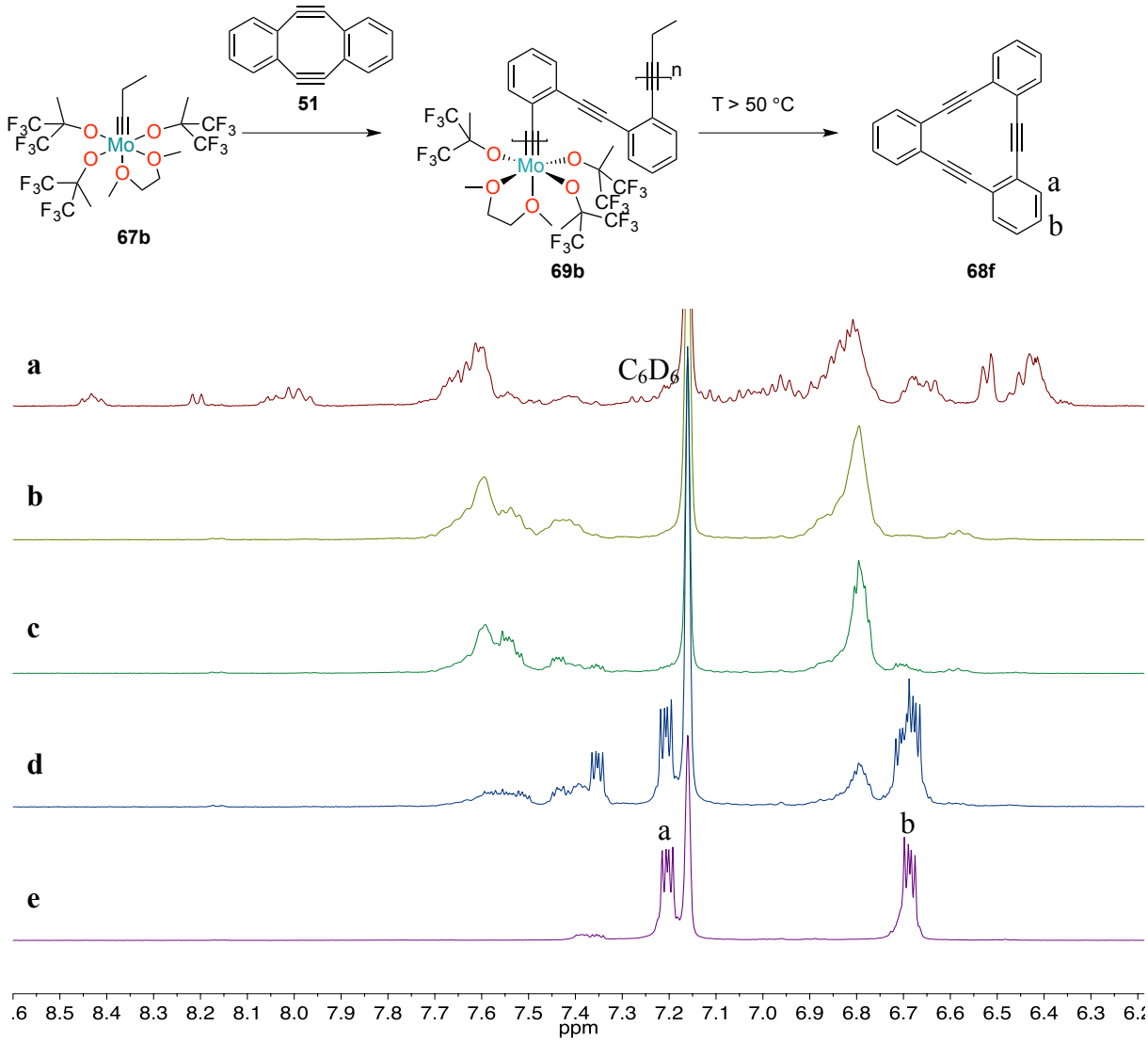

Figure 5.12 Dependence of backbiting on polymerization temperature in C_6D_6 using catalyst **67b**. ^{1}H NMR of polymerization after (a) 5 min at 25 °C, (b) 4 h at 25 °C, (c) 60 min at 50 °C, (d) 60 min at 80 °C, and (d) 40 h at 80 °C.

5.4 Polymerization of Electron-Rich Diynes

Diynes **51**, **60a**, and **60b** readily undergo ring-opening alkyne metathesis polymerization (Scheme 5.9). The reaction of diyne **51** with catalyst **67c** in toluene was sampled at various time points (Figure 5.13). During the first 5 h of ROAMP, the number average molecular weight increases linearly with time, which is expected for a living polymerization (Figure 5.13b). Size-exclusion chromatography shows a bimodal distribution of polymer populations that converge to a single monomodal peak after 8 h to give a final polydispersity index (PDI) of 1.6 (Figure 5.13a). This PDI is exceptionally low for conjugated polymer systems and can be considered as evidence for the high-degree of control during the polymerization process. In contrast,

monomers **60a** and **60b** are electron rich, and their polymerization with catalyst **67c** is complete within 30 sec. SEC shows these polymers have a number average molecular weight of 15,000 and PDI of 1.5 (Figure 5.14).

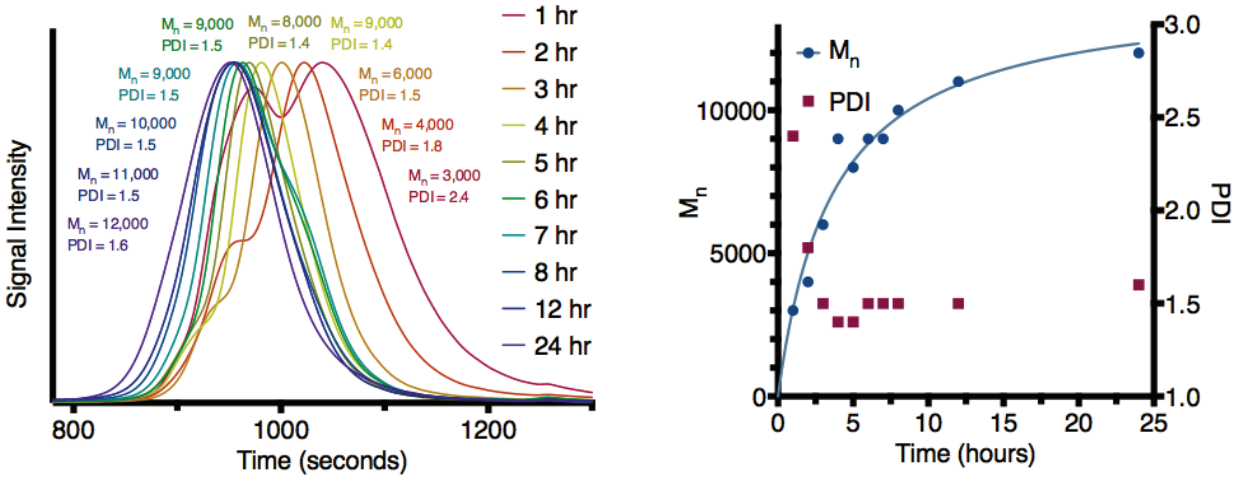

Figure 5.13 Dependence of ROAMP on time. (a) SEC profile of the polymerization of strained diyne **51** with catalyst **67c** at various time points. (b) Number average molecular weight (M_n) plotted with PDI for the same time points.

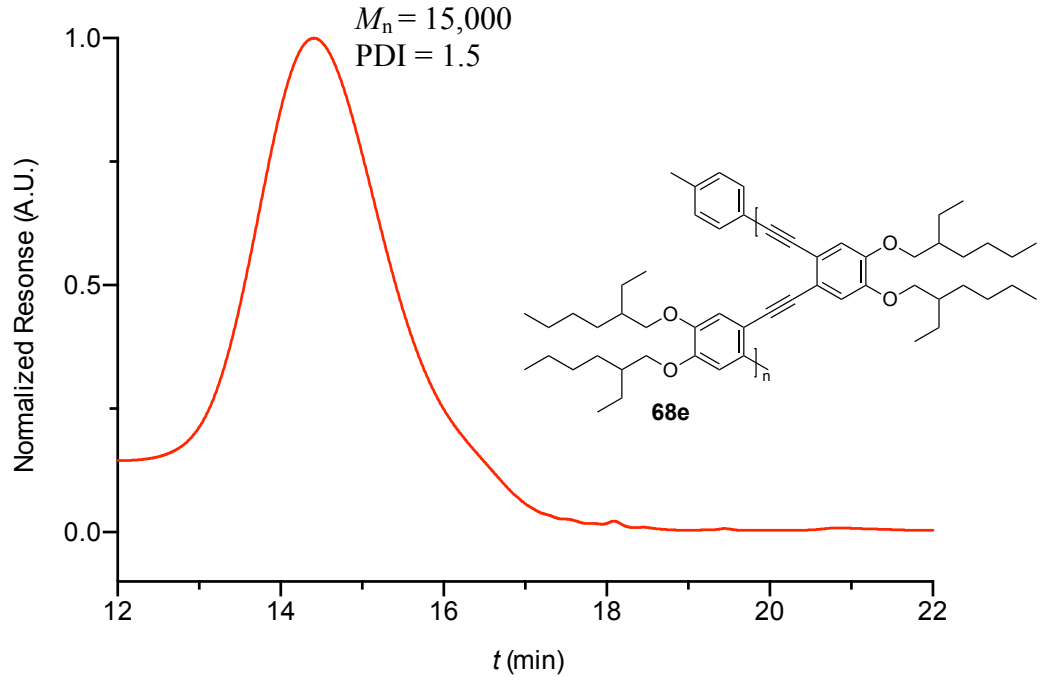

Figure 5.14 Size-exclusion chromatography of polymer **68e**.

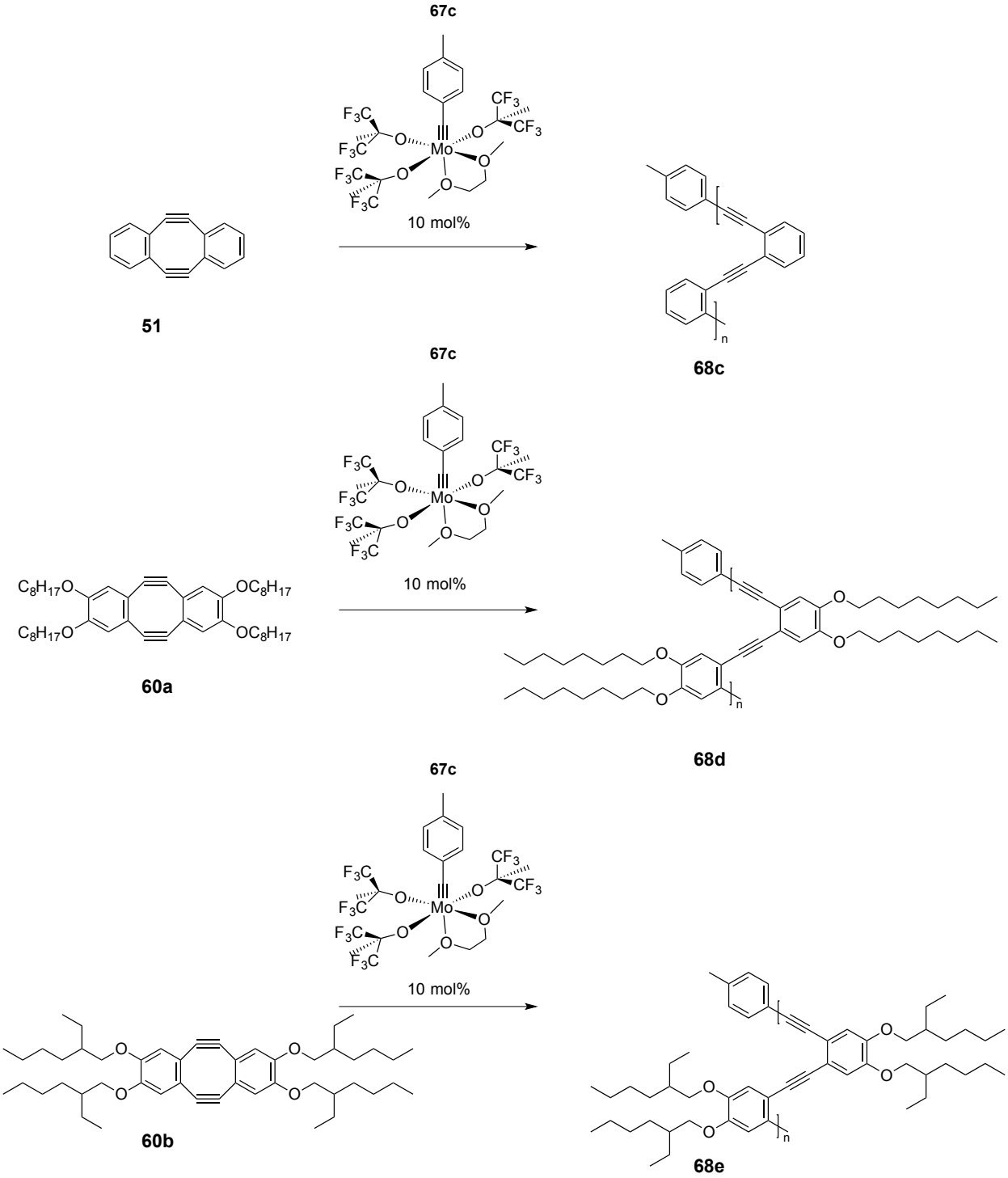

Scheme 5.9 Successful polymerization of diynes **51**, **60a**, and **60b**.

Despite the fast kinetics of this polymerization, the resulting polymers **68d** and **68e** are exceptionally pure and stable as evidenced by their ^{1}H and $^{13}C\{^{1}H\}$NMR spectra (Figure 5.15).

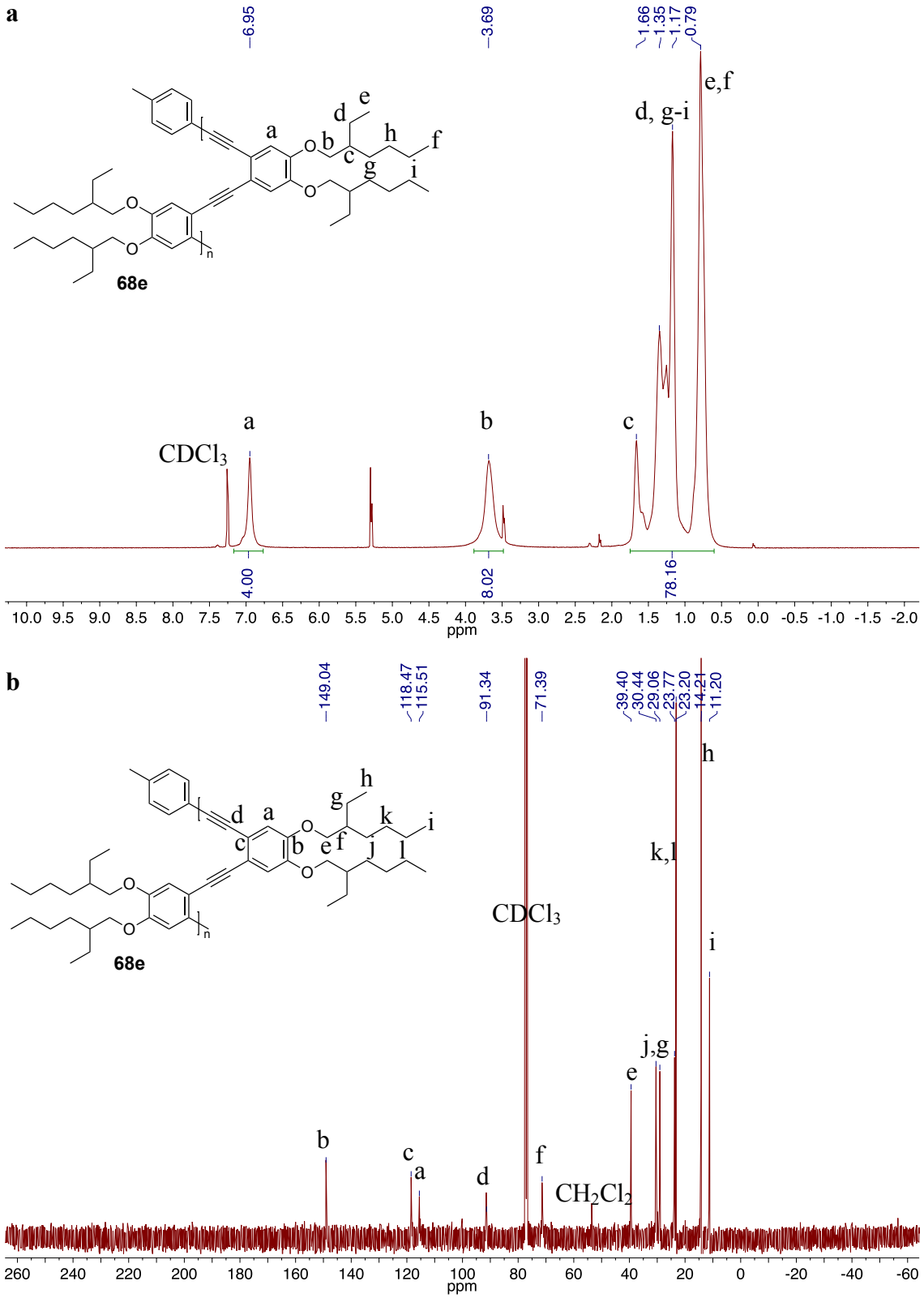

Figure 5.15 (a) ^{1}H NMR and (b) $^{13}C\{^{1}H\}$ NMR of polymer **68e**.

5.5 AFM and SEM Investigation of Poly(*o*-Phenylene Ethynylene)

In order to gain an understanding of the self-assembly properties of this polymer, Atomic Force Microscopy (AFM) was used to study these materials. The polymers had a pronounced tendency to form fibers as demonstrated by the topography images (Figure 5.16).

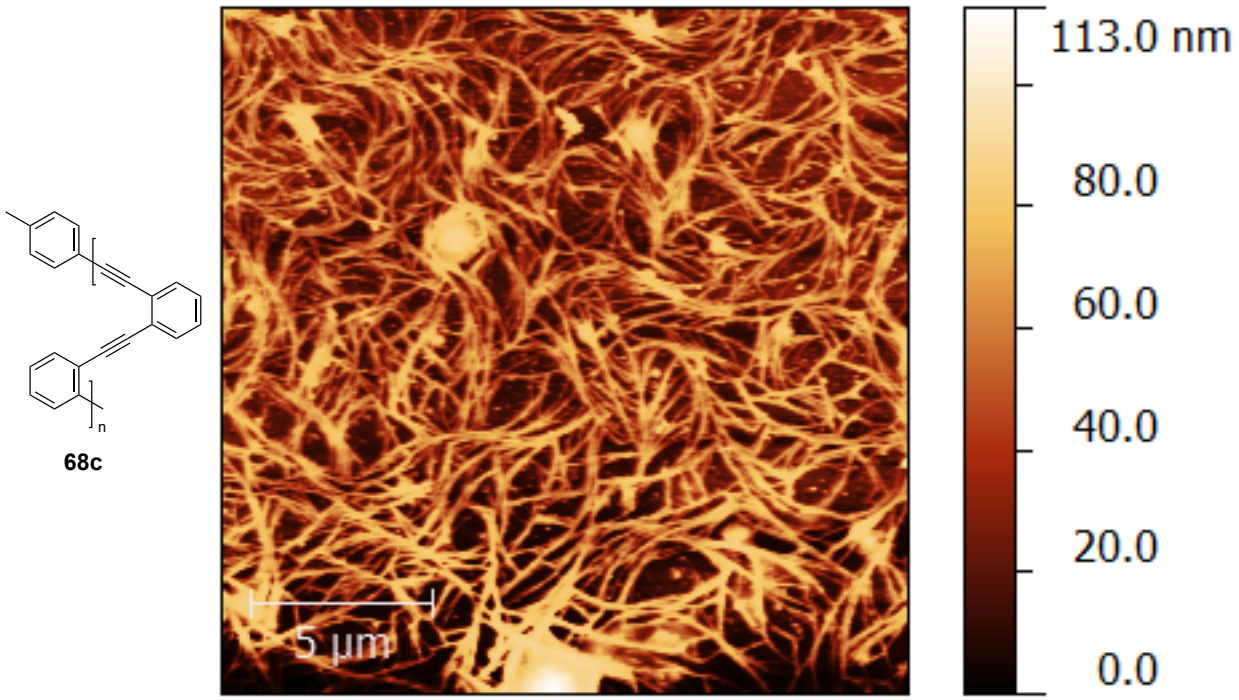

Figure 5.16 AFM topography of o-PPE **68c**.

Two types of polymer conformations could lead to this behavior. Foldameric structures could lead to helical assemblies analogous to the behavior observed by Tew for oligomeric *o*-phenylene ethynylene (Scheme 5.10).[138]

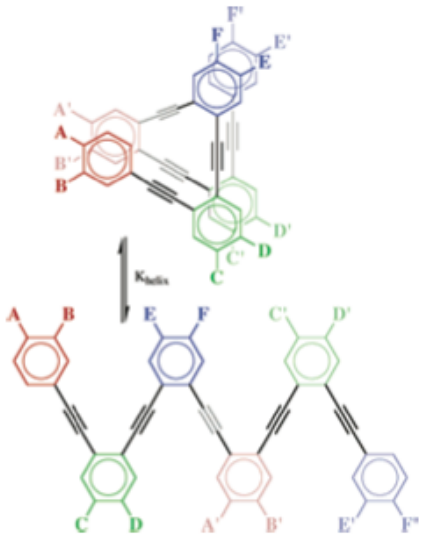

Scheme 5.10 Solvent driven folding of *o*-phenylene ethynylene [reproduced from ref. 138].

The linear, open-chain conformation of the polymer could lead to nanostructuration via π-π stacking of the planar, aromatic units. The fact that these fibers were only observed after slow evaporation of *o*-dichlorobenzene implies that the latter mechanism is more likely to be the operant one.

In contrast, cyclic polymer **68b** was found to form spherical structures on the order of 300 nm – 3 microns (Figure 5.17). This is reasonable, since it is difficult to for the cyclic polymers to exhibit the same kind of folding or π-π stacking as its linear counterpart.

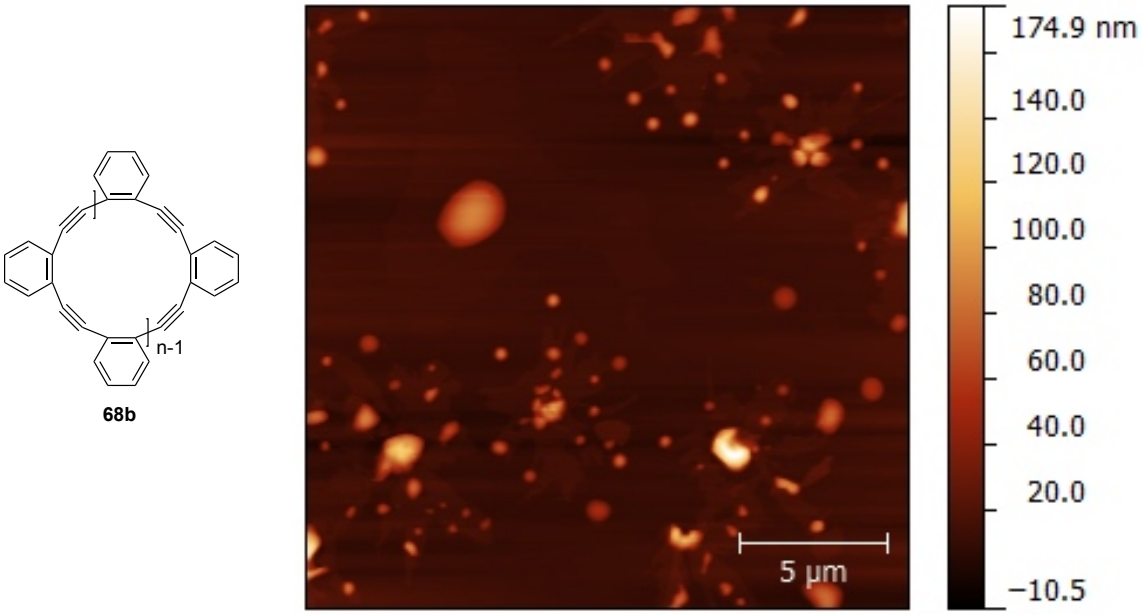

Figure 5.17 AFM topography of cyclic polymer **68b**.

While AFM is useful for the study of nanoscale phenomenon, SEM is an important tool for the determination of self-assembly over much larger length scales. Dropcasting **68e** from $CHCl_3$ onto SiO_2 revealed helical structures that were on the order of 10 x 100 microns (Figure 5.18).

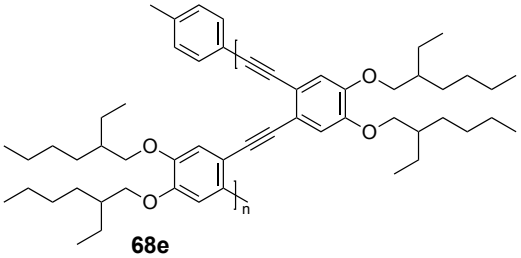

68e

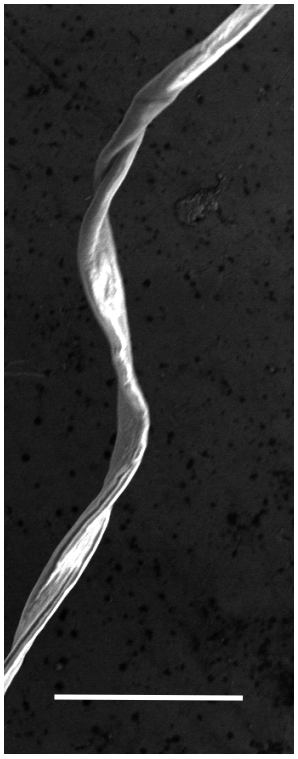

Figure 5.18 SEM image of **68e** on SiO_2. Scale bar 100 microns.

In this chapter, poly(*o*-phenylene ethynylene) and alkoxylated analogs were synthesized by Ring-Opening Alkyne Metathesis Polymerization (ROAMP). The resulting polymers were either cyclic or linear, which could be selected for based on the catalyst employed. A carbon-13 labeled diyne monomer was synthesized, and *in situ* NMR experiments revealed the origin of selectivity for cyclic or linear structures. In short, polymers with the least sterically hindered endgroups produced the greatest amount of cyclic polymers. In addition, it was determined that this mixture of cylic and linear polymers could be purified by Soxlet extraction with hexanes. In order to prevent the catalyst from biting into the middle of the polymer chain, solvent and temperature conditions were carefully optimized. The novel electron-rich strained alkynes reported in this chapter rapidly polymerize with molybdenum carbynes, a fact that will be useful in future applications. It was also discovered that these polymers have remarkable self-assembly properties, as determined by AFM and SEM. The ability to form micron-sized, conjugated fibers will likely find applications in future organic electronic devices. Further studies will yield mechanistic insight into the nature of this self-assembly, which will ultimately lead to control over the supramolecular assembly process over multiple length scales. Additionally, the precise control of conjugated polymer precursors will advance the synthesis of graphene nanoribbons by increasing the library of materials available for Scholl oxidation.

Chapter 6
From ROAMP to Graphene Nanoribbons

In the sixth chapter of this thesis, the rationale and progress for utilizing ROAMP in the fabrication of bottom-up graphene nanoribbons is described. Particular emphasis is placed on the role of a newly developed copper-catalyzed benzannulation of polymeric alkynes. The use of this reaction to convert alkynes into fluorinated naphthalenes is discussed. The resulting aromatic materials were subjected to cyclodehydrogenation conditions and the products were analyzed by UHV-STM and Raman spectroscopy.

6.1 Introduction

The pursuit of poly(*o*-phenylene) has been an outstanding challenge in organic synthesis for over 60 years.[148–153] Because of the unique access to ortho-substituted conjugated polymers from ROAMP in the Fischer Group, an excellent opportunity to synthesize poly(*o*-phenylene) as a precursor to GNRs is presented. Additionally, since cyclic poly(*o*-phenylene ethynylene) is obtained by ROAMP, benzannulation and cyclodehydrogenation could provide access to short segments of atomically-precise carbon nanotubes (Scheme 6.1).

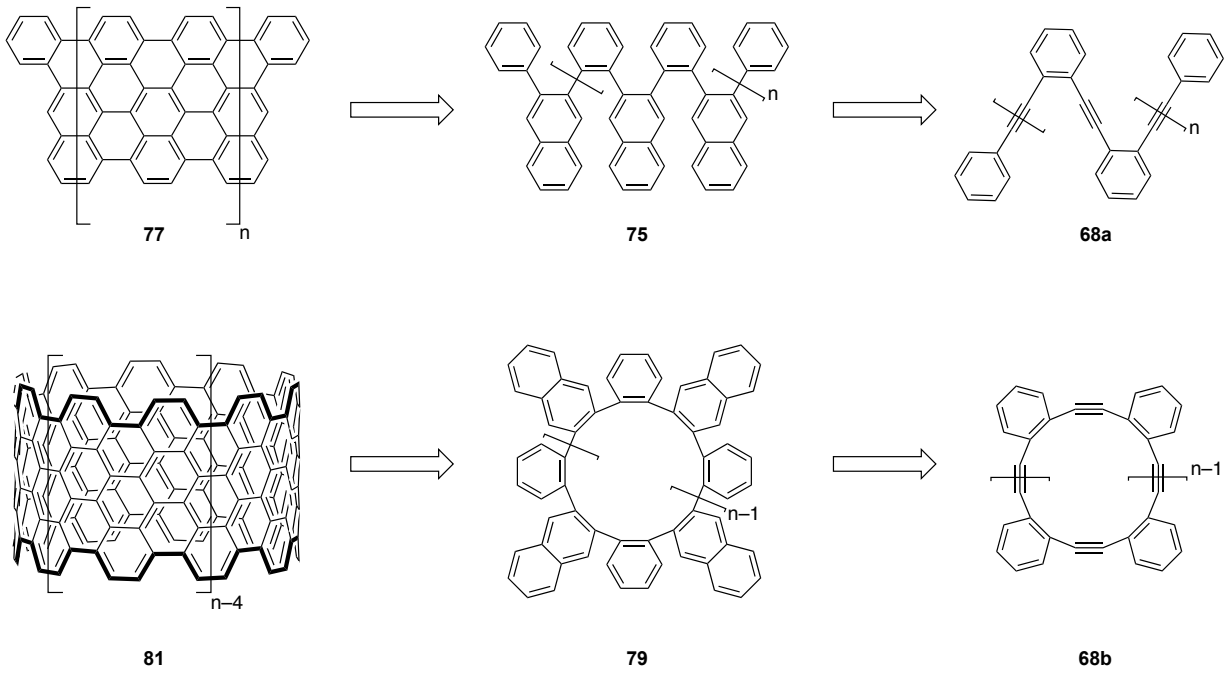

Scheme 6.1 Retrosynthetic analysis of n=8 armchair GNRs from linear poly(*o*-phenylene ethynylene) and carbon nanotubes from cyclic poly(*o*-phenylene ethynylene).

Recent progress in the benzannulation chemistry of alkynes has made phenylene ethynylene an attractive candidate for poly(*o*-phenylene) synthesis. The group of Yamamoto demonstrated a copper catalyzed benzannulation with excellent scope (Scheme 6.2).[154] The mechanism proceeds by coordination of the copper catalyst to the alkyne in reagent **a**. This activates the alkyne and predisposes it to intramolecular attack from the oxygen in the aldehyde, forming a highly reactive pyrylium **c**. This species readily undergoes cycloaddition with an alkyne starting material to give **f**. Under appropriate reaction conditions, the metal can be protonated off of **f** to give **k** which quickly collapses to yield the intended naphthalene ring **l**. Compound **f** could also collapse in a different fashion to yield benzylic ketone **h**.

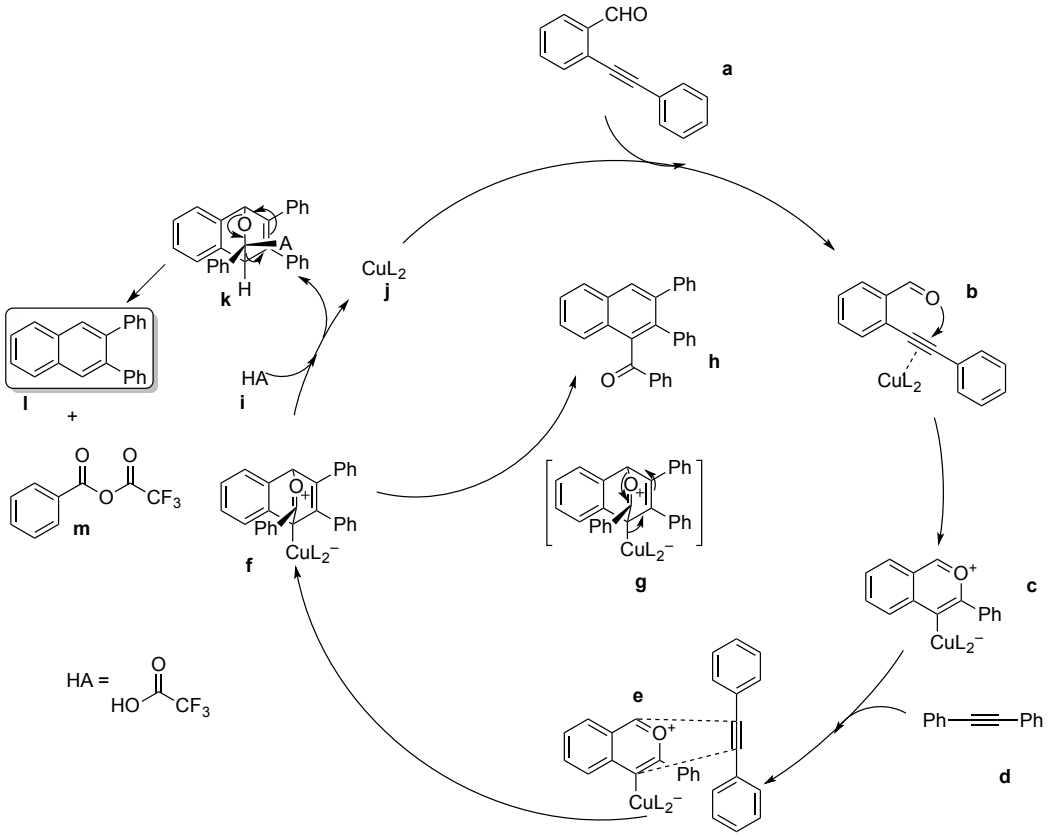

Scheme 6.2 Proposed mechanism of Yamamoto benzannulation [modified from ref. 154].

More recently, the Dichtel Group demonstrated that Yamamoto benzannulation could be used to quantitatively convert all of the triple bonds in poly(*p*-phenylene ethynylene) to new naphthalene rings (Scheme 6.3).[155] If this polymer were to undergo Scholl oxidation, however, it would not possess uniform armchair edges. Moreover, there is a rotational degree of freedom between each naphthalene and adjacent triphenyl that would lead to non-regioregular structures.

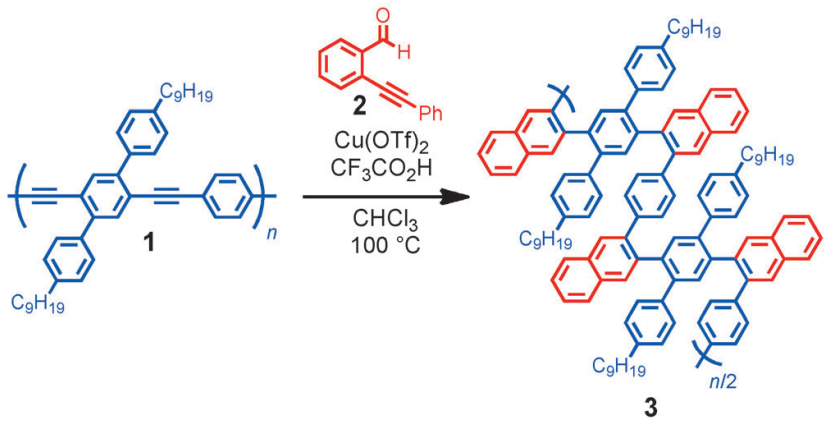

Scheme 6.3 Benzannulation of phenylene ethynylene [reproduced from ref. 155].

The bottom-up pursuit of carbon nanotubes (CNTs) has also intensified in recent years. In 2013, the group of Itami utilized a carbon nanoring template to grow CNTs with narrow polydispersity in width (Figure 6.1).[156]

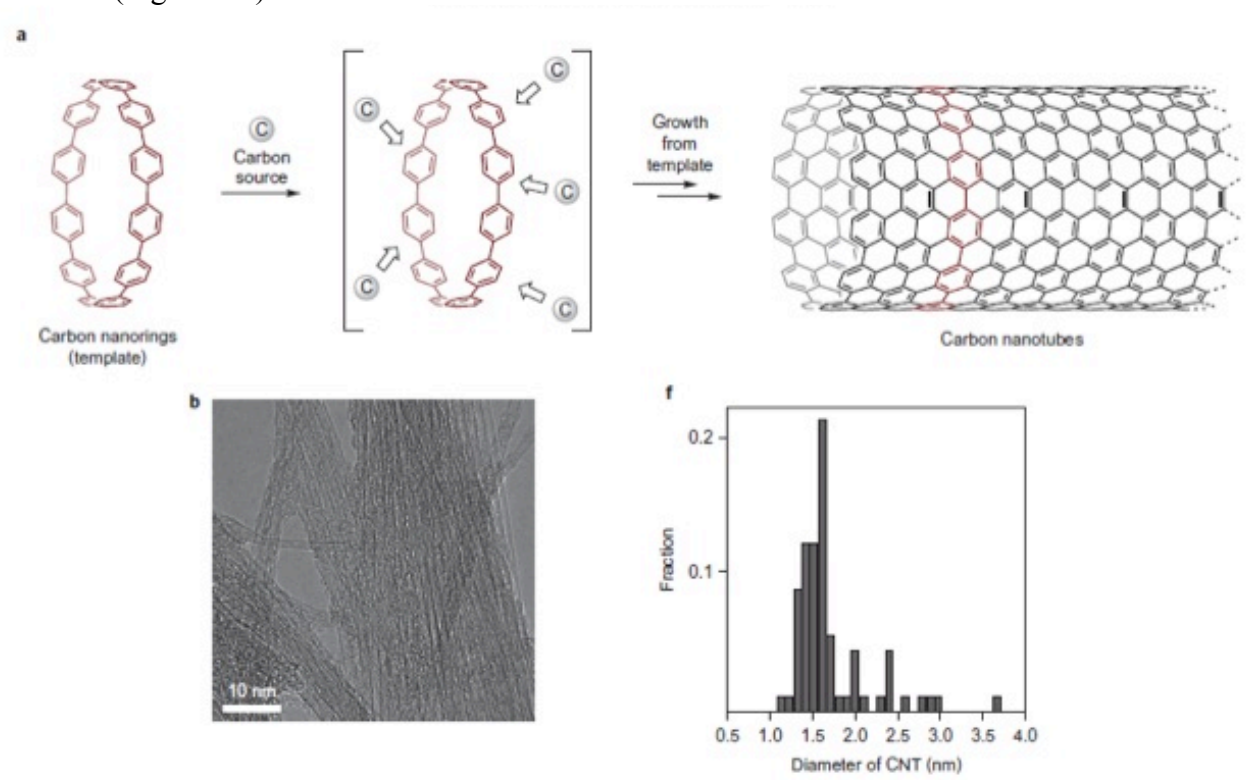

Figure 6.1 Synthesis of CNTs from molecular templates. (a) Schematic representation of the growth process from a molecular precursor. (b) TEM image of CNTs produced by this method with (f) distribution of widths [modified from ref. 156].

While this approach represents a step towards a rational bottom-up synthesis of carbon nanotubes, the diameters of the nanotubes were still far from uniform. The group of Klaus Müllen has attempted a bottom-up synthesis of carbon nanotubes, unsuccessfully, in 2014.[157] The incompleteness of the Scholl reaction in that case was attributed to strain created in partially cyclodehydrogenating a CNT molecular precursor.

Since then, the Müllen Group has studied simpler cyclic analogs of CNTs (Scheme 6.4).[158] In this case, a 1,2-phenyl shift is observed to take place during Scholl oxidation in order to alleviate the cumulative strain from successive cyclizations (Scheme 6.4a).

Even with strategically placed methyl groups, 1,2-phenyl shifts were still observed (Scheme 6.4b). However, when this macrocycle was increased in size by 6 phenyl rings, oxidative cyclodehydrogenation with ferric chloride proceeded to completion. This proves that the ineffectiveness of the Scholl oxidation in small, cyclic structures is due to the greater strain in smaller CNTs compared with larger CNTs.

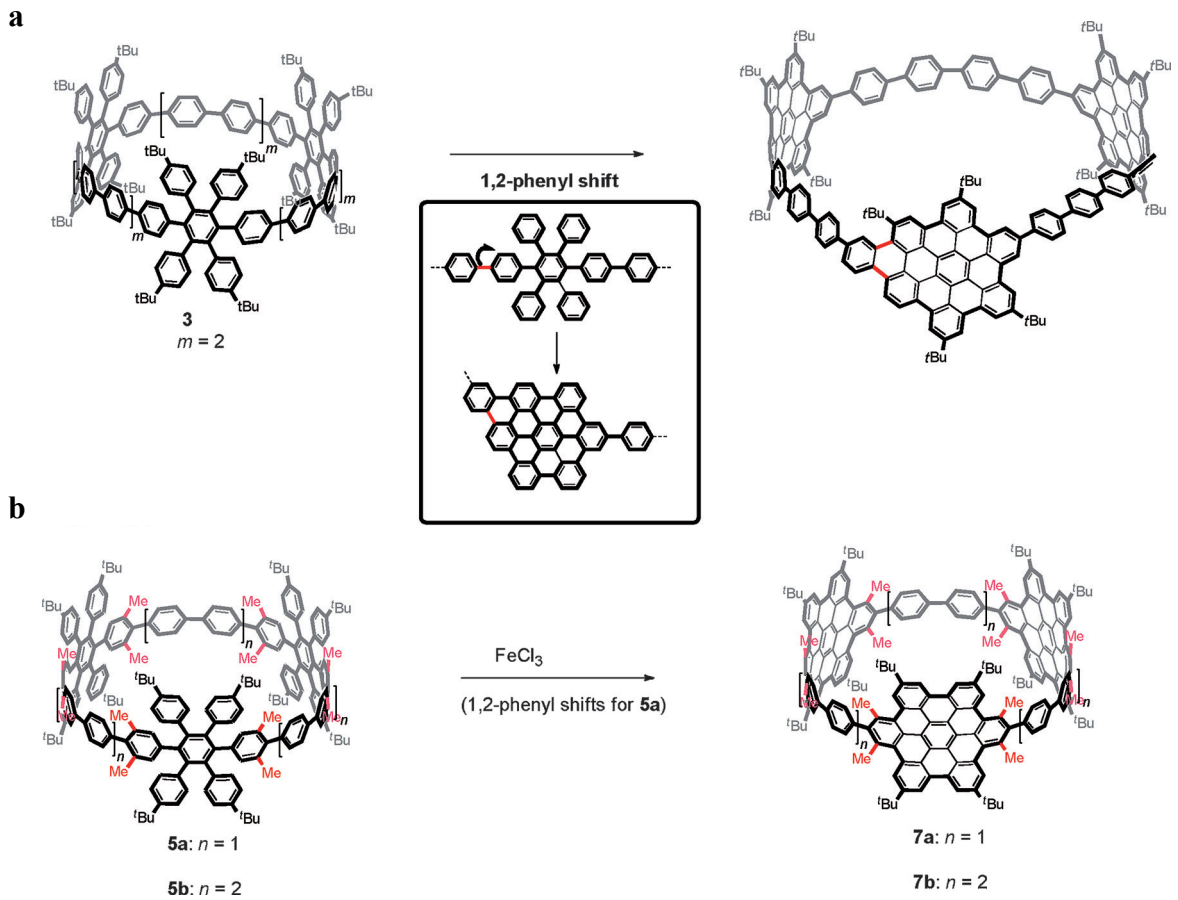

Scheme 6.4 Attempted cyclodehydrogenation of bottom-up CNT analogs by the Müllen Group. The Scholl oxidation produces 1,2-phenyl shifts in the case of (a) but not (b), provided the macrocycle is large enough [modified from ref. 158].

Therefore the bottom-up synthesis of both GNRs and CNTs from poly(phenylenes) remains an elusive goal in the fields of chemistry, materials science, and physics. The work reported in this chapter was conducted in collaboration with Giang Nguyen of the Crommie group.

6.2. Benzannulation of Cyclic and Linear Poly(*o*-Phenylene Ethynylene)

Following the strategy outlined by Dichtel, linear poly(o-phenylene ethynylene)s **68a** was benzannulated to obtain the corresponding poly(*o*-phenylene naphthalene)s **75** and **76** (Scheme 6.5). Likewise, the analogous cyclic poly(*o*-phenylene naphthalene)s **79** and **80** were obtained by benzannulation of cyclic poly(o-phenylene ethynylene) **68b** (Scheme 6.6). The products were characterized by size-exclusion chromatography (Figure 6.2). Cyclodehydrogenation of **77** and **78** was attempted and the products were subjected to characterization by UHV-STM (Figures 6.3 and 6.4) and Raman spectroscopy (Figure 6.5).

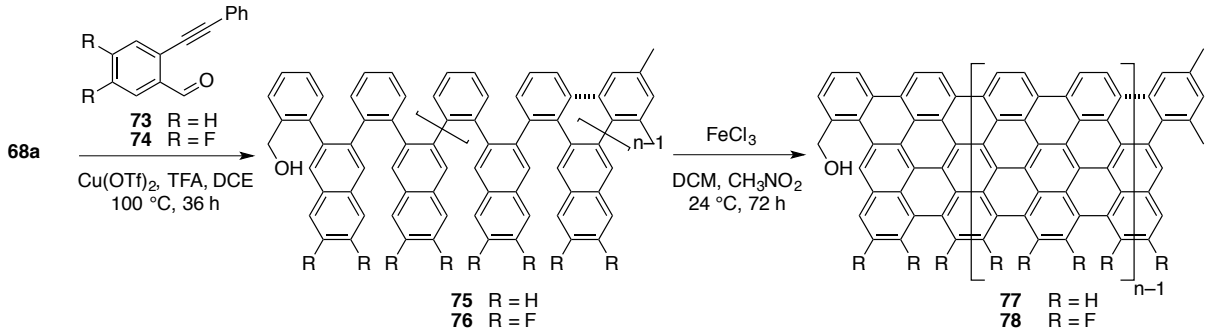

Scheme 6.5 Benzannulation of polymer **68a** from ROAMP and subsequent Scholl oxidation.

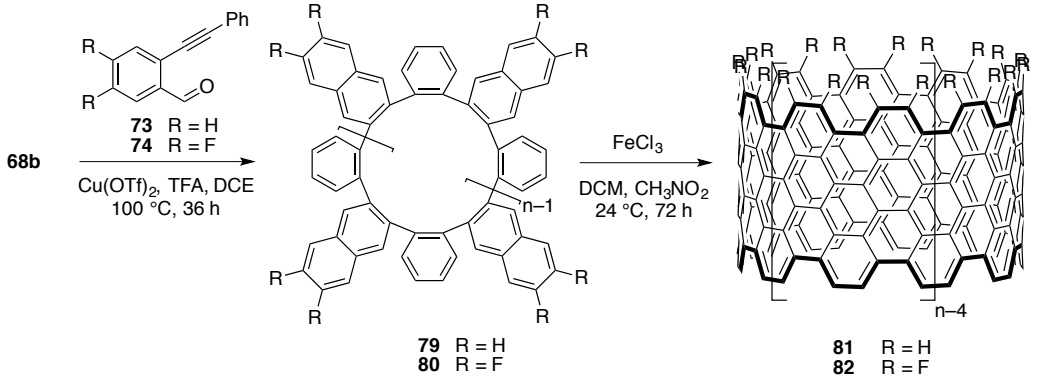

Scheme 6.6 Benzannulation of polymer **68b** from ROAMP and subsequent Scholl oxidation.

The benzannulation of poly(phenylene ethynylene) produces alternating benzene and naphthalene rings. For ortho-substituted phenylene ethynylene, the benzene and naphthalene rings are forced to adopt positions on opposites sides of the polymer backbone. This creates an opportunity to differentially substitute graphene nanoribbons with doping substituents on only one side of the GNR. In the case of fluorine substitution, this would lead to an interesting GNR with a very large dipole moment. Accordingly, a fluorinated benzannulation reagent was synthesized (Scheme 6.7) and tested on model compounds (Schemes 6.8 and 6.10).

To synthesize novel benzannulation reagent **74**, carboxylic acid **83** was nitrated and reduced to give aniline **84** (Scheme 6.7). Sandmeyer reaction yielded **85**, which could be reduced with borane in THF and oxidized with Dess-Martin periodinane to give the desired aldehyde **86**. Sonogashira coupling provided the desired fluorinated benzannulation reagent **74**.

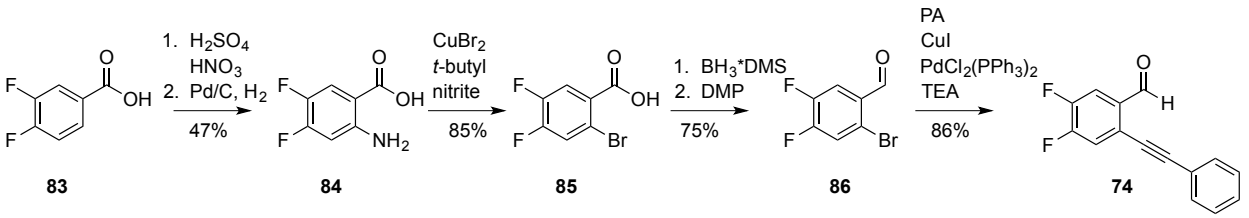

Scheme 6.7 Synthesis of fluorinated benzannulation reagent **74**.

Benzannulation of diphenylacetylene with electron-deficient benzannulation reagent **74** proceeded in excellent yield, while the corresponding electron-rich benzannulation reagent **88**, which was synthesized by a reported procedure, furnished an unexpected product (Scheme 6.8).

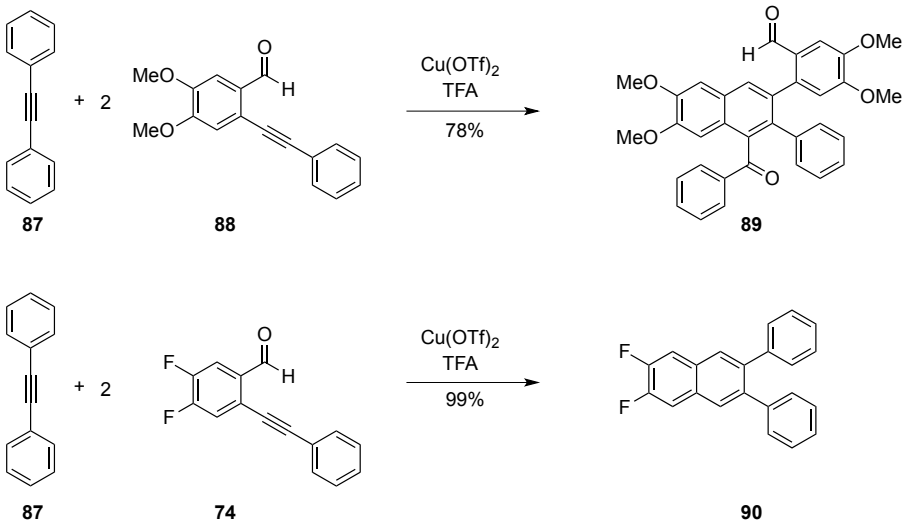

Scheme 6.8 Test reactions of electron-rich and electron-deficient benzannulation reagents.

A mechanistic view of this reaction suggests that the unexpected major product forms due to the fact that alkyne **88** is itself a better dieneophile than diphenylacetylene (Scheme 6.9). After formation of the desired pyrilium ion **91**, if a preferential reaction occurs with alkyne **88** over alkyne **87**, bridged intermediate **92** will be formed. If the copper catalyst is protonated off of this intermediate as expected, **93** will be formed. This compound will immediately collapse to produce **94**. However, if the copper catalyst in **92** is not protonated, this compound can fall apart to produce **89**, which was the major product observed by ^{1}H NMR, ^{13}C NMR, and EI-HR-MS.

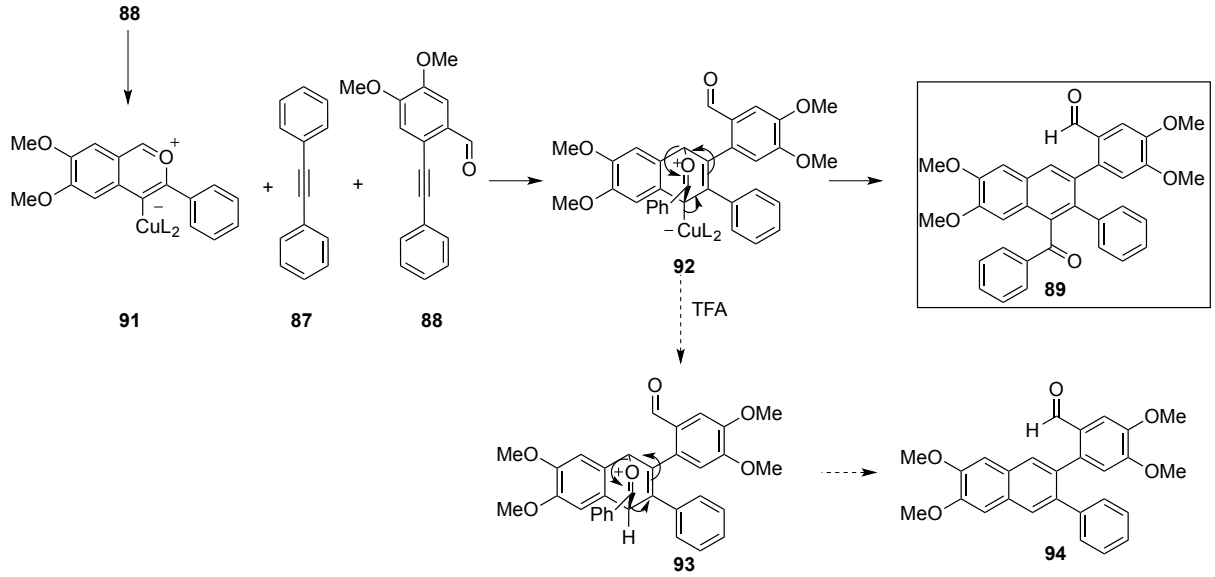

Scheme 6.9 Proposed mechanism of electron-rich benzannulation reactions.

While the electron-rich benzannulation reagent failed to produce the desired product, the electron-deficient benzannulation reagent worked in near-quantitative yield. This was true even for model systems containing two alkynes (Scheme 6.10).

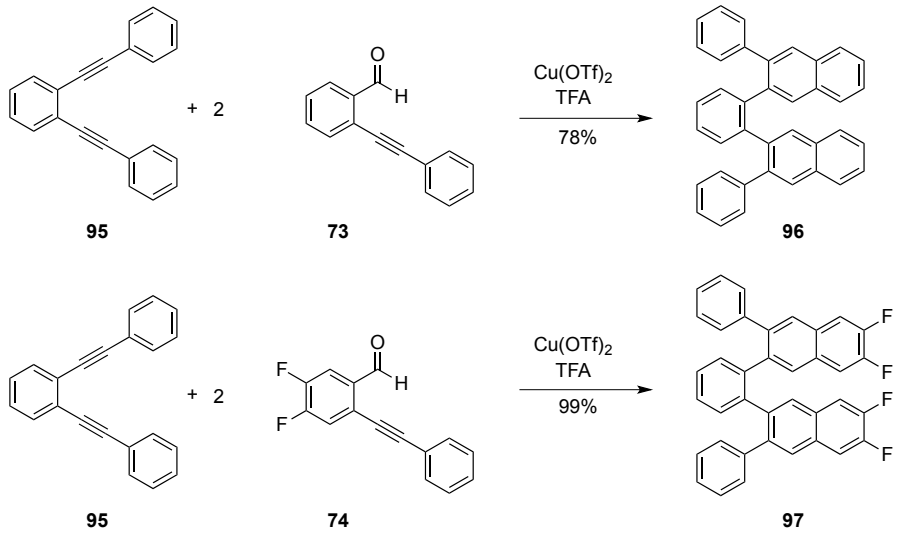

Scheme 6.10 Benzannulation reactions of model phenylene ethynylene systems.

With the success of the benzannulation established on these model *o*-phenylene ethynylene compounds, the reaction was attempted on poly(*o*-phenylene ethynylene)s **68a** and **68b** to yield linear polymers **75**–**76** and cyclic polymers **79**–**80**, respectively. These benzannulation products were studied by size-exclusion chromatography (Figure 6.2).

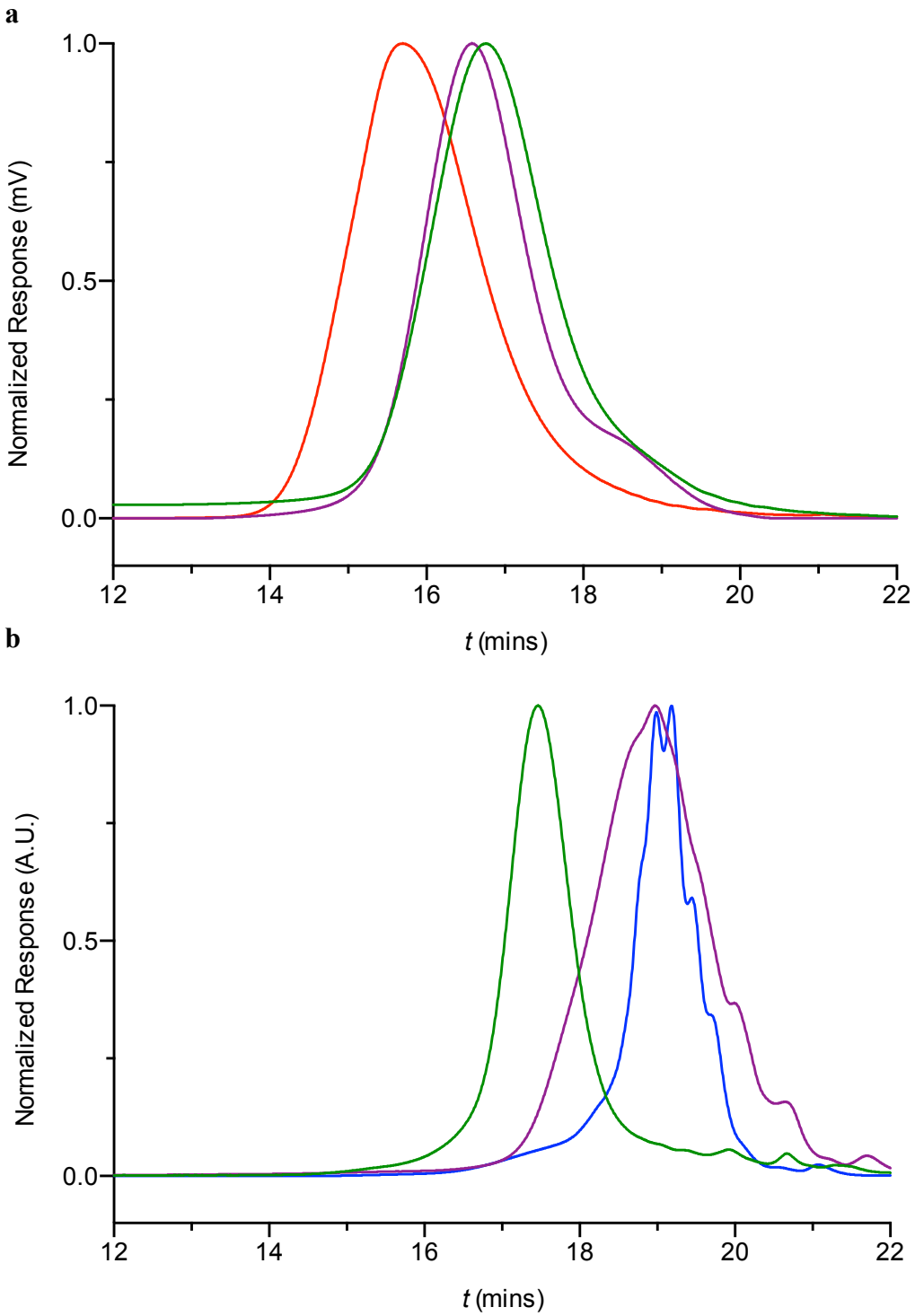

Figure 6.2 SEC of polymers **68a,b** and benzannulation products (a) **75,76** and (b) **79,80**. Color scheme: (a) linear poly(*o*-phenylene ethynylene) **68a** (red), linear poly(*o*-phenylene naphthalene) **75** (purple), linear poly(*o*-phenylene 6,7-difluoronapthalene) **76** (green). (b) cyclic poly(*o*-phenylene ethynylene) **68b** (blue), cyclic poly(*o*-phenylene naphthalene) **79** (purple), and cyclic poly(*o*-phenylene 6,7-difluoronapthalene) **80** (green).

Size-exclusion chromatography (SEC) analysis of the benzannulation of linear poly(*o*-phenylene ethynylene) **68a** (red curve) shows benzannulation product **75** (purple curve) is shifted to longer retention time (Figure 6.2a). This is consistent with the previous observation made by Dichtel for poly(*p*-phenylene ethynylene).[155] This is also true for the fluorinated benzannulation product **76** (green curve). Even though an increase in molecular weight is expected after benzannulation, the products are retained longer in SEC because the hydrodynamic radii of these polymers are smaller compared to polymer **68a**.

The benzannulation products of cyclic polymer **68b** (blue curve) exhibit very different SEC behavior (Figure 6.2b) than their linear counterparts. For benzannulation product **79** (purple curve), the SEC retention time is unchanged and the peak is merely broadened. This is reasonable, since the hydrodynamic radius of a cyclic polymer should be unaffected by new naphthalene rings. For the fluorinated benzannulation product **80** (green curve), the SEC retention time is markedly reduced. Comparing linear, fluorinated benzannulated polymer **76** with cyclic fluorinated benzannulated polymer **80** reveals that the SEC retention times are almost identical. This implies that during the benzannulation process, polymer **80** actually changes from cyclic to linear form, and is identical to linear polymer **76**.

The structures of **75**, **76**, **79**, and **80** could not be assigned unambiguously by ^{1}H or $^{13}C\{^{1}H\}$ NMR, due to very broad resonances observed for these polymers. Instead, the benzannulated polymers were subjected to cyclodehydrogenation conditions, either by Scholl oxidation in solution or by annealing on Au(111), and studied by UHV-STM and Raman spectroscopy.

8.3 UHV-STM and Raman Spectroscopy of GNRs from ROAMP

The benzannulated polymers were subjected to Scholl oxidation with ferric chloride and surface-assisted cyclodehydrogenation on Au(111). The resulting GNRs were characterized by STM (Figures 6.3 and 6.4) and Raman spectroscopy (Figure 6.5).

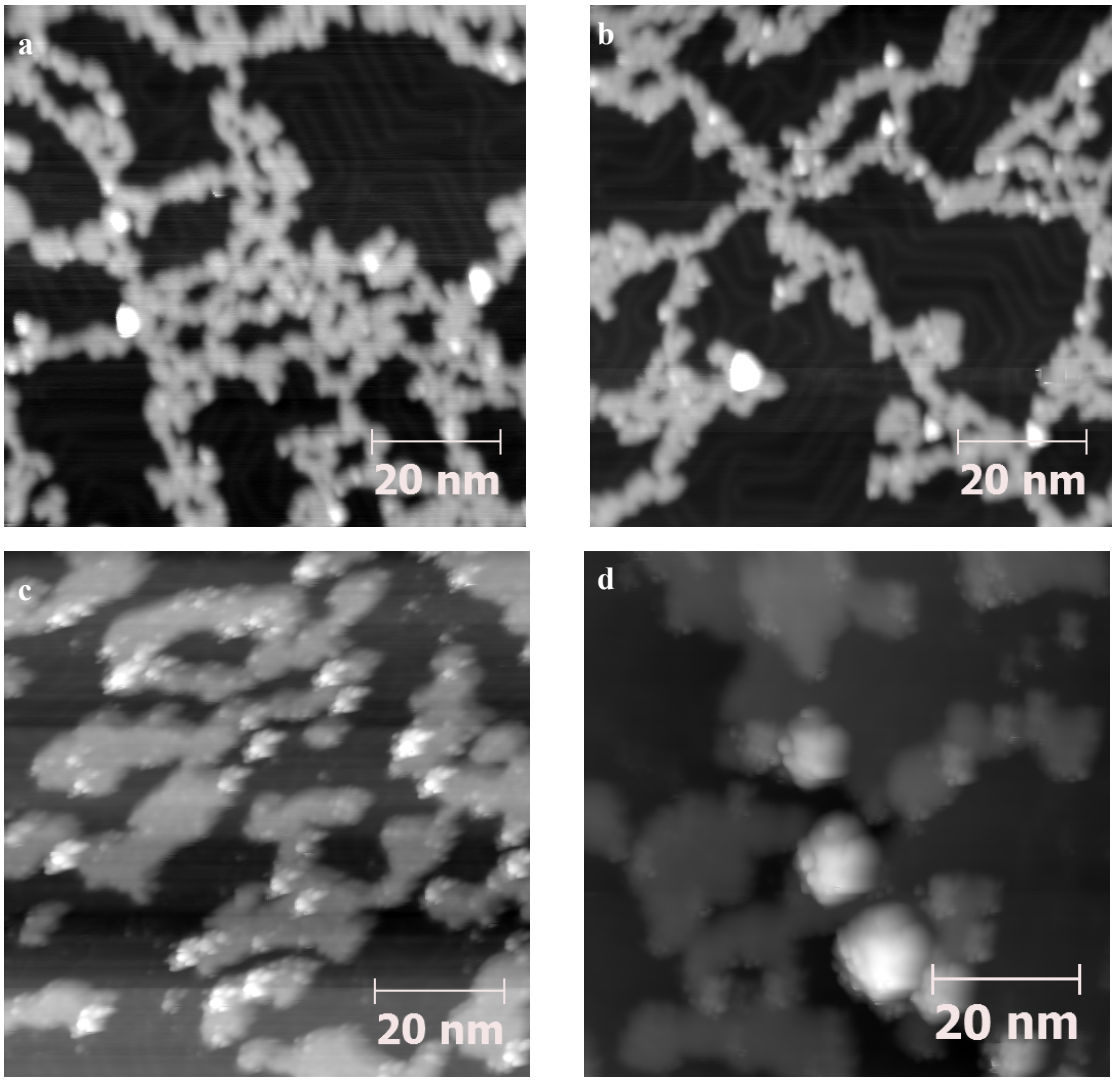

Figure 6.3 STM image of GNR **77** after annealing polymer **75** to (a,b) 300 °C and (c,d) 440 °C on Au(111).

Figure 6.3a,b shows the presence of high-aspect ratio structures after annealing polymer **75** at 300 °C on Au(111). While these structures have lengths, widths, and heights consistent with the expected GNR, they are considerably less regioregular than expected. After annealing to 440 °C, the cyclodehydrogenation reaction loses selectivity, and aromatic rings fuse intermolecularly to create islands of graphene (Figure 6.3c,d).

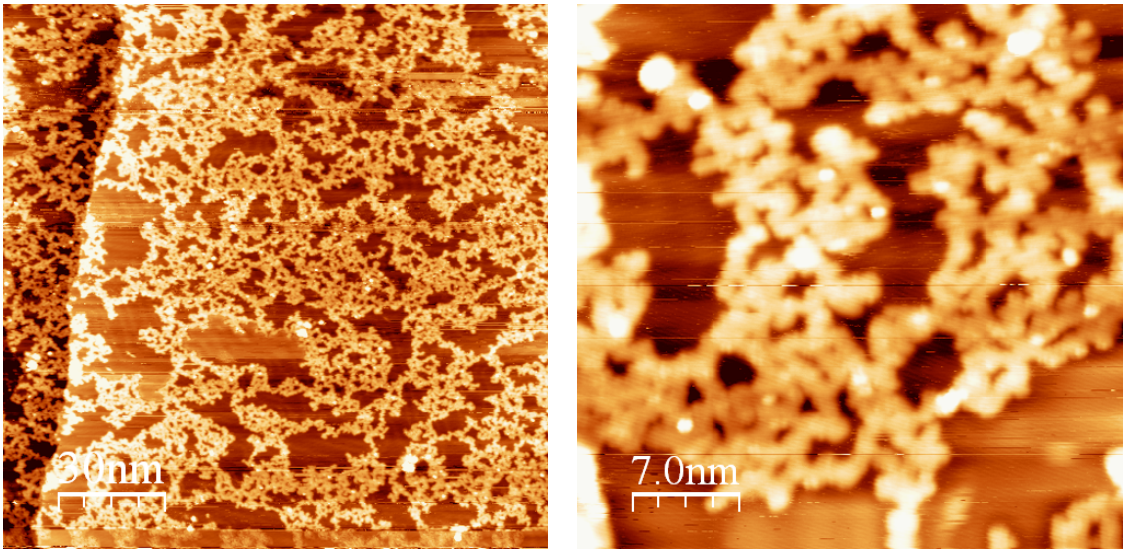

Figure 6.4 STM images of **78** after annealing polymer **76** at 400 °C on Au(111).

A similar observation was made after annealing fluorinated polymer **76** to 400 °C on Au(111) (Figure 6.4). Very flat structures with high-aspect ratios were observed by STM. As before, the dimensions of this structure are consistent with GNRs, but the structure is lacking the precision expected for atomically-precise GNRs. A proposed hypothesis for this observation is shown in Scheme 6.10. GNRs **77** and **78** obtained in solution from the reaction of polymers **75** and **76** with ferric chloride were also studied by STM, but the aggregation of the pre-formed GNRs made their visualization in STM extremely difficult.

The rearrangement of *o*-phenylenes during Scholl oxidation has been studied in detail by the King Group.[159] They determined by X-ray crystallography that under the arenium cation mechanism during Scholl oxidation, a 1,2-phenyl shift is possible. In the case of polymers **75** and **76**, a 1,2-phenyl shift with concurrent Scholl oxidation would lead to kinks in the GNR (Scheme 6.11). The resulting polymer would have a highly irregular structure with completely graphitized portions along the backbone. The kinked structure will also have free rotation around the migrated single bonds, causing additional degrees of freedom and structural complexity. However, the structure will not be fully graphitized, and would more closely resemble a graphene quantum dot than a GNR. This proposed structure is consistent with the STM observations in Figures 6.3 and 6.4. Furthermore, it helps to explain the fluorescence background observed in the Raman spectra (Figure 6.5).

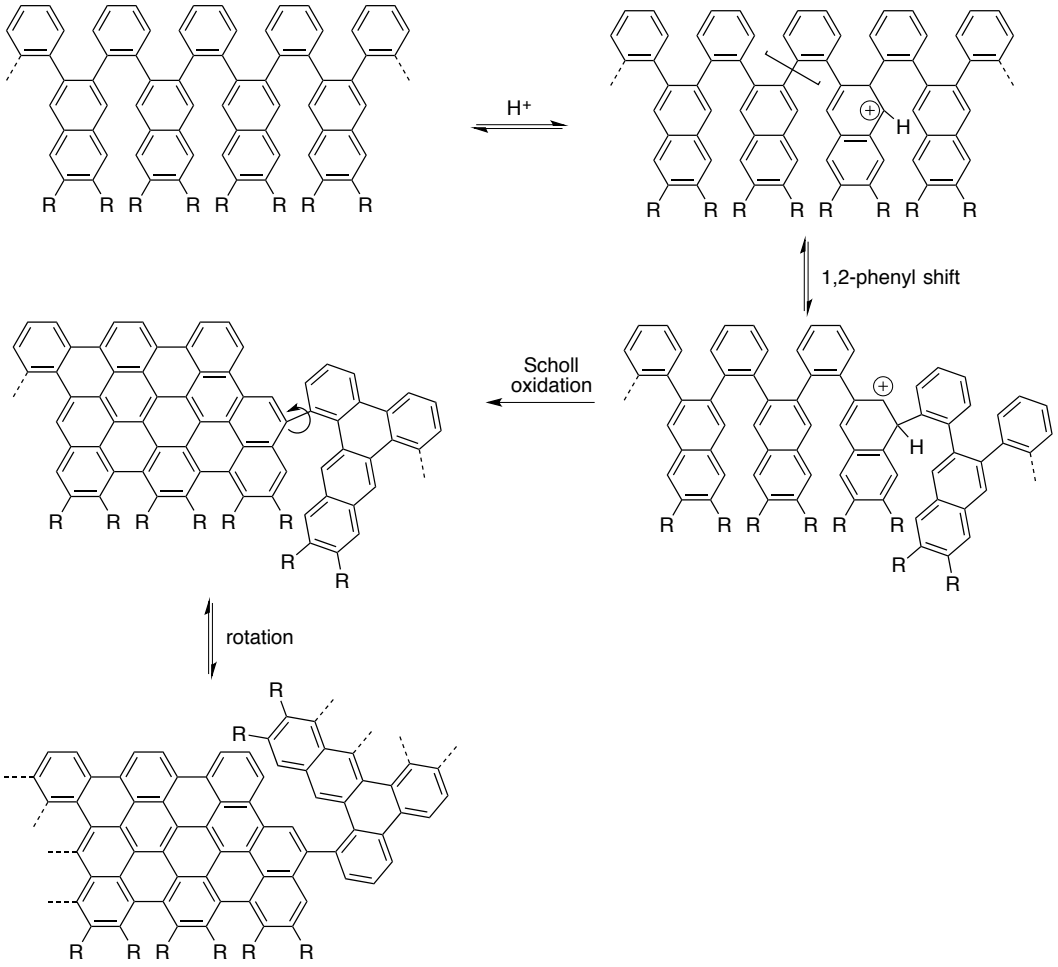

Scheme 6.11 Mechanistic hypothesis explaining the lack of structural regularity resulting from the Scholl reaction of *o*-phenylenes.

The raman spectra obtained for GNRs **77** and **78** also confirm the lack of structural regularity. The Raman measurement in these cases is extremely hampered by the background fluorescence signal (Figure 6.5a). As graphene nanoribbons are expected to quench their own fluorescence in the solid-state, these highly luminescent structures more closely resemble quantum dots of nanographenes than GNRs. This behavior likely results from the kinks present in the structure as proposed in Scheme 6.9. After correcting for the background fluorescence and multiplying the remaining signal, the experimental spectra closely resembled their predicted spectra (Figure 6.7b,c).

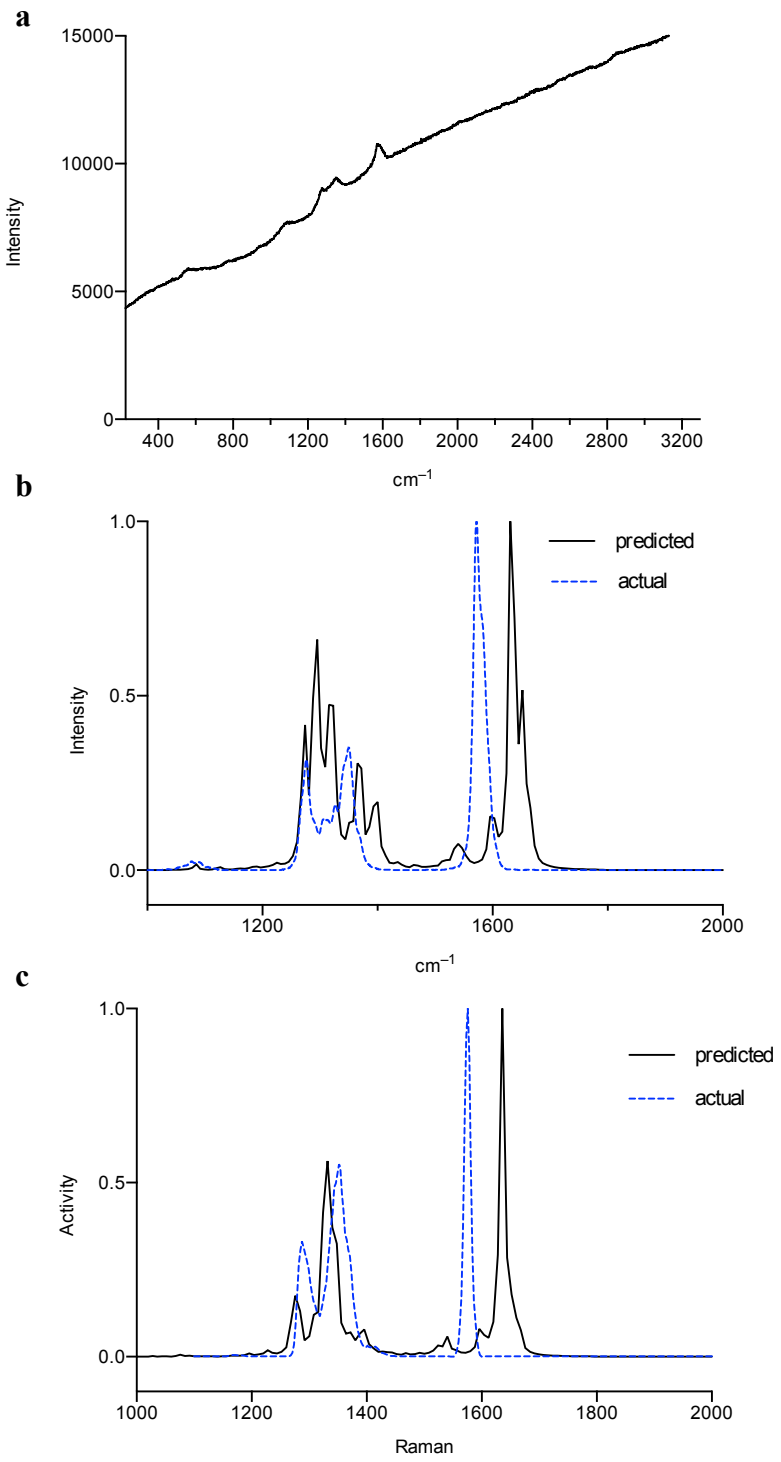

Figure 6.5 (a) Typical Raman spectrum of GNR **77** produced by the Scholl oxidation of polymer **75**. Comparison between predicted and experimental Raman spectra for (b) GNR **77** and (c) fluorinated GNR **78** after the fluorescence background is subtracted and the signal is multiplied.

In conclusion, the benzannulation and graphitization of cyclic and linear poly(*o*-phenylene ethynylene) was demonstrated by STM and Raman spectroscopy. Benzannulation of model compounds demonstrated that this reaction is highly effective for electron-deficient benzannulation reagents. However, complex products were observed in the case of electron-rich benzannulation reagents. This benzannulation reaction was applied to the linear and cyclic polymers obtained from ROAMP in the previous chapter and the resulting products were studied by size-exclusion chromatography. For the linear polymers, the benzannulation is consistent with the previous report of Dichtel provided for the analogous para-substituted system. The fluorinated cyclic polymers, however, displayed unexpected SEC behavior and further investigation of these structures is warranted. The linear, benzannulated polymers obtained by this method were cyclodehydrogenated both by the Scholl oxidation and surface-catalysis on Au(111). The direct visualization of these structures by UHV-STM provides evidence for the presence of highly planar, sp^2 hybridized structures. The lack of regularity and atomic-precision, however, indicates that a 1,2-phenyl shift, as proposed by King and coworkers, is possible. However, further improvement of the cyclodehydrogenation process could lead to a new class of conjugated polymers that serve as precursors for doped graphene nanoribbons.

Chapter 7
Summary and Outlook

7.1 Summary

In this work, the bottom-up synthesis of doped graphene nanoribbons from molecular and polymeric precursors was reported. In Chapter 2, the first example of substitutional boron doping of graphene nanoribbons was reported. Doping of this armchair nanoribbon introduced a mid-gap state that lowered the band gap to 0.8 eV. This nanoribbon was studied extensively by UHV-STM and nc-AFM to show the complex interaction of the precisely located boron atoms with the underlying gold substrate. In Chapter 3, a porphyrin containing four bromoanthracene motifs was synthesized. It was demonstrated that this porphyrin could be sublimed and imaged in UHV-STM. Additionally, a model porphyrin-anthracene dimer was synthesized and studied by UHV-STM. In Chapter 4, gram-scale syntheses of four doped graphene nanoribbons were completed. These materials were characterized completely and used successfully in hydrogen storage, carbon dioxide reduction, and Li-ion battery applications. In Chapter 5, the development of Ring-Opening Alkyne Metathesis Polymerization for conjugated materials was presented. A library of highly strained and reactive diyne monomers was synthesized and polymerized by ROAMP to give linear or cyclic polymers. In Chapter 6, the resulting polymers from ROAMP are subjected to benzannulation and Scholl oxidation. The analysis of the complex mixture resulting from this reaction is ongoing. In the remaining chapters, complete experimental procedures and characterization for all new compounds are provided, as well as additional information that could be useful to the reader.

7.2 Outlook

The synthesis of novel nanomaterials with tailored properties for energy and electronics applications remains a pressing goal in chemistry and materials science. The work reported in this thesis advances this objective through the development of many types of doped graphene nanoribbons, either by surface-catalysis or from solution synthesis. As demonstrated in this work, bottom-up GNRs are certainly going to have an enormous impact on renewable energy. In particular, it was shown in this work that doped graphene nanoribbons could stabilize a wide variety of ligand-free nanoparticles through π-π^* interactions, as determined by XPS. Depending on the choice of metal nanoparticle, these hybrid GNR-nanoparticle systems were remarkably effective at hydrogen storage, carbon dioxide reduction, and Li-ion battery applications. The development of ROAMP as a tool to create conjugated polymers is a definite advancement for polymer chemistry. The ability to utilize these polymers as precursors to graphene nanoribbons remains an ongoing effort, but would greatly add to the flexibility of bottom-up GNR chemistry. As the synthesis of carbon-based nanomaterials continues to improve, there is a great deal to be optimistic about as these materials find many new and exciting applications in energy and electronics.

Chapter 8
Experimental Section

8.1 Materials and General Methods

Unless otherwise stated, all manipulations of air and/or moisture sensitive compounds were carried out in oven-dried glassware, under an atmosphere of Nitrogen. All solvents and reagents were purchased from Alfa Aesar, Spectrum Chemicals, Acros Organics, TCI America, and Sigma-Aldrich and were used as received unless otherwise noted. Organic solvents were dried by passing through a column of alumina and were degassed by vigorous bubbling of N_2 or Ar through the solvent for 20 min. Flash column chromatography was performed on SiliCycle silica gel (particle size 40–63 μm). Thin layer chromatography was carried out using SiliCycle silica gel 60 Å F-254 precoated plates (0.25 mm thick) and visualized by UV absorption. All ^{1}H and ^{13}C NMR spectra were recorded on Bruker AV-600, DRX-500, and AV-500, AV-400, AVB-400, and AV-300 MHz spectrometers, and are referenced to residual solvent peaks ($CDCl_3$ ^{1}H NMR δ = 7.26 ppm, ^{13}C NMR δ = 77.16 ppm; CD_2Cl_2 ^{1}H NMR δ = 5.32 ppm, ^{13}C NMR δ = 54.00 ppm; [D_8]THF ^{1}H NMR δ = 1.78 ppm, ^{13}C NMR δ = 67.21 ppm; $C_2D_2Cl_4$ ^{1}H NMR δ = 6.0 ppm, ^{13}C NMR δ = 73.78 ppm). ESI mass spectrometry was performed on a Finnigan LTQFT (Thermo) spectrometer in positive ionization mode. MALDI mass spectrometry was performed on a Voyager-DE PRO (Applied Biosystems Voyager System 6322) in positive mode using a matrix of dithranol. Gel permeation chromatography (GPC) was carried out on a LC/MS Agilent 1260 Infinity set up with a guard and two Agilent Polypore 300 X 7.5 mm columns at 35 °C. All GPC analyses were performed on a 0.2 mg/mL solution of polymer in $CHCl_3$. An injection volume of 25 μL and a flow rate of 1 mL/min were used. Calibration was based on narrow polydispersity polystyrene standards ranging from M_w = 100 to 4,068,981. X-ray crystallography was performed on Bruker-AXS APEX II Quazar Single Crystal X-ray Diffractometer, using a Microfocus Sealed Source (Incoatec IμS; Mo-Kα radiation), Kappa Geometry with DX (Bruker-AXS build) goniostat, a Bruker APEX II detector, QUAZAR multilayer mirrors as the radiation monochromator, and Oxford Cryostream 700. All crystallographic data was refined with SHELXL-97, solved with SIR-2007, visualized with ORTEP-32, and finalized with WinGX. AFM was performed on Asylum MFP-3D microscope in AC mode. SEM was performed on FEI Quanta 3D FEG FIB at the Biomolecular Nanotechnology Center at UC Berkeley. STM imaging was performed using a home-built UHV low-temperature STM at 13 K, an Omicron LT-STM at 4.5 K, and an Omicron VT-STM operating at 298 K. A tungsten tip was used for topographic STM measurements. Raman spectroscopy was recorded using a LabRam ARAMIS automated scanning confocal microscope. TGA was measured using a TA Instruments Q5000IR TGA-MS instrument. ICP-OES was performed on a Varian 720 Series instrument. XPS was performed on a PHI 5400 X-ray system. TEM was performed using a JEOL 2100-F 200 kV Field-Emission Analytical Transmission Electron Microscope. Compounds **2–7**, **10–15**, **18–33c**, **35a**, **35c**, **36–40**, **45–52**, **61–66**, **67a–c**, and **73** were synthesized according to literature procedures.

8.2 Synthetic Procedures

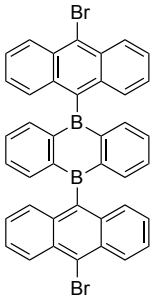

1

5,10-bis(10-bromoanthracen-9-yl)-5,10-dihydroboranthrene (**1**) A 100 mL Schlenk tube was charged with 9,10-dibromoanthracene (**2**) (0.21 g, 0.60 mmol) in dry Et_2O (20 mL) and cooled to −78 °C. *n*BuLi (2.5 M, 0.25 mL, 0.63 mmol) was added and the reaction mixture was stirred at −78 °C for 15 min before warming to 24 °C over 1 h. The reaction mixture was cooled to −78 °C and a solution of **3** (0.10 g, 0.30 mmol) in dry toluene (12.5 mL) was added dropwise at −78 °C and slowly warmed to 24 °C over 18 h. The resulting orange precipitate was filtered and washed with cold Et_2O (10 mL) and MeOH (10 mL). Recrystallization from dry $C_2H_2Cl_4$ yielded **1** (0.14 g, 0.2 mmol, 67%) as an orange solid. M.p.: >350 °C (decomp.); ^{1}H NMR (400 MHz, $C_2D_2Cl_4$, 25 °C) δ = 8.68 (d, J = 8.0 Hz, 4H), 7.72 (d, J = 8.0 Hz, 4H), 7.70–7.64 (m, 4H), 7.45–7.38 (m, 8H), 7.35–7.30 (m, 4H) ppm; ^{13}C{^{1}H} NMR (125 MHz, $C_2D_2Cl_4$, 25 °C) δ = 145.4, 142.5, 140.1, 134.2, 134.1, 130.1, 129.8, 128.1, 127.1, 124.9, 122.7 ppm; ^{11}B NMR (192 MHz, $CDCl_3$, 25 °C) δ = 72.97 ppm; EI-HR-MS (m/z): $[C_{40}H_{24}B_2Br_2]^+$, calcd for $[^{12}C_{40}H_{24}{}^{11}B_2{}^{79}Br^{81}Br]$ 686.0410; found 686.0422.

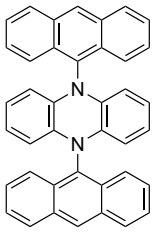

8

5,10-di(anthracen-9-yl)-5,10-dihydrophenazine (**8**) A 100 mL Schlenk flask was charged with 9-bromoanthracene (1.10 g, 4.4 mmol), 5,10-dihydrophenazine (**7**) (0.40 g, 2.2 mmol), and NaO*t*Bu (0.63 g, 6.6 mmol) in dry toluene (10 mL) at 24 °C in a Nitrogen-filled glovebox. $Pd(dba)_2$ (0.20 g, 0.4 mmol) and P(*t*Bu)$_3$ (0.05 g, 0.3 mmol) were mixed in toluene (10 mL) and added to the reaction mixture. After dilution with toluene (10 mL), stirring was continued for 24 h. The mixture was filtered through celite, washed with EtOAc, and concentrated. Recrystallization from EtOAc yielded **8** (0.10 g, 0.2 mmol, 8%) as a brown solid. EI-HR-MS (m/z): $[C_{40}H_{26}N_2]^+$, calcd for $[^{12}C_{40}H_{26}N_2]$ 534.2096; found 534.2086.

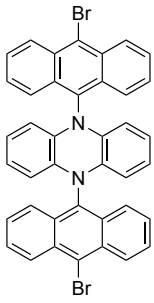

9

5,10-bis(10-bromoanthracen-9-yl)-5,10-dihydrophenazine (**9**) A 100 mL round bottom flask was charged under open atmosphere with **8** (0.01 g, 9.0 μmol) in CH_2Cl_2 (50 mL). A solution of Br_2 (0.3 mL, 5 μl / mL in CH_2Cl_2) was added and stirred for 3 h at 24 °C. The reaction was quenched with H_2O (10 mL), extracted with CH_2Cl_2 (50 mL), dried over $MgSO_4$, and concentrated. Recrystallization from EtOAc yielded **9** (0.01 g, 9.0 μmol, 99%) as a yellow solid. MALDI-HR-MS (m/z): $[C_{40}H_{24}N_2Br_2]^+$, calcd for $[^{12}C_{40}H_{24}N_2{}^{79}Br_2]$ 690.0301; found 690.0096.

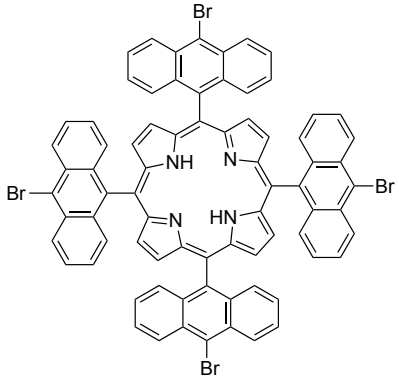

16

5,10,15,20-tetrakis(10-bromoanthracen-9-yl)porphyrin (**16**) A 100 mL Schlenk flask was charged under N_2 with 9,10-dibromoanthracene (**13**) (0.82 g, 2.4 mmol) in Et_2O (12 mL) and cooled to −78 °C. *n*BuLi (2.5 M, 2.4 mmol, 1.0 mL) was added and the reaction mixture was stirred for 30 min before warming to 24 °C. 2-formylpyrrole (**14**) was added and stirred for 1 h. The reaction mixture was carefully transferred under N_2 to a solution of toluene / propionic acid (5:3 mL) at 100 °C and stirring was continued for 3 h. After cooling to 24 °C, the reaction was quenched with TEA (6 mL) and concentrated. Column chromatography (SiO_2; 8:2 CH_2Cl_2 : hexanes) and recrystallization from CH_2Cl_2 / MeOH yielded **16** (0.01 g, 6.0 μmol, 2%) as a purple crystalline solid. ^{1}H NMR (400 MHz, $CDCl_3$, 25 °C) δ = 8.78 (d, J = 9.0 Hz, 8H), 8.10 (s, 8H), 7.55 (dd, J = 7.0, 2.0 Hz, 8H), 7.18 (d, J = 8.0 Hz, 8H), 7.06 (dd, J = 6.0, 2.0 Hz, 8H), −1.75 (s, 2H) ppm; $^{13}C\{^1H\}$ NMR (126 MHz, CD_2Cl_2, 25 °C) δ = 139.0, 136.3, 131.9, 130.3, 129.6, 128.4, 128.2, 127.6, 127.5, 126.9, 126.6 ppm; MALDI-HR-MS (m/z): $[C_{76}H_{42}Br_4N_4]^+$, calcd for $[^{12}C_{76}H_{42}{}^{79}Br_4N_4]$ 1326.0143; found 1325.4969.

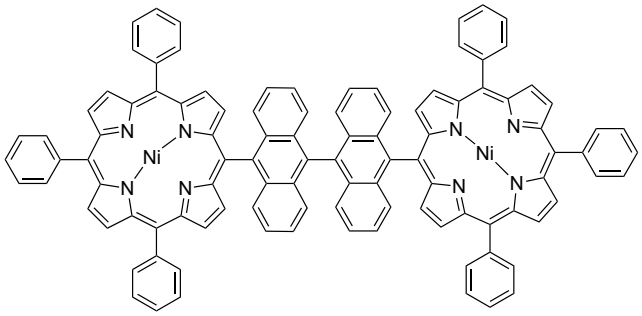

17

Nickel 5-(5-([9,9'-bianthracen]-10-yl)-10,15,20-triphenylporphyrin),10,15,20-tetrakis porphyrin (**17**) A 100 mL sealable Schlenk flask was charged under N_2 with Cs_2CO_3 (0.10 g, 0.3 mmol) in THF (20 mL). Porphyrin **18** (0.08 g, 120 μmol), boronic ester **27** (0.04 g, 60 μmol), $PdCl_2(PPh_3)_2$ (0.01 g, 12 μmol), and Ph_3As (0.01 g, 18 μmol) were added and the tube was sealed. The mixture was stirred for 48 h at 67 °C in the dark. After cooling to 24 °C, the mixture was quenched with H_2O (50 mL), extracted with CH_2Cl_2 (50 mL), dried over $MgSO_4$, and concentrated. Column chromatography (SiO_2; 9:1 CH_2Cl_2/ hexanes) and recrystallization from CH_2Cl_2 / MeOH yielded **17** (0.01 g, 5 μmol, 9%) as a purple crystalline solid. ^{1}H NMR (300 MHz, $CDCl_3$, 25 °C) δ = 8.79 (s, 8H), 8.77 (d, J = 5.0 Hz, 4H), 8.55 (d, *J* = 5.0 Hz, 4H), 8.09–8.06 (m, 12H), 7.74–7.68 (m, 22H), 7.34–7.28 (m, 8H), 7.13–7.08 (m, 4H) ppm; ^{13}C{^{1}H} NMR (126 MHz, $CDCl_3$, 25 °C) δ = 162.8, 158.2, 150.2, 148.8, 148.5, 148.2, 144.3, 144.2, 144.1, 143.1, 140.9, 139.7, 136.6, 134.7, 133.9, 133.2, 132.7, 132.4, 131.2, 129.3, 128.0, 127.9, 127.1, 127.0, 126.0, 126.0, 119.4 ppm; MALDI-HR-MS (m/z): $[C_{104}H_{62}N_8Ni_2]^+$, calcd for $[^{12}C_{104}H_{62}N_8{}^{58}Ni_2]$ 1538.3804; found 1538.2407.

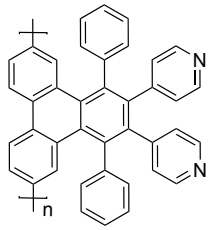

34b

poly(6,11-(4,4'-(1,4-diphenyltriphenylene-2,3-diyl)dipyridine)) (**34b**) A 100 mL sealable Schlenk flask was charged in a nitrogen-filled glovebox with $Ni(COD)_2$ (1.22 g, 3.6 mmol), 2,2'-bipyridine (0.56 g, 3.6 mmol), COD (0.56 g, 3.6 mmol), and DMF (10 mL). The flask was sealed, removed from the glovebox, and the reaction mixture was stirred for 30 min at 60 °C. Monomer **33b** (0.60 g, 0.9 mmol) in toluene (30 mL) was degassed for 30 min and added to the catalyst solution. The reaction mixture was stirred for 72 h at 80 °C. After cooling to 24 °C, the reaction mixture was poured into MeOH / H_2O (150 : 30 mL), and filtered. Washing with HCl (1M aq., 250 mL), H_2O (250 mL), MeOH (100 mL), NaOH (1M aq., 250 mL), H_2O (250 mL), MeOH (100 mL), and hexanes (100 mL) yielded **34b** (0.40 g, 83%) as a yellow solid. ^{1}H NMR (300 MHz, $CDCl_3$, 25 °C) δ = 8.18 (br, 4H), 7.13 (br, 10H), 6.65 (s, 4H) ppm.

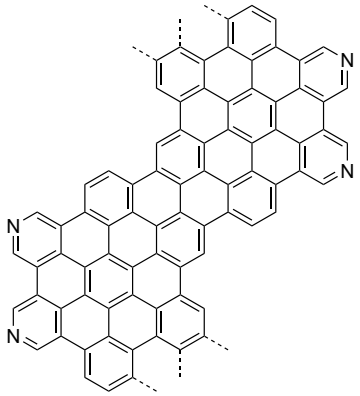

35b

2N-GNR (**35b**) A 1000 mL three-neck round-bottom flask was charged under N_2 with polymer **34b** (0.50 g) in dry CH_2Cl_2 (500 mL). $FeCl_3$ (35.0 g, 216.0 mmol) in CH_3NO_2 (35 mL) was added dropwise while a stream of N_2 was passed through the solution. The reaction mixure was stirred for 72 h at 24 °C, then poured into MeOH (300 mL) and filtered. Washing with MeOH (200 mL), HCl (1M aq., 200 mL), KOH (1M aq., 500 mL), MeOH (100 mL), H_2O (200 mL), MeOH (100 mL), and THF (200 mL) yielded **35b** (0.450 g, 91%) as a black solid.

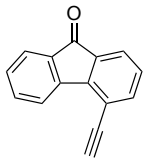

41

4-ethynyl-9*H*-fluoren-9-one (**41**) A 100 mL Schlenk flask was charged under N_2 with aldehyde **40** (0.47 g, 2.2 mmol) in THF (50 mL). Dimethyl (1-diazo-2-oxopropyl)phosphonate (10% in CH_3CN, 4.2 mL, 0.42 g, 2.2 mmol), K_2CO_3 (0.41 g, 3.0 mmol), and MeOH (10 mL) were added and stirred for 14 h at 24 °C. The reaction mixture was quenched with H_2O (50 mL) and extracted with EtOAc (50 mL, 3x). The combined organic phases were dried over $MgSO_4$ and concentrated on a rotary evaporator. Recrystallization from EtOAc yielded **41** (0.46 g, 2.2 mmol, 99%) as a yellow solid. ^{1}H NMR (400 MHz, $CDCl_3$, 25 °C) δ = 8.31 (d, *J* = 7.6 Hz, 1H), 7.70–7.65 (m, 2H), 7.58–7.53 (m, 2H), 7.34 (t, J = 12.0 Hz, 1H), 7.27 (d, J = 16 Hz, 1H), 3.50 (s, 1H) ppm; $^{13}C\{^1H\}$ NMR (151 MHz, $CDCl_3$, 25 °C) δ = 192.9, 144.7, 143.9, 139.1, 134.9, 134.4, 134.0, 129.5, 128.7, 124.5, 124.2, 123.1, 116.2, 83.0, 81.2 ppm; EI-HR-MS (m/z): $[C_{15}H_8O]^+$, calcd for $[^{12}C_{15}H_8O]$ 204.0575; found 204.0576.

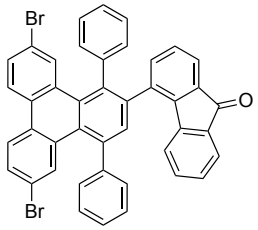

42

4-(6,11-dibromo-1,4-diphenyltriphenylen-2-yl)-9*H*-fluoren-9-one (**42**) A 25 mL sealable Schlenk flask was charged under N_2 with alkyne **41** (0.11 g, 0.5 mmol) and **31** (0.30 g, 0.5 mmol) in *o*-xylene (1.5 mL). The flask was sealed and the reaction mixture stirred for 16 h at 160 °C. After cooling to 24 °C, the mixture was dissolved in a minimal amount of CH_2Cl_2 and precipitated with MeOH. The product was further purified by trituration with cold CH_2Cl_2 to yield **42** (0.31 g, 0.4 mmol, 76%) as a yellow solid. ^{1}H NMR (400 MHz, CD_2Cl_2, 25 °C) δ = 8.31 (d, *J* = 2.0 Hz, 1H), 8.30 (d, J = 2.0 Hz, 1H), 7.87 (d, *J* = 2.0 Hz, 1H), 7.70 (d, *J* = 2.0 Hz, 1H), 7.69 (s, 1H), 7.62–7.45 (m, 8H), 7.24–7.10 (m, 7H), 7.06–7.04 (m, 2H), 6.69 (d, *J* = 7.4 Hz, 1H) ppm; ^{13}C{^{1}H} NMR (126 MHz, CD_2Cl_2, 25 °C) δ = 193.9, 144.9, 143.7, 142.3, 141.1, 139.9, 139.0, 138.0, 137.8, 137.7, 137.3, 135.1, 134.8, 134.8, 133.2, 133.2, 132.7, 132.6, 132.0, 131.9, 131.5, 130.9, 130.6, 130.6, 130.4, 130.3, 130.2, 130.0, 123.0, 129.8, 129.2, 129.2, 129.1, 129.1, 128.7, 128.3, 127.9, 125.3, 125.3, 124.3, 123.5, 123.2, 120.5 ppm; EI-HR-MS (m/z): [$C_{43}H_{24}OBr_2$], calcd for [$^{12}C_{43}H_{24}O^{79}Br_2$] 714.0194; found 714.0186.

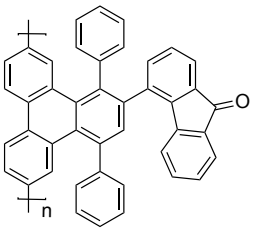

43

poly(6,11-(1,4-diphenyltriphenylen-2-yl)-9*H*-fluoren-9-one) (**43**) A 100 mL sealable Schlenk flask was charged in a Nitrogen-filled glovebox with $Ni(COD)_2$ (0.32 g, 1.2 mmol), 2,2'-bipyridine (0.20 g, 1.2 mmol), COD (0.13 g, 1.2 mmol), and DMF (6 mL). The flask was sealed, removed from the glovebox, and the reaction mixture stirred for 30 min at 60 °C. Monomer **42** (0.20 g, 0.3 mmol) in toluene (20 mL) was degassed for 30 min and added to the catalyst solution. The reaction mixture was heated for 72 h at 80 °C. After cooling to 24 °C, the mixture was poured into MeOH / H_2O (50 : 10 mL), and filtered. Washing with HCl (1M aq., 250 mL), H_2O (250 mL), MeOH (100 mL), NaOH (1M aq., 250 mL), H_2O (250 mL), MeOH (100 mL), and hexanes (100 mL) yielded **43** (0.14 g, 87%) as a yellow solid. ^{1}H NMR (600 MHz, $CDCl_3$, 25 °C) δ = 8.15 (br, 4H), 7.49 (br, 6H), 7.19 (br, 4H), 7.05 (br, 6H), 6.63 (br, 4H) ppm.

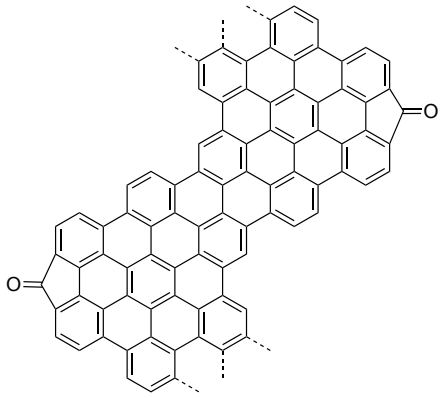

44

CO-GNR (**44**) A 500 mL three-neck round-bottom flask was charged under N_2 with polymer **43** (0.12 g) in dry CH_2Cl_2 (250 mL). $FeCl_3$ (9.0 g, 55.2 mmol) in CH_3NO_2 (9 mL) was added dropwise while a stream of N_2 was passed through the solution. The reaction mixure was stirred for 48 h at 24 °C, then poured into MeOH (300 mL) and filtered. Washing with MeOH (200 mL), HCl (1M aq., 200 mL), KOH (1M aq., 500 mL), MeOH (100 mL), H_2O (200 mL), MeOH (100 mL), and THF (200 mL) yielded **44** (0.12 g, 99%) as a dark red solid.

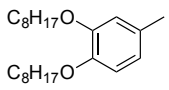

53a

4-methyl-1,2-bis(octyloxy)benzene (**53a**) A 500 mL Schlenk flask was charged under N_2 with 4-methylbenzene-1,2-diol (10.0 g, 80.6 mmol) in dry DMF (50 mL). 1-Bromooctane (40.0 g, 207.0 mmol) and K_2CO_3 (38.0 g, 275.0 mmol) were added and the reaction mixture stirred for 48 h at 100 °C. The solution was cooled to 24 °C, basified to pH 12 with NaOH, extracted with CH_2Cl_2 (100 mL) and the organic layer was washed with H_2O (50 mL) and NaCl (sat. aq., 50 mL), dried over $MgSO_4$ and concentrated under reduced pressure. Column chromatography (SiO_2; hexanes) yielded **53a** (20.2 g, 58.0 mmol, 72%) as a colorless oil. ^{1}H NMR (500 MHz, $CDCl_3$, 25 °C) δ = 6.80 (d, J = 8.0 Hz, 1H), 6.73 (s, 1H), 6.69 (d, J = 8.0 Hz 1H), 4.00–3.96 (m, 4H), 2.30 (s, 3H), 1.86–1.78 (m, 4H), 1.52–1.45 (m, 4H), 1.41–1.26 (m, 16H), 0.92–0.90 (m, 6H) ppm; ^{13}C{^{1}H} NMR (126 MHz, $CDCl_3$, 25 °C) δ =149.2, 147.1, 130.8, 121.2, 115.2, 114.5, 77.4, 77.2, 76.9, 69.8, 69.3, 32.0, 31.9, 29.6, 29.5, 29.5, 29.4, 26.2, 22.8, 21.1, 14.2 ppm; ESI-HR-MS (m/z): $[C_{23}H_{40}O_2Na]^+$, calcd for $[^{12}C_{23}H_{40}O_2{}^{23}Na]$ 371.2921; found 371.2919.

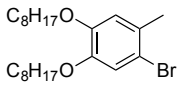

54a

1-bromo-2-methyl-4,5-bis(octyloxy)benzene (**54a**) A 250 mL round bottom flask was charged with **53a** (10.35 g, 32.5 mmol) in DMF (35 mL). NBS (5.75 g, 32.5 mmol) in DMF (25 mL) was added dropwise at 24 °C open to the air and stirred for 1 h after addition. The organic layer was extracted with EtOAc (100 mL), washed with H_2O (100 mL) and NaCl (sat. aq., 50 mL), dried over $MgSO_4$, and concentrated on a rotary evaporator. Column chromatography (SiO_2; hexanes) yielded **54a** (12.0 g, 28.1 mmol, 95%) as a white solid. ^{1}H NMR (600 MHz, $CDCl_3$, 25 °C) δ = 7.01 (s, 1H), 6.74 (s, 1H), 3.94–3.93 (m, 4H), 2.30 (s, 3H), 1.83–1.75 (m, 4H), 1.49–1.42 (m, 4H), 1.39–1.25 (m, 16H), 0.93–0.88 (m, 6H) ppm; ^{13}C{^{1}H} NMR (151 MHz, $CDCl_3$, 25 °C) δ = 148.5, 148.1, 129.9, 118.1, 116.5, 114.8, 69.8, 69.7, 65.9, 31.9, 29.5, 29.4, 29.4, 26.1, 22.8, 22.4, 15.4, 14.2 ppm; EI-HR-MS (m/z): $[C_{23}H_{39}O_2Br]^+$, calcd for $[^{12}C_{23}H_{39}O_2{}^{79}Br]$ 426.2133; found 426.2141.

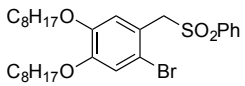

56a

1-bromo-4,5-bis(octyloxy)-2-((phenylsulfonyl)methyl)benzene (**56a**) A 250 mL round bottom flask was charged under N_2 with **54a** (8.52 g, 20.0 mmol) in CCl_4 (40 mL). NBS (3.92 g, 22.0 mmol) and AIBN (0.48 g, 2.9 mmol) were added and the reaction mixture stirred for 3 h at 78 °C. The solution was cooled to 24 °C, filtered, washed with CCl_4 (10 mL), and the filtrate was concentrated under reduced pressure. The solid obtained was recrystallized with hexanes and used without further purification. An oven dried 250 mL round bottom flask was charged under N_2 with the solid obtained previously in DMF (30 mL). Benzenesulfinic acid sodium salt (3.94 g, 24.0 mmol) was added and the reaction mixture was stirred for 3 h at 80 °C. After cooling to 24 °C, H_2O (100 mL) and EtOAc (100 mL) were added and the organic layer was washed with H_2O (50 mL) and NaCl (sat. aq., 50 mL), dried over $MgSO_4$, and concentrated on a rotary evaporator. Recrystallization from EtOAc / hexanes yielded **56a** (5.9 g, 10.4 mmol, 52%) as a white solid. ^{1}H NMR (500 MHz, $CDCl_3$, 25 °C) δ = 7.65–7.59 (m, 3H), 7.44 (t, J = 8.5 Hz, 2H), 6.93 (s, 1H), 6.85 (s, 1H), 4.47 (s, 2H), 3.94–3.91 (m, 4H), 1.83–1.77 (m, 5H), 1.47–1.42 (m, 5H), 1.39–1.28 (m, 22H), 0.90–0.87 (m, 8H) ppm; ^{13}C{^{1}H} NMR (126 MHz, $CDCl_3$, 25 °C) δ = 150.2, 148.5, 138.2, 133.8, 129.0, 128.9, 119.9, 117.0, 116.7, 116.4, 69.5, 61.6, 31.9, 31.9, 31.7, 29.5, 29.4, 29.3, 29.3, 29.2, 29.2, 29.1, 26.1, 26.0, 22.8, 22.8, 14.2 ppm; ESI-HR-MS (m/z): $[C_{29}H_{43}O_4BrNaS]^+$, calcd for $[^{12}C_{29}H_{43}O_4{}^{79}Br^{23}Na^{32}S]$ 589.1958; found 589.1967.

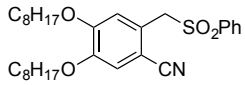

57a

4,5-bis(octyloxy)-2-((phenylsulfonyl)methyl)benzonitrile (**57a**) A 250 mL Schlenk flask was charged under N_2 with **56a** (3.51 g, 6.2 mmol) in NMP (50 mL). CuCN (2.8 g, 31.0 mmol) was added and the reaction mixture stirred for 16 h at 200 °C. After cooling to 24 °C, NH_4OH (120 mL, 30% aq.) was added and stirred for 3 h, filtered, and the filtered solid was washed with H_2O (100 mL). Column Chromatography (SiO_2; DCM) yielded **57a** (0.94 g, 1.8 mmol, 30%) as a white solid. ^{1}H NMR (500 MHz, $CDCl_3$, 25 °C) δ = 7.70 (d, J = 7.5 Hz, 2H), 7.64 (t, J = 7.5 Hz, 1H), 7.49 (t, J = 8.0 Hz, 2H), 7.00 (s, 1H), 6.87 (s, 1H), 4.47 (s, 2H), 4.03 (d, J = 6.5 Hz, 2H), 3.94 (d, J = 6.5 Hz 2H), 1.87–1.78 (m, 4H), 1.50–1.41 (m, 4H), 1.39–1.28 (m, 16H), 0.89–0.87 (m, 6H) ppm; ^{13}C{^{1}H} NMR (126 MHz, $CDCl_3$, 25 °C) δ = 152.8, 149.4, 137.5, 134.3, 129.3, 128.8, 125.4, 117.2, 115.4, 115.2, 105.4, 77.4, 77.4, 77.2, 76.9, 69.5, 69.4, 60.4, 31.9, 29.4, 29.4, 29.3, 29.0, 28.9, 26.0, 22.8, 14.2 ppm; ESI-HR-MS (m/z): $[C_{30}H_{43}O_4NNaS]^+$, calcd for $[^{12}C_{30}H_{43}O_4N^{23}Na^{32}S]$ 536.2805; found 536.2814.

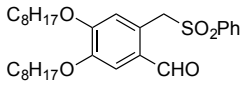

58a

4,5-bis(octyloxy)-2-((phenylsulfonyl)methyl)benzaldehyde (**58a**) A 100 mL Schlenk flask was charged under N_2 with **57a** (0.86 g, 1.7 mmol,) in THF (20 mL) and cooled to 0 °C. DIBAL (1.0 M in heptanes, 4.5 mL, 4.5 mmol) was added dropwise. The ice bath was removed and the reaction stirred for 2 h at 24 °C. After cautiously quenching with HCl (1% aq., 50 mL), the solution was stirred for 30 min, extracted with EtOAc (100 mL), dried over $MgSO_4$, and concentrated on a rotary evaporator. Column chromatography (SiO_2; CH_2Cl_2) yielded **58a** (0.42 g, 0.8 mmol, 48%) as a yellow solid. ^{1}H NMR (500 MHz, $CDCl_3$, 25 °C) δ = 9.66 (s, 1H), 7.67 (d, J = 7.0 Hz, 2H), 7.59 (t, J = 7.5 Hz, 1H), 7.45 (t, J = 7.5 Hz, 2H), 7.19 (s, 1H), 6.80 (s, 1H), 4.90 (s, 2H), 4.05–3.99 (m, 4H), 1.86–1.81 (m, 4H), 1.50–1.44 (m, 4H), 1.38–1.26 (m, 16H), 0.91–0.87 (m, 6H) ppm; ^{13}C{^{1}H} NMR (126 MHz, $CDCl_3$, 25 °C) δ = 189.9, 153.4, 149.4, 138.1, 134.0, 129.0, 128.9, 127.8, 123.5, 116.9, 116.5, 69.5, 57.5, 32.0, 29.5, 29.5, 29.4, 29.2, 29.1, 26.1, 26.1, 22.9, 14.3 ppm; ESI-HR-MS (m/z): $[C_{30}H_{45}O_5S]^+$, calcd for $[^{12}C_{30}H_{45}O_5{}^{32}S]$ 517.2982; found 517.2994.

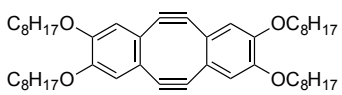

60a

2,3,14,15-tetra(octyloxy)-5,6,11,12-tetradehydrodibenzo[a,e]cyclooctene (**60a**) A 250 mL round bottom flask was charged under N_2 with **58a** (0.42 g, 0.8 mmol) in dry THF (24 mL) and cooled to −78 °C. Diethyl chlorophosphate (0.14 mL, 1.0 mmol) and LiHMDS (1.0 M in THF, 1.6 mL, 1.6 mmol) were added and the solution stirred for 30 min at −78 °C, then for 1.5 h at 24 °C.

After cooling to −78 °C, LDA (2.0M in THF, 4.0 mmol, 2.0 mL) was added and stirred for 2 h. The reaction mixture was quenched with NH_4Cl (aq., 50 mL), extracted with EtOAc (100 mL), dried over $MgSO_4$, and concentrated on a rotary evaporator. Column chromatography (SiO_2; 2:3 CH_2Cl_2 : hexanes) yielded **60a** (0.10 g, 0.1 mmol, 32%) as a yellow solid. ^{1}H NMR (500 MHz, $CDCl_3$, 25 °C) δ = 6.24 (s, 4H), 3.85 (t, *J* = 7.0 Hz, 8H), 1.76–1.70 (m, 8H), 1.43–1.37 (m, 8H), 1.33–1.27 (m, 32H), 0.89–0.86 (m, 12H) ppm; $^{13}C\{^1H\}$ NMR (126 MHz, $CDCl_3$, 25 °C) δ = 149.0, 126.0, 113.6, 108.7, 77.4, 77.2, 76.9, 69.5, 31.9, 29.5, 29.4, 29.3, 26.1, 22.8, 14.2 ppm; ESI-HR-MS (m/z): $[C_{48}H_{72}O_4]^+$, calcd for $[^{12}C_{48}H_{72}O_4]$ 712.5425; found 712.5436.

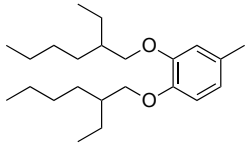

53b

1,2-bis((2-ethyloctyl)oxy)-4-methylbenzene (**53b**) Synthesized according in a similar manner as compound **53a**. 4-methylbenzene-1,2-diol (10.0 g, 80.6 mmol) yielded 6.34 g of **53b** (6.34g, 18.2 mmol, 35%) as a colorless oil. ^{1}H NMR (600 MHz, $CDCl_3$, 25 °C) δ = 6.80 (d, J = 7.8 Hz, 1H), 6.73 (s, 1H), 6.69 (d, J = 8.4 Hz, 1H), 3.87–3.84 (m, 4H), 2.31 (s, 3H), 1.80–1.77 (m, 2H), 1.59–1.30 (m, 16H), 0.98–0.91 (m, 12H) ppm; $^{13}C\{^1H\}$ NMR (126 MHz, $CDCl_3$, 25 °C) δ = 149.6, 147.4, 130.6, 121.0, 114.9, 114.9, 114.3, 114.3, 77.4, 77.2, 76.9, 72.1, 71.6, 39.8, 39.7, 31.7, 30.7, 29.3, 24.0, 24.0, 24.0, 23.2, 22.8, 21.1, 14.3, 11.3 ppm; EI-HR-MS (m/z): $[C_{23}H_{40}O_2]^+$, calcd for $[^{12}C_{23}H_{40}O_2]$ 348.3028; found 348.3032.

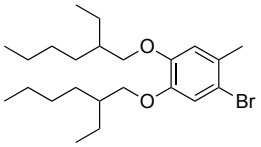

54b

1-bromo-4,5-bis((2-ethyloctyl)oxy)-2-methylbenzene (**54b**) Synthesized in a similar manner as compound **54a**. **53b** (6.28 g, 18.0 mmol) yielded **54b** (7.32 g, 17.2 mmol, 95%) as a brown oil. ^{1}H NMR (600 MHz, $CDCl_3$, 25 °C) δ = 7.01 (s, 1H), 6.74 (s, 1H), 3.85–3.81 (m, 4H), 2.30 (s, 3H), 1.76–1.72 (m, 2H), 1.54–1.28 (m, 16H), 0.94–0.90 (m, 12H) ppm; $^{13}C\{^1H\}$ NMR (151 MHz, $CDCl_3$, 25 °C) δ = 148.9, 129.7, 117.7, 116.1, 114.6, 77.4, 77.2, 76.9, 72.1, 72.0, 60.5, 39.7, 39.7, 30.7, 29.2, 29.2, 24.0, 24.0, 23.2, 22.4, 14.3, 14.2, 11.3 ppm; EI-HR-MS (m/z): $[C_{23}H_{39}O_2Br]^+$, calcd for $[^{12}C_{23}H_{39}O_2{}^{79}Br]$ 426.2133; found 426.2134.

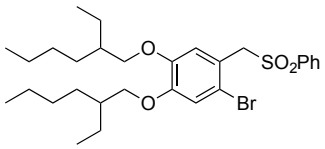

56b

1-bromo-4,5-bis((2-ethyloctyl)oxy)-2-((phenylsulfonyl)methyl)benzene (**56b**) Synthesized in a similar manner as compound **56a**. **54b** (7.32 g, 17.2 mmol) yielded **56b** (3.59 g, 6.4 mmol, 37%) as a yellow oil. ^{1}H NMR (500 MHz, $CDCl_3$, 25 °C) δ = 7.66 (dd, J = 7.5, 1.0 Hz, 2H), 7.60 (t, J = 8.0 Hz, 1H), 7.45 (t, J = 8.0 Hz, 2H), 6.87 (s, 1H), 6.85 (s, 1H), 4.47 (s, 2H), 3.80–3.76 (m, 4H), 1.76–1.71 (m, 2H), 1.52–1.26 (m, 16H), 0.96–0.85 (m, 12H) ppm; ^{13}C{^{1}H} NMR (126 MHz, $CDCl_3$, 25 °C) δ = 150.5, 148.8, 138.2, 133.9, 129.0, 129.0, 119.6, 116.7, 116.3, 116.2, 77.4, 77.2, 76.9, 71.8, 71.7, 61.6, 39.6, 39.5, 31.7, 31.7, 30.7, 30.7, 30.6, 30.6, 29.2, 29.2, 24.0, 24.0, 24.0, 23.2, 23.1, 22.8, 14.2, 14.2, 14.2, 11.3, 11.3 ppm; ESI-HR-MS (m/z): $[C_{29}H_{42}O_4BrS]^-$, calcd for $[^{12}C_{29}H_{42}O_4{}^{79}Br^{32}S]$ 565.1993; found 565.1994.

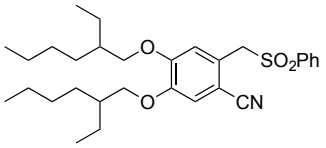

57b

4,5-bis((2-ethyloctyl)oxy)-2-((phenylsulfonyl)methyl)benzonitrile (**57b**) Synthesized in a similar manner as compound **57a**. **56b** (3.59 g, 6.3 mmol) yielded **57b** (1.91 g, 3.7 mmol, 59%) as a white solid. ^{1}H NMR (500 MHz, $CDCl_3$, 25 °C) δ = 7.72 (dd, J = 7.0,1.5 Hz, 2H), 7.64 (t, J = 7.5 Hz, 1H), 7.50 (t, J = 7.5 Hz, 2H), 6.96 (s, 1H), 6.88 (s, 1H), 4.47 (s, 2H), 3.90–3.85 (m, 2H), 3.84–3.78 (m, 2H), 1.80–1.72 (m, 2H), 1.54–1.29 (m, 16H), 0.95–0.88 (m, 12H) ppm; ^{13}C{^{1}H} NMR (126 MHz, $CDCl_3$, 25 °C) δ = 153.1, 149.7, 137.6, 134.2, 129.3, 128.9, 125.2, 117.3, 115.1, 115.0, 105.3, 77.4, 77.2, 76.9, 71.8, 71.7, 60.4, 39.4, 39.4, 30.6, 30.6, 29.2, 29.1, 24.0, 23.9, 23.9, 23.1, 23.1, 14.8, 11.3, 11.3 ppm; ESI-HR-MS (m/z): $[C_{30}H_{42}O_4NS]^-$, calcd for $[^{12}C_{30}H_{42}O_4N^{32}S]$ 512.2840; found 512.2839.

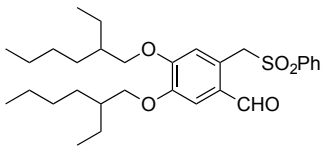

58b

4,5-bis((2-ethyloctyl)oxy)-2-((phenylsulfonyl)methyl)benzaldehyde (**58b**) Synthesized in a similar manner as compound **58a**. **57b** (0.96 g, 1.9 mmol) yielded **58b** (0.62 g, 1.2 mmol, 63%) as a colorless solid. ^{1}H NMR (400 MHz, $CDCl_3$, 25 °C) δ = 9.69 (s, 1H), 7.69 (d, J = 7.6 Hz, 2H), 7.60 (t, J = 7.6 Hz, 1H), 7.46 (t, J = 7.6 Hz, 2H), 7.19 (s, 1H), 6.75 (s, 1H), 4.89 (s, 2H), 3.94–3.88 (m, 2H), 3.87–3.81 (m, 2H), 1.80–1.74 (m, 2H), 1.54–1.30 (m, 16H), 0.96–0.91 (m,

12H) ppm; $^{13}C\{^{1}H\}$ NMR (126 MHz, $CDCl_3$, 25 °C) δ = 189.9, 153.6, 149.7, 138.1, 133.9, 129.0, 128.9, 127.7, 123.3, 116.6, 115.9, 77.4, 77.2, 76.9, 71.7, 71.7, 71.6, 71.6, 57.5, 39.5, 39.4, 30.7, 30.6, 30.6, 30.6, 29.2, 29.2, 24.0, 24.0, 24.0, 23.1, 14.2, 11.3 ppm; ESI-HR-MS (m/z): $[C_{30}H_{44}O_5NaS]^+$, calcd for $[^{12}C_{30}H_{44}O_5{}^{23}Na^{32}S]$ 539.2802; found 539.2804.

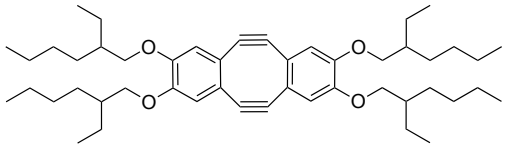

60b

2,3,14,15-tetra((2-ethylhexyl)oxy)-5,6,11,12-tetradehydrodibenzo[a,e]cyclooctene (**60b**) Synthesized in a similar manner as compound **60a**. **58b** (0.52 g, 1.0 mmol) yielded **60b** (0.14 g, 0.15 mmol, 38%) as a yellow oil. ^{1}H NMR (600 MHz, $CDCl_3$, 25 °C) δ = 6.24 (s, 4H), 3.72 (t, J = 15.0 Hz, 8H), 1.68–1.66 (m, 4H), 1.46–1.29 (m, 32H), 0.90–0.88 (m, 24H) ppm; $^{13}C\{^{1}H\}$ NMR (151 MHz, $CDCl_3$, 25 °C) δ = 149.4, 125.9, 113.5, 108.7, 77.4, 77.2, 76.9, 71.8, 39.6, 30.6, 30.6, 29.2, 24.0, 24.0, 23.2, 14.2, 11.3 ppm; EI-HR-MS (m/z): $[C_{64}H_{43}N_8]^+$, calcd for $[^{12}C_{64}H_{43}N_8]$ 923.3611; found 923.3635.

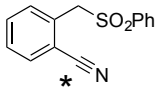

71

2-((phenylsulfonyl)methyl)benzonitrile (**71**) A 50 mL Schlenk flask was charged under N_2 with **70** (1.00 g, 3.20 mmol), and $Cu^{13}CN$ (0.29 g, 3.20 mmol) in NMP (6 mL). The reaction mixture was stirred for 11 h at 210 °C. The reaction mixture was cooled and diluted with H_2O (50 mL) and EtOAc (50 mL), and filtered. The solid was washed with additional H_2O (50 mL) and EtOAc (50 mL). The filtrate was extracted with EtOAc (3x, 50 mL) and the combined organic phases were washed with saturated aqueous NaCl (3x, 100 mL), dried over $MgSO_4$, and concentrated on a rotary evaporator. Column chromatography (SiO_2; CH_2Cl_2 (100 mL) then 1:1 hexane/ EtOAc) yielded **71** (0.68 g, 2.64 mmol, 83%) as a colorless solid. ^{1}H NMR (400 MHz, $CDCl_3$, 25 °C) δ = 7.72–7.63 (m, 5H), 7.57–7.44 (m, 4H), 4.57 (s, 2H) ppm; $^{13}C\{^{1}H\}$ NMR (151 MHz, $CDCl_3$, 25 °C) δ = 137.7, 134.4, 133.1, 132.9, 132.4, 132.3, 131.8, 129.6, 129.4, 128.9, 116.7, 60.6 ppm; ESI-HR-MS (m/z): $[^{12}C_{13}{}^{13}C_1H_{11}NO_2NaS]^+$ calcd for $[^{12}C_{13}{}^{13}C_1H_{11}NO_2{}^{23}Na^{32}S]$ 281.0436; found 281.0438.

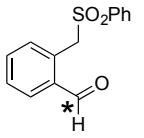

72

2-((phenylsulfonyl)methyl)benzaldehyde (**72**) A 100 mL Schlenk flask was charged under N_2 with **71** (0.60 g, 2.30 mmol) in THF (20 mL). The reaction mixture cooled to −78 °C and DIBAL (5.80 mL in hexanes, 5.80 mmol) was added dropwise. The cold bath was removed and the reaction mixture was stirred for 2.5 h at 24 °C. The reaction mixture was cooled to 0 °C and quenched with 6:1 NH_4Cl (sat. aq.) and HCl (6M, aq.) (50 mL). The quenched mixture was stirred for 1 h at 24 °C then diluted with H_2O (50 mL) and extracted with EtOAc (3x, 50 mL). The combined organic phases were washed with saturated aqueous NaCl (200 mL), dried over $MgSO_4$, and concentrated on a rotary evaporator. Column chromatography (SiO_2; CH_2Cl_2) and recrystallization with EtOAc yielded **3** (0.25 g, 0.96 mmol, 42%) as a white solid. ^{1}H NMR (300 MHz, $CDCl_3$, 25 °C) δ = 9.82 (d, J = 177 Hz, 1H), 7.76–7.67 (m, 3H), 7.63–7.58 (m, 3H), 7.48–7.43 (m, 3H), 5.04 (s, 2H) ppm; $^{13}C\{^1H\}$ NMR (151 MHz, $CDCl_3$, 25 °C) δ = 192.1, 138.3, 134.8, 134.5, 134.4, 134.4, 133.9, 133.6, 129.5, 128.9, 128.7, 57.7 ppm; ESI-HR-MS (m/z): $[^{12}C_{13}{}^{13}C_1H_{12}O_3NaS]^+$, calcd for $[^{12}C_{13}{}^{13}C_1H_{12}O_3{}^{23}Na{}^{32}S]$ 284.0433; found 284.0436.

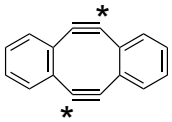

***51**

5,6,11,12-tetradehydrodibenzo[a,e]cyclooctene (***51**) An oven dried 250 mL round bottom flask was charged under N_2 with **72** (0.26 g, 1.0 mmol) in dry THF (30 mL) and cooled to −78 °C. Diethyl chlorophosphate (0.17 mL, 1.2 mmol) and LiHMDS (1.0 M in THF, 2.0 mL, 2.0 mmol) were added and the solution was stirred for 30 min, then for 1.5 h at 24 °C. After cooling to −78 °C, LDA (2.0M in THF, 2.5 mL, 5.0 mmol) was added and stirred for 2 h. The reaction was quenched with NH_4Cl (aq., 50 mL), extracted with EtOAc (3x, 50 mL), dried over $MgSO_4$, concentrated under reduced pressure. Column chromatography (SiO_2, 2:3 CH_2Cl_2 : hexanes) yielded ***51** (55 mg, 0.3 mmol, 56%) as a yellow solid. ^{1}H NMR (400 MHz, $CDCl_3$, 25 °C) δ = 6.95–6.91 (m, 4H), 6.75–6.72 (m, 4H) ppm; $^{13}C\{^1H\}$ NMR (101 MHz, $CDCl_3$, 25 °C) δ = 133.1, 129.2, 127.5, 109.5 ppm; EI-HR-MS (m/z): $[^{12}C_{14}{}^{13}C_2H_8]^+$, calcd for $[^{12}C_{14}{}^{13}C_2H_8]$ 202.0693; found 202.0698.

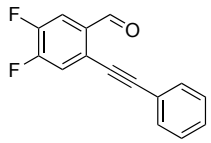

74

4,5-difluoro-2-(phenylethynyl)benzaldehyde (**74**) A 250 mL Schlenk flask was charged under N_2 with **86** ([3.66 g, 16.80 mmol]), $PdCl_2(PPh_3)_2$ (0.23 g, 0.40 mmol, 2 mol%), CuI (0.04 g, 0.20 mmol), and TEA (100 mL). The reaction mixture was degassed with N_2 for 10 min, then phenylacetylene (2.70 mL, 24.80 mmol) was added dropwise and the reaction mixture was stirred for 12 h at 50 °C. The cooled reaction mixture was diluted with H_2O (100 mL) and extracted with CH_2Cl_2 (3x, 50 mL). The combined organic phases were washed with saturated aqueous NaCl (200 mL), dried over $MgSO_4$, and concentrated on a rotary evaporator. Column chromatography (SiO_2; 9:1 hexane: EtOAc) yielded **6** (3.37 g, 14.0 mmol, 84%) as a beige solid. ^{1}H NMR (300 MHz, $CDCl_3$, 25 °C) δ = 10.52 (d, J = 3.2 Hz ,1H) 7.76 (dd, *J* = 10.1, 8.2 Hz, 1H), 7.57–7.54 (m, 2H), 7.48–7.38 (m, 4H) ppm; ^{13}C{^{1}H} NMR (126 MHz, $CDCl_3$, 25 °C) δ = 189.2, 164.6, 153.6 (d, J = 261 Hz), 150.80 (d, J = 245.2 Hz), 133.5, 132.0, 129.7, 128.8, 124.3, 121.9 (d, J = 24.0 Hz), 116.3 (d, J = 18.3 Hz), 97.1, 82.8 ppm; ^{19}F NMR (400 MHz, $CDCl_3$, 25 °C) δ = −126.0 – −126.3 (m, 1F), −132.2 – −132.5 (m, 1F) ppm; EI-HR-MS (m/z): $[C_{15}H_8OF_2]^+$, calcd for $[^{12}C_{15}H_8OF_2]$ 242.0543; found 242.0544.

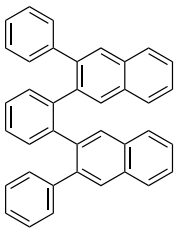

96

1,2-bis(3-phenylnaphthalen-2-yl)benzene (**96**) A 25 mL sealable Schlenk tube was charged under N_2 with **95** ([0.06 g, 0.20 mmol]), dry $C_2H_2Cl_2$ (3 mL), **73** (0.20 mg, 1.0 mmol), $Cu(OTf)_2$ (0.04 g, 0.12 mmol), and TFA (0.19 mL, 2.5 mmol). The tube was sealed and the reaction mixture stirred for 3 h at 100 °C. The cooled reaction mixture was neutralized with $NaHCO_3$ (sat. aq., 50 mL) and extracted with CH_2Cl_2 (3x, 50 mL). The combined organic phases were washed with $NaHCO_3$ (sat. aq., 100 mL), NaCl (sat. aq., 100 mL), dried over $MgSO_4$, and concentrated on a rotary evaporator. Column chromatography (SiO_2; 9:1 hexane: EtOAc) yielded **96** (0.11 g, 0.20 mmol, 99%) as a colorless solid. ^{1}H NMR (400 MHz, $CDCl_3$, 22 °C) δ = 7.69–7.67 (m, 2H), 7.49–7.36 (m, 12H), 7.15 (t, J = 7.4 Hz, 2H), 6.91 (t, J = 7.5 Hz, 4H), 6.48–6.46 (m, 6H) ppm; ^{13}C{^{1}H } NMR (151 MHz, $CDCl_3$, 22 °C) δ = 141.4, 141.2, 139.0, 138.3, 132.6, 132.5, 131.9, 131.0, 129.3, 128.5, 128.0, 127.7, 127.6, 127.5, 126.1, 125.8, 125.4 ppm; EI-HR-MS (m/z): $[C_{38}H_{26}]^+$, calcd for $[^{12}C_{38}H_{26}]$ 482.2035; found 482.2043.

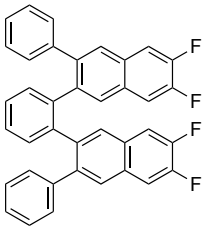

97

1,2-bis(6,7-difluoro-3-phenylnaphthalen-2-yl)benzene (**97**) Similarly, **95** ([0.06 g, 0.20 mmol]), dry $C_2H_2Cl_2$ (3 mL), **74** (0.24 mg, 1.0 mmol), $Cu(OTf)_2$ (0.04 g, 0.12 mmol), and TFA (0.19 mL, 2.5 mmol) yielded **97** (0.10 g, 0.18 mmol, 92%) as a yellow solid. ^{1}H NMR (400 MHz, $CDCl_3$, 25 °C) δ = 7.50 (dd, J = 5.6, 3.4 Hz, 2H), 7.40 (dd, J = 10.9, 7.9 Hz, 2H), 7.33 (dd, J = 5.6, 3.4 Hz, 2H), 7.28 (s, 2H), 7.19–7.11 (m, 4H), 6.92 (t, J = 7.6 Hz, 4H), 6.43 (d, J = 7.6 Hz, 4H), 6.35 (s, 2H) ppm; ^{13}C{^{1}H } NMR (151 MHz, $CDCl_3$, 25 °C) δ = 150.9, 149.2, 140.7, 140.5, 139.2, 138.6, 131.9, 130.3, 129.3, 129.2, 129.1, 128.1, 127.7, 127.2, 126.5, 113.9, 113.1 ppm; ^{19}F NMR (400 MHz, $CDCl_3$, 25 °C) δ = −136.3 – −136.4 (m, 2F), −136.8 – −136.9 (m, 2F) ppm; ESI-HR-MS (m/z): $[C_{38}H_{22}F_4]^+$, calcd for $[C_{38}H_{22}F_4]$ 554.1658; found 554.1664.

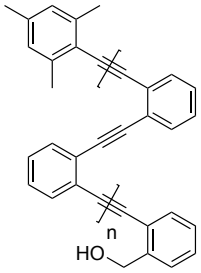

68a

poly(*o*-phenylene ethynylene) (**68a)** A 5 mL vial was charged in a Nitrogen-glovebox with **51** (0.02 g, 0.10 mmol) in toluene (1.5 mL). Catalyst **67a** (3.8 mg, 5 μmol, 5 mol%) in toluene (0.6 mL) was added rapidly and the reaction mixture stirred for 3 h at 24 °C. The reaction mixture was removed from the glovebox and quenched with MeOH (10 mL). Filtration and washing with MeOH (30 mL) yielded **10** (0.02 g, 82%) as a brown solid. ^{1}H NMR (500 MHz, THF-d_8, 25 °C) δ = 7.56 (br, 70H), 7.22 (br, 70H), 2.22 (s, 2H) ppm; ^{13}C NMR (126 MHz, THF-d_8, 25 °C) δ = 133.2, 129.3, 96.9, 93.4 ppm.

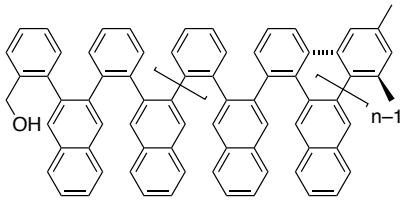

75

poly(*o*-phenylene naphthalene) (**75)** A 25 mL sealable Schlenk flask was charged under N_2 with polymer **68a** (0.01 g, 0.08 mmol) and 1,2-dichloroethane (5 mL, anhydrous) and heated for 1 h at 100 °C until the polymer was dissolved. After cooling to 25 °C, **73** (0.10 g, 0.5 mmol), $Cu(OTf)_2$ (0.02 g, 0.05 mmol), and TFA (0.08 mL, 1.0 mmol) were added and the flask was sealed and the reaction mixture heated for 24 h at 100 °C. After cooling, the reaction was quenched with sat. aq. $NaHCO_3$ (50 mL) and extracted with CH_2Cl_2 (50 mL). The organic layer was with sat. aq. $NaHCO_3$ (3x, 50 mL) and NaCl (sat. aq., 50 mL), dried over $MgSO_4$, and concentrated on a rotary evaporator. The solid obtained was dissolved in a minimal amount of acetone and precipitation with MeOH yielded a solid that was subjected once more to the above benzannulation procedure to obtain **75** as a brown solid (0.01 g, 56%). ^{1}H NMR (500 MHz, THF-d_8, 25 °C) δ = 8.42–6.35 (m, 20 H) ppm; ^{13}C NMR (126 MHz, THF-d_8, 25 °C); δ = 139.9, 128.3 ppm.

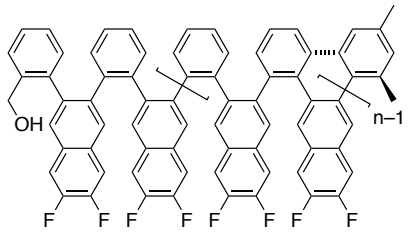

76

poly(o-phenylene 6,7-difluoronaphthalene) (**76**) A 25 mL sealable Schlenk flask was charged under N_2 with polymer **68a** (0.01 g, 0.08 mmol) and 1,2-dichloroethane (5 mL, anhydrous) and heated for 1 h at 100 °C until the polymer was dissolved. After cooling to 25 °C, **74** (0.12 g, 0.5 mmol), $Cu(OTf)_2$ (0.02 g, 0.05 mmol), and TFA (0.08 mL, 1.0 mmol) were added and the flask was sealed and the reaction mixture stirred for 24 h at 100 °C. After cooling, the reaction was quenched with sat. aq. $NaHCO_3$ (50 mL) and extracted with CH_2Cl_2 (50 mL). The organic layer was washed with sat. aq. $NaHCO_3$ (3x, 50 mL) and NaCl (sat. aq., 50 mL), dried over $MgSO_4$, and concentrated on a rotary evaporator. The solid obtained was dissolved in a minimal amount of acetone and precipitation with MeOH yielded a solid that was subjected once more to the above benzannulation procedure to obtain **76** as a brown solid (0.01 g, 65%). ^{1}H NMR (500 MHz, THF-d_8, 25 °C) δ = 7.57 (m, 16 H) ppm; ^{13}C NMR (151 MHz, THF-d_8, 25 °C) δ = 139.9, 129.6 ppm.

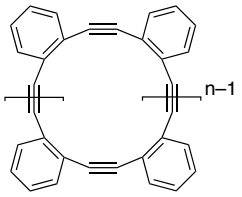

68b

cyclo(*o*-phenylene ethynylene) (**68b**) A 20 mL vial was charged in a Nitrogen-glovebox with **51** (0.06 g, 0.03 mmol) in toluene (5.5 mL). Catalyst **67a** (43 mg, 55 μmol, 20 mol%) in toluene (0.5 mL) was added rapidly and the mixture was stirred for 20 h at 24 °C. The reaction mixture was removed from the glovebox and quenched with MeOH (10 mL), filtered, and washed with MeOH (50 mL). The solid obtained was subjected to Soxlet extraction with hexanes and the soluble extract yielded **68b** (0.01 g, 13%) upon concentration with a rotary evaporator as a brown solid. ^{1}H NMR (300 MHz, $CDCl_3$, 25 °C) δ = 7.45 (m, 2H), 7.12 (m, 2H) ppm; ^{13}C NMR (151 MHz, $CDCl_3$, 25 °C) δ = 132.2, 128.1, 125.7, 92.6 ppm.

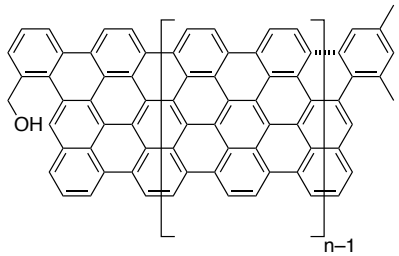

77

n = 8 AGNR (**77**) A 100 mL three-neck round-bottom flask was charged under N_2 with polymer **75** (0.005 g) and CH_2Cl_2 (75 mL, anhydrous). $FeCl_3$ (0.75 g, 4.6 mmol) in CH_3NO_2 (2 mL) was added dropwise while a stream of N_2 was passed through the solution. The reaction mixure was stirred for 48 h at 24 °C, then poured into MeOH (100 mL) and filtration yielded **77** (0.004 g, 80%) as a dark purple solid after washing with additional MeOH (100 mL).

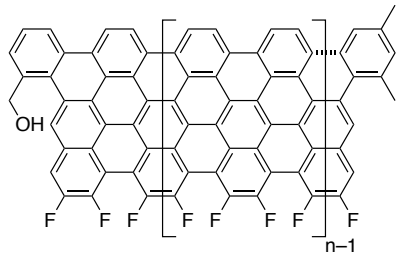

78

n=8 fluorinated AGNR (**78)** A 100 mL three-neck round-bottom flask was charged under N_2 with polymer **76** (0.003 g) and CH_2Cl_2 (75 mL, anhydrous). $FeCl_3$ (0.50 g, 4.6 mmol) in CH_3NO_2 (2 mL) was added dropwise while a stream of N_2 was passed through the solution. The reaction mixure was stirred for 48 h at 24 °C, then poured into MeOH (100 mL) and filtration yielded **78** (0.002 g, 66%) as a dark purple solid after washing with additional MeOH (100 mL).

Chapter 9
Appendix

9.1 Crystal Structure Data for Boron-Doped GNR Monomer 1

Table 9.1.1 Crystal data and structure refinement for boron-doped GNR monomer **1**.

Empirical formula	C46 H30 B2 Br2 Cl12	
Formula weight	1189.54	
Temperature	100(2) K	
Wavelength	0.71073 Å	
Crystal system	Triclinic	
Space group	P -1	
Unit cell dimensions	a = 8.6046(3) Å	a= 82.148(2)°.
	b = 9.8632(4) Å	b= 82.067(2)°.
	c = 14.5013(6) Å	g = 74.011(2)°.
Volume	1165.48(8) $Å^3$	
Z	1	
Density (calculated)	1.695 Mg/m^3	
Absorption coefficient	2.462 mm^{-1}	
F(000)	590	
Crystal size	0.040 x 0.030 x 0.020 mm^3	
Theta range for data collection	1.425 to 25.395°.	
Index ranges	-10<=h<=10, -11<=k<=11, -17<=l<=17	
Reflections collected	42257	
Independent reflections	4281 [R(int) = 0.0543]	
Completeness to theta = 25.000°	100.0 %	
Absorption correction	Semi-empirical from equivalents	
Max. and min. transmission	0.862 and 0.779	
Refinement method	Full-matrix least-squares on F^2	
Data / restraints / parameters	4281 / 0 / 280	
Goodness-of-fit on F^2	1.036	
Final R indices [I>2sigma(I)]	R1 = 0.0387, wR2 = 0.0810	
R indices (all data)	R1 = 0.0556, wR2 = 0.0887	
Extinction coefficient	n/a	
Largest diff. peak and hole	1.270 and -0.666 $e.Å^{-3}$	

Table 9.1.2 Atomic coordinates (x 10^4) and equivalent isotropic displacement parameters ($Å^2$x 10^3). U(eq) is defined as one third of the trace of the orthogonalized U^{ij} tensor.

	x	y	z	U(eq)
C(1)	1531(4)	-3136(3)	8468(2)	10(1)
C(2)	810(4)	-2647(4)	7631(2)	10(1)
C(3)	-581(4)	-3063(4)	7466(2)	14(1)
C(4)	-1290(5)	-2624(4)	6655(3)	19(1)
C(5)	-636(5)	-1734(4)	5949(3)	20(1)
C(6)	667(5)	-1282(4)	6071(3)	18(1)
C(7)	1438(4)	-1709(4)	6920(2)	12(1)
C(8)	2781(4)	-1280(4)	7095(2)	13(1)
C(9)	3582(4)	-1782(3)	7899(2)	11(1)
C(10)	4991(4)	-1409(4)	8078(3)	16(1)
C(11)	5696(4)	-1919(4)	8883(3)	19(1)
C(12)	5043(5)	-2835(4)	9571(3)	20(1)
C(13)	3713(4)	-3225(4)	9429(2)	15(1)
C(14)	2921(4)	-2730(4)	8595(2)	11(1)
C(15)	-368(4)	-3424(4)	10101(2)	10(1)
C(16)	-722(4)	-1966(4)	10173(2)	14(1)
C(17)	-1805(4)	-1341(4)	10891(3)	17(1)
C(18)	1119(4)	-5731(4)	9202(2)	10(1)
C(19)	2195(4)	-6387(4)	8483(2)	15(1)
C(20)	2551(4)	-7837(4)	8439(3)	16(1)
C(21)	1486(5)	6919(5)	2531(3)	36(1)
C(22)	1781(6)	8317(5)	2582(3)	38(1)
C(23)	5779(4)	5164(4)	5070(2)	15(1)
B(1)	772(5)	-4103(4)	9258(3)	10(1)
Cl(1)	526(1)	6416(1)	3656(1)	34(1)
Cl(2)	3284(1)	5622(1)	2194(1)	32(1)
Cl(3)	3186(1)	8257(1)	3373(1)	32(1)
Cl(4)	2458(2)	8960(1)	1406(1)	36(1)
Cl(5)	5356(1)	6930(1)	5362(1)	22(1)

Cl(6)	7134(1)	4987(1)	4033(1)	29(1)
Br(1)	3531(1)	83(1)	6202(1)	22(1)

Table 9.1.3 Bond lengths [Å] and angles [°] for **1**.

C(1)-C(14)	1.404(5)	C(15)-C(16)	1.401(5)
C(1)-C(2)	1.404(5)	C(15)-C(18)#1	1.421(5)
C(1)-B(1)	1.578(5)	C(15)-B(1)	1.561(5)
C(2)-C(3)	1.426(5)	C(16)-C(17)	1.387(5)
C(2)-C(7)	1.440(5)	C(16)-H(16)	0.9500
C(3)-C(4)	1.363(5)	C(17)-C(20)#1	1.384(5)
C(3)-H(3)	0.9500	C(17)-H(17)	0.9500
C(4)-C(5)	1.415(5)	C(18)-C(19)	1.396(5)
C(4)-H(4)	0.9500	C(18)-C(15)#1	1.421(5)
C(5)-C(6)	1.356(5)	C(18)-B(1)	1.562(5)
C(5)-H(5)	0.9500	C(19)-C(20)	1.386(5)
C(6)-C(7)	1.436(5)	C(19)-H(19)	0.9500
C(6)-H(6)	0.9500	C(20)-C(17)#1	1.384(5)
C(7)-C(8)	1.399(5)	C(20)-H(20)	0.9500
C(8)-C(9)	1.399(5)	C(21)-C(22)	1.483(6)
C(8)-Br(1)	1.916(3)	C(21)-Cl(2)	1.772(4)
C(9)-C(10)	1.425(5)	C(21)-Cl(1)	1.795(5)
C(9)-C(14)	1.447(5)	C(21)-H(21)	1.0000
C(10)-C(11)	1.360(5)	C(22)-Cl(3)	1.762(4)
C(10)-H(10)	0.9500	C(22)-Cl(4)	1.812(5)
C(11)-C(12)	1.417(5)	C(22)-H(22)	1.0000
C(11)-H(11)	0.9500	C(23)-C(23)#2	1.509(7)
C(12)-C(13)	1.352(5)	C(23)-Cl(6)	1.768(4)
C(12)-H(12)	0.9500	C(23)-Cl(5)	1.776(4)
C(13)-C(14)	1.430(5)	C(23)-H(23)	1.0000
C(13)-H(13)	0.9500		

C(14)-C(1)-C(2)	119.0(3)	C(1)-C(2)-C(3)	120.6(3)
C(14)-C(1)-B(1)	120.6(3)	C(1)-C(2)-C(7)	121.3(3)
C(2)-C(1)-B(1)	120.5(3)	C(3)-C(2)-C(7)	118.0(3)

C(4)-C(3)-C(2)	121.9(3)	C(1)-C(14)-C(9)	121.3(3)
C(4)-C(3)-H(3)	119.1	C(13)-C(14)-C(9)	117.9(3)
C(2)-C(3)-H(3)	119.1	C(16)-C(15)-C(18)#1	118.4(3)
C(3)-C(4)-C(5)	119.6(3)	C(16)-C(15)-B(1)	121.1(3)
C(3)-C(4)-H(4)	120.2	C(18)#1-C(15)-B(1)	120.5(3)
C(5)-C(4)-H(4)	120.2	C(17)-C(16)-C(15)	121.5(3)
C(6)-C(5)-C(4)	121.2(3)	C(17)-C(16)-H(16)	119.3
C(6)-C(5)-H(5)	119.4	C(15)-C(16)-H(16)	119.3
C(4)-C(5)-H(5)	119.4	C(20)#1-C(17)-C(16)	120.0(3)
C(5)-C(6)-C(7)	120.8(3)	C(20)#1-C(17)-H(17)	120.0
C(5)-C(6)-H(6)	119.6	C(16)-C(17)-H(17)	120.0
C(7)-C(6)-H(6)	119.6	C(19)-C(18)-C(15)#1	118.9(3)
C(8)-C(7)-C(6)	123.9(3)	C(19)-C(18)-B(1)	120.9(3)
C(8)-C(7)-C(2)	117.8(3)	C(15)#1-C(18)-B(1)	120.2(3)
C(6)-C(7)-C(2)	118.3(3)	C(20)-C(19)-C(18)	121.6(3)
C(9)-C(8)-C(7)	123.0(3)	C(20)-C(19)-H(19)	119.2
C(9)-C(8)-Br(1)	118.5(3)	C(18)-C(19)-H(19)	119.2
C(7)-C(8)-Br(1)	118.4(3)	C(17)#1-C(20)-C(19)	119.6(3)
C(8)-C(9)-C(10)	124.3(3)	C(17)#1-C(20)-H(20)	120.2
C(8)-C(9)-C(14)	117.6(3)	C(19)-C(20)-H(20)	120.2
C(10)-C(9)-C(14)	118.2(3)	C(22)-C(21)-Cl(2)	112.7(3)
C(11)-C(10)-C(9)	121.2(3)	C(22)-C(21)-Cl(1)	106.8(3)
C(11)-C(10)-H(10)	119.4	Cl(2)-C(21)-Cl(1)	112.4(3)
C(9)-C(10)-H(10)	119.4	C(22)-C(21)-H(21)	108.3
C(10)-C(11)-C(12)	120.8(3)	Cl(2)-C(21)-H(21)	108.3
C(10)-C(11)-H(11)	119.6	Cl(1)-C(21)-H(21)	108.3
C(12)-C(11)-H(11)	119.6	C(21)-C(22)-Cl(3)	113.3(3)
C(13)-C(12)-C(11)	120.1(3)	C(21)-C(22)-Cl(4)	107.1(3)
C(13)-C(12)-H(12)	120.0	Cl(3)-C(22)-Cl(4)	111.4(3)
C(11)-C(12)-H(12)	120.0	C(21)-C(22)-H(22)	108.3
C(12)-C(13)-C(14)	121.8(3)	Cl(3)-C(22)-H(22)	108.3
C(12)-C(13)-H(13)	119.1	Cl(4)-C(22)-H(22)	108.3
C(14)-C(13)-H(13)	119.1	C(23)#2-C(23)-Cl(6)	110.3(3)
C(1)-C(14)-C(13)	120.8(3)	C(23)#2-C(23)-Cl(5)	109.7(3)

Cl(6)-C(23)-Cl(5)	108.8(2)
C(23)#2-C(23)-H(23)	109.3
Cl(6)-C(23)-H(23)	109.3
Cl(5)-C(23)-H(23)	109.3
C(15)-B(1)-C(18)	119.3(3)
C(15)-B(1)-C(1)	119.7(3)
C(18)-B(1)-C(1)	120.9(3)

Symmetry transformations used to generate equivalent atoms:
#1 -x,-y-1,-z+2 #2 -x+1,-y+1,-z+1

Table 9.1.4 Anisotropic displacement parameters ($Å^2 x\ 10^3$) for **1**. The anisotropic displacement factor exponent takes the form: $-2p^2[\ h^2 a^{*2} U^{11} + ... + 2\ h\ k\ a^*\ b^*\ U^{12}\ ]$

	U^{11}	U^{22}	U^{33}	U^{23}	U^{13}	U^{12}
C(1)	11(2)	8(2)	9(2)	-3(1)	2(1)	0(1)
C(2)	8(2)	10(2)	10(2)	-2(1)	0(1)	1(1)
C(3)	15(2)	15(2)	13(2)	1(2)	-2(2)	-6(2)
C(4)	17(2)	20(2)	21(2)	0(2)	-8(2)	-6(2)
C(5)	27(2)	20(2)	13(2)	2(2)	-10(2)	-4(2)
C(6)	25(2)	14(2)	13(2)	2(2)	-2(2)	-4(2)
C(7)	14(2)	8(2)	10(2)	-3(1)	1(1)	0(1)
C(8)	17(2)	9(2)	11(2)	-1(1)	4(2)	-4(2)
C(9)	11(2)	7(2)	15(2)	-3(1)	2(1)	-1(1)
C(10)	14(2)	10(2)	25(2)	-3(2)	0(2)	-3(2)
C(11)	12(2)	17(2)	29(2)	-3(2)	-7(2)	-4(2)
C(12)	22(2)	18(2)	22(2)	0(2)	-11(2)	-4(2)
C(13)	16(2)	13(2)	15(2)	2(2)	-5(2)	-4(2)
C(14)	12(2)	8(2)	11(2)	-4(1)	1(1)	1(1)
C(15)	10(2)	12(2)	9(2)	1(1)	-5(1)	-3(1)
C(16)	15(2)	10(2)	15(2)	2(2)	-2(2)	-3(2)
C(17)	21(2)	9(2)	20(2)	-4(2)	-3(2)	-2(2)
C(18)	7(2)	14(2)	8(2)	-1(1)	-4(1)	-2(1)
C(19)	16(2)	16(2)	12(2)	0(2)	0(2)	-6(2)
C(20)	13(2)	18(2)	15(2)	-7(2)	2(2)	1(2)
C(21)	25(2)	35(3)	49(3)	-12(2)	-14(2)	-1(2)
C(22)	34(3)	29(3)	51(3)	-10(2)	-22(2)	2(2)
C(23)	14(2)	16(2)	14(2)	-2(2)	1(2)	-2(2)
B(1)	9(2)	14(2)	8(2)	3(2)	-7(2)	-3(2)
Cl(1)	26(1)	40(1)	38(1)	3(1)	4(1)	-17(1)
Cl(2)	27(1)	25(1)	44(1)	-14(1)	-1(1)	-2(1)
Cl(3)	40(1)	23(1)	39(1)	-3(1)	-23(1)	-11(1)
Cl(4)	50(1)	29(1)	29(1)	13(1)	-11(1)	-18(1)
Cl(5)	24(1)	19(1)	25(1)	-6(1)	-4(1)	-8(1)

Cl(6)	25(1)	30(1)	31(1)	-9(1)	15(1)	-11(1)
Br(1)	31(1)	20(1)	19(1)	2(1)	-1(1)	-14(1)

Table 9.1.5 Hydrogen coordinates (x 10^4) and isotropic displacement parameters (Å^{2}x 10^3) for **1**.

	x	y	z	U(eq)
H(3)	-1026	-3663	7935	17
H(4)	-2219	-2913	6563	23
H(5)	-1119	-1448	5379	23
H(6)	1075	-676	5589	21
H(10)	5445	-792	7627	20
H(11)	6637	-1657	8985	22
H(12)	5540	-3177	10133	24
H(13)	3293	-3844	9895	17
H(16)	-208	-1393	9720	16
H(17)	-2034	-348	10922	20
H(19)	2695	-5826	8014	18
H(20)	3304	-8263	7950	19
H(21)	706	7038	2056	43
H(22)	724	8985	2790	46
H(23)	6298	4492	5590	18

9.2 Crystal Structure Data for C-GNR Monomer 33a

Table 9.2.1 Crystal data and structure refinement for C-GNR Monomer **33a**

Empirical formula	C42 H26 Br2	
Formula weight	690.45	
Temperature	100(2) K	
Wavelength	0.71073 Å	
Crystal system	Triclinic	
Space group	P -1	
Unit cell dimensions	a = 6.7761(2) Å	a= 89.7330(10)°.

	b = 14.0538(4) Å	b= 83.8380(10)°.
	c = 16.6056(5) Å	g = 76.8270(10)°.
Volume	1530.52(8) $Å^3$	
Z	2	
Density (calculated)	1.498 Mg/m^3	
Absorption coefficient	2.679 mm^{-1}	
F(000)	696	
Crystal size	0.200 x 0.200 x 0.050 mm^3	
Theta range for data collection	1.488 to 25.364°.	
Index ranges	-8<=h<=8, -16<=k<=16, -19<=l<=20	
Reflections collected	42733	
Independent reflections	5597 [R(int) = 0.0278]	
Completeness to theta = 25.000°	99.9 %	
Absorption correction	Semi-empirical from equivalents	
Max. and min. transmission	0.7452 and 0.6122	
Refinement method	Full-matrix least-squares on F^2	
Data / restraints / parameters	5597 / 0 / 397	
Goodness-of-fit on F^2	1.056	
Final R indices [I>2sigma(I)]	R1 = 0.0246, wR2 = 0.0640	
R indices (all data)	R1 = 0.0274, wR2 = 0.0660	
Extinction coefficient	n/a	
Largest diff. peak and hole	0.668 and -0.218 $e.Å^{-3}$	

Table 9.2.2 Atomic coordinates (x 10^4) and equivalent isotropic displacement parameters ($Å^2$x 10^3) for **33a**. U(eq) is defined as one third of the trace of the orthogonalized U^{ij} tensor.

	x	y	z	U(eq)
C(1)	5764(3)	3827(1)	7673(1)	15(1)
C(2)	6457(3)	2918(1)	8018(1)	15(1)
C(3)	8112(3)	2224(1)	7619(1)	16(1)
C(4)	9010(3)	2421(1)	6862(1)	16(1)
C(5)	8153(3)	3298(1)	6463(1)	14(1)
C(6)	8566(3)	3413(1)	5580(1)	14(1)
C(7)	9393(3)	2600(1)	5055(1)	16(1)
C(8)	9645(3)	2707(1)	4233(1)	16(1)
C(9)	9078(3)	3615(1)	3879(1)	17(1)
C(10)	8205(3)	4407(1)	4380(1)	17(1)
C(11)	7907(2)	4333(1)	5227(1)	14(1)
C(12)	6903(2)	5177(1)	5745(1)	14(1)
C(13)	6533(3)	6134(1)	5441(1)	15(1)
C(14)	5664(3)	6940(1)	5928(1)	16(1)
C(15)	5186(3)	6799(1)	6749(1)	15(1)
C(16)	5484(3)	5877(1)	7069(1)	15(1)
C(17)	6298(3)	5042(1)	6571(1)	14(1)
C(18)	6694(3)	4048(1)	6908(1)	14(1)
C(19)	3880(3)	4481(1)	8102(1)	16(1)
C(20)	2059(3)	4618(1)	7757(1)	19(1)
C(21)	245(3)	5141(2)	8162(1)	24(1)
C(22)	237(3)	5540(2)	8926(1)	27(1)
C(23)	2044(3)	5424(1)	9269(1)	24(1)
C(24)	3861(3)	4897(1)	8865(1)	19(1)
C(25)	5552(3)	2700(1)	8840(1)	17(1)
C(26)	3570(3)	2572(1)	8982(1)	21(1)
C(27)	2785(3)	2369(2)	9754(1)	25(1)
C(28)	3952(3)	2315(2)	10398(1)	26(1)
C(29)	5920(3)	2449(1)	10262(1)	24(1)

C(30)	6717(3)	2630(1)	9488(1)	20(1)
C(31)	8719(3)	1245(1)	8001(1)	18(1)
C(32)	7357(3)	632(1)	8032(1)	24(1)
C(33)	7808(3)	-273(2)	8390(1)	33(1)
C(34)	9620(4)	-574(2)	8730(1)	36(1)
C(35)	10989(3)	20(2)	8699(1)	32(1)
C(36)	10550(3)	924(1)	8328(1)	24(1)
C(37)	10982(3)	1758(1)	6525(1)	16(1)
C(38)	11191(3)	763(1)	6367(1)	23(1)
C(39)	13069(3)	182(2)	6082(1)	29(1)
C(40)	14771(3)	577(2)	5953(1)	29(1)
C(41)	14588(3)	1563(2)	6108(1)	27(1)
C(42)	12701(3)	2147(1)	6393(1)	19(1)
Br(1)	10821(1)	1595(1)	3556(1)	21(1)
Br(2)	4067(1)	7896(1)	7451(1)	21(1)

Table 9.2.3 Bond lengths [Å] and angles [°] for **33a**.

C(1)-C(2)	1.399(2)
C(1)-C(18)	1.422(2)
C(1)-C(19)	1.503(2)
C(2)-C(3)	1.413(2)
C(2)-C(25)	1.495(2)
C(3)-C(4)	1.391(3)
C(3)-C(31)	1.501(2)
C(4)-C(5)	1.430(2)
C(4)-C(37)	1.498(2)
C(5)-C(18)	1.418(2)
C(5)-C(6)	1.478(2)
C(6)-C(7)	1.411(3)
C(6)-C(11)	1.414(2)
C(7)-C(8)	1.369(3)
C(7)-H(7)	0.9500
C(8)-C(9)	1.393(3)
C(8)-Br(1)	1.8973(18)
C(9)-C(10)	1.373(3)
C(9)-H(9)	0.9500
C(10)-C(11)	1.405(3)
C(10)-H(10)	0.9500
C(11)-C(12)	1.458(3)
C(12)-C(13)	1.413(2)
C(12)-C(17)	1.413(2)
C(13)-C(14)	1.373(3)
C(13)-H(13)	0.9500
C(14)-C(15)	1.391(3)
C(14)-H(14)	0.9500
C(15)-C(16)	1.377(3)
C(15)-Br(2)	1.8986(18)
C(16)-C(17)	1.408(3)
C(16)-H(16)	0.9500

C(17)-C(18)	1.480(2)
C(19)-C(20)	1.390(3)
C(19)-C(24)	1.395(3)
C(20)-C(21)	1.386(3)
C(20)-H(20)	0.9500
C(21)-C(22)	1.387(3)
C(21)-H(21)	0.9500
C(22)-C(23)	1.382(3)
C(22)-H(22)	0.9500
C(23)-C(24)	1.388(3)
C(23)-H(23)	0.9500
C(24)-H(24)	0.9500
C(25)-C(26)	1.390(3)
C(25)-C(30)	1.392(3)
C(26)-C(27)	1.389(3)
C(26)-H(26)	0.9500
C(27)-C(28)	1.387(3)
C(27)-H(27)	0.9500
C(28)-C(29)	1.384(3)
C(28)-H(28)	0.9500
C(29)-C(30)	1.386(3)
C(29)-H(29)	0.9500
C(30)-H(30)	0.9500
C(31)-C(36)	1.387(3)
C(31)-C(32)	1.397(3)
C(32)-C(33)	1.385(3)
C(32)-H(32)	0.9500
C(33)-C(34)	1.384(3)
C(33)-H(33)	0.9500
C(34)-C(35)	1.380(3)
C(34)-H(34)	0.9500
C(35)-C(36)	1.394(3)
C(35)-H(35)	0.9500
C(36)-H(36)	0.9500

C(37)-C(42)	1.392(3)
C(37)-C(38)	1.397(3)
C(38)-C(39)	1.382(3)
C(38)-H(38)	0.9500
C(39)-C(40)	1.386(3)
C(39)-H(39)	0.9500
C(40)-C(41)	1.385(3)
C(40)-H(40)	0.9500
C(41)-C(42)	1.389(3)
C(41)-H(41)	0.9500
C(42)-H(42)	0.9500

C(2)-C(1)-C(18)	120.04(16)
C(2)-C(1)-C(19)	116.49(15)
C(18)-C(1)-C(19)	123.09(15)
C(1)-C(2)-C(3)	120.37(16)
C(1)-C(2)-C(25)	120.25(15)
C(3)-C(2)-C(25)	119.24(15)
C(4)-C(3)-C(2)	120.23(16)
C(4)-C(3)-C(31)	121.71(16)
C(2)-C(3)-C(31)	117.80(15)
C(3)-C(4)-C(5)	119.60(16)
C(3)-C(4)-C(37)	118.76(15)
C(5)-C(4)-C(37)	121.32(15)
C(18)-C(5)-C(4)	119.29(16)
C(18)-C(5)-C(6)	118.09(15)
C(4)-C(5)-C(6)	122.29(15)
C(7)-C(6)-C(11)	117.79(16)
C(7)-C(6)-C(5)	121.50(16)
C(11)-C(6)-C(5)	120.26(16)
C(8)-C(7)-C(6)	121.08(17)
C(8)-C(7)-H(7)	119.5
C(6)-C(7)-H(7)	119.5
C(7)-C(8)-C(9)	121.68(17)

C(7)-C(8)-Br(1)	119.42(14)
C(9)-C(8)-Br(1)	118.89(13)
C(10)-C(9)-C(8)	117.86(17)
C(10)-C(9)-H(9)	121.1
C(8)-C(9)-H(9)	121.1
C(9)-C(10)-C(11)	122.47(17)
C(9)-C(10)-H(10)	118.8
C(11)-C(10)-H(10)	118.8
C(10)-C(11)-C(6)	119.00(16)
C(10)-C(11)-C(12)	121.49(16)
C(6)-C(11)-C(12)	119.49(16)
C(13)-C(12)-C(17)	118.88(16)
C(13)-C(12)-C(11)	121.40(16)
C(17)-C(12)-C(11)	119.72(16)
C(14)-C(13)-C(12)	122.11(16)
C(14)-C(13)-H(13)	118.9
C(12)-C(13)-H(13)	118.9
C(13)-C(14)-C(15)	118.24(16)
C(13)-C(14)-H(14)	120.9
C(15)-C(14)-H(14)	120.9
C(16)-C(15)-C(14)	121.63(16)
C(16)-C(15)-Br(2)	118.76(14)
C(14)-C(15)-Br(2)	119.61(13)
C(15)-C(16)-C(17)	120.71(16)
C(15)-C(16)-H(16)	119.6
C(17)-C(16)-H(16)	119.6
C(16)-C(17)-C(12)	118.25(16)
C(16)-C(17)-C(18)	121.50(16)
C(12)-C(17)-C(18)	120.02(16)
C(5)-C(18)-C(1)	118.88(16)
C(5)-C(18)-C(17)	118.01(15)
C(1)-C(18)-C(17)	123.01(15)
C(20)-C(19)-C(24)	118.69(16)
C(20)-C(19)-C(1)	118.94(16)

C(24)-C(19)-C(1)	122.20(16)
C(21)-C(20)-C(19)	121.13(18)
C(21)-C(20)-H(20)	119.4
C(19)-C(20)-H(20)	119.4
C(20)-C(21)-C(22)	119.73(18)
C(20)-C(21)-H(21)	120.1
C(22)-C(21)-H(21)	120.1
C(23)-C(22)-C(21)	119.66(18)
C(23)-C(22)-H(22)	120.2
C(21)-C(22)-H(22)	120.2
C(22)-C(23)-C(24)	120.69(18)
C(22)-C(23)-H(23)	119.7
C(24)-C(23)-H(23)	119.7
C(23)-C(24)-C(19)	120.08(18)
C(23)-C(24)-H(24)	120.0
C(19)-C(24)-H(24)	120.0
C(26)-C(25)-C(30)	118.68(17)
C(26)-C(25)-C(2)	122.10(16)
C(30)-C(25)-C(2)	119.22(16)
C(27)-C(26)-C(25)	120.37(18)
C(27)-C(26)-H(26)	119.8
C(25)-C(26)-H(26)	119.8
C(28)-C(27)-C(26)	120.41(18)
C(28)-C(27)-H(27)	119.8
C(26)-C(27)-H(27)	119.8
C(29)-C(28)-C(27)	119.51(18)
C(29)-C(28)-H(28)	120.2
C(27)-C(28)-H(28)	120.2
C(28)-C(29)-C(30)	120.03(18)
C(28)-C(29)-H(29)	120.0
C(30)-C(29)-H(29)	120.0
C(29)-C(30)-C(25)	120.97(18)
C(29)-C(30)-H(30)	119.5
C(25)-C(30)-H(30)	119.5

C(36)-C(31)-C(32)	118.60(18)
C(36)-C(31)-C(3)	123.45(17)
C(32)-C(31)-C(3)	117.95(17)
C(33)-C(32)-C(31)	120.81(19)
C(33)-C(32)-H(32)	119.6
C(31)-C(32)-H(32)	119.6
C(34)-C(33)-C(32)	120.0(2)
C(34)-C(33)-H(33)	120.0
C(32)-C(33)-H(33)	120.0
C(35)-C(34)-C(33)	119.88(19)
C(35)-C(34)-H(34)	120.1
C(33)-C(34)-H(34)	120.1
C(34)-C(35)-C(36)	120.2(2)
C(34)-C(35)-H(35)	119.9
C(36)-C(35)-H(35)	119.9
C(31)-C(36)-C(35)	120.5(2)
C(31)-C(36)-H(36)	119.7
C(35)-C(36)-H(36)	119.7
C(42)-C(37)-C(38)	118.63(17)
C(42)-C(37)-C(4)	118.27(16)
C(38)-C(37)-C(4)	123.05(17)
C(39)-C(38)-C(37)	120.32(19)
C(39)-C(38)-H(38)	119.8
C(37)-C(38)-H(38)	119.8
C(38)-C(39)-C(40)	120.59(19)
C(38)-C(39)-H(39)	119.7
C(40)-C(39)-H(39)	119.7
C(41)-C(40)-C(39)	119.74(18)
C(41)-C(40)-H(40)	120.1
C(39)-C(40)-H(40)	120.1
C(40)-C(41)-C(42)	119.7(2)
C(40)-C(41)-H(41)	120.1
C(42)-C(41)-H(41)	120.1
C(41)-C(42)-C(37)	120.98(18)

C(41)-C(42)-H(42)	119.5
C(37)-C(42)-H(42)	119.5

Symmetry transformations used to generate equivalent atoms:

Table 9.2.4 Anisotropic displacement parameters ($Å^2 x\ 10^3$) for **33a**. The anisotropic displacement factor exponent takes the form: $-2p^2[\ h^2 a^{*2} U^{11} + ... + 2\ h\ k\ a^*\ b^*\ U^{12}\ ]$

	U^{11}	U^{22}	U^{33}	U^{23}	U^{13}	U^{12}
C(1)	14(1)	15(1)	16(1)	0(1)	-3(1)	-5(1)
C(2)	14(1)	14(1)	17(1)	2(1)	-3(1)	-5(1)
C(3)	17(1)	15(1)	18(1)	2(1)	-4(1)	-4(1)
C(4)	18(1)	13(1)	16(1)	-1(1)	-2(1)	-5(1)
C(5)	13(1)	15(1)	16(1)	1(1)	-2(1)	-5(1)
C(6)	11(1)	17(1)	16(1)	2(1)	-2(1)	-5(1)
C(7)	13(1)	16(1)	18(1)	2(1)	-2(1)	-5(1)
C(8)	13(1)	19(1)	16(1)	-2(1)	-1(1)	-5(1)
C(9)	15(1)	24(1)	14(1)	2(1)	-2(1)	-8(1)
C(10)	15(1)	18(1)	19(1)	5(1)	-3(1)	-7(1)
C(11)	10(1)	17(1)	17(1)	2(1)	-2(1)	-5(1)
C(12)	11(1)	15(1)	16(1)	2(1)	-3(1)	-4(1)
C(13)	14(1)	18(1)	15(1)	5(1)	-2(1)	-6(1)
C(14)	14(1)	13(1)	21(1)	5(1)	-4(1)	-4(1)
C(15)	12(1)	14(1)	19(1)	-1(1)	-2(1)	-3(1)
C(16)	13(1)	16(1)	16(1)	3(1)	-2(1)	-4(1)
C(17)	11(1)	16(1)	17(1)	2(1)	-2(1)	-3(1)
C(18)	13(1)	16(1)	15(1)	2(1)	-4(1)	-4(1)
C(19)	19(1)	12(1)	15(1)	4(1)	1(1)	-4(1)
C(20)	22(1)	17(1)	17(1)	3(1)	-1(1)	-5(1)
C(21)	16(1)	25(1)	29(1)	6(1)	-2(1)	-2(1)
C(22)	24(1)	24(1)	28(1)	1(1)	8(1)	1(1)
C(23)	35(1)	18(1)	18(1)	0(1)	4(1)	-5(1)
C(24)	23(1)	17(1)	16(1)	2(1)	-2(1)	-6(1)
C(25)	21(1)	12(1)	17(1)	2(1)	0(1)	-3(1)
C(26)	23(1)	20(1)	21(1)	4(1)	-4(1)	-7(1)
C(27)	21(1)	26(1)	28(1)	7(1)	1(1)	-7(1)
C(28)	32(1)	23(1)	20(1)	7(1)	3(1)	-3(1)
C(29)	29(1)	24(1)	17(1)	3(1)	-5(1)	-2(1)

C(30)	18(1)	20(1)	21(1)	1(1)	-1(1)	-2(1)
C(31)	24(1)	15(1)	13(1)	2(1)	2(1)	-1(1)
C(32)	24(1)	20(1)	27(1)	3(1)	2(1)	-5(1)
C(33)	35(1)	20(1)	43(1)	8(1)	6(1)	-8(1)
C(34)	41(1)	21(1)	37(1)	13(1)	8(1)	3(1)
C(35)	35(1)	29(1)	26(1)	7(1)	-4(1)	6(1)
C(36)	26(1)	21(1)	22(1)	2(1)	-3(1)	-2(1)
C(37)	18(1)	16(1)	13(1)	3(1)	-2(1)	-1(1)
C(38)	31(1)	17(1)	19(1)	4(1)	1(1)	-4(1)
C(39)	42(1)	16(1)	21(1)	1(1)	2(1)	5(1)
C(40)	24(1)	33(1)	21(1)	1(1)	0(1)	12(1)
C(41)	18(1)	39(1)	22(1)	-2(1)	-3(1)	-3(1)
C(42)	20(1)	20(1)	18(1)	0(1)	-4(1)	-3(1)
Br(1)	25(1)	20(1)	18(1)	-4(1)	0(1)	-5(1)
Br(2)	25(1)	14(1)	20(1)	1(1)	0(1)	-1(1)

Table 9.2.5 Hydrogen coordinates (x 10^4) and isotropic displacement parameters (Å^{2}x 10^3) for **33a**.

	x	y	z	U(eq)
H(7)	9782	1969	5276	19
H(9)	9288	3684	3309	20
H(10)	7787	5029	4146	20
H(13)	6897	6224	4882	18
H(14)	5397	7577	5710	19
H(16)	5137	5804	7632	18
H(20)	2058	4348	7233	22
H(21)	-988	5227	7919	29
H(22)	-1004	5892	9211	33
H(23)	2042	5707	9788	29
H(24)	5094	4820	9108	22
H(26)	2748	2624	8547	25
H(27)	1442	2266	9843	30
H(28)	3403	2187	10927	31
H(29)	6725	2418	10700	29
H(30)	8080	2707	9398	24
H(32)	6106	837	7803	29
H(33)	6874	-686	8403	40
H(34)	9921	-1190	8985	43
H(35)	12235	-187	8932	38
H(36)	11512	1324	8298	28
H(38)	10036	484	6455	27
H(39)	13195	-493	5975	34
H(40)	16058	173	5758	35
H(41)	15748	1837	6020	32
H(42)	12582	2822	6500	23

9.3 Crystal Structure Data for 4N-GNR Monomer 33c

Table 9.3.1 Crystal data and structure refinement for 4N-GNR Monomer **33c**.

Empirical formula	C38 H22 Br2 N4	
Formula weight	694.41	
Temperature	100(2) K	
Wavelength	0.71073 Å	
Crystal system	Monoclinic	
Space group	P 21/n	
Unit cell dimensions	a = 13.0402(4) Å	a= 90°.
	b = 11.4737(3) Å	b= 95.2780(10)°.
	c = 20.3125(6) Å	g = 90°.
Volume	3026.26(15) $Å^3$	
Z	4	
Density (calculated)	1.524 Mg/m^3	
Absorption coefficient	2.713 mm^{-1}	
F(000)	1392	
Crystal size	0.160 x 0.080 x 0.040 mm^3	
Theta range for data collection	1.784 to 25.380°.	
Index ranges	-15<=h<=15, -13<=k<=13, -24<=l<=24	
Reflections collected	73179	
Independent reflections	5550 [R(int) = 0.0548]	
Completeness to theta = 25.000°	100.0 %	
Absorption correction	Semi-empirical from equivalents	
Max. and min. transmission	0.7452 and 0.6419	
Refinement method	Full-matrix least-squares on F^2	
Data / restraints / parameters	5550 / 0 / 397	
Goodness-of-fit on F^2	1.080	
Final R indices [I>2sigma(I)]	R1 = 0.0350, wR2 = 0.0819	
R indices (all data)	R1 = 0.0452, wR2 = 0.0882	
Extinction coefficient	n/a	
Largest diff. peak and hole	0.754 and -0.438 $e.Å^{-3}$	

Table 9.3.2 Atomic coordinates (x 10^4) and equivalent isotropic displacement parameters ($Å^2$x 10^3) for **33c**. U(eq) is defined as one third of the trace of the orthogonalized U^{ij} tensor.

	x	y	z	U(eq)
C(1)	5133(2)	3520(2)	3103(1)	14(1)
C(2)	6149(2)	3420(2)	3385(1)	16(1)
C(3)	6372(2)	3315(2)	4074(1)	14(1)
C(4)	5577(2)	3102(2)	4474(1)	15(1)
C(5)	4554(2)	2998(2)	4169(1)	15(1)
C(6)	3740(2)	2420(2)	4506(1)	15(1)
C(7)	3993(2)	1565(2)	4989(1)	16(1)
C(8)	3228(2)	984(3)	5278(1)	20(1)
C(9)	2193(2)	1216(3)	5098(1)	23(1)
C(10)	1936(2)	2000(3)	4600(1)	23(1)
C(11)	2700(2)	2608(3)	4284(1)	18(1)
C(12)	2448(2)	3359(3)	3714(1)	19(1)
C(13)	1426(2)	3741(3)	3546(1)	23(1)
C(14)	1161(2)	4392(3)	2994(2)	22(1)
C(15)	1932(2)	4700(3)	2599(1)	18(1)
C(16)	2936(2)	4368(2)	2750(1)	17(1)
C(17)	3225(2)	3681(2)	3308(1)	16(1)
C(18)	4313(2)	3385(2)	3512(1)	15(1)
C(19)	4979(2)	3694(3)	2369(1)	17(1)
C(20)	4532(2)	2818(3)	1968(1)	23(1)
C(21)	4389(2)	2973(3)	1289(2)	29(1)
C(22)	4677(2)	4001(3)	1003(1)	31(1)
C(23)	5130(2)	4875(3)	1396(1)	27(1)
C(24)	5292(2)	4721(3)	2077(1)	21(1)
C(25)	8652(2)	3290(3)	2259(2)	28(1)
C(26)	7222(2)	2436(3)	2588(1)	22(1)
C(27)	7022(2)	3414(3)	2955(1)	17(1)
C(28)	7704(2)	4334(3)	2930(1)	21(1)
C(29)	9422(2)	3637(3)	4856(2)	26(1)

C(30)	8215(2)	2622(3)	4229(1)	19(1)
C(31)	7459(2)	3421(3)	4363(1)	18(1)
C(32)	7794(2)	4342(3)	4773(1)	22(1)
C(33)	5781(2)	3055(2)	5210(1)	17(1)
C(34)	6546(2)	2351(3)	5529(1)	19(1)
C(35)	6696(2)	2329(3)	6217(1)	24(1)
C(36)	6079(2)	2990(3)	6592(1)	27(1)
C(37)	5317(2)	3686(3)	6280(1)	25(1)
C(38)	5174(2)	3725(3)	5595(1)	20(1)
N(1)	8531(2)	4286(2)	2582(1)	25(1)
N(2)	8046(2)	2356(2)	2236(1)	27(1)
N(3)	8775(2)	4463(2)	5023(1)	26(1)
N(4)	9202(2)	2709(2)	4474(1)	22(1)
Br(1)	1589(1)	5595(1)	1825(1)	25(1)
Br(2)	3619(1)	-177(1)	5916(1)	24(1)

Table 9.3.3 Bond lengths [Å] and angles [°] for **33c**.

C(1)-C(2)	1.399(4)
C(1)-C(18)	1.422(4)
C(1)-C(19)	1.498(4)
C(2)-C(3)	1.408(4)
C(2)-C(27)	1.497(4)
C(3)-C(4)	1.396(4)
C(3)-C(31)	1.488(3)
C(4)-C(5)	1.423(4)
C(4)-C(33)	1.496(4)
C(5)-C(18)	1.415(4)
C(5)-C(6)	1.472(4)
C(6)-C(7)	1.405(4)
C(6)-C(11)	1.406(4)
C(7)-C(8)	1.375(4)
C(7)-H(7)	0.9500
C(8)-C(9)	1.392(4)
C(8)-Br(2)	1.895(3)
C(9)-C(10)	1.371(4)
C(9)-H(9)	0.9500
C(10)-C(11)	1.418(4)
C(10)-H(10)	0.9500
C(11)-C(12)	1.456(4)
C(12)-C(17)	1.413(4)
C(12)-C(13)	1.414(4)
C(13)-C(14)	1.365(4)
C(13)-H(13)	0.9500
C(14)-C(15)	1.389(4)
C(14)-H(14)	0.9500
C(15)-C(16)	1.371(4)
C(15)-Br(1)	1.896(3)
C(16)-C(17)	1.404(4)
C(16)-H(16)	0.9500

C(17)-C(18)	1.480(3)
C(19)-C(20)	1.388(4)
C(19)-C(24)	1.396(4)
C(20)-C(21)	1.386(4)
C(20)-H(20)	0.9500
C(21)-C(22)	1.381(5)
C(21)-H(21)	0.9500
C(22)-C(23)	1.379(5)
C(22)-H(22)	0.9500
C(23)-C(24)	1.393(4)
C(23)-H(23)	0.9500
C(24)-H(24)	0.9500
C(25)-N(2)	1.330(4)
C(25)-N(1)	1.335(4)
C(25)-H(25)	0.9500
C(26)-N(2)	1.348(4)
C(26)-C(27)	1.384(4)
C(26)-H(26)	0.9500
C(27)-C(28)	1.385(4)
C(28)-N(1)	1.345(4)
C(28)-H(28)	0.9500
C(29)-N(4)	1.333(4)
C(29)-N(3)	1.334(4)
C(29)-H(29)	0.9500
C(30)-N(4)	1.340(3)
C(30)-C(31)	1.392(4)
C(30)-H(30)	0.9500
C(31)-C(32)	1.391(4)
C(32)-N(3)	1.339(4)
C(32)-H(32)	0.9500
C(33)-C(38)	1.394(4)
C(33)-C(34)	1.395(4)
C(34)-C(35)	1.394(4)
C(34)-H(34)	0.9500

C(35)-C(36)	1.383(4)
C(35)-H(35)	0.9500
C(36)-C(37)	1.382(4)
C(36)-H(36)	0.9500
C(37)-C(38)	1.388(4)
C(37)-H(37)	0.9500
C(38)-H(38)	0.9500

C(2)-C(1)-C(18)	119.1(2)
C(2)-C(1)-C(19)	117.0(2)
C(18)-C(1)-C(19)	123.8(2)
C(1)-C(2)-C(3)	121.0(2)
C(1)-C(2)-C(27)	120.2(2)
C(3)-C(2)-C(27)	118.8(2)
C(4)-C(3)-C(2)	119.8(2)
C(4)-C(3)-C(31)	121.1(2)
C(2)-C(3)-C(31)	119.1(2)
C(3)-C(4)-C(5)	118.5(2)
C(3)-C(4)-C(33)	121.0(2)
C(5)-C(4)-C(33)	120.4(2)
C(18)-C(5)-C(4)	120.2(2)
C(18)-C(5)-C(6)	118.2(2)
C(4)-C(5)-C(6)	121.5(2)
C(7)-C(6)-C(11)	119.2(2)
C(7)-C(6)-C(5)	120.4(2)
C(11)-C(6)-C(5)	119.8(2)
C(8)-C(7)-C(6)	120.2(2)
C(8)-C(7)-H(7)	119.9
C(6)-C(7)-H(7)	119.9
C(7)-C(8)-C(9)	121.3(3)
C(7)-C(8)-Br(2)	118.2(2)
C(9)-C(8)-Br(2)	120.5(2)
C(10)-C(9)-C(8)	119.0(3)
C(10)-C(9)-H(9)	120.5

C(8)-C(9)-H(9)	120.5
C(9)-C(10)-C(11)	121.5(3)
C(9)-C(10)-H(10)	119.3
C(11)-C(10)-H(10)	119.3
C(6)-C(11)-C(10)	118.5(3)
C(6)-C(11)-C(12)	119.1(2)
C(10)-C(11)-C(12)	122.3(2)
C(17)-C(12)-C(13)	119.2(3)
C(17)-C(12)-C(11)	119.8(2)
C(13)-C(12)-C(11)	121.0(3)
C(14)-C(13)-C(12)	122.0(3)
C(14)-C(13)-H(13)	119.0
C(12)-C(13)-H(13)	119.0
C(13)-C(14)-C(15)	118.1(3)
C(13)-C(14)-H(14)	120.9
C(15)-C(14)-H(14)	120.9
C(16)-C(15)-C(14)	121.8(3)
C(16)-C(15)-Br(1)	118.9(2)
C(14)-C(15)-Br(1)	119.3(2)
C(15)-C(16)-C(17)	121.0(3)
C(15)-C(16)-H(16)	119.5
C(17)-C(16)-H(16)	119.5
C(16)-C(17)-C(12)	117.7(2)
C(16)-C(17)-C(18)	122.2(2)
C(12)-C(17)-C(18)	119.8(2)
C(5)-C(18)-C(1)	118.1(2)
C(5)-C(18)-C(17)	117.4(2)
C(1)-C(18)-C(17)	124.4(2)
C(20)-C(19)-C(24)	119.0(3)
C(20)-C(19)-C(1)	119.9(3)
C(24)-C(19)-C(1)	121.1(3)
C(21)-C(20)-C(19)	120.1(3)
C(21)-C(20)-H(20)	119.9
C(19)-C(20)-H(20)	119.9

C(22)-C(21)-C(20)	120.7(3)
C(22)-C(21)-H(21)	119.6
C(20)-C(21)-H(21)	119.6
C(23)-C(22)-C(21)	119.7(3)
C(23)-C(22)-H(22)	120.1
C(21)-C(22)-H(22)	120.1
C(22)-C(23)-C(24)	120.0(3)
C(22)-C(23)-H(23)	120.0
C(24)-C(23)-H(23)	120.0
C(23)-C(24)-C(19)	120.4(3)
C(23)-C(24)-H(24)	119.8
C(19)-C(24)-H(24)	119.8
N(2)-C(25)-N(1)	127.6(3)
N(2)-C(25)-H(25)	116.2
N(1)-C(25)-H(25)	116.2
N(2)-C(26)-C(27)	122.7(3)
N(2)-C(26)-H(26)	118.7
C(27)-C(26)-H(26)	118.7
C(26)-C(27)-C(28)	116.4(3)
C(26)-C(27)-C(2)	120.6(3)
C(28)-C(27)-C(2)	122.9(3)
N(1)-C(28)-C(27)	122.5(3)
N(1)-C(28)-H(28)	118.8
C(27)-C(28)-H(28)	118.8
N(4)-C(29)-N(3)	127.4(3)
N(4)-C(29)-H(29)	116.3
N(3)-C(29)-H(29)	116.3
N(4)-C(30)-C(31)	123.5(3)
N(4)-C(30)-H(30)	118.2
C(31)-C(30)-H(30)	118.2
C(32)-C(31)-C(30)	115.3(2)
C(32)-C(31)-C(3)	122.3(3)
C(30)-C(31)-C(3)	122.4(3)
N(3)-C(32)-C(31)	122.9(3)

N(3)-C(32)-H(32)	118.5
C(31)-C(32)-H(32)	118.5
C(38)-C(33)-C(34)	118.5(3)
C(38)-C(33)-C(4)	118.9(2)
C(34)-C(33)-C(4)	122.6(2)
C(35)-C(34)-C(33)	120.3(3)
C(35)-C(34)-H(34)	119.9
C(33)-C(34)-H(34)	119.9
C(36)-C(35)-C(34)	120.4(3)
C(36)-C(35)-H(35)	119.8
C(34)-C(35)-H(35)	119.8
C(37)-C(36)-C(35)	119.7(3)
C(37)-C(36)-H(36)	120.2
C(35)-C(36)-H(36)	120.2
C(36)-C(37)-C(38)	120.2(3)
C(36)-C(37)-H(37)	119.9
C(38)-C(37)-H(37)	119.9
C(37)-C(38)-C(33)	120.9(3)
C(37)-C(38)-H(38)	119.5
C(33)-C(38)-H(38)	119.5
C(25)-N(1)-C(28)	115.5(3)
C(25)-N(2)-C(26)	115.3(3)
C(29)-N(3)-C(32)	115.7(3)
C(29)-N(4)-C(30)	115.1(3)

Symmetry transformations used to generate equivalent atoms:

Table 9.3.4 Anisotropic displacement parameters ($Å^2 x\ 10^3$) for **33c**. The anisotropic displacement factor exponent takes the form: $-2p^2[\ h^2 a^{*2} U^{11} + ... + 2\ h\ k\ a^*\ b^*\ U^{12}\ ]$

	U^{11}	U^{22}	U^{33}	U^{23}	U^{13}	U^{12}
C(1)	15(1)	11(1)	18(1)	-1(1)	3(1)	0(1)
C(2)	16(1)	12(1)	20(1)	-1(1)	5(1)	-1(1)
C(3)	15(1)	9(1)	20(1)	-1(1)	3(1)	1(1)
C(4)	16(1)	10(1)	18(1)	-1(1)	2(1)	1(1)
C(5)	16(1)	12(1)	17(1)	-1(1)	4(1)	1(1)
C(6)	16(1)	14(2)	16(1)	-3(1)	4(1)	-2(1)
C(7)	15(1)	17(2)	18(1)	-4(1)	2(1)	0(1)
C(8)	24(1)	18(2)	16(1)	2(1)	3(1)	-1(1)
C(9)	18(1)	28(2)	24(2)	2(1)	8(1)	-5(1)
C(10)	14(1)	29(2)	26(2)	1(1)	5(1)	-1(1)
C(11)	16(1)	19(2)	20(1)	-1(1)	2(1)	-1(1)
C(12)	17(1)	19(2)	19(1)	-4(1)	2(1)	0(1)
C(13)	14(1)	27(2)	27(2)	-1(1)	6(1)	0(1)
C(14)	16(1)	24(2)	27(2)	-1(1)	0(1)	4(1)
C(15)	20(1)	15(2)	19(1)	2(1)	-2(1)	1(1)
C(16)	19(1)	16(2)	17(1)	-2(1)	4(1)	0(1)
C(17)	15(1)	14(2)	20(1)	-5(1)	2(1)	0(1)
C(18)	16(1)	10(1)	19(1)	-2(1)	2(1)	-2(1)
C(19)	11(1)	24(2)	18(1)	-1(1)	5(1)	2(1)
C(20)	21(1)	24(2)	25(2)	-1(1)	4(1)	-2(1)
C(21)	26(2)	39(2)	22(2)	-8(1)	3(1)	-3(1)
C(22)	24(2)	54(2)	15(1)	3(2)	3(1)	0(2)
C(23)	19(2)	39(2)	23(2)	10(1)	6(1)	1(1)
C(24)	16(1)	26(2)	22(2)	1(1)	4(1)	0(1)
C(25)	21(2)	36(2)	27(2)	8(1)	11(1)	7(1)
C(26)	20(1)	24(2)	24(2)	0(1)	7(1)	2(1)
C(27)	12(1)	22(2)	15(1)	4(1)	2(1)	2(1)
C(28)	20(1)	24(2)	18(1)	2(1)	5(1)	0(1)
C(29)	16(1)	34(2)	27(2)	3(1)	3(1)	-5(1)

C(30)	16(1)	19(2)	21(1)	1(1)	2(1)	-2(1)
C(31)	15(1)	20(2)	18(1)	4(1)	6(1)	-3(1)
C(32)	17(1)	25(2)	25(2)	-2(1)	6(1)	-2(1)
C(33)	15(1)	18(2)	18(1)	-1(1)	3(1)	-6(1)
C(34)	17(1)	22(2)	19(1)	2(1)	3(1)	-4(1)
C(35)	20(1)	27(2)	24(2)	9(1)	-3(1)	-8(1)
C(36)	39(2)	28(2)	15(1)	-1(1)	3(1)	-11(2)
C(37)	37(2)	18(2)	20(2)	-5(1)	11(1)	-7(1)
C(38)	22(1)	15(2)	23(1)	0(1)	5(1)	-2(1)
N(1)	16(1)	33(2)	27(1)	6(1)	7(1)	-1(1)
N(2)	26(1)	30(2)	28(1)	0(1)	12(1)	5(1)
N(3)	19(1)	32(2)	28(1)	-5(1)	2(1)	-6(1)
N(4)	14(1)	26(2)	26(1)	4(1)	3(1)	-1(1)
Br(1)	26(1)	23(1)	26(1)	6(1)	0(1)	6(1)
Br(2)	27(1)	22(1)	23(1)	5(1)	4(1)	-4(1)

Table 9.3.5 Hydrogen coordinates (x 10^4) and isotropic displacement parameters (Å^{2}x 10^3) for **33c**.

	x	y	z	U(eq)
H(7)	4694	1387	5116	20
H(9)	1672	838	5317	28
H(10)	1230	2138	4464	28
H(13)	909	3538	3826	27
H(14)	468	4627	2883	27
H(16)	3445	4607	2472	21
H(20)	4324	2111	2159	28
H(21)	4091	2366	1017	34
H(22)	4562	4106	539	37
H(23)	5332	5581	1201	32
H(24)	5617	5318	2345	25
H(25)	9240	3242	2016	33
H(26)	6759	1796	2585	27
H(28)	7583	5026	3169	25
H(29)	10120	3720	5029	31
H(30)	8022	1980	3949	23
H(32)	7307	4910	4880	26
H(34)	6966	1885	5276	23
H(35)	7225	1858	6431	29
H(36)	6178	2966	7061	33
H(37)	4890	4139	6535	30
H(38)	4655	4215	5385	24

9.4.1 N=7 AGNR Quantum Espresso Code

```
RELAX CALCULATION INPUT
&CONTROL
            calculation = 'relax' ,
            pseudo_dir = '/usr/software/espresso-5.1.1/pseudo' ,
            prefix = '7AGNR' ,
            forc_conv_thr = 1.0D-3 ,
 /
 &SYSTEM
                ibrav = 8,
                a = 4.25,
                b = 40,
                c = 40,
                nat = 18,
                ntyp = 2,
                ecutwfc = 90.0 ,
                ecutrho = 270.0 ,
 /
 &ELECTRONS
                conv_thr = 0.0001,
 /
&IONS
/
ATOMIC_SPECIES
   C   12.01070  C.pbe-mt_gipaw.UPF
   H   1.007940  H.pbe-mt_fhi.UPF
ATOMIC_POSITIONS angstrom
C       2.481081972   1.737801521   0.104651858
C       1.770673111   0.500322584   0.104718157
C       0.349147737   0.500450253   0.104736154
C      -0.360463651   1.738017967   0.104657682
C       0.349980802   2.975242580   0.104652033
C       1.771511825   2.975111191   0.104661314
C       2.470988354  -0.729854271   0.104798653
C       1.741052417  -1.939215059   0.104891805
C       0.377643646  -1.938957814   0.104875125
C      -0.351862047  -0.729545350   0.104797843
C      -0.350351501   4.205391540   0.104706321
C       0.379616882   5.415186295   0.104791734
C       1.743071636   5.414923253   0.104807911
C       2.472509920   4.205066718   0.104713692
H       2.259233812  -2.893211880   0.105045935
H      -0.141480205  -2.892436936   0.104984124
```

```
H      -0.138623393   6.369184901   0.104943612
H       2.262268682   6.368422506   0.104966049
K_POINTS automatic
 32 1 1   0 0 0

NON SELF-CONSISTENT INPUT
&CONTROL
            calculation = 'nscf' ,
            pseudo_dir = '/usr/software/espresso-5.1.1/pseudo' ,
            outdir = '/home/cloke/quantum_espresso/7AGNR_norm_con/238512',
            prefix = '7AGNR' ,
            forc_conv_thr = 1.0D-3 ,
/
 &SYSTEM
                ibrav = 8,
                a = 4.25,
                b = 40,
                c = 40,
                nat = 18,
                ntyp = 2,
                ecutwfc = 90.0 ,
                ecutrho = 270.0 ,
                nbnd = 35,
/
 &ELECTRONS
              conv_thr = 0.0001,
/
&IONS
/
ATOMIC_SPECIES
   C   12.01070  C.pbe-mt_gipaw.UPF
   H   1.007940  H.pbe-mt_fhi.UPF
ATOMIC_POSITIONS angstrom
C       2.481081972   1.737801521   0.104651858
C       1.770673111   0.500322584   0.104718157
C       0.349147737   0.500450253   0.104736154
C      -0.360463651   1.738017967   0.104657682
C       0.349980802   2.975242580   0.104652033
C       1.771511825   2.975111191   0.104661314
C       2.470988354  -0.729854271   0.104798653
C       1.741052417  -1.939215059   0.104891805
C       0.377643646  -1.938957814   0.104875125
C      -0.351862047  -0.729545350   0.104797843
C      -0.350351501   4.205391540   0.104706321
```

```
C       0.379616882   5.415186295   0.104791734
C       1.743071636   5.414923253   0.104807911
C       2.472509920   4.205066718   0.104713692
H       2.259233812  -2.893211880   0.105045935
H      -0.141480205  -2.892436936   0.104984124
H      -0.138623393   6.369184901   0.104943612
H       2.262268682   6.368422506   0.104966049
K_POINTS automatic
 32 1 1   0 0 0

DENSITY OF STATES INPUT
&DOS
                prefix = '7AGNR',
                outdir = '/home/cloke/quantum_espresso/7AGNR_norm_con/238512/' ,
                fildos = '7AGNR_fildos' ,
                ngauss = 0,
                degauss = 0.000073499,
                DeltaE = 0.01,
/

BAND STRUCTURE INPUT
&BANDS
                prefix = '7AGNR' ,
                outdir = '/home/cloke/quantum_espresso/7AGNR_norm_con/238512',
                filband = '7AGNR_bands_filband' ,
/

VISUALIZATION OF VALENCE BAND INPUT
&INPUTPP
                prefix = '7AGNR',
                outdir = '/home/cloke/quantum_espresso/7AGNR_norm_con/238512',
               filplot = '7AGNR_VB_filplot',
               plot_num = 7,
               kpoint = 1,
               kband = 30,
/
 &PLOT
                 nfile = 1,
                 weight(1) = 1.0,
                 fileout = '7AGNR_VB_fileout',
                 iflag = 3,
                 output_format = 6,
                 interpolation = 'fourier',
/
```

```
VISUALIZATION OF CONDUCTION BAND INPUT
&INPUTPP
                prefix = '7AGNR' ,
                outdir = '/home/cloke/quantum_espresso/7AGNR_norm_con/238512' ,
                filplot = '7AGNR_CB_2_filplot_xcrysden' ,
                plot_num = 7,
                kpoint = 1,
                kband = 32,
/
 &PLOT
                 nfile = 1 ,
                 weight(1) = 1.0,
                 fileout = '7AGNR_CB_2_fileout_xcrysden' ,
                 iflag = 3 ,
                 output_format = 5,
                 interpolation = 'fourier' ,
/
```

9.4.2 Boron-Doped n=7 AGNR Quantum Espresso Code

```
RELAX CALCULATION INPUT
&CONTROL
            calculation = 'relax',
            !verbosity = 'high',
            prefix = 'Bdoped',
            pseudo_dir = "/usr/software/espresso-5.1.1/pseudo",
            forc_conv_thr = 1.0D-3,
/
 &SYSTEM
                 ibrav = 8,
                 a = 13.075
                 b = 30
                 c = 30
                 nat = 54,
                 ntyp = 3,
                 ecutwfc = 90.0 ,
                 ecutrho = 360.0 ,
/
 &ELECTRONS
               conv_thr = 0.0001,
/
&IONS
```

```
/
ATOMIC_SPECIES
   C   12.01070  C.pbe-mt_fhi.UPF
   B   10.81100  B.pbe-mt_fhi.UPF
   H   1.007940  H.pbe-mt_fhi.UPF
ATOMIC_POSITIONS angstroms
C       5.810774031  -2.473686403   0.000000000
C       5.810774031   2.473686403   0.000000000
C       5.096606885  -1.237106152   0.000000000
C       3.656352771  -1.236098557   0.000000000
C       2.921579696  -2.484411566   0.000000000
C       3.674948545  -3.657850953   0.000000000
C       5.066132112  -3.656144553   0.000000000
C       5.066132112   3.656144553   0.000000000
C       3.674948545   3.657850953   0.000000000
C       2.921579696   2.484411566   0.000000000
C       3.656352771   1.236098557   0.000000000
C       5.096606885   1.237106152   0.000000000
C       1.446812130  -2.536643515   0.000000000
C       1.446812130   2.536643515   0.000000000
C       0.707341280  -1.337551318   0.000000000
C      -0.707341280  -1.337551318   0.000000000
C      -1.446812130  -2.536643515   0.000000000
C      -0.695236870  -3.738218282   0.000000000
C       0.695236870  -3.738218282   0.000000000
C       0.695236870   3.738218282   0.000000000
C      -0.695236870   3.738218282   0.000000000
C      -1.446812130   2.536643515   0.000000000
C      -0.707341280   1.337551318   0.000000000
C       0.707341280   1.337551318   0.000000000
C      -2.921579696  -2.484411566   0.000000000
C      -2.921579696   2.484411566   0.000000000
C      -5.810874031  -2.473486403   0.000000000
C      -5.066132112  -3.656044553   0.000000000
C      -3.674948545  -3.657750953   0.000000000
C      -3.674948545   3.657750953   0.000000000
C      -5.066132112   3.656044553   0.000000000
C      -5.810874031   2.473486403   0.000000000
C      -5.096606885   1.237006152   0.000000000
C      -3.656352771   1.235998557   0.000000000
H       3.173790934  -4.624055449   0.000000000
H       5.570473821  -4.620039689   0.000000000
H       5.570473821   4.620039689   0.000000000
H       3.173790934   4.624055449   0.000000000
```

```
H       -1.192843781  -4.708124336   0.000000000
H        1.192843781  -4.708124336   0.000000000
H        1.192843781   4.708124336   0.000000000
H       -1.192843781   4.708124336   0.000000000
H       -5.570573821  -4.619939689   0.000000000
H       -3.173890934  -4.624055449   0.000000000
H       -3.173890934   4.624055449   0.000000000
H       -5.570573821   4.619939689   0.000000000
C        2.966080402   0.000000000   0.000000000
C       -5.809979962   0.000000000   0.000000000
C       -2.966080402   0.000000000   0.000000000
C       -3.656352771  -1.235998557   0.000000000
C       -5.096606885  -1.237006152   0.000000000
B        1.445667566   0.000000000   0.000000000
B       -1.445667566   0.000000000   0.000000000
C        5.810079962   0.000000000   0.000000000
K_POINTS automatic
32 1 1 0 0 0

NON SELF-CONSISTENT INPUT
&CONTROL
            calculation = 'nscf',
            !verbosity = 'high',
            prefix = 'Bdoped',
            pseudo_dir = "/usr/software/espresso-5.1.1/pseudo",
            outdir='/home/cloke/quantum_espresso/Bdoped_norm_conserving/238567',
            forc_conv_thr = 1.0D-3,
 /
 &SYSTEM
                ibrav = 8,
                a = 13.075
                b = 30
                c = 30
                nat = 54,
                ntyp = 3,
                ecutwfc = 90.0 ,
                ecutrho = 360.0 ,
                nbnd=100,
 /
 &ELECTRONS
              conv_thr = 0.0001,
 /
&IONS
/
```

```
ATOMIC_SPECIES
   C  12.01070  C.pbe-mt_fhi.UPF
   B  10.81100  B.pbe-mt_fhi.UPF
   H  1.007940  H.pbe-mt_fhi.UPF
ATOMIC_POSITIONS angstroms
C       5.810774031  -2.473686403   0.000000000
C       5.810774031   2.473686403   0.000000000
C       5.096606885  -1.237106152   0.000000000
C       3.656352771  -1.236098557   0.000000000
C       2.921579696  -2.484411566   0.000000000
C       3.674948545  -3.657850953   0.000000000
C       5.066132112  -3.656144553   0.000000000
C       5.066132112   3.656144553   0.000000000
C       3.674948545   3.657850953   0.000000000
C       2.921579696   2.484411566   0.000000000
C       3.656352771   1.236098557   0.000000000
C       5.096606885   1.237106152   0.000000000
C       1.446812130  -2.536643515   0.000000000
C       1.446812130   2.536643515   0.000000000
C       0.707341280  -1.337551318   0.000000000
C      -0.707341280  -1.337551318   0.000000000
C      -1.446812130  -2.536643515   0.000000000
C      -0.695236870  -3.738218282   0.000000000
C       0.695236870  -3.738218282   0.000000000
C       0.695236870   3.738218282   0.000000000
C      -0.695236870   3.738218282   0.000000000
C      -1.446812130   2.536643515   0.000000000
C      -0.707341280   1.337551318   0.000000000
C       0.707341280   1.337551318   0.000000000
C      -2.921579696  -2.484411566   0.000000000
C      -2.921579696   2.484411566   0.000000000
C      -5.810874031  -2.473486403   0.000000000
C      -5.066132112  -3.656044553   0.000000000
C      -3.674948545  -3.657750953   0.000000000
C      -3.674948545   3.657750953   0.000000000
C      -5.066132112   3.656044553   0.000000000
C      -5.810874031   2.473486403   0.000000000
C      -5.096606885   1.237006152   0.000000000
C      -3.656352771   1.235998557   0.000000000
H       3.173790934  -4.624055449   0.000000000
H       5.570473821  -4.620039689   0.000000000
H       5.570473821   4.620039689   0.000000000
H       3.173790934   4.624055449   0.000000000
H      -1.192843781  -4.708124336   0.000000000
```

```
H       1.192843781  -4.708124336   0.000000000
H       1.192843781   4.708124336   0.000000000
H      -1.192843781   4.708124336   0.000000000
H      -5.570573821  -4.619939689   0.000000000
H      -3.173890934  -4.624055449   0.000000000
H      -3.173890934   4.624055449   0.000000000
H      -5.570573821   4.619939689   0.000000000
C       2.966080402   0.000000000   0.000000000
C      -5.809979962   0.000000000   0.000000000
C      -2.966080402   0.000000000   0.000000000
C      -3.656352771  -1.235998557   0.000000000
C      -5.096606885  -1.237006152   0.000000000
B       1.445667566   0.000000000   0.000000000
B      -1.445667566   0.000000000   0.000000000
C       5.810079962   0.000000000   0.000000000
K_POINTS automatic
32 1 1 0 0 0

DENSITY OF STATES INPUT
&DOS
                prefix = 'Bdoped',
                outdir = '/home/cloke/quantum_espresso/Bdoped_norm_conserving/238567' ,
                fildos = 'Bdoped_fildos',
                ngauss = 0 ,
                degauss = 0.00293996,
                DeltaE = 0.01 ,
 /


BAND STRUCTURE CALCULATION INPUT
&BANDS
                prefix = 'Bdoped' ,
                outdir = '/home/cloke/quantum_espresso/Bdoped_norm_conserving/238567' ,
                filband = 'filband' ,
 /

VISUALIZATION OF VALENCE BAND INPUT
&INPUTPP
                prefix = '3_Bdoped' ,
                outdir = '/home/cloke/quantum_espresso/3_Bdoped/223569' ,
                filplot = '3_Bdoped_VB_filplot' ,
                plot_num = 7,
               kpoint = 1,
               kband = 89,
```

```
/
 &PLOT
                 nfile = 1 ,
                 weight(1) = 1.0,
                 fileout = '3_Bdoped_VB_fileout' ,
                 iflag = 3 ,
                 output_format = 5 ,
                 interpolation = 'fourier' ,
/
VISUALIZATION OF CONDUCTION BAND INPUT
&INPUTPP
                prefix = '3_Bdoped' ,
                outdir = '/home/cloke/quantum_espresso/3_Bdoped/223569' ,
                filplot = '3_Bdoped_CB_filplot' ,
                plot_num = 7,
                kpoint = 1,
                kband = 90,
/
 &PLOT
                 nfile = 1 ,
                 weight(1) = 1.0,
                 fileout = '3_Bdoped_CB_fileout' ,
                 iflag = 3 ,
                 output_format = 5 ,
                 interpolation = 'fourier' ,
/
```

9.4.3 Chevron-type GNR Quantum Espresso Code

C-GNR **35a**

```
SELF-CONSISTENT CALCULATION INPUT
&CONTROL
            calculation = 'scf' ,
            pseudo_dir = '/usr/software/espresso-5.1.1/pseudo/' ,
            prefix = 'C_chevron' ,
            verbosity = 'high' ,
            forc_conv_thr = 1.0D-3 ,
/
 &SYSTEM
            ibrav = 8,
              celldm(1) = 32.31,
              celldm(2) = 5,
              celldm(3) = 20,
              nat = 108,
```

```
              ntyp = 2,
              ecutwfc = 5,
              ecutrho = 20,
/
 &ELECTRONS
              conv_thr = 0.000001 ,
              diagonalization = 'cg' ,
              mixing_beta = 0.3,
              mixing_ndim = 4,
/
 &IONS
/
ATOMIC_SPECIES
   C   12.01070  C.pbe-mt_fhi.UPF
   H    1.00794  H.pbe-mt_fhi.UPF
ATOMIC_POSITIONS angstrom
C       -2.58830      28.97900      -0.86330
C       -1.89040      30.21470      -0.86330
C       -2.66050      31.40380      -0.86330
C       -4.05220      31.39170      -0.86330
C       -4.71360      30.16780      -0.86330
C       -4.01040      28.93700      -0.86330
C       -1.85790      27.75990      -0.86330
C       -2.51760      26.50500      -0.86330
C       -1.80040      25.28660      -0.86320
C       -0.30460      25.31880      -0.86330
C        0.35970      26.56700      -0.86330
C       -0.35340      27.79230      -0.86330
C        0.32400      29.04180      -0.86330
C       -3.94330      26.46310      -0.86320
C       -2.50240      24.05970      -0.86320
C        0.44970      24.12340      -0.86330
C        1.78590      26.58660      -0.86330
C        1.74660      29.06100      -0.86330
C        2.39620      30.32100      -0.86340
C        1.68270      31.51530      -0.86340
C        0.29180      31.46740      -0.86330
C       -0.42650      30.24620      -0.86330
C       -4.67650      27.68510      -0.86330
C       -6.08200      27.60490      -0.86320
C       -6.75280      26.39100      -0.86320
C       -6.06700      25.16440      -0.86320
C       -4.64320      25.20850      -0.86320
C       -3.92270      23.98790      -0.86320
```

C	-4.62040	22.74320	-0.86320
C	-3.87950	21.54130	-0.86320
C	-2.41950	21.63590	-0.86320
C	-1.73200	22.79700	-0.86320
C	-0.26570	22.82870	-0.86320
C	0.47110	21.69830	-0.86320
C	1.93380	21.66680	-0.86320
C	2.62240	22.89950	-0.86330
C	1.87180	24.11290	-0.86330
C	2.53910	25.36330	-0.86330
C	3.96350	25.38050	-0.86330
C	4.59580	26.63550	-0.86330
C	3.87340	27.81940	-0.86330
C	2.46580	27.83900	-0.86330
C	-6.03300	22.70850	-0.86320
C	4.03520	22.92540	-0.86330
C	4.71090	24.17390	-0.86330
C	4.76640	21.70350	-0.86330
C	6.18310	21.72720	-0.86330
C	6.84650	22.95770	-0.86330
C	6.12600	24.15130	-0.86330
C	6.89610	20.52370	-0.86330
C	6.25740	19.27920	-0.86320
C	7.00270	18.08870	-0.86320
C	4.83830	19.23130	-0.86320
C	6.37370	16.83950	-0.86320
C	4.09040	20.45530	-0.86320
C	2.66890	20.44170	-0.86320
C	2.05020	19.16960	-0.86320
C	2.77670	17.97660	-0.86320
C	4.18360	17.96240	-0.86320
C	4.96090	16.76640	-0.86320
C	4.36590	15.47740	-0.86310
C	5.15480	14.31040	-0.86310
C	6.55660	14.40560	-0.86320
C	7.16530	15.67190	-0.86320
C	-6.76180	23.92670	-0.86320
C	-8.17470	23.84320	-0.86320
C	-8.84310	22.61990	-0.86320
C	-8.12740	21.41920	-0.86320
C	-6.71100	21.45620	-0.86320
C	-8.78820	20.18630	-0.86320
C	-8.79090	17.74950	-0.86320
C	-8.09680	18.97060	-0.86320

```
C       -8.10930     16.52840     -0.86320
C       -6.67710     18.98330     -0.86320
C       -8.85070     15.32830     -0.86320
C       -8.18890     14.08900     -0.86320
C       -6.78430     14.05340     -0.86320
C       -6.04550     15.25290     -0.86320
C       -6.69460     16.51540     -0.86320
C       -5.96880     17.74360     -0.86320
C       -4.56370     17.81800     -0.86320
C       -3.88880     19.04110     -0.86320
C       -4.56140     20.28560     -0.86320
C       -5.98210     20.23820     -0.86320
H       -4.60930     32.31760     -0.86330
H        2.19940     32.46430     -0.86340
H       -6.71270     28.47590     -0.86320
H       -7.82680     26.45330     -0.86320
H       -1.90940     20.70280     -0.86320
H        0.00160     20.74420     -0.86320
H        5.66610     26.74410     -0.86340
H        4.46630     28.71670     -0.86340
H        6.71740     25.05010     -0.86340
H        0.98220     19.04690     -0.86310
H        2.20470     17.06440     -0.86310
H        4.68110     13.33910     -0.86310
H       -8.80450     24.71540     -0.86320
H       -3.95350     16.93090     -0.86320
H       -2.81650     18.96430     -0.86320
H       -4.97220     15.16350     -0.86320
H        3.29740     15.34230     -0.86310
H       -6.26980     13.10320     -0.86320
H       -5.78770     30.22560     -0.86330
H        3.46690     30.42490     -0.86340
H        7.16360     13.51170     -0.86320
H       -8.75740     13.17020     -0.86320
H       -2.20470     32.37840     -0.86330
H       -0.20570     32.42140     -0.86340
K_POINTS automatic
 8 1 1   0 0 0


NON- SELF-CONSISTENT CALCULATION INPUT
&CONTROL
            calculation = 'nscf' ,
            pseudo_dir = '/usr/software/espresso-5.1.1/pseudo/' ,
```

```
outdir='/home/cloke/quantum_espresso/Chevron_type/scf/updated_C_coords/248882',
                prefix = 'C_chevron' ,
                verbosity = 'high' ,
                forc_conv_thr = 1.0D-3 ,
/
&SYSTEM
                ibrav = 8,
                celldm(1) = 32.31,
                celldm(2) = 5,
                celldm(3) = 20,
                nat = 108,
                ntyp = 2,
                ecutwfc = 5,
                ecutrho = 20,
                nbnd=184,
/
&ELECTRONS
               conv_thr = 0.000001 ,
               diagonalization = 'cg' ,
               mixing_beta = 0.3,
               mixing_ndim = 4,
/
&IONS
/
ATOMIC_SPECIES
   C   12.01070  C.pbe-mt_fhi.UPF
   H    1.00794  H.pbe-mt_fhi.UPF
ATOMIC_POSITIONS angstrom
C       -2.58830      28.97900      -0.86330
C       -1.89040      30.21470      -0.86330
C       -2.66050      31.40380      -0.86330
C       -4.05220      31.39170      -0.86330
C       -4.71360      30.16780      -0.86330
C       -4.01040      28.93700      -0.86330
C       -1.85790      27.75990      -0.86330
C       -2.51760      26.50500      -0.86330
C       -1.80040      25.28660      -0.86320
C       -0.30460      25.31880      -0.86330
C        0.35970      26.56700      -0.86330
C       -0.35340      27.79230      -0.86330
C        0.32400      29.04180      -0.86330
C       -3.94330      26.46310      -0.86320
C       -2.50240      24.05970      -0.86320
```

C	0.44970	24.12340	-0.86330
C	1.78590	26.58660	-0.86330
C	1.74660	29.06100	-0.86330
C	2.39620	30.32100	-0.86340
C	1.68270	31.51530	-0.86340
C	0.29180	31.46740	-0.86330
C	-0.42650	30.24620	-0.86330
C	-4.67650	27.68510	-0.86330
C	-6.08200	27.60490	-0.86320
C	-6.75280	26.39100	-0.86320
C	-6.06700	25.16440	-0.86320
C	-4.64320	25.20850	-0.86320
C	-3.92270	23.98790	-0.86320
C	-4.62040	22.74320	-0.86320
C	-3.87950	21.54130	-0.86320
C	-2.41950	21.63590	-0.86320
C	-1.73200	22.79700	-0.86320
C	-0.26570	22.82870	-0.86320
C	0.47110	21.69830	-0.86320
C	1.93380	21.66680	-0.86320
C	2.62240	22.89950	-0.86330
C	1.87180	24.11290	-0.86330
C	2.53910	25.36330	-0.86330
C	3.96350	25.38050	-0.86330
C	4.59580	26.63550	-0.86330
C	3.87340	27.81940	-0.86330
C	2.46580	27.83900	-0.86330
C	-6.03300	22.70850	-0.86320
C	4.03520	22.92540	-0.86330
C	4.71090	24.17390	-0.86330
C	4.76640	21.70350	-0.86330
C	6.18310	21.72720	-0.86330
C	6.84650	22.95770	-0.86330
C	6.12600	24.15130	-0.86330
C	6.89610	20.52370	-0.86330
C	6.25740	19.27920	-0.86320
C	7.00270	18.08870	-0.86320
C	4.83830	19.23130	-0.86320
C	6.37370	16.83950	-0.86320
C	4.09040	20.45530	-0.86320
C	2.66890	20.44170	-0.86320
C	2.05020	19.16960	-0.86320
C	2.77670	17.97660	-0.86320
C	4.18360	17.96240	-0.86320

C	4.96090	16.76640	-0.86320
C	4.36590	15.47740	-0.86310
C	5.15480	14.31040	-0.86310
C	6.55660	14.40560	-0.86320
C	7.16530	15.67190	-0.86320
C	-6.76180	23.92670	-0.86320
C	-8.17470	23.84320	-0.86320
C	-8.84310	22.61990	-0.86320
C	-8.12740	21.41920	-0.86320
C	-6.71100	21.45620	-0.86320
C	-8.78820	20.18630	-0.86320
C	-8.79090	17.74950	-0.86320
C	-8.09680	18.97060	-0.86320
C	-8.10930	16.52840	-0.86320
C	-6.67710	18.98330	-0.86320
C	-8.85070	15.32830	-0.86320
C	-8.18890	14.08900	-0.86320
C	-6.78430	14.05340	-0.86320
C	-6.04550	15.25290	-0.86320
C	-6.69460	16.51540	-0.86320
C	-5.96880	17.74360	-0.86320
C	-4.56370	17.81800	-0.86320
C	-3.88880	19.04110	-0.86320
C	-4.56140	20.28560	-0.86320
C	-5.98210	20.23820	-0.86320
H	-4.60930	32.31760	-0.86330
H	2.19940	32.46430	-0.86340
H	-6.71270	28.47590	-0.86320
H	-7.82680	26.45330	-0.86320
H	-1.90940	20.70280	-0.86320
H	0.00160	20.74420	-0.86320
H	5.66610	26.74410	-0.86340
H	4.46630	28.71670	-0.86340
H	6.71740	25.05010	-0.86340
H	0.98220	19.04690	-0.86310
H	2.20470	17.06440	-0.86310
H	4.68110	13.33910	-0.86310
H	-8.80450	24.71540	-0.86320
H	-3.95350	16.93090	-0.86320
H	-2.81650	18.96430	-0.86320
H	-4.97220	15.16350	-0.86320
H	3.29740	15.34230	-0.86310
H	-6.26980	13.10320	-0.86320
H	-5.78770	30.22560	-0.86330

```
H        3.46690      30.42490      -0.86340
H        7.16360      13.51170      -0.86320
H       -8.75740      13.17020      -0.86320
H       -2.20470      32.37840      -0.86330
H       -0.20570      32.42140      -0.86340
K_POINTS automatic
 8 1 1   0 0 0
```

2N-GNR **35b**

```
SELF-CONSISTENT CALCULATION INPUT
&CONTROL
            calculation = 'scf' ,
            pseudo_dir = '/usr/software/espresso-5.1.1/pseudo/' ,
            prefix = '2N_chevron' ,
            verbosity = 'high' ,
            forc_conv_thr = 1.0D-3 ,
/
&SYSTEM
                ibrav = 8,
                celldm(1) = 32.31,
                celldm(2) = 5,
                celldm(3) = 20,
                nat = 104,
                ntyp = 3,
                ecutwfc = 5,
                ecutrho = 20,
/
&ELECTRONS
              conv_thr = 0.000001 ,
              diagonalization = 'cg' ,
              mixing_beta = 0.3,
              mixing_ndim = 4,
/
&IONS
/
ATOMIC_SPECIES
  C   12.01070  C.pbe-mt_fhi.UPF
  N   14.00670  N.pbe-mt_fhi.UPF
  H    1.00794  H.pbe-mt_fhi.UPF
ATOMIC_POSITIONS angstrom
C        1.58280      23.73490      -0.86330
C        0.87780      24.95120      -0.86330
C        1.55260      26.11890      -0.86330
N        2.86630      26.07460      -0.86330
```

C	3.60010	24.97510	-0.86330
C	2.98980	23.77170	-0.86330
C	0.89300	22.50460	-0.86330
C	1.58320	21.27810	-0.86330
C	0.89490	20.04830	-0.86330
C	-0.59980	20.04830	-0.86330
C	-1.28840	21.27780	-0.86330
C	-0.59840	22.50450	-0.86330
C	-1.28840	23.73470	-0.86320
C	3.00460	21.29020	-0.86330
C	1.62790	18.84630	-0.86330
C	-1.33280	18.84620	-0.86330
C	-2.70980	21.28990	-0.86320
C	-2.69540	23.77140	-0.86320
C	-3.30600	24.97460	-0.86320
N	-2.57250	26.07420	-0.86320
C	-1.25870	26.11870	-0.86320
C	-0.58370	24.95120	-0.86320
C	3.68930	22.53990	-0.86330
C	5.09230	22.52350	-0.86330
C	5.80830	21.32780	-0.86330
C	5.16450	20.07130	-0.86330
C	3.74060	20.06190	-0.86330
C	3.05050	18.82150	-0.86330
C	3.77890	17.59930	-0.86330
C	3.06490	16.37940	-0.86330
C	1.60010	16.42920	-0.86330
C	0.88250	17.57000	-0.86330
C	-0.58730	17.56990	-0.86330
C	-1.30470	16.42910	-0.86330
C	-2.76960	16.37940	-0.86330
C	-3.48380	17.59910	-0.86330
C	-2.75530	18.82140	-0.86330
C	-3.44560	20.06160	-0.86320
C	-4.86950	20.07090	-0.86320
C	-5.51330	21.32730	-0.86320
C	-4.79750	22.52310	-0.86320
C	-3.39460	22.53950	-0.86320
C	5.19240	17.61010	-0.86330
C	-4.89730	17.60980	-0.86320
C	-5.59440	18.84930	-0.86320
C	-5.60680	16.37630	-0.86330
C	-7.02420	16.37460	-0.86320
C	-7.70780	17.59520	-0.86320

C	-7.00830	18.80250	-0.86320
C	-7.71610	15.15670	-0.86320
C	-7.05410	13.92420	-0.86330
C	-7.76690	12.71180	-0.86330
C	-5.63440	13.90940	-0.86330
C	-7.08730	11.48840	-0.86330
C	-4.90630	15.14170	-0.86330
C	-3.48340	15.14470	-0.86330
C	-2.84000	13.88290	-0.86330
C	-3.55030	12.68070	-0.86330
C	-4.95290	12.65910	-0.86330
C	-5.68240	11.44330	-0.86330
C	-5.06050	10.24600	-0.86330
N	-5.80150	9.14590	-0.86330
C	-7.12430	9.08780	-0.86330
C	-7.76980	10.26250	-0.86330
C	5.88960	18.84980	-0.86330
C	7.30350	18.80270	-0.86330
C	8.00300	17.59550	-0.86330
C	7.31940	16.37500	-0.86330
C	5.90190	16.37670	-0.86330
C	8.01140	15.15740	-0.86330
C	8.06290	12.71290	-0.86330
C	7.34960	13.92490	-0.86330
C	7.38370	11.48930	-0.86320
C	5.92990	13.90980	-0.86330
C	8.06680	10.26380	-0.86320
C	7.42180	9.08880	-0.86320
N	6.09900	9.14640	-0.86320
C	5.35740	10.24620	-0.86320
C	5.97870	11.44370	-0.86320
C	5.24870	12.65940	-0.86320
C	3.84610	12.68080	-0.86320
C	3.13550	13.88300	-0.86320
C	3.77890	15.14480	-0.86330
C	5.20170	15.14200	-0.86330
H	5.63720	23.45720	-0.86330
H	6.88070	21.42350	-0.86330
H	1.10960	15.48450	-0.86330
H	-0.81420	15.48440	-0.86330
H	-6.58560	21.42310	-0.86320
H	-5.34270	23.45660	-0.86320
H	-7.61120	19.69420	-0.86320
H	-1.77020	13.77370	-0.86330

```
H        -3.00380       11.74830       -0.86330
H         7.90680       19.69420       -0.86330
H         3.29990       11.74810       -0.86320
H         2.06570       13.77360       -0.86320
H        -0.75070       27.07180       -0.86320
H        -4.38440       25.03300       -0.86320
H         1.01290       27.05440       -0.86320
H         4.67780       25.04510       -0.86330
H         4.28000       10.17110       -0.86320
H         7.98170        8.16530      -0.86320
H        -3.98160       10.19790       -0.86330
H        -7.62280        8.12970       -0.86330
K_POINTS automatic
 8 1 1   0 0 0

NON- SELF-CONSISTENT CALCULATION INPUT
&CONTROL
            calculation = 'nscf' ,
            pseudo_dir = '/usr/software/espresso-5.1.1/pseudo/' ,
            outdir='/home/cloke/quantum_espresso/Chevron_type/scf/2N/4th_try/248728',
            prefix = '2N_chevron' ,
            verbosity = 'high' ,
            forc_conv_thr = 1.0D-3 ,
/
 &SYSTEM
             ibrav = 8,
             celldm(1) = 32.31,
             celldm(2) = 5,
             celldm(3) = 20,
             nat = 104,
             ntyp = 3,
             ecutwfc = 5,
             ecutrho = 20,
             nbnd=184,
/
 &ELECTRONS
              conv_thr = 0.000001 ,
        diagonalization = 'cg' ,
        mixing_beta = 0.3,
        mixing_ndim = 4,
/
 &IONS
 /
ATOMIC_SPECIES
```

```
   C   12.01070  C.pbe-mt_fhi.UPF
   N   14.00670  N.pbe-mt_fhi.UPF
   H    1.00794  H.pbe-mt_fhi.UPF
ATOMIC_POSITIONS angstrom
   C    -1.930500000   12.218400000   -0.863100000
   C    -1.234100000   13.461800000   -0.863100000
   C    -1.946000000   14.613100000   -0.863200000
   N    -3.265900000   14.552000000   -0.863200000
   C    -3.983800000   13.441600000   -0.863200000
   C    -3.351600000   12.244100000   -0.863100000
   C    -1.233900000   10.988800000   -0.863100000
   C    -1.945500000    9.765600000   -0.863100000
   C    -1.238600000    8.539700000   -0.863100000
   C     0.182000000    8.539700000   -0.863100000
   C     0.888900000    9.765600000   -0.863100000
   C     0.177300000   10.988700000   -0.863100000
   C     0.874000000   12.218400000   -0.863100000
   C    -3.361300000    9.773100000   -0.863100000
   C    -1.956100000    7.318100000   -0.863100000
   C     0.899500000    7.318200000   -0.863100000
   C     2.304700000    9.773100000   -0.863100000
   C     2.294900000   12.244100000   -0.863100000
   C     2.927200000   13.441600000   -0.863100000
   N     2.209300000   14.552100000   -0.863100000
   C     0.889300000   14.613100000   -0.863100000
   C     0.177500000   13.461900000   -0.863100000
   C    -4.049600000   11.015900000   -0.863100000
   C    -5.453100000   10.994200000   -0.863100000
   C    -6.160200000    9.796200000   -0.863100000
   C    -5.508200000    8.544800000   -0.863100000
   C    -4.085000000    8.543600000   -0.863100000
   C    -3.381800000    7.312900000   -0.863100000
   C    -4.107700000    6.085500000   -0.863100000
   C    -3.414200000    4.851800000   -0.863100000
   C    -2.007600000    4.913200000   -0.863100000
   C    -1.241500000    6.097500000   -0.863100000
   C     0.184800000    6.097400000   -0.863100000
   C     0.951000000    4.913200000   -0.863100000
   C     2.357600000    4.851800000   -0.863100000
   C     3.051000000    6.085500000   -0.863100000
   C     2.325300000    7.312900000   -0.863100000
   C     3.028500000    8.543600000   -0.863100000
   C     4.451600000    8.544800000   -0.863100000
   C     5.103700000    9.796200000   -0.863100000
```

C	4.396500000	10.994200000	-0.863100000
C	2.993000000	11.016000000	-0.863100000
C	-5.524100000	6.084800000	-0.863100000
C	4.467500000	6.084800000	-0.863100000
C	5.169900000	7.321600000	-0.863100000
C	5.179600000	4.847600000	-0.863100000
C	6.597100000	4.851200000	-0.863200000
C	7.281300000	6.069800000	-0.863100000
C	6.583300000	7.275200000	-0.863200000
C	7.294500000	3.639600000	-0.863200000
C	6.639000000	2.406600000	-0.863200000
C	7.426200000	1.092500000	-0.863200000
C	5.213500000	2.363500000	-0.863100000
C	6.647500000	-0.196100000	-0.863100000
C	4.488100000	3.604600000	-0.863100000
C	3.067700000	3.615300000	-0.863100000
C	2.424400000	2.357400000	-0.863100000
C	3.133300000	1.157200000	-0.863100000
C	4.538100000	1.110200000	-0.863100000
C	5.249900000	-0.177700000	-0.863100000
C	4.542200000	-1.332900000	-0.863100000
N	5.234000000	-2.474700000	-0.863100000
C	6.562500000	-2.601100000	-0.863100000
C	7.277200000	-1.456800000	-0.863100000
C	-6.226500000	7.321600000	-0.863100000
C	-7.639900000	7.275200000	-0.863100000
C	-8.337800000	6.069800000	-0.863100000
C	-7.653700000	4.851200000	-0.863100000
C	-6.236200000	4.847600000	-0.863100000
C	-8.351100000	3.639600000	-0.863200000
C	-8.482900000	1.092500000	-0.863200000
C	-7.695500000	2.406600000	-0.863100000
C	-7.704100000	-0.196000000	-0.863100000
C	-6.270000000	2.363600000	-0.863100000
C	-8.333800000	-1.456800000	-0.863300000
C	-7.619100000	-2.601000000	-0.863300000
N	-6.290700000	-2.474700000	-0.863200000
C	-5.598800000	-1.332900000	-0.863200000
C	-6.306500000	-0.177700000	-0.863200000
C	-5.594600000	1.110200000	-0.863100000
C	-4.189900000	1.157200000	-0.863200000
C	-3.481100000	2.357400000	-0.863100000
C	-4.124300000	3.615300000	-0.863100000
C	-5.544700000	3.604500000	-0.863100000

```
   H     -6.017300000   11.915500000   -0.863100000
   H     -7.232800000    9.888600000   -0.863100000
   H     -1.489300000    3.981200000   -0.863100000
   H      0.432700000    3.981200000   -0.863100000
   H      6.176300000    9.888600000   -0.863100000
   H      4.960700000   11.915500000   -0.863100000
   H      7.189900000    8.164600000   -0.863100000
   H      1.353700000    2.250200000   -0.863100000
   H      2.560900000    0.241200000   -0.863100000
   H     -8.246600000    8.164600000   -0.863100000
   H     -3.617600000    0.241300000   -0.863200000
   H     -2.410300000    2.250200000   -0.863200000
   H     -1.434400000   15.564300000   -0.863300000
   H      0.393100000   15.572400000   -0.863100000
   H     -8.126300000   -3.554500000   -0.863300000
   H      7.011500000   -3.583300000   -0.863100000
   H     -4.519000000   -1.355800000   -0.863200000
   H      3.462600000   -1.304800000   -0.863100000
   H     -5.062400000   13.495900000   -0.863300000
   H      4.006400000   13.482500000   -0.863100000
K_POINTS automatic
 8 1 1   0 0 0
```

4N-GNR **35c**

```
SELF-CONSISTENT CALCULATION INPUT
&CONTROL
            calculation = 'scf' ,
            pseudo_dir = '/usr/software/espresso-5.1.1/pseudo/' ,
            prefix = '4N_chevron',
            verbosity = 'high' ,
            forc_conv_thr = 1.0D-3 ,
/
&SYSTEM
              ibrav = 8,
              celldm(1) = 32.31,
              celldm(2) = 5,
              celldm(3) = 20,
              nat = 100,
              ntyp = 3,
              ecutwfc = 5,
              ecutrho = 20,
/
&ELECTRONS
             conv_thr = 0.000001,
```

```
                diagonalization = 'cg' ,
                mixing_beta = 0.3,
                mixing_ndim = 4,
 /
ATOMIC_SPECIES
   C   12.01070  C.pbe-mt_fhi.UPF
   N   14.00670  N.pbe-mt_fhi.UPF
   H    1.00794  H.pbe-mt_fhi.UPF
ATOMIC_POSITIONS angstrom
C         1.58280       23.73490       -0.86330
C         0.87780       24.95120       -0.86330
N         1.55260       26.11890       -0.86330
C         2.86630       26.07460       -0.86330
N         3.60010       24.97510       -0.86330
C         2.98980       23.77170       -0.86330
C         0.89300       22.50460       -0.86330
C         1.58320       21.27810       -0.86330
C         0.89490       20.04830       -0.86330
C        -0.59980       20.04830       -0.86330
C        -1.28840       21.27780       -0.86330
C        -0.59840       22.50450       -0.86330
C        -1.28840       23.73470       -0.86320
C         3.00460       21.29020       -0.86330
C         1.62790       18.84630       -0.86330
C        -1.33280       18.84620       -0.86330
C        -2.70980       21.28990       -0.86320
C        -2.69540       23.77140       -0.86320
N        -3.30600       24.97460       -0.86320
C        -2.57250       26.07420       -0.86320
N        -1.25870       26.11870       -0.86320
C        -0.58370       24.95120       -0.86320
C         3.68930       22.53990       -0.86330
C         5.09230       22.52350       -0.86330
C         5.80830       21.32780       -0.86330
C         5.16450       20.07130       -0.86330
C         3.74060       20.06190       -0.86330
C         3.05050       18.82150       -0.86330
C         3.77890       17.59930       -0.86330
C         3.06490       16.37940       -0.86330
C         1.60010       16.42920       -0.86330
C         0.88250       17.57000       -0.86330
C        -0.58730       17.56990       -0.86330
C        -1.30470       16.42910       -0.86330
C        -2.76960       16.37940       -0.86330
```

C	-3.48380	17.59910	-0.86330
C	-2.75530	18.82140	-0.86330
C	-3.44560	20.06160	-0.86320
C	-4.86950	20.07090	-0.86320
C	-5.51330	21.32730	-0.86320
C	-4.79750	22.52310	-0.86320
C	-3.39460	22.53950	-0.86320
C	5.19240	17.61010	-0.86330
C	-4.89730	17.60980	-0.86320
C	-5.59440	18.84930	-0.86320
C	-5.60680	16.37630	-0.86330
C	-7.02420	16.37460	-0.86320
C	-7.70780	17.59520	-0.86320
C	-7.00830	18.80250	-0.86320
C	-7.71610	15.15670	-0.86320
C	-7.05410	13.92420	-0.86330
C	-7.76690	12.71180	-0.86330
C	-5.63440	13.90940	-0.86330
C	-7.08730	11.48840	-0.86330
C	-4.90630	15.14170	-0.86330
C	-3.48340	15.14470	-0.86330
C	-2.84000	13.88290	-0.86330
C	-3.55030	12.68070	-0.86330
C	-4.95290	12.65910	-0.86330
C	-5.68240	11.44330	-0.86330
N	-5.06050	10.24600	-0.86330
C	-5.80150	9.14590	-0.86330
N	-7.12430	9.08780	-0.86330
C	-7.76980	10.26250	-0.86330
C	5.88960	18.84980	-0.86330
C	7.30350	18.80270	-0.86330
C	8.00300	17.59550	-0.86330
C	7.31940	16.37500	-0.86330
C	5.90190	16.37670	-0.86330
C	8.01140	15.15740	-0.86330
C	8.06290	12.71290	-0.86330
C	7.34960	13.92490	-0.86330
C	7.38370	11.48930	-0.86320
C	5.92990	13.90980	-0.86330
C	8.06680	10.26380	-0.86320
N	7.42180	9.08880	-0.86320
C	6.09900	9.14640	-0.86320
N	5.35740	10.24620	-0.86320
C	5.97870	11.44370	-0.86320

```
C        5.24870      12.65940      -0.86320
C        3.84610      12.68080      -0.86320
C        3.13550      13.88300      -0.86320
C        3.77890      15.14480      -0.86330
C        5.20170      15.14200      -0.86330
H        3.39190      27.01740      -0.86330
H       -3.09820      27.01690      -0.86320
H        5.63720      23.45720      -0.86330
H        6.88070      21.42350      -0.86330
H        1.10960      15.48450      -0.86330
H       -0.81420      15.48440      -0.86330
H       -6.58560      21.42310      -0.86320
H       -5.34270      23.45660      -0.86320
H       -7.61120      19.69420      -0.86320
H       -1.77020      13.77370      -0.86330
H       -3.00380      11.74830      -0.86330
H       -5.27510       8.20350      -0.86330
H        7.90680      19.69420      -0.86330
H        3.29990      11.74810      -0.86320
H        2.06570      13.77360      -0.86320
H        5.57290       8.20400      -0.86320
K_POINTS automatic
 32 1 1   0 0 0


NON- SELF-CONSISTENT CALCULATION INPUT
&CONTROL
           calculation = 'nscf' ,
           pseudo_dir = '/usr/software/espresso-5.1.1/pseudo/' ,
           prefix = '4N_chevron',
           outdir='/home/cloke/quantum_espresso/Chevron_type/scf/updated_4N_coords/249222',
           verbosity = 'high' ,
           forc_conv_thr = 1.0D-3 ,
/
 &SYSTEM
           ibrav = 8,
              celldm(1) = 32.31,
              celldm(2) = 5,
              celldm(3) = 20,
              nat = 100,
              ntyp = 3,
              ecutwfc = 5,
              ecutrho = 20,
              nbnd=184,
```

```
/
 &ELECTRONS
                conv_thr = 0.000001,
                diagonalization = 'cg' ,
                mixing_beta = 0.3,
                mixing_ndim = 4,
/
ATOMIC_SPECIES
   C   12.01070  C.pbe-mt_fhi.UPF
   N   14.00670  N.pbe-mt_fhi.UPF
   H    1.00794  H.pbe-mt_fhi.UPF
ATOMIC_POSITIONS angstrom
C         1.58280       23.73490       -0.86330
C         0.87780       24.95120       -0.86330
N         1.55260       26.11890       -0.86330
C         2.86630       26.07460       -0.86330
N         3.60010       24.97510       -0.86330
C         2.98980       23.77170       -0.86330
C         0.89300       22.50460       -0.86330
C         1.58320       21.27810       -0.86330
C         0.89490       20.04830       -0.86330
C        -0.59980       20.04830       -0.86330
C        -1.28840       21.27780       -0.86330
C        -0.59840       22.50450       -0.86330
C        -1.28840       23.73470       -0.86320
C         3.00460       21.29020       -0.86330
C         1.62790       18.84630       -0.86330
C        -1.33280       18.84620       -0.86330
C        -2.70980       21.28990       -0.86320
C        -2.69540       23.77140       -0.86320
N        -3.30600       24.97460       -0.86320
C        -2.57250       26.07420       -0.86320
N        -1.25870       26.11870       -0.86320
C        -0.58370       24.95120       -0.86320
C         3.68930       22.53990       -0.86330
C         5.09230       22.52350       -0.86330
C         5.80830       21.32780       -0.86330
C         5.16450       20.07130       -0.86330
C         3.74060       20.06190       -0.86330
C         3.05050       18.82150       -0.86330
C         3.77890       17.59930       -0.86330
C         3.06490       16.37940       -0.86330
C         1.60010       16.42920       -0.86330
C         0.88250       17.57000       -0.86330
```

C	-0.58730	17.56990	-0.86330
C	-1.30470	16.42910	-0.86330
C	-2.76960	16.37940	-0.86330
C	-3.48380	17.59910	-0.86330
C	-2.75530	18.82140	-0.86330
C	-3.44560	20.06160	-0.86320
C	-4.86950	20.07090	-0.86320
C	-5.51330	21.32730	-0.86320
C	-4.79750	22.52310	-0.86320
C	-3.39460	22.53950	-0.86320
C	5.19240	17.61010	-0.86330
C	-4.89730	17.60980	-0.86320
C	-5.59440	18.84930	-0.86320
C	-5.60680	16.37630	-0.86330
C	-7.02420	16.37460	-0.86320
C	-7.70780	17.59520	-0.86320
C	-7.00830	18.80250	-0.86320
C	-7.71610	15.15670	-0.86320
C	-7.05410	13.92420	-0.86330
C	-7.76690	12.71180	-0.86330
C	-5.63440	13.90940	-0.86330
C	-7.08730	11.48840	-0.86330
C	-4.90630	15.14170	-0.86330
C	-3.48340	15.14470	-0.86330
C	-2.84000	13.88290	-0.86330
C	-3.55030	12.68070	-0.86330
C	-4.95290	12.65910	-0.86330
C	-5.68240	11.44330	-0.86330
N	-5.06050	10.24600	-0.86330
C	-5.80150	9.14590	-0.86330
N	-7.12430	9.08780	-0.86330
C	-7.76980	10.26250	-0.86330
C	5.88960	18.84980	-0.86330
C	7.30350	18.80270	-0.86330
C	8.00300	17.59550	-0.86330
C	7.31940	16.37500	-0.86330
C	5.90190	16.37670	-0.86330
C	8.01140	15.15740	-0.86330
C	8.06290	12.71290	-0.86330
C	7.34960	13.92490	-0.86330
C	7.38370	11.48930	-0.86320
C	5.92990	13.90980	-0.86330
C	8.06680	10.26380	-0.86320
N	7.42180	9.08880	-0.86320

```
C         6.09900       9.14640      -0.86320
N         5.35740      10.24620       -0.86320
C         5.97870      11.44370       -0.86320
C         5.24870      12.65940       -0.86320
C         3.84610      12.68080       -0.86320
C         3.13550      13.88300       -0.86320
C         3.77890      15.14480       -0.86330
C         5.20170      15.14200       -0.86330
H         3.39190      27.01740       -0.86330
H        -3.09820      27.01690       -0.86320
H         5.63720      23.45720       -0.86330
H         6.88070      21.42350       -0.86330
H         1.10960      15.48450       -0.86330
H        -0.81420      15.48440       -0.86330
H        -6.58560      21.42310       -0.86320
H        -5.34270      23.45660       -0.86320
H        -7.61120      19.69420       -0.86320
H        -1.77020      13.77370       -0.86330
H        -3.00380      11.74830       -0.86330
H        -5.27510       8.20350      -0.86330
H         7.90680      19.69420       -0.86330
H         3.29990      11.74810       -0.86320
H         2.06570      13.77360       -0.86320
H         5.57290       8.20400      -0.86320
K_POINTS automatic
  32 1 1   0 0 0
```

CO-GNR **44**

```
SELF-CONSISTENT CALCULATION INPUT
&CONTROL
                calculation = 'scf' ,
                pseudo_dir = '/usr/software/espresso-5.1.1/pseudo/' ,
                prefix = 'ketone',
                verbosity = 'high',
                forc_conv_thr = 1.0D-3,
/
 &SYSTEM
                 ibrav = 8,
                 celldm(1) = 32.31,
                 celldm(2) = 5,
                 celldm(3) = 20,
                 nat = 108,
                 ntyp = 3,
                 ecutwfc = 4,
```

```
            ecutrho = 16 ,
/
&ELECTRONS
            conv_thr = 0.000001,
            mixing_beta = 0.3,
            mixing_ndim = 4,
            diagonalization = 'cg',
/
&IONS
/
&CELL
/
ATOMIC_SPECIES
   C   12.01070  C.pbe-mt_fhi.UPF
   O   15.99900  O.pbe-mt_fhi.UPF
   H    1.00794  H.pbe-mt_fhi.UPF
ATOMIC_POSITIONS angstrom
C       -2.22860      18.04690      -0.86320
C       -1.50940      19.22770      -0.86320
C       -1.96570      20.52960      -0.86320
C       -3.37250      20.64710      -0.86320
C       -4.18000      19.46690      -0.86320
C       -3.63140      18.13890      -0.86320
C       -1.54170      16.82310      -0.86320
C       -2.24120      15.61290      -0.86320
C       -1.54300      14.38970      -0.86320
C       -0.04210      14.39140      -0.86320
C        0.65440      15.61600      -0.86320
C       -0.04710      16.82500      -0.86320
C        0.63780      18.05030      -0.86320
C       -3.66560      15.64710      -0.86320
C       -2.27730      13.19210      -0.86320
C        0.69320      13.19460      -0.86320
C        2.07880      15.65310      -0.86320
C        2.04030      18.14620      -0.86320
C        2.58580      19.47620      -0.86320
C        1.77520      20.65500      -0.86320
C        0.36880      20.53280      -0.86320
C       -0.08350      19.22960      -0.86320
C       -4.35240      16.90890      -0.86320
C       -5.75610      16.87760      -0.86320
C       -6.46260      15.67410      -0.86320
C       -5.81750      14.41760      -0.86320
C       -4.39460      14.41340      -0.86320
```

C	-3.70090	13.17160	-0.86320
C	-4.42630	11.94700	-0.86320
C	-3.70960	10.72860	-0.86320
C	-2.24460	10.77940	-0.86320
C	-1.52740	11.91920	-0.86320
C	-0.05580	11.92070	-0.86320
C	0.66210	10.78160	-0.86320
C	2.12690	10.73290	-0.86320
C	2.84260	11.95200	-0.86320
C	2.11680	13.17630	-0.86320
C	2.80890	14.41940	-0.86320
C	4.23150	14.42540	-0.86320
C	4.87470	15.68320	-0.86320
C	4.16730	16.88670	-0.86320
C	2.76330	16.91660	-0.86320
C	-5.83930	11.95260	-0.86320
C	4.25520	11.95940	-0.86320
C	4.95370	13.19950	-0.86320
C	4.96050	10.72160	-0.86320
C	6.37690	10.71720	-0.86320
C	7.06290	11.93710	-0.86320
C	6.36720	13.14750	-0.86320
C	7.06370	9.49650	-0.86320
C	6.39950	8.26390	-0.86320
C	7.11690	7.05510	-0.86320
C	4.98020	8.24560	-0.86320
C	6.45980	5.81950	-0.86320
C	4.25940	9.48550	-0.86320
C	2.83830	9.49680	-0.86320
C	2.19220	8.23900	-0.86320
C	2.89220	7.03240	-0.86320
C	4.29780	6.99080	-0.86320
C	5.04630	5.77770	-0.86320
C	4.42010	4.50320	-0.86320
C	5.18030	3.31780	-0.86320
C	6.58390	3.38060	-0.86320
C	7.22260	4.63260	-0.86320
C	-6.53910	13.19190	-0.86320
C	-7.95300	13.13870	-0.86320
C	-8.64760	11.92770	-0.86320
C	-7.96000	10.70890	-0.86320
C	-6.54360	10.71450	-0.86320
C	-8.64560	9.48790	-0.86320
C	-8.69670	7.04710	-0.86320

```
C       -7.98020      8.25620     -0.86320
C       -8.03860      5.81210     -0.86320
C       -6.56090      8.23920     -0.86320
C       -8.80040      4.62480     -0.86320
C       -8.16060      3.37340     -0.86320
C       -6.75710      3.31170     -0.86320
C       -5.99770      4.49770     -0.86320
C       -6.62500      5.77150     -0.86320
C       -5.87730      6.98520     -0.86320
C       -4.47170      7.02820     -0.86320
C       -3.77270      8.23510     -0.86320
C       -4.42010      9.49210     -0.86320
C       -5.84120      9.47940     -0.86320
H       -3.83190     21.62490      -0.86320
H        2.22880     21.63570      -0.86320
H       -6.32950     17.79020      -0.86320
H       -7.53530     15.76240      -0.86320
H       -1.75160      9.83730     -0.86320
H        0.17000      9.83880     -0.86320
H        5.94730     15.77180      -0.86320
H        4.73920     17.80050      -0.86320
H        6.97150     14.03810      -0.86320
H        1.12240      8.13460     -0.86320
H        2.29930      6.13370     -0.86320
H        4.68290      2.35840     -0.86320
H       -8.55870     14.02840      -0.86320
H       -3.87800      6.12990     -0.86320
H       -2.70270      8.13210     -0.86320
H       -4.92630      4.38770     -0.86320
H        3.34880      4.39200     -0.86320
C       -0.80010     21.45980      -0.86320
O       -0.80290     22.68930      -0.86320
H       -6.25860      2.35360     -0.86320
C        7.67580      2.45050     -0.86320
O        7.67580      1.37230     -0.86320
H       -5.25680     19.54940      -0.86320
H        3.65600     19.62100      -0.86320
K_POINTS automatic
 8 1 1   0 0 0


NON- SELF-CONSISTENT CALCULATION INPUT

&CONTROL
```

```
            calculation = 'nscf' ,
            pseudo_dir = '/usr/software/espresso-5.1.1/pseudo/' ,
            outdir='/home/cloke/quantum_espresso/Chevron_type/scf/ketone/248727',
            prefix = 'ketone',
            verbosity = 'high',
            forc_conv_thr = 1.0D-3,
/
&SYSTEM
            ibrav = 8,
            celldm(1) = 32.31,
            celldm(2) = 5,
            celldm(3) = 20,
            nat = 108,
            ntyp = 3,
            ecutwfc = 4,
            ecutrho = 16 ,
            nbnd = 192,
/
&ELECTRONS
            conv_thr = 0.000001,
            mixing_beta = 0.3,
            mixing_ndim = 4,
            diagonalization = 'cg',
/
&IONS
/
&CELL
/
ATOMIC_SPECIES
  C   12.01070  C.pbe-mt_fhi.UPF
  O   15.99900  O.pbe-mt_fhi.UPF
  H    1.00794  H.pbe-mt_fhi.UPF
ATOMIC_POSITIONS angstrom
C       -2.22860      18.04690      -0.86320
C       -1.50940      19.22770      -0.86320
C       -1.96570      20.52960      -0.86320
C       -3.37250      20.64710      -0.86320
C       -4.18000      19.46690      -0.86320
C       -3.63140      18.13890      -0.86320
C       -1.54170      16.82310      -0.86320
C       -2.24120      15.61290      -0.86320
C       -1.54300      14.38970      -0.86320
C       -0.04210      14.39140      -0.86320
C        0.65440      15.61600      -0.86320
```

C	-0.04710	16.82500	-0.86320
C	0.63780	18.05030	-0.86320
C	-3.66560	15.64710	-0.86320
C	-2.27730	13.19210	-0.86320
C	0.69320	13.19460	-0.86320
C	2.07880	15.65310	-0.86320
C	2.04030	18.14620	-0.86320
C	2.58580	19.47620	-0.86320
C	1.77520	20.65500	-0.86320
C	0.36880	20.53280	-0.86320
C	-0.08350	19.22960	-0.86320
C	-4.35240	16.90890	-0.86320
C	-5.75610	16.87760	-0.86320
C	-6.46260	15.67410	-0.86320
C	-5.81750	14.41760	-0.86320
C	-4.39460	14.41340	-0.86320
C	-3.70090	13.17160	-0.86320
C	-4.42630	11.94700	-0.86320
C	-3.70960	10.72860	-0.86320
C	-2.24460	10.77940	-0.86320
C	-1.52740	11.91920	-0.86320
C	-0.05580	11.92070	-0.86320
C	0.66210	10.78160	-0.86320
C	2.12690	10.73290	-0.86320
C	2.84260	11.95200	-0.86320
C	2.11680	13.17630	-0.86320
C	2.80890	14.41940	-0.86320
C	4.23150	14.42540	-0.86320
C	4.87470	15.68320	-0.86320
C	4.16730	16.88670	-0.86320
C	2.76330	16.91660	-0.86320
C	-5.83930	11.95260	-0.86320
C	4.25520	11.95940	-0.86320
C	4.95370	13.19950	-0.86320
C	4.96050	10.72160	-0.86320
C	6.37690	10.71720	-0.86320
C	7.06290	11.93710	-0.86320
C	6.36720	13.14750	-0.86320
C	7.06370	9.49650	-0.86320
C	6.39950	8.26390	-0.86320
C	7.11690	7.05510	-0.86320
C	4.98020	8.24560	-0.86320
C	6.45980	5.81950	-0.86320
C	4.25940	9.48550	-0.86320

C	2.83830	9.49680	-0.86320
C	2.19220	8.23900	-0.86320
C	2.89220	7.03240	-0.86320
C	4.29780	6.99080	-0.86320
C	5.04630	5.77770	-0.86320
C	4.42010	4.50320	-0.86320
C	5.18030	3.31780	-0.86320
C	6.58390	3.38060	-0.86320
C	7.22260	4.63260	-0.86320
C	-6.53910	13.19190	-0.86320
C	-7.95300	13.13870	-0.86320
C	-8.64760	11.92770	-0.86320
C	-7.96000	10.70890	-0.86320
C	-6.54360	10.71450	-0.86320
C	-8.64560	9.48790	-0.86320
C	-8.69670	7.04710	-0.86320
C	-7.98020	8.25620	-0.86320
C	-8.03860	5.81210	-0.86320
C	-6.56090	8.23920	-0.86320
C	-8.80040	4.62480	-0.86320
C	-8.16060	3.37340	-0.86320
C	-6.75710	3.31170	-0.86320
C	-5.99770	4.49770	-0.86320
C	-6.62500	5.77150	-0.86320
C	-5.87730	6.98520	-0.86320
C	-4.47170	7.02820	-0.86320
C	-3.77270	8.23510	-0.86320
C	-4.42010	9.49210	-0.86320
C	-5.84120	9.47940	-0.86320
H	-3.83190	21.62490	-0.86320
H	2.22880	21.63570	-0.86320
H	-6.32950	17.79020	-0.86320
H	-7.53530	15.76240	-0.86320
H	-1.75160	9.83730	-0.86320
H	0.17000	9.83880	-0.86320
H	5.94730	15.77180	-0.86320
H	4.73920	17.80050	-0.86320
H	6.97150	14.03810	-0.86320
H	1.12240	8.13460	-0.86320
H	2.29930	6.13370	-0.86320
H	4.68290	2.35840	-0.86320
H	-8.55870	14.02840	-0.86320
H	-3.87800	6.12990	-0.86320
H	-2.70270	8.13210	-0.86320

```
H       -4.92630      4.38770     -0.86320
H        3.34880      4.39200     -0.86320
C       -0.80010     21.45980      -0.86320
O       -0.80290     22.68930      -0.86320
H       -6.25860      2.35360     -0.86320
C        7.67580      2.45050     -0.86320
O        7.67580      1.37230     -0.86320
H       -5.25680     19.54940      -0.86320
H        3.65600     19.62100      -0.86320
K_POINTS automatic
 8 1 1   0 0 0
```

9.5 List of Abbreviations used

GNRs	-	graphene nanoribbons
AGNRs	-	armchair graphene nanoribbons
B-7AGNRs	-	boron doped n = 7 armchair graphene nanoribbon
N7AGNRs	-	nitrogen doped n = 7 armchair graphene nanoribbon
CNTs	-	carbon nanotubes
MWCNTs	-	multi-wall carbon nanotubes
ROAMP	-	ring-opening alkyne metathesis polymerization
SEC	-	size-exclusion chromatography
TEM	-	transmission electron microscopy
SEM	-	scanning electron microscopy
AFM	-	atomic force microscopy
TGA	-	thermogravimetric analysis
DSC	-	differential scanning calorimetry
XPS	-	x-ray photoelectron spectroscopy
XRD	-	x-ray diffraction
GPC	-	gel permeation chromatography
SEC	-	size-exclusion chromatography
NC-AFM	-	non-contact atomic force microscopy
STM	-	scanning tunneling microscopy
STS	-	scanning tunneling spectroscopy
CVD	-	chemical vapor deposition
FET	-	field-effect transistor
CNT	-	carbon nanotube
VLSI	-	very large scale integration
UHV	-	ultra-high vacuum
ORTEP	-	Oak Ridge thermal ellipsoid plot
DFT	-	density functional theory
LDA	-	local density approximation
DOS	-	density of states
VB	-	valence band
CB	-	conduction band
MALDI	-	matrix assisted laser desorption ionization
NMR	-	nuclear magnetic resonance
BN	-	boron-nitride
DOE	-	Department of Energy
CV	-	cyclic voltammetry

References

(1) Novoselov, K.S.; Geim, A.K.; Morozov, S.V.; Jiang, D.; Zhang, Y.; Dubonos, S.V.; Grigorieva, I.V.; Firsov, A. A. *Science* **2004**, *306*, 666–669.

(2) Meyer, J. C.; Kisielowski, C.; Erni, R.; Rossell, M. D.; Crommie, M. F.; Zettl, A. *Nano Lett.* **2008**, *8*, 3582–3586.

(3) Yang, H.; Mayne, A. J.; Boucherit, M.; Comtet, G.; Dujardin, G.; Kuk, Y. *Nano Lett.* **2010**, *10*, 943–947.

(4) Dreyer, D. R.; Ruoff, R. S.; Bielawski, C. W. *Angew. Chemie - Int. Ed.* **2010**, *49*, 9336–9344.

(5) Boehm, H. P.; Clauss, A. *Z. Naturforsch* **1962**, *17b*, 1–6.

(6) Wallace, P. R. *Phys. Rev.* **1947**, *71*, 622–634.

(7) Boehm, H. P.; Setton, R.; Stumpp, E. *Carbon* **1986**, *24*, 241–245.

(8) http://www.statista.com/statistics/267366/world-graphite-production/

(9) http://northerngraphite.com/graphite-labs/graphite-price/

(10) Hummers, W.S.; Offeman, R. E. *J. Am. Chem. Soc* **1957**, *208*, 1937–1937.

(11) Zhu, Y.; Murali, S.; Cai, W.; Li, X.; Suk, J. W.; Potts, J. R.; Ruoff, R. S. *Adv. Mater.* **2010**, *22*, 3906–3924.

(12) Stankovich, S.; Dikin, D. A.; Piner, R. D.; Kohlhaas, K. A.; Kleinhammes, A.; Jia, Y.; Wu, Y.; Nguyen, S. T.; Ruoff, R. S. *Carbon* **2007**, *45*, 1558–1565.

(13) Tung, V. C.; Allen, M. J.; Yang, Y.; Kaner, R. B. *Nat. Nanotechnol.* **2009**, *4*, 25–29.

(14) Berger, C.; Wu, X.; Brown, N.; Naud, C.; Li, X.; Song, Z.; Mayou, D.; Li, T.; Hass, J.; Marchenkov, A.; Conrad, E. H.; First, P. N.; De Heer, W. A. *Science* **2006**, *312*, 1191–1196.

(15) Allen, M. J.; Tung, V. C.; Kaner, R. B. *Chem. Rev.* **2010**, *110*, 132–145.

(16) Miller, D. L.; Kubista, K. D.; Rutter, G. M.; Ruan, M.; de Heer, W. A.; Kindermann, M.; First, P. N.; Stroscio, J. A. *Nat. Phys.* **2010**, *6*, 811–817.

(17) Lee, J.; Lee, E. K.; Joo, W.; Jang, Y.; Kim, B.; Lim, J. Y.; Choi, S.; Ahn, S. J.; Ahn, J. R.; Park, M.; Yang, C.; Choi, B. L.; Hwang, S.; Whang, D. *Science* **2014**, *344*, 286–290.

(18) Li, X.; Magnuson, C. W.; Venugopal, A.; Tromp, R. M.; Hannon, J. B.; Vogel, E. M.; Colombo, L.; Ruoff, R. S.; Ruo, R. S. *J. Am. Chem. Soc.* **2011**, *133*, 2816–2819.

(19) Li, X.; Cai, W.; An, J.; Kim, S.; Nah, J.; Yang, D.; Piner, R.; Velamakanni, A.; Jung, I.; Tutuc, E.; Banerjee, S. K.; Colombo, L.; Ruoff, R. S. *Science* **2009**, *324*, 1312–1314.

(20) Ma, T.; Ren, W.; Liu, Z.; Huang, L.; Ma, L.; Ma, X.; Zhang, Z. *ACS Nano* **2014**, *8*, 12806–12813.

(21) Ahn, J.-H.; Hong, B. H. *Nat. Nanotechnol.* **2014**, *9*, 737–738.

(22) Torrisi, F.; Coleman, J. N. *Nat. Nanotechnol.* **2014**, *9*, 738–739.

(23) Raccichini, R.; Varzi, A.; Passerini, S.; Scrosati, B. *Nat. Nanotechnol.* **2014**, *14*, 271–279.

(24) Liu, J. *Nat. Nanotechnol.* **2014**, *9*, 739–741.

(25) Böhm, S. *Nat. Nanotechnol.* **2014**, *9*, 741–742.

(26) Drndić, M. *Nat. Nanotechnol.* **2014**, *9*, 743.

(27) Kostarelos, K.; Novoselov, K. S. *Nat. Nanotechnol.* **2014**, *9*, 744–745.

(28) Han, W.; Kawakami, R. K.; Gmitra, M.; Fabian, J. *Nat. Nanotechnol.* **2014**, *9*, 794–807.

(29) Siochi, E. J. *Nat. Nanotechnol.* **2014**, *9*, 745–747.

(30) Chen, J.; Jang, C.; Xiao, S.; Ishigami, M.; Fuhrer, M. S. *Nat. Nanotechnol.* **2008**, *3*, 8–11.

(31) Akturk, A.; Goldsman, N. *Appl. Phys. Lett.* **2014**, *103*, 0537021–0537028.

(32) Pallecchi, E.; Lafont, F.; Cavaliere, V.; Schopfer, F.; Mailly, D.; Poirier, W.; Ouerghi, A. *Sci. Rep.* **2014**, *4*, 1–7.

(33) Ungersboeck, E.; Dhar, S.; Member, S.; Karlowatz, G.; Sverdlov, V.; Kosina, H.; Selberherr, S. *IEEE Trans. Electron Devices* **2007**, *54*, 2183–2190.

(34) Schwierz, F. *Nat. Nanotechnol.* **2010**, *5*, 487–496.

(35) Andrei, E. Y.; Li, G.; Du, X. *Reports Prog. Phys.* **2012**, *75*, 056501–056547.

(36) Beenakker, C. W. *J. Rev. Mod. Phys.* **2007**, *80*, 1–20.

(37) Yang, L.; Park, C. H.; Son, Y. W.; Cohen, M. L.; Louie, S. G. *Phys. Rev. Lett.* **2007**, *99*, 6–9.

(38) Yang, L.; Cohen, M. L.; Louie, S. G. *Phys. Rev. Lett.* **2008**, *101*, 1–4.

(39) Son, Y.-W.; Cohen, M. L.; Louie, S. G. *Nature* **2006**, *444*, 347–349.

(40) Konishi, A.; Hirao, Y.; Matsumoto, K.; Kurata, H.; Kishi, R.; Shigeta, Y.; Nakano, M.; Tokunaga, K.; Kamada, K.; Kubo, T. *J. Am. Chem. Soc.* **2013**, *135*, 1430–1437.

(41) Abbas, A. N.; Liu, G.; Liu, B.; Zhang, L.; Liu, H.; Ohlberg, D.; Wu, W.; Zhou, C. *ACS Nano* **2014**, *8*, 1538–1546.

(42) Bachtold, A.; Hadley, P.; Nakanishi, T.; Dekker, C. *Science* **2001**, *294*, 1317–1320.

(43) Kosynkin, D. V; Higginbotham, A. L.; Sinitskii, A.; Lomeda, J. R.; Dimiev, A.; Price, B. K.; Tour, J. M. *Nature* **2009**, *458*, 872–876.

(44) Rangel, N. L.; Sotelo, J. C.; Seminario, J. M. *J. Chem. Phys.* **2009**, *131*, 1–5.

(45) Jiao, L.; Zhang, L.; Wang, X.; Diankov, G.; Dai, H. *Nature* **2009**, *458*, 877–880.

(46) Li, X.; Wang, X.; Zhang, L.; Lee, S.; Dai, H. *Science* **2008**, *319*, 1229–1232.

(47) Derenskyi, V.; Gomulya, W.; Rios, J. M. S.; Fritsch, M.; Fröhlich, N.; Jung, S.; Allard, S.; Bisri, S. Z.; Gordiichuk, P.; Herrmann, A.; Scherf, U.; Loi, M. A. *Adv. Mater.* **2014**, *26*, 5969–5975.

(48) Choi, S-J.; Wang, C.; Lo, C.C.; Bennett, P.; Javey, A.; Bokor, J. *Appl. Phys. Lett.* **2012**, *101*, 1121041–1121044.

(49) Choi, S. J.; Bennett, P.; Takei, K.; Wang, C.; Lo, C. C.; Javey, A.; Bokor, J. *ACS Nano* **2013**, *7*, 798–803.

(50) Wang, X.; Ouyang, Y.; Li, X.; Wang, H.; Guo, J.; Dai, H. *Phys. Rev. Lett.* **2008**, *100*, 100–103.

(51) Wang, X.; Ouyang, Y.; Jiao, L.; Wang, H.; Xie, L.; Wu, J.; Guo, J.; Dai, H. *Nat. Nanotechnol.* **2011**, *6*, 563–567.

(52) Jiao, L.; Wang, X.; Diankov, G.; Wang, H.; Dai, H. *Nat. Nanotechnol.* **2010**, *5*, 321–325.

(53) Cai, J.; Ruffieux, P.; Jaafar, R.; Bieri, M.; Braun, T.; Blankenburg, S.; Muoth, M.; Seitsonen, A. P.; Saleh, M.; Feng, X.; Müllen, K.; Fasel, R. *Nature* **2010**, *466*, 470–473.

(54) Kim, W. Y.; Kim, K. S. *Nat. Nanotechnol.* **2008**, *3*, 408–412.

(55) Son, Y. W.; Cohen, M. L.; Louie, S. G. *Phys. Rev. Lett.* **2006**, *97*, 1–4.

(56) Barone, V.; Hod, O.; Scuseria, G. E. *Nano Lett.* **2006**, *6*, 2748–2754.

(57) Zhang, X.; Yazyev, O. V.; Feng, J.; Xie, L.; Tao, C.; Chen, Y. C.; Jiao, L.; Pedramrazi, Z.; Zettl, A.; Louie, S. G.; Dai, H.; Crommie, M. F. *ACS Nano* **2013**, *7*, 198–202.

(58) Terrones, H.; Lv, R.; Terrones, M.; Dresselhaus, M. S. *Reports Prog. Phys.* **2012**, *75*, 1–30.

(59) Martins, T. B.; Miwa, R. H.; Da Silva, A. J. R.; Fazzio, a. *Phys. Rev. Lett.* **2007**, *98*, 3–6.

(60) Yan, Q.; Huang, B.; Yu, J.; Zheng, F.; Zang, J.; Wu, J. *Nano Lett.* **2007,** *7***,** 1469–1473.

(61) Avouris, P.; Chen, Z.; Perebeinos, V. *Nat. Nanotechnol.* **2007**, *2*, 605–615.

(62) Qi, Z. J.; Daniels, C.; Hong, S. J.; Park, Y. W.; Meunier, V.; Drndi, M. *ACS Nano* **2015**, *9,* 3510–3520.

(63) Pan, M.; Girão, E. C.; Jia, X.; Bhaviripudi, S.; Li, Q.; Kong, J.; Meunier, V.; Dresselhaus, M. S. *Nano Lett.* **2012**, *12*, 1928–1933.

(64) Tao, C.; Jiao, L.; Yazyev, O. V.; Chen, Y.-C.; Feng, J.; Zhang, X.; Capaz, R. B.; Tour, J. M.; Zettl, A.; Louie, S. G.; Dai, H.; Crommie, M. F. *Nat. Phys.* **2011**, *7*, 616–620.

(65) Chen, Y. C.; De Oteyza, D. G.; Pedramrazi, Z.; Chen, C.; Fischer, F. R.; Crommie, M. F. *ACS Nano* **2013**, *7*, 6123–6128.

(66) Chen, Y-C.; Cao, T.; Chen, C.; Pedramrazi, Z.; Haberer, D.; de Oteyza, D. G.; Fischer, F. R.; Louie, S. G.; Crommie, M. F. *Nat. Nanotechnol.* **2015**, *10*, 156–160.

(67) Basagni, A.; Sedona, F.; Pignedoli, C. A.; Cattelan, M.; Nicolas, L.; Casarin, M.; Sambi, M. *J. Am. Chem. Soc.* **2015**, *137*, 1802–1808.

(68) Narita, A.; Verzhbitskiy, I. A.; Frederickx, W.; Mali, K.S.; Jensen, S. A.; Hansen, M. R.; Bonn, M.; De Feyter, S.; Casiraghi, C.; Feng, X.; Müllen, K. *ACS Nano* **2014**, *8*, 11622–11630.

(69) Talirz, L.; Söde, H.; Cai, J.; Ruffieux, P.; Blankenburg, S.; Jafaar, R.; Berger, R.; Feng, X.; Müllen, K.; Passerone, D.; Fasel, R.; Pignedoli, C. A. *J. Am. Chem. Soc.* **2013**, *135*, 2060–2063.

(70) Cai, J.; Pignedoli, C. A.; Talirz, L.; Ruffieux, P.; Söde, H.; Liang, L.; Meunier, V.; Berger, R.; Li, R.; Feng, X.; Müllen, K.; Fasel, R. *Nat. Nanotechnol.* **2014**, *9*, 896–900.

(71) Bronner, C.; Stremlau, S.; Gille, M.; Brauße, F.; Haase, A.; Hecht, S.; Tegeder, P. *Angew. Chemie - Int. Ed.* **2013**, *52*, 4422–4425.

(72) Vo, T. H.; Shekhirev, M.; Kunkel, D. A.; Morton, M. D.; Berglund, E.; Kong, L.; Wilson, P. M.; Dowben, P. A.; Enders, A.; Sinitskii, A. *Nat. Commun.* **2014**, *5*, 3189.

(73) Bieller, S.; Zhang, F.; Bolte, M.; Bats, J. W.; Lerner, H.; Wagner, M. *Synthesis* **2004**, *23*, 2107–2113.

(74) Hoffend, C.; Schödel, F.; Bolte, M.; Lerner, H. W.; Wagner, M. *Chem. - A Eur. J.* **2012**, *18*, 15394–15405.

(75) Blankenburg, S.; Cai, J.; Ruffieux, P.; Jaafar, R.; Passerone, D.; Feng, X.; Müllen, K.; Fasel, R.; Pignedoli, C. A. *ACS Nano* **2012**, *6*, 2020–2025.

(76) Ruffieux, P.; Cai, J.; Plumb, N. C.; Patthey, L.; Prezzi, D.; Ferretti, A.; Molinari, E.; Feng, X.; Müllen, K.; Pignedoli, C. A..; Fasel, R. *ACS Nano* **2012**, *6*, 6930–6935.

(77) Batra, A.; Cvetko, D.; Kladnik, G.; Adak, O.; Cardoso, C.; Ferretti, A.; Prezzi, D.; Molinari, E.; Morgante, A.; Venkataraman, L. *Chem. Sci.* **2014**, *00*, 1–5.

(78) Bronner, C.; Tegeder, P. *J. Phys. Chem. C* **2015**, *119*, 486–493.

(79) Dou, C.; Saito, S.; Matsuo, K.; Hisaki, I.; Yamaguchi, S. *Angew. Chemie - Int. Ed.* **2012**, *51*, 12206–12210.

(80) Björk, J.; Stafström, S.; Hanke, F. *J. Am. Chem. Soc.* **2011**, *133*, 14884–14887.

(81) Fleming, I. *Nature* **1967**, *216*, 151–152.

(82) Schuller, D. J.; Zhu, W.; Stojiljkovic, I.; Wilks, a.; Poulos, T. L. *Biochemistry* **2001**, *40*, 11552–11558.

(83) Gray, E. G. *Nature* **1955**, *175*, 642–643.

(84) Bottari, G.; Trukhina, O.; Ince, M.; Torres, T. *Coord. Chem. Rev.* **2012**, *256*, 2453–2477.

(85) Shelnutt, J. A.; Medforth, C. J. Self-Assembled Porphyrin Nanostructures and Their Potential Applications. In *Organic Nanomaterials: Synthesis, Characterization, and Device Applications*; Torres, T.; Bottari, G., Ed.; John Wiley & Sons, Inc: Hoboken, NJ, 2013; pp 103–130.

(86) Medforth, C. J.; Wang, Z.; Martin, K. E.; Song, Y.; Jacobsen, J. L.; Shelnutt, J. A. *Chem. Commun.* **2009**, *47*, 7261–7277.

(87) Son, H.; Jin, S.; Patwardhan, S.; Wezenberg, S. J.; Jeong, N. C.; So, M.; Wilmer, C. E.; Sarjeant, A. A.; Schatz, G. C.; Snurr, R. Q.; Farha, O. K.; Wiederrecht, G. P.; Hupp, J. T. *J. Am. Chem. Soc.* **2013**, *135*, 862–869.

(88) Farha, O. K.; Shultz, A. M.; Sarjeant, A. A.; Nguyen, S. T.; Hupp, J. T. *J. Am. Chem. Soc.* **2011**, *133*, 5652–5655.

(89) Gao, D.; Zhou, H.; Wang, J.; Miao, S.; Yang, F.; Wang, G.; Wang, J.; Bao, X. *J. Am. Chem. Soc.* **2015**, *137*, 4288–4291.

(90) Fateeva, A.; Chater, P. A.; Ireland, C. P.; Tahir, A. A.; Khimyak, Y. Z.; Wiper, P. V; Darwent, J. R.; Rosseinsky, M. J. *Angew. Chem. Int. Ed.* **2012**, *124*, 7558–7562.

(91) Lafferentz, L.; Eberhardt, V.; Dri, C.; Africh, C.; Comelli, G.; Esch, F.; Hecht, S.; Grill, L. *Nat. Chem.* **2012**, *4*, 215–220.

(92) O'Sullivan, M. C.; Sprafke, J. K.; Kondratuk, D. V; Rinfray, C.; Claridge, T. D. W.; Saywell, A.; Blunt, M. O.; O'Shea, J. N.; Beton, P. H.; Malfois, M.; Anderson, H. L. *Nature* **2011**, *469*, 72–75.

(93) Davis, M.; Senge, M. O.; Locos, O. B. *Z. Naturforsch* **2010**, *65*, 1–40.

(94) Davis, N. K. S.; Thompson, A. L.; Anderson, H. L. *J. Am. Chem. Soc.* **2011**, *133*, 30–31.

(95) Haq, S.; Hanke, F.; Sharp, J.; Persson, M.; Amabilino, D. B.; Raval, R. *ACS Nano* **2014**, *8*, 8856–8870.

(96) Ito, S.; Wehmeier, M.; Brand, J. D.; Kübel, C.; Epsch, R.; Rabe, J. P.; Müllen, K. *Chem. Eur. J.* **2000**, *6*, 4327–4342.

(97) CRC Handbook. *CRC Handb.* **2011**, 12–114.

(98) Schlapbach, L.; Züttel, A. *Nature* **2001**, *414*, 353–358.

(99) Jeon, K.-J.; Moon, H. R.; Ruminski, A. M.; Jiang, B.; Kisielowski, C.; Bardhan, R.; Urban, J. J. *Nat. Mater.* **2011**, *10*, 286–290.

(100) US Department of Energy. Status of Hydrogen Storage Technologies. http://energy.gov/eere/fuelcells/status-hydrogen-storage-technologies

(101) Kumar, B.; Llorente, M.; Froehlich, J.; Dang, T.; Sathrum, A.; Kubiak, C. P. *Annu. Rev. Phys. Chem.* **2012**, *63*, 541–569.

(102) Kang, P.; Meyer, T. J.; Brookhart, M. *Chem. Sci.* **2013**, *4*, 3497–3502.

(103) Kang, P.; Zhang, S.; Meyer, T. J.; Brookhart, M. *Angew. Chemie - Int. Ed.* **2014**, *53*, 8709–8713.

(104) Sampson, M. D.; Nguyen, A. D.; Grice, K. a; Moore, C. E.; Rheingold, A. L.; Kubiak, C. P. *J. Am. Chem. Soc.* **2014**, *136*, 5460–5471.

(105) Manthiram, K.; Surendranath, Y.; Alivisatos, A. P. *J. Am. Chem. Soc.* **2014**, *136*, 7237–7240.

(106) Feng, X.; Jiang, K.; Fan, S.; Kanan, M. W. *J. Am. Chem. Soc.* **2015**, *137*, 4606–4609.

(107) Koh, J. H.; Jeon, H. S.; Jee, M. S.; Nursanto, E. B.; Lee, H.; Hwang, Y. J.; Min, B. K. *J. Phys. Chem. C.* **2015**, *119*, 883–889.

(108) Mistry, H.; Reske, R.; Zeng, Z.; Zhao, Z.; Strasser, P.; Cuenya, B. R. *J. Am. Chem. Soc.* **2014**, *136*, 16473–16476.

(109) Zhu, W.; Michalsky, R.; Metin, Ö.; Lv, H.; Guo, S.; Wright, C. J.; Sun, X.; Peterson, A. A.; Sun, S. *J. Am. Chem. Soc.* **2013**, *135*, 16833–16836.

(110) Zhu, W.; Zhang, Y.-J.; Zhang, H.; Lv, H.; Li, Q.; Michalsky, R.; Peterson, A. A.; Sun, S. *J. Am. Chem. Soc.* **2014**, *136*, 16132–16135.

(111) Manthiram, K.; Beberwyck, B. J.; Alivisatos, A. P. *J. Am. Chem. Soc.* **2014**, *136*, 13319–13325.

(112) Alves, D. C. B.; Silva, R.; Voiry, D.; Asefa, T.; Chhowalla, M. *Mater. Renew. Sustain. Energy* **2015**, *4*, 1–7.

(113) Kim, D.; Resasco, J.; Yu, Y.; Asiri, A. M.; Yang, P. *Nat. Commun.* **2014**, *5*, 1–8.

(114) Medina-Ramos, J.; Pupillo, R. C.; Keane, T. P.; DiMeglio, J. L.; Rosenthal, J. *J. Am. Chem. Soc.* **2015**, *137*, 5021–5027.

(115) Medina-Ramos, J.; Dimeglio, J. L.; Rosenthal, J. *J. Am. Chem. Soc.* **2014**, *136*, 8361–8367.

(116) Buqa, H.; Goers, D.; Holzapfel, M.; Spahr, M. E.; Novák, P. *J. Electrochem. Soc.* **2005**, *152*, A474–A481.

(117) Chan, C. K.; Peng, H.; Liu, G.; McIlwrath, K.; Zhang, X. F.; Huggins, R. A.; Cui, Y. *Nat. Nanotechnol.* **2008**, *3*, 31–35.

(118) Li, L.; Kovalchuk, A.; Tour, J. M. *Nano Res.* **2014**, *7*, 1319–1326.

(119) Li, L.; Kovalchuk, A.; Fei, H.; Peng, Z.; Li, Y.; Kim, N. D.; Xiang, C.; Yang, Y.; Ruan, G.; Tour, J. M. *Adv. Energy Mater.* **2015**, *5*, 1–6.

(120) Li, L.; Raji, A. R. O.; Tour, J. M. *Adv. Mater.* **2013**, *25*, 6298–6302.

(121) Lin, J.; Peng, Z.; Xiang, C.; Ruan, G.; Yan, Z.; Natelson, D.; Tour, J. M. *ACS Nano* **2013**, *7*, 6001–6006.

(122) Mohamedi, M.; Lee, S.-J.; Takahashi, D.; Nishizawa, M.; Itoh, T.; Uchida, I. *Electrochim. Acta* **2001**, *46*, 1161–1168.

(123) Noerochim, L.; Wang, J.-Z.; Chou, S.-L.; Li, H.-J.; Liu, H.-K. *Electrochim. Acta* **2010**, *56*, 314–320.

(124) Cheng, Y-J.; Yang, S-H.; Hsu, C-S. *Chem. Rev.* **2009**, *109*, 5868–5923.

(125) Weber, J.; Thomas, A. *J. Am. Chem. Soc.* **2008**, *130*, 6334–6335.

(126) Friend, R. H.; Friend, R. H.; Gymer, R. W.; Gymer, R. W.; Holmes, a. B.; Burroughes, J. H.; Holmes, a. B.; Burroughes, J. H.; Marks, R. N.; Taliani, C.; Marks, R. N.; Bradley, D. D. C.; Taliani, C.; Bradley, D. D. C.; Dos Santos, D. a.; Lo, M.; Bredas, J. L.; Logdlund, M.; Salaneck, W. R.; Salaneck, W. R.; Dos Santos, D. a.; Bre, J. L.; Slyke, V. *Nature* **1999**, *397*, 121–128.

(127) Reineke, S.; Lindner, F.; Schwartz, G.; Seidler, N.; Walzer, K.; Lüssem, B.; Leo, K. *Nature* **2009**, *459*, 234–238.

(128) Kanimozhi, C.; Yaacobi-gross, N.; Chou, K. W.; Amassian, A.; Anthopoulos, T. D.; Patil, S. *J. Am. Chem. Soc.* **2012**, *134*, 16532–16535.

(129) Knopfmacher, O.; Hammock, M. L.; Appleton, A. L.; Schwartz, G.; Mei, J.; Lei, T.; Pei, J.; Bao, Z. *Nat. Commun.* **2014**, *5*, 2954.

(130) Jagtap, S. P.; Mukhopadhyay, S.; Coropceanu, V.; Brizius, G. L.; Brédas, J. L.; Collard, D. M. *J. Am. Chem. Soc.* **2012**, *134*, 7176–7185.

(131) Breen, C. A.; Tischler, J. R.; Bulović, V.; Swager, T. M. *Adv. Mater.* **2005**, *17*, 1981–1985.

(132) Sudeep, P. K.; James, P. V.; Thomas, K. G.; Kamat, P. V. *J. Phys. Chem. A* **2006**, *110*, 5642–5649.

(133) Wang, Y.; Park, J. S.; Leech, J. P.; Miao, S.; Bunz, U. H. F. *Macromolecules* **2007**, *40*, 1843–1850.

(134) Bunz, U. H. F. *Macromol. Rapid Commun.* **2009**, *30*, 772–805.

(135) Khan, A.; Hecht, S. *J. Polym. Sci. Part A Polym. Chem.* **2006**, *44*, 1619–1627.

(136) Grubbs, R. H.; Kratz, D. *Chem. Ber.* **1993**, *126*, 149–157.

(137) Jones, T. V.; Slutsky, M. M.; Laos, R.; de Greef, T.F.A.; Tew, G. N. *J. Am. Chem. Soc.* **2005**, *127*, 17235–17240.

(138) Blatchly, R. A.; Tew, G. N. *J. Org. Chem.* **2003**, *68*, 8780–8785.

(139) Banno, M.; Yamaguchi, T.; Nagai, K.; Kaiser, C.; Hecht, S.; Yashima, E. *J. Am. Chem. Soc.* **2012**, *134*, 8718–8728.

(140) Zhu, N.; Hu, W.; Han, S.; Wang, Q.; Zhao, D. *Org. Lett.* **2008**, *10*, 4283–4286.

(141) Jones, T. V; Slutsky, M. M.; Laos, R. M.; Greef, T. F.; Tew, G. N. *J. Am. Chem. Soc.* **2005**, *127*, 17235–17240.

(142) Fischer, F. R.; Nuckolls, C. *Angew. Chemie - Int. Ed.* **2010**, *49*, 7257–7260.

(143) Sedbrook, D. F.; Paley, D. W.; Steigerwald, M. L.; Nuckolls, C.; Fischer, F. R. *Macromolecules* **2012**, *45*, 5040–5044.

(144) Bellone, D. E.; Bours, J.; Menke, E. H.; Fischer, F. R. *J. Am. Chem. Soc.* **2015**, *137*, 850–856.

(145) Orita, A.; Hasegawa, D.; Nakano, T.; Otera, J. *Chem. - A Eur. J.* **2002**, 9, 2000–2004.

(146) Yang, J.; Swager, T. M. *J. Am. Chem. Soc.* **1998**, *120*, 11864–11873.

(147) Marsden, J. A.; Palmer, G. J.; Haley, M. M.; Klemm, L. H. *Eur. J. Org. Chem.* **2003**, *13*, 2355–2369.

(148) Ando, S.; Ohta, E.; Kosaka, A.; Hashizume, D.; Koshino, H.; Fukushima, T.; Aida, T. *J. Am. Chem. Soc.* **2012**, *134*, 11084–11087.

(149) Kajitani, T.; Suna, Y.; Kosaka, A.; Osawa, T.; Fujikawa, S.; Takata, M.; Fukushima, T.; Aida, T. *J. Am. Chem. Soc.* **2013**, *135*, 14564–14567.

(150) Wittig, G.; Lehmann, G. *Chem. Ber.* **1957**, *90*, 875–891

(151) Winkler H.J.S., Wittig, G. *J. Org. Chem.* **1963**, *28*, 1733–1740.

(152) Blake, A. J.; Cooke, P. A.; Doyle, K. J.; Gair, S.; Simpkins, N. S. *Tetehedron Lett.* **1998**, *39*, 9093–9096.

(153) Ohta, E.; Sato, H.; Ando, S.; Kosaka, A.; Fukushima, T.; Hashizume, D.; Yamasaki, M.; Hasegawa, K.; Muraoka, A.; Ushiyama, H.; Yamashita, K.; Aida, T. *Nat. Chem.* **2011**, *3*, 68–73.

(154) Asao, N.; Nogami, T.; Lee, S.; Yamamoto, Y. *J. Am. Chem. Soc.* **2003**, *125*, 10921–10925.

(155) Arslan, H.; Saathoff, J. D.; Bunck, D. N.; Clancy, P.; Dichtel, W. R. *Angew. Chemie - Int. Ed.* **2012**, *51*, 12051–12054.

(156) Omachi, H.; Nakayama, T.; Takahashi, E.; Segawa, Y.; Itami, K. *Nat. Chem.* **2013**, *5*, 572–576.

(157) Golling, F. E.; Quernheim, M.; Wagner, M.; Nishiuchi, T.; Müllen, K. *Angew. Chemie – Int. Ed.* **2014**, *53*, 1525–1528.

(158) Quernheim, M.; Golling, F. E.; Zhang, W.; Wagner, M.; Räder, H.-J.; Nishiuchi, T.; Müllen, K. *Angew. Chemie Int. Ed.* **2015**, 10341–10346.

(159) Ormsby, J.L.; Black, T.D.; Hilton, C.L.; Bharat; King, B.T. *Tetrahedron* **2008**, *64*, 11370–11378.